In Vivo Dynamic AFM Mapping of Viscoelastic Properties of the Primary Plant Cell Wall



Jacob Seifert

Wadham College

University of Oxford

A thesis submitted for the degree of

Doctor of Philosophy

Hilary 2018

Acknowledgements

I want to thank my supervisors Ian Moore and Sonia Contera for creating such an exciting interdisciplinary project. I am very grateful for their decision that I was the most suitable candidate for this project and for their fantastic supervision. At the same time they gave me the space and even encouraged me to form and develop the project on my own and taylor it to my strengths. Overall the colaboration between Plant Sciences and Physics opened an exciting new world to me and gave me insights into the difficulties and strengths of projects bewteen different fields. This experience allowed me to develop my personality to a new level which I appreciate very much.

I am very grateful for the guidance and help of our academic administrator Gem Toes-Chrichton through all the admin procedures over the years. I would have struggled a lot more without it.

I would further like to express my gratitude to the work of our lab technician Caroline O'Brian, whose work allowed a smooth running process in the lab. I also would like to say thanks to Sarah Rodgers for taking care of purchases which was often not as easy as it should be.

I appreciate the passion for science of Alexis Peaucelle, who welcomed me to Cambridge to share his knowlegde about AFM imaging on plant organs. I am very thankful that he recognized my work as relevant for the field.

I am grateful for the input during conferences and seminars from academics from many different fields.

Additionally, I also want to thank the Moore Lab for a great time, in particular Charlotte Kirchhelle for teaching me a lot about biology and its scientific methods. I enjoyed our scientific and general discussions in the Turf or Uniclub very much. These discussions helped me not only to have a better understanding of the scientific problems but also to relax after exhausting days in the lab.

My thanks also belongs to the Contera Lab. I am particularly happy about the fact that Michael Lherbette started his Masters project when I started my DPhil project and we could learn about the AFM and Oxford together, which made the beginning of the project much easier. I want to thank Andrea Illeana Bonilla-Brunner for helping me with the materials and the indentation experiments to test the stability of the FIV method and also that she showed Michael and me a lot about Oxford's night-life. I am also very glad that Andrea taught me how to play Dominoes, which was a nice substitute for playing Skat which would be the German equivalent pub activity. Furthermore, I am very thankful for the many discussions I had with Zeinab Al-Rekabi, Alba Rosa Piacenti, and Casey Adams, about viscoelasticity and dynamic responses.

I also value the friendship of the Husain Lab (Neuroscience) whose members accepted me as an honorary lab member and friend and thus provided another social fixpoint in Oxford.

I am very glad for the support of my partner Annika Kienast. She helped me proof-reading the thesis but even more important was her emotional support during the period of the project. I am very happy to have her on my side and that she is so understanding with me focussing on science.

I also want to thank my fellow students during my Undergraduate studies and my Masters in Dresden, without whom I would not have become the physicist and person I am today. Special thanks belongs to Felix Fritzsch who always knew my strengths better than I did and helped me achieve my best. Felix also deserves special recognition for correcting my thesis for mathematical inconsistencies concerning notation and reasoning.

I am very happy that I have met my dear friend Eduardo Queiroz with whom I shared many memorable moments from the very beginning of the project.

Finally, I want to thank the Leverhulme Trust for funding this very exciting project including my PhD position.

Abstract

Plant development is a complex multiscale process out of thermodynamic equilibrium. While sophisticated mathematical models of this process exist, there are only a few studies which provide experimental evidence. At the cellular level, unidirectional plant growth can be described by the viscoelastic Maxwell (MW) model. At the subcellular level more complicated thermodynamic models exist for which experimental proof is missing, due to the lack of suitable experimental methods. Modern approaches in multifrequency AFM enable high resolution viscoelastic mapping for cells and polymers. However, these methods are based on the viscoelastic Kelvin-Voigt model and, therefore, the viscoelastic properties cannot be associated with plant growth. I provide a link between the generalised MW model and the AFM cantilever observables. Then I show that the primary plant cell wall (CW) behaves, at the subcellular level, like a standard linear solid (SLS). I further use the description of the CW as a SLS and the spatial information of the dynamic modulus to determine the characteristic quantities k_∞, k_M, η, and τ of the SLS with spatial resolution. The application of two eigenmodes suggests that it is possible to extend the approach from the SLS description to reconstruct the relaxation modulus of polymer networks. This is demonstrated by the stiffness k_2 and relaxation time τ_2 which are increased and decreased, respectively, compared to the first eigenmode. Finally, using the example of whole living seedlings of the plant *Arabidopsis thaliana*, I use this theoretical framework to demonstrate, that the viscoelastic properties at a subcellular level can be linked to thermodynamic models of plant growth. I show that these can be derived using the Onsager principle I develop a non-equilibrium approach to describe the time evolution of thermodynamic systems. Moreover, pharmacological and genetic manipulation of young seedlings indicates that these viscoelastic measurements can be used as an analytical tool to characterise CW deficiencies.

Contents

1 Introduction **1**

1.1 The Primary Plant Cell Wall . . . 3

1.1.1 Cell Wall Components: The Molecular Structure . . . 3

1.1.2 Cell Wall Architectures . . . 8

1.1.2.1 The Tethered Network Model . . . 8

1.1.2.2 The Mechanical Hotspot Hypothesis . . . 9

1.1.2.3 Cell Walls in a Cellular Context . . . 10

1.2 What are Mechanical Properties? . . . 10

1.2.1 Elasticity, Viscosity, and Viscoelasticity . . . 11

1.3 Multiscale – Continuum Mechanics Versus Molecular Mechanisms . . . 17

1.4 Plant Growth . . . 22

1.4.1 Growth Factors . . . 24

1.4.2 Cell Growth: A Conceptual Description . . . 25

1.4.3 Mathematical Models of Cellular Growth . . . 27

1.4.3.1 The Lockhart Model . . . 28

1.4.3.2 The Dyson, Band, Jensen Model . . . 29

1.4.3.3 The Veytsman-Cosgrove Model . . . 32

1.5 Experimental Determination of Plant Cell Wall Mechanics . . . 36

2 Materials and Methods **43**

2.1 Plant Material and Sample Preparation . . . 43

2.1.1 Wildtype Seedlings . . . 43

2.1.2 Pharmacological Interventions . . . 45

2.2 Preparation of Hypocotyl Casts and Moulds . . . 47

2.3 Atomic Force Microscopy . . . 48

2.3.1 Dynamic Mechanical Mapping . . . 48

2.3.2 Force-Volume Measurements . . . 50

2.4 Photographs . . . 50
2.5 Confocal Microscopy . . . 50
2.5.1 Determination of Cell Wall Thickness . . . 50
2.6 Data Analysis . . . 52
2.6.1 AFM Library . . . 52
2.6.2 Hydrodynamic Calibration . . . 54
2.6.3 Computational Extraction of Cell Walls . . . 54
2.6.4 Statistical Analysis and Data Representation of the Mechanical Properties . . . 56
2.6.5 Cell Length and Growth Velocity . . . 57
2.6.6 Hypocotyl Length . . . 57
2.6.7 Measuring Cell Wall Thickness from Confocal Microscopy Slices 58

I Development of AFM Based Techniques and Theory for Quantitative Mapping of Live Tissues of *Arabidopsis thaliana* 60

3 Accurate Imaging With AFM on *Arabidopsis* Hypocotyl Tissues 62
3.1 Contact Mode – Stiffness And Topography And Cantilever Design . . 63
3.1.1 Basic Imaging And Artefacts . . . 63
3.1.1.1 Topography Artefacts . . . 63
3.1.2 Sample Artefacts . . . 70
3.1.2.1 Cell Damage During Data Acquisition . . . 71
3.1.2.2 Artefacts During Sample Preparation . . . 72
3.1.3 Force Volume Measurements . . . 73
3.1.3.1 Derivation of the Hertz Model for a Conical Indentation of an Inclined Half-Space . . . 73
3.1.3.2 The Force Response of an Axisymmetric Cone Indenting an Inclined Half-Space . . . 75
3.1.4 Determination of the Contact Point: Force-Indentation Variation (FIV) . . . 78
3.1.5 The Effect of Noise on the Determination of the Contact Point 81
3.1.6 Cantilever Artefacts . . . 83
3.2 Tapping Mode – Topography And Hydrodynamic Interactions . . . 85
3.2.1 Hydrodynamic effects . . . 85
3.2.2 Reproducibly of AFM Measurements . . . 90

3.3 Summary 91

4 Quantitative Mechanical Properties Mapping With AFM 92

4.1 A Model for Dynamic AFM Mapping of Linear Viscoelastic Materials 93
4.2 Choosing the indentation model 100
4.3 The Maxwell Approximation 106
4.4 Quantitative Viscoelastic Properties Mapping of Primary Plant Cell Walls Using Dynamic AFM 108
4.5 Comparison with Previously Reported Values of Elastic Modulus . . . 111
4.6 The Relevant Timescale of The Cell Wall Response Can Be Used to Understand the Underlying Mechanism of Cell Growth 112
4.7 Local Distribution of Material Properties to Test the Validity of the Viscoelastic Model 115
4.8 Reconstruction of the Generalised Maxwell Model in the Plant Cell Wall Using Stress Gradients 119
4.9 Summary 134

II Biophysics of Plant Growth 136

5 Hypocotyl Growth: Cell Wall Properties Link to Cellular Growth 138

5.1 Deriving the Growth Equations for Plant Growth from First Principles 139
5.2 The Effect of Cell Geometry on the Measurements of Mechanical Properties 143
5.2.1 Estimation of the Cell Wall Thickness 144
5.2.2 Cell Length and Mechanical Properties 147
5.3 Determination of the Yield Threshold From Plasmolysis Experiments 148
5.4 Comparison of The Viscoelastic Properties of Different Cell Types . . 151
5.5 Physiological Relevance of Viscoelasticity 158
5.5.1 Cellulose Reduction 160
5.5.2 Pectin Matrix Alteration 165
5.6 The Relation Between Plant Growth And Viscoelastic Properties . . 173
5.7 Change of Viscoelastic Properties at Dark-Light Transitions 178
5.8 Exploring New Realms – An Investigation of The RAB-E1d Phenotype 184
5.9 Summary 195

6 Conclusions, General Discussion, and Outlook **198**
6.1 Biophysical Findings 198
6.1.1 Measurement Accuracy 199
6.1.2 Mechanical Properties of the Cell Wall 201
6.1.3 Connecting Plant Growth with Mechanical Properties 201
6.1.4 Experimental Results 205
6.2 Biological Findings 208
6.3 Future Work 214
6.4 Relevance Beyond Plant Biophysics 220

Bibliography **224**

List of Figures

1.1 Structure of a β-1,4-glucose linked glucan chain. 3
1.2 Homogalacturonan salt bridges. 6
1.3 Models of cell wall (CW) architectures. 8
1.4 Plant CW in the cellular context of adjacent cells after cell division. The different angles of the CMFs indicate the different orientations of the fibres in the different lamellae. The wall structure is from the side view, in contrast to the top view of one lamella in fig. 1.3b. 10
1.5 Elastic deformation 11
1.6 Viscoelastic models. 13
1.7 Cellular growth. 26
1.8 Dyson CW model. 31

2.1 *A. thaliana* seedling on AFM sample holder. 44
2.2 Chemically treated seedlings. 45
2.3 Rab seedlings. 46
2.4 Illustration of measured cross section of confocal measurements. The circles represent cells in a cross section of a cylindrical hypocotyl. The dashed line shows the height at which the CW thickness was measured. 51
2.5 Representation of the programmed AFM library showing hierarchy and dependencies of the python classes as well as the underlying functions of the individual classes. 53
2.6 Cell length measurements. 56

3.1 Resolution of a step function. 65
3.2 Feature size dependant resolution. 66
3.3 Artefacts at a cylindrical tissue 68
3.4 Tissue induced artefacts in real data. 69
3.5 Cell damage. 71
3.6 Schematic projection of cylinder and inclined half-space. 76

3.7 Attenuation factor $f(\alpha, \beta)$ for an inclined half-space. 77
3.8 Graphical representation of the determination of the contact point using the FIV method. 80
3.9 Contact point (CP) data 81
3.10 Indentation artefacts. 83
3.11 The effect of the hydrodynamic coupling on the oscillating cantilever. 86
3.12 Latex replica: measurements of the topographical contribution. 87
3.13 The hydrodynamic coupling for a short lever. 88
3.14 Topographic artefacts during a dynamic AFM scan. 89
3.15 Reproducibility of a dynamic atomic force microscopy (AFM) scan. . 91

4.1 Justification of the indentation model. 101
4.2 Half opening angle α of a Nanosensors PPP-NCAuLD tip. 102
4.3 Dynamic mechanical flowchart. 105
4.4 Weight functions in the MW approximation. 107
4.5 Dynamic viscoelastic maps of the plant CW. 110
4.6 Behaviour of the inverse loss tangent. 113
4.7 Local distribution of material properties. 115
4.8 Maps of MW approximation. 116
4.9 Mechanical gradients of the first eigenmode. 122
4.10 SLS behaviour of measurements with the first eigenmode. 123
4.11 Derived standard-linear solid (SLS) quantities for the first eigenmode. 125
4.12 Stored and dissipated energy relation of measurements with the second eigenmode of the cantilever. 129
4.13 Mechanical gradients of the second eigenmode. 130
4.14 Derived SLS quantities for the second eigenmode. 132

5.1 Change of the hoop factor 145
5.2 CW thickness determined by confocal microscopy. 146
5.3 Relation between viscoelastic properties of the plant CW and cell length. 147
5.4 Strain stiffening for a linear elastic material 149
5.5 Schematic of a pavement cell. 152
5.6 Viscoelastic properties of pavement cells. 153
5.7 Viscoelastic properties of turgid guard cells. 156
5.8 Mechanical asymmetry in guard cells. 157
5.9 Viscoelasticity of IXB treated seedlings. 159
5.10 Inverse loss tangent of IXB treated seedlings. 161

5.11 SLS quantities of IXB treated seedlings. 162
5.12 Summary of IXB treatment. 164
5.13 Viscoelastic of ECG treated seedlings. 166
5.14 Inverse loss tangent of ECG treated seedlings. 168
5.15 SLS quantities of ECG treated seedlings. 170
5.16 Summary of ECG treatment. 171
5.17 Mechanical properties and growth gradient along the hypocotyl. . . . 174
5.18 Hypocotyl growth. 175
5.19 Cell length and growth rate. 176
5.20 Growth mechanics. 178
5.21 Viscoelastic for dark light transitions. 179
5.22 Inverse loss tangent for dark light transitions. 181
5.23 SLS quantities for dark light transitions. 182
5.24 Summary of dark light transition. 183
5.25 Viscoelastic of RAB-E1d. 186
5.26 Inverse loss tangent of RAB-E1d. 187
5.27 SLS quantities of RAB-E1d. 189
5.28 Viscoelastic properties of plasmolysed RAB-E1d. 190
5.29 Inverse loss tangent of plasmolysed RAB-E1d. 192
5.30 SLS quantities of plasmolysed RAB-E1d. 194
5.31 Summary of the Rab-E1d mutant under turgid conditinos. 196
5.32 Summary of the Rab-E1d mutant under flaccid conditinos. 197

List of Symbols

Symbol	Description	Unit
A_0	cantilever deflection	m
A_1	cantilever oscillation amplitude of 1^{st} eigenmode	m
A_2	cantilever oscillation amplitude of 2^{nd} eigenmode	m
ϕ_1	cantilever phase of 1^{st} eigenmode	rad
ϕ_2	cantilever phase of 2^{nd} eigenmode	rad
δ	indentation	m
Φ	cell wall extensibility	$\mathrm{Pa}^{-1}\,\mathrm{s}^{-1}$
F	force	$\mathrm{N\,m}^{-1}$
f	frequency	Hz
E''	loss modulus	$\mathrm{N\,m}^{-1}$ in 1D, Pa in 3D
ω	angular velocity	rad Hz
ν	Poisson's ratio	Pa
τ	relaxation time	s
k	spring constant	$\mathrm{N\,m}^{-1}$ in 1D, Pa in 3D
E'	storage modulus	$\mathrm{N\,m}^{-1}$ in 1D, Pa in 3D
ε	strain	-
σ	stress	Pa
P_t	turgor pressure	Pa
η	viscosity	$\mathrm{N\,m}^{-1}\,\mathrm{s}$ in 1D, Pa s in 3D
Y	yield threshold	Pa
E	Young's modulus	Pa

Chapter 1

Introduction

Adaptation to environmental processes, is one of the characteristics of life. Fundamental for this mechanism are dynamic processes that occur during development, especially growth and shape remodelling, which play a crucial role for optimising adaptation (Thompson, 1917; Hamant, 2017). Thompson (1917) pointed out that the phenomenon of growth is essentially a physical problem. He combined many ideas of early natural philosophers, suggesting that simple mathematical transformations are determined by the mechanical properties of the biological structures and the force field in which they evolve. Although this can be used to describe shape development, Thompson could not elaborate on the molecular complexity of the mechanical description underpinning this procedure. It is important to note that at the time he wrote the book modern polymer physics, a thermodynamic theory, did not exist. Nowadays, polymer physics is mostly used in biology for the description of protein folding (Bryngelson et al., 1995; Plotkin and Onuchic, 2002; Woodside et al., 2006), and of certain aspects of collagen mechanics and cytoskeletal activity in mammalian cells (MacKintosh et al., 1995; Discher et al., 2005; Gardel et al., 2004; Guo et al., 2012). Although these approaches are mostly descriptions at the limit of equilibrium thermodynamics, they give insights into the molecular mechanisms of complex me-

chanical behaviours of cells. Even more exciting are the application of approaches from non-equilibrium thermodynamics to biological signalling (Heimburg, 1998; Heimburg and Jackson, 2005; Heimburg, 2007) and bacterial reproduction (Kachman et al., 2017; Horowitz and England, 2017; England, 2013). These examples clearly show that modern physics can contribute to a more profound understanding of biology. And indeed that biology could also teach us new physics (Schrödinger, 1944; Delbrück, 1949).

The most common scheme for shape adaptation in nature is the cell wall (CW), present not only in plants but also in bacteria, algae, fungi, and archea. One of the most complex CWs is the primary plant CW. This is the wall which enables the plant to grow, in contrast to the secondary plant CW, which provides permanent stability and protection after the cessation of growth (Cosgrove and Jarvis, 2012).

The aim of the thesis is to determine, for the first time, viscoelastic properties of plant growth at a subcellular level with nanoscale resolution. Moreover, I attempt to integrate thermodynamics and polymer physics approaches to create a link between the mechanical properties, which will be obtained from dynamic atomic force microscopy (AFM) experiments, and plant development.

In this chapter I will introduce first, the biochemical composition of the primary CW. This will be followed by the relevant mathematical and experimental, mechanical, concepts and methods, which are necessary to understand the current scientific picture and the work in this thesis. Finally, I will present some mathematical descriptions of plant cell growth and I will review the most relevant experiments and techniques which give us the knowledge about plant CW mechanics.

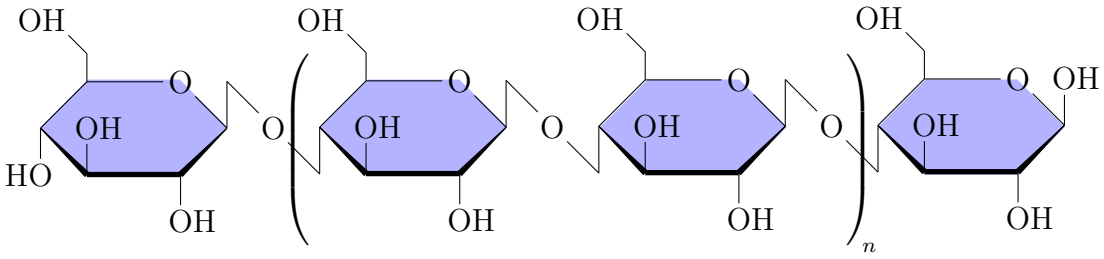


Figure 1.1: Structure of a β-1,4-glucose linked glucan chain.

1.1 The Primary Plant Cell Wall

The plant CW is a complex composite polymeric material made principally from several very distinct polysaccharides. In this work we are only interested in plant growth so I will only focus on the growing, primary, plant CW. In this section I shall cover the molecular structure of the different polymers contributing to the architecture and then I introduce different architectural hypotheses of the plant CW. Finally, I will discuss the implications of the different models and how they could be used to explain the mechanics.

1.1.1 Cell Wall Components: The Molecular Structure

The plant CW is a composite material made from three groups of polysaccharides, namely cellulose, hemicelluloses (HCs), and pectic polysaccharides or pectins (see fig. 1.3b) and a few structural proteins (Cosgrove, 2005). The polysaccharides make the major contribution to the mechanical properties (Wang et al., 2012), therefore, proteins are usually not considered in models of CWs with respect to mechanical behaviour. The polysaccharide components have very different polymeric structures, causing diverse mechanical properties, such as resistance against shear and loading forces caused by biotic or abiotic stresses.

Cellulose is a glucan made from β-1,4-glucose (see Figure 1.1). It allows the molecules to form crystalline cellulose microfibrils (CMFs) made from 18 to 36 glucan

chains (Ding et al., 2014; Thomas et al., 2013; Newman et al., 2013), however, the exact number of chains is not known. Its crystallinity requires that it is synthesised directly at the plasma membrane (PM), this is done by three types of cellulose synthase (CESA) subunits (CESA1, CESA3, CESA6), which form a hexameric rosette complex. Each CESA subunit synthesises a glucose chain which associate to form a CMF with a hexagonal shape of 3 nm–5 nm. The CMFs can have two crystalline structures, Iα and Iβ allomorphs, which correspond to a triclinic and monoclinic Bravais lettice, respectively (Poletto et al., 2013; Wang et al., 2016). The anisotropy in the crystal structure causes different mechanical properties in different directions (see section 1.3). The mechanical properties can be compromised by crystal defects, which are introduced by β-1,3 linked glucoses and by entrapped HCs (Cosgrove, 2005), but it is not clear if this is harnessed by the plant to modify the mechanical properties of cellulose. Moreover, the dense crystalline structure gives enzymes almost no space to act on them, which makes them very robust to enzymatic degradation (Cosgrove, 2005). Furthermore, the beam-like structure of the CMFs provides anisotropy to the CW and has a major contribution to stability, growth direction, and cell shape (Gendreau et al., 1997; Derbyshire et al., 2007). Its specific structure is crucial for cross-links in the network between HCs and pectins. Hydrophobic surfaces provide space for cross-links with the HCs, whereas hydrophilic areas interact with the pectins (Ding et al., 2014).

Hemicelluloses are polymer chains with a β-1,4-glucose backbone, like cellulose, but they are not crystalline owing to the presence of side-chains (Scheller and Ulvskov, 2010). Unlike cellulose they are synthesised in the Golgi and then delivered to the PM where they can be integrated into the existing network. Their binding properties arise from their side-chains, such as the xylosyl residues in Xyloglucan (XG), which is the most abundant HC in primary CWs of dicots (Scheller and Ulvskov, 2010; Pauly et al.,

2013) and it seems to play a crucial role in CW expansion (Cosgrove, 2005). Therefore, most models of primary plant CWs assume XG is the most important HC in those walls. Moreover, for physical models, properties such as the cross-linking between different polymeric structures is more important than the exact chemical composition, even though the precise structure determines the kind and strength of the cross-links. HCs appear to be non-covalently cross-linked to cellulose. Additionally, it was thought for a long time that the CMF-XG network was separate from the pectic network (Pauly et al., 2013; Cosgrove, 2014) but recent results suggest chemical bonds between all three components (Wang et al., 2015; Wang and Hong, 2016). Furthermore, XG was considered to control the stress relaxation in growing plant CWs, because it was found that HCs in CMF networks gain flexibility (Chanliaud et al., 2002) and expansins act on them (Cosgrove, 2005). However, mutants with no XG (Cavalier et al., 2008) showed no significantly altered phenotype, and recent insights into the distribution of pectin, a high percentage of which bind to CMFs, have shown that models of distinct polymer networks in the CW are not an appropriate description (Wang et al., 2012). Nevertheless, XG plays a significant role in stress relaxation and in cell growth and might create biomechanical 'hot-spots' (Park and Cosgrove, 2012a; Cosgrove, 2014) between CMFs. Cosgrove defines biomechanical 'hot-spots' as cross-links between CMFs.

Pectin is a polymer gel made from highly branched pectic polysaccharides, one of the most complex biopolymers. It provides mechanical compliance and porosity to the plant CW. While it is clear that the compliance is relevant for growth, the contribution to the porosity remains unknown. Their synthesis also happens in the Golgi and, like the HCs, they are transported to the PM from where they can diffuse into the CW before they are integrated into the existing polymer network. Pectins bind both to the CMFs, covering them from about 25 %–50 % (Wang et al., 2012), and to

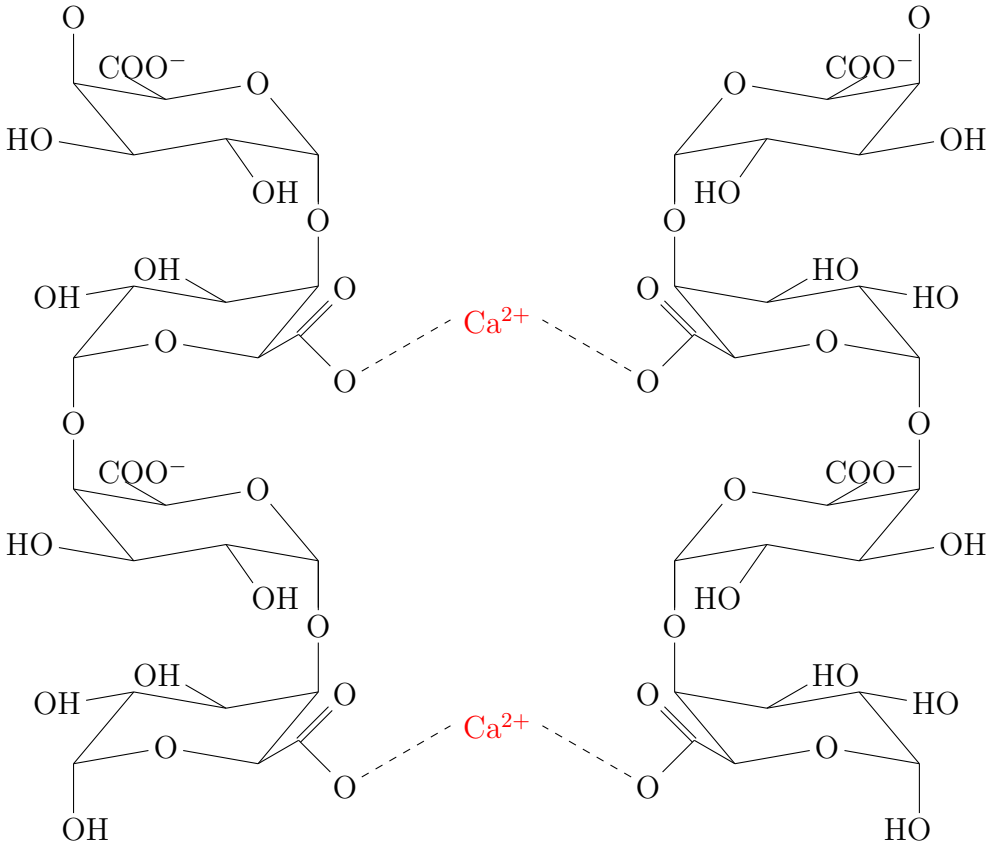


Figure 1.2: Structure of homoglacturonan building salt bridges with ionic calcium.

the HCs (Pauly et al., 2013; Popper and Fry, 2008). The most abundant pectins in primary CWs are homogalacturonan (HG), rhamnogalacturonan (RG) I and II. HG contributes about 65 % to the pectic network in primary CWs and is made only from the α-1,4 GalA backbone. It builds salt bridges with ionic calcium between esterified residues (Atmodjo et al., 2013) (see Figure 1.2). The latter mechanism is used to control the stiffness of the gel, which was investigated by Peaucelle et al. (2011, 2012, 2015) and Braybrook et al. (2012). RG I contributes about 20 %–35 % to the pectic network and has a disaccharide backbone made from galacturonic acid (GalA) and rhamnose (Rha) $[4)$-α-D-GalA-$(1,2)$-α-L-Rha-$(1,]_n$. The least abundant RG II (about 10 %) links by borate ester dimers to HG and seems to be vital for plants (Atmodjo et al., 2013). These three different structures link covalently to each other via their backbones, but it is not known how the pectin network is built from this (Atmodjo et al., 2013).

It is known that diverse molecular mechanisms exist to overcome different kinds of stresses, pectin for example provides stability, flexibility and porosity to the plant CW. Furthermore, the matrix polysaccharides are well known to have crucial tasks in stress relaxation (Cosgrove, 1997), but it is not clear how these mechanisms exactly act. Investigations of artificial CWs showed that both pectins and xyloglucan are crucial for stiffness and extensibility of these networks (Chanliaud et al., 2002). While the CMFs mainly contribute to the elastic behaviour of CWs, the matrix polysaccharides are responsible for the viscoelastic behaviour (Cosgrove, 2014). More recently it was found, that hydrated CWs show not only viscoelastic, but also poroelastic behaviour (Lopez-Sanchez et al., 2014).



Figure 1.3: Models of CW architectures. (a), shows the tethered network model, where cellulose is cross-linked exclusively by hemicelluloses. This network is embed into the pectin gel (not shown) which binds to both cellulose and HC. (b), shows the mechanical hot-spot model where cellulose binds closely to each other by HCs, however, direct cross-links cannot be excluded. Furthermore, the whole network is embedded into a pectin network which does cross-link to both cellulose and HCs.

1.1.2 Cell Wall Architectures

Above we have seen that the CW components can bind in different ways to each other, which will influence the specific architecture of the wall and consequently the mechanical behaviour of the CW. The complexity of the CW makes it very difficult to discover the exact structure of the primary plant CW. Moreover, it is very likely that different cell types display different structural arrangements. Here I will discuss the structure of the most likely arrangements, which are the tethered network model and the mechanical hot-spot hypothesis.

1.1.2.1 The Tethered Network Model

Although the tethered network model seems to be outdated, it is important to cover it because most of the existing thermodynamic models of plant growth were designed using this type of wall architecture and those models should not to be rejected entirely, because they might still explain fundamental mechanical relations between wall architecture and its expansion. The tethered network model assumes that there are no direct cross-links between the CMFs, but instead they are cross-linked by HCs (fig. 1.3a), which also bind to the pectins. These connections can be realised in several

ways (Cosgrove, 2005)

(i) Hemicelluloses bind spontaneously to the surface of cellulose by hydrogen bonds.

(ii) Hemicelluloses become entrapped during CMF formation. The free ends can bind to pectins or to the surface of a CMF.

(iii) Hemicelluloses are coating CMFs and the free ends bind to other matrix polysaccharides with no direct link to other CMFs.

(iv) XGs link covalently to pectins and this macromolecule adheres to the CMFs.

(v) Hemicelluloses bind cellulose by cross-links made by ferulic acid esters, which can also bind to other hemicelluloses or to pectins.

1.1.2.2 The Mechanical Hotspot Hypothesis

The tethered network model was most popular until about five years ago. At this time it was thought that no direct cellulose cross-links and no covalent bonds between HCs and CMFs existed. Recent solid state nuclear magnetic resonance (SSNMR) studies, however, showed that the links between pectins and HCs and between CMFs are much closer than previously expected (Dick-Pérez et al., 2011; Dick-Perez et al., 2012; Wang and Hong, 2016; Wang et al., 2015). Moreover, molecular dynamic (MD) simulations and *in vitro* experiments showed that XGs bind very closely to CMFs (Zhao et al., 2014; Villares et al., 2015). Additionally, recent structural AFM studies showed that CMFs are locally very close to each other and form mechanical 'hot-spots' (fig. 1.3b), hence the name and the revision of the model (Park and Cosgrove, 2012a; Zhang et al., 2014a, 2016; Ding and Himmel, 2006; Ding et al., 2014). Therefore, in the mechanical hot-spot model the CMFs are highly coated by HCs and thus form mechanical hot-spots. Moreover, the pectins bind to the CMFs as well as to the pectins. This leads to a huge structural variety and probably to more fine tuned growth control.

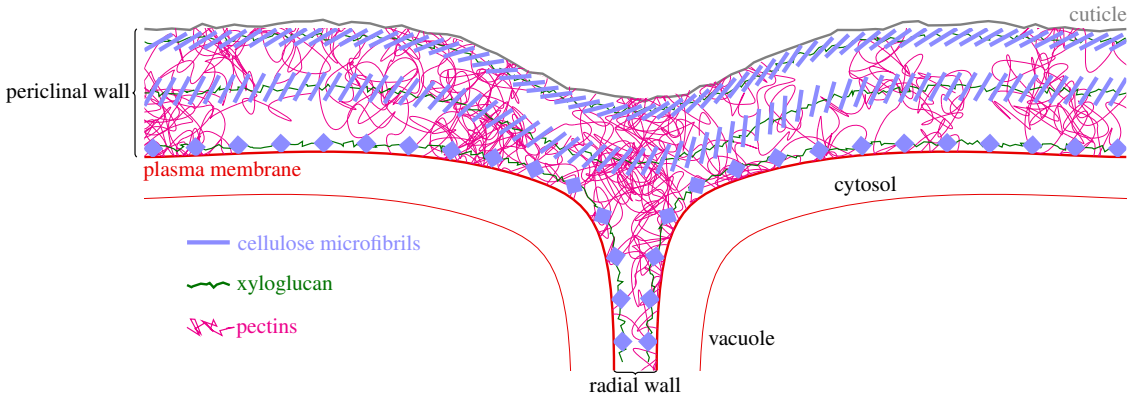


Figure 1.4: Plant CW in the cellular context of adjacent cells after cell division. The different angles of the CMFs indicate the different orientations of the fibres in the different lamellae. The wall structure is from the side view, in contrast to the top view of one lamella in fig. 1.3b.

1.1.2.3 Cell Walls in a Cellular Context

It is important to realize that both of the models above only describe how lamellae of CMFs are formed and they provide possible mechanisms for stress relaxation in the CW. More generally, in a cellular context (fig. 1.4) the CW consists of at least three lamellae of cellulose (for epidermal cells are expected to have about 100 lamellae of about 40 nm thickness (Zhang et al., 2016)), which can be described with the appropriate model from above. While pectins can be found throughout the walls it is not clear how exactly cellular force microscopys (CFMs) and XGs are distributed. Furthermore, it is also unknown whether adjacent lamellae have XG or direct cross-links or whether these are only formed by pectins. Finally, it should be mentioned that aerial organs, such as the shoot or leaves, are covered by a thin wax layer, the cuticle, which prevents water evaporation.

1.2 What are Mechanical Properties?

The mechanics of plant development is an extremely interdisciplinary field with contributions from biology, chemistry, engineering, mathematics, and physics. This variety

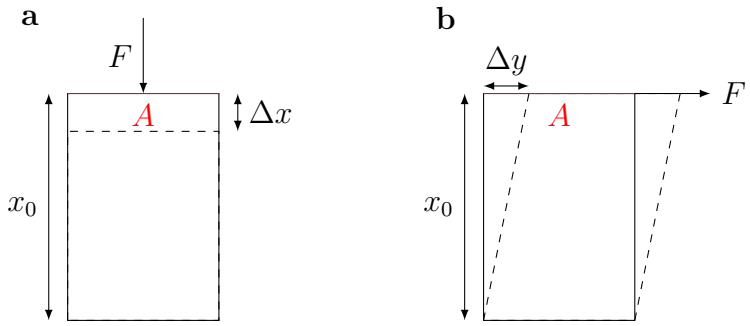


Figure 1.5: Elastic deformation. (a) shows a deformation under normal stress $\sigma = F/A$, which is related to the strain ε by Young's modulus E as $\sigma = E\varepsilon$. (b) shows a deformation under shear stress $\sigma_{\parallel} = F/A$, which is related to the shear strain γ by the shear modulus G as $\sigma_{\parallel} = G\gamma$.

of contributing subjects means that terms which are used to describe CW expansion, can differ slightly in their meaning. In this section I introduce terms, such as viscoelasticity, and mathematical models, e.g. the Kelvin-Voigt (KV) or Maxwell (MW) model, from continuum mechanics, which are commonly used in the mathematical description of plant growth. To avoid complicated tensor notation, the mechanical deformations will be considered in only one dimension. In the following section I will outline the molecular origin of elasticity for crystals and polymers.

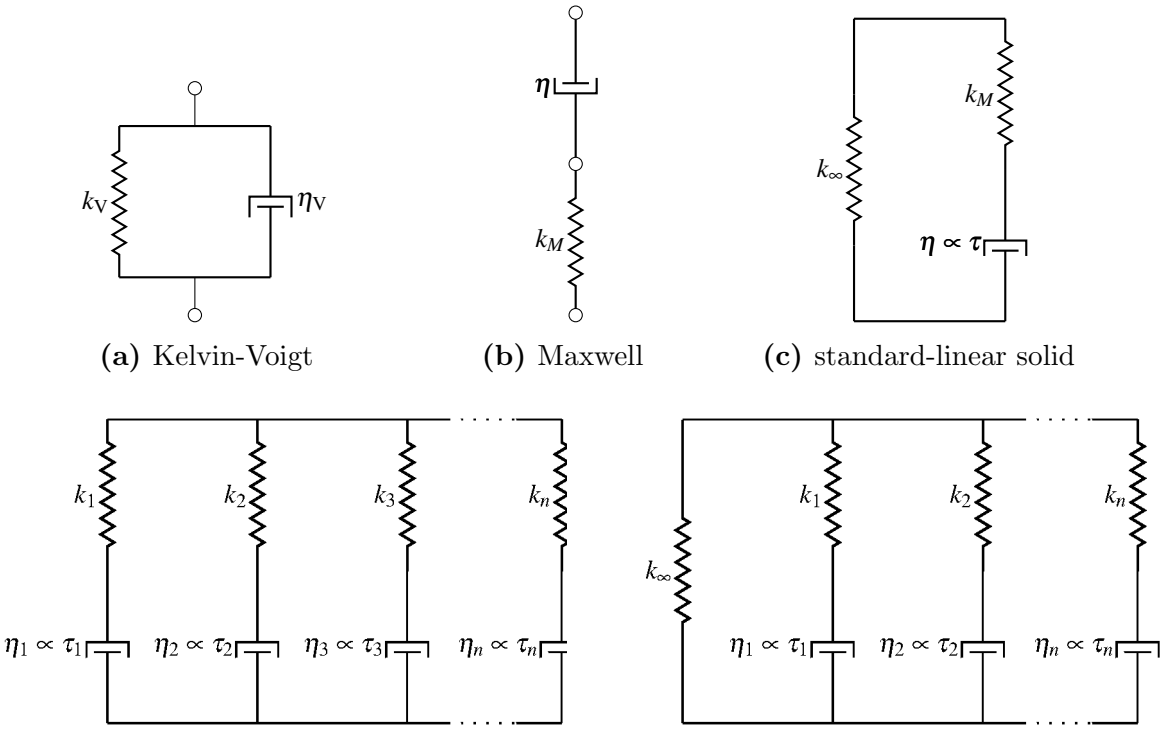
1.2.1 Elasticity, Viscosity, and Viscoelasticity

The most basic descriptions of mechanical properties are linear elasticity, already introduced by Robert Hooke in 1660 (Hooke, 1678), and linear viscosity (Newtonian fluids). In the first case the force F is proportional to the displacement $\Delta x = x - x_0$, i.e. $F = k\Delta x$ and the proportionality constant k is called spring constant. x is the dimension of extension and x_0 is the offset in the case the spring is extended ($x < 0$) and if the spring is compressed ($x > 0$). In the second case the force is proportional to the velocity $\dot{x} = \frac{\mathrm{d}x}{\mathrm{d}t} = v$, i.e. $F = \eta\dot{x}$ and the proportionality constant η is called viscosity. While the spring constant is a quantity which describes the energy which can be recovered from the system, the viscosity describes the energy

which is dissipated by the system. This can be applied directly to materials, where we have slightly different terms. Instead of a force we use the normal stress $\sigma = F/A$, which is force per contact area A and we obtain $\sigma = E\varepsilon$ with the proportionality constant E being Young's or the elastic modulus and $\varepsilon = \Delta x/x_0$ being the resultant strain, which is the relative deformation of the material (fig. 1.5a). In this case x_0 is the initial dimension of the body and $\Delta x = x - x_0$, where x is the dimension after deformation. For an infinitesimal deformation this changes to $\varepsilon = \mathrm{d}x/x = \mathrm{d}\ln x$, which is called the true or logarithmic strain. The same principle applies for the shear stress $\sigma_{\parallel} = G\gamma$, with the shear strain $\gamma = \Delta y/x_0$ and the shear modulus $G = E/2(1+\nu)$ (fig. 1.5b), with Poisson's ratio $\nu = -\frac{\mathrm{d}\varepsilon_y}{\mathrm{d}\varepsilon_x}$. The Poisson's ratio describes how the material compensates for the deformation in one direction by a deformational response in another direction. For the viscosity we obtain $\sigma = \eta\dot{\varepsilon}$.[1] It might seem strange to introduce a quantity from fluid mechanics (viscosity) to plant growth but the importance of this is that polymeric materials display a combination of both elastic and viscose behaviour, called viscoelasticity. Viscoelastic responses depend on the timescale on which the system is observed. In general, the shorter the timescale the more elastic and the longer the timescale the more viscose behaviour can be observed. This implies that polymers store and dissipate energy. The storage of energy means that it remains in the system and can be recovered by releasing the stress, while energy dissipation means that the energy is converted into heat.

The simplest viscoelastic models one could imagine are a combination of an elastic element (a spring) and a viscose element (a dashpot) either in parallel, which is called the Kelvin-Voigt model, or in series, the Maxwell model (figs. 1.6a and 1.6b). The Kelvin-Voigt model can be described by the following partial differential equation (PDE)

[1] Notice that η has now units of Pa $\times$ s instead of N $\times$ s



(a) Kelvin-Voigt **(b)** Maxwell **(c)** standard-linear solid

(d) General Maxwell **(e)** General SLS

Figure 1.6: Viscoelastic models can be represented by combinations of springs and dashpots, which represent elasticity and viscosity, respectively. A spring and a dashpot in parallel represent the KV model (a), which represent the damped harmonic oscillator. A spring and a dashpot in series describe the MW model (b), model that describes a viscoelastic fluid. The simplest viscoelastic solid, which describes the time-scale behaviour correctly is given by a spring parallel to the MW model (c).

$$\sigma = \sigma_{\text{spring}} + \sigma_{\text{dashpot}} = E\varepsilon + \eta\frac{\partial\varepsilon}{\partial t}. \tag{1.1}$$

The PDE for the Maxwell model is:

$$\frac{\partial\varepsilon}{\partial t} = \frac{\partial\varepsilon_{\text{dashpot}}}{\partial t} + \frac{\partial\varepsilon_{\text{spring}}}{\partial t} = \frac{\sigma}{\eta} + \frac{1}{k}\frac{\partial\sigma}{\partial t}. \tag{1.2}$$

The simplest experiments to obtain information about material properties are the deformation with a constant stress σ_0, which is called a creep experiment, and the application of a constant strain ε_0, which is called a stress relaxation experiment. For a creep experiment eq. (1.1) leads to the following solution for the KV model

$$\varepsilon(t) = \frac{\sigma_0}{E}\left(1 - e^{-\frac{t}{\tau}}\right), \tag{1.3}$$

with $\tau = \eta/E$. For the MW model eq. (1.2) results in

$$\varepsilon(t) = \frac{\sigma_0}{\eta}t. \tag{1.4}$$

Creep experiments provide the relaxation function of a material. These solutions show two important characteristics about these two models. On the one hand, from eq. (1.3) the first problem of the KV model appears, which is that at short times, or equivalent long relaxation timescales, the KV material lacks the instantaneous elastic deformation. On the other hand, from eq. (1.4) it is immediately visible that a MW material displays the behaviour of a fluid and keeps on deforming forever. This is also

obvious if one looks at the schematic of a Maxwell material as in fig. 1.6b that after the instantaneous deformation the only responding part of the model is the dashpot, which describes linear viscosity, i.e. a fluid.

For a stress-relaxation experiment we obtain for the KV model from eq. (1.1)

$$\sigma(t) = E\varepsilon_0.$$

This is another non-physical behaviour of the KV model, because at any constant strain the system just stays with the force of the spring. The problem is that the dahspot and the spring are parallel. It takes some additional force ($F = \eta\dot{\varepsilon}$) for the extension, but after that, only the force of the spring has to be held. The MW model leads to (with eq. (1.2))

$$\sigma(t) = \sigma_0 e^{-\frac{t}{\tau}}.$$

This exponential decay of the applied force has relevance for plant growth as we will see later.

The third possibility to obtain information about material properties is through an oscillatory deformation of the sample. For an oscillatory strain $\varepsilon(t, \omega) = Ae^{i\omega t}$ we obtain for the Kelvin-Voigt model

$$\sigma(t) = (E + i\omega\eta)\, Ae^{i\omega t} \equiv E^* Ae^{i\omega t} = E^*\varepsilon(t).$$

E^* is called the complex modulus and

$$\mathrm{Re}\{E^*\} \equiv E' = E \qquad\qquad \mathrm{Im}\{E^*\} \equiv E'' = \omega\eta \tag{1.5}$$

are the storage (E') and loss (E'') moduli, respectively. Re and Im mean that the real and imaginary part of a complex number is taken. The same approach for the MW model leads to

$$\sigma(t) = E\frac{\omega^2\tau^2 - i\omega\tau}{1+\omega^2\tau^2}Ae^{i\omega t} + \frac{i\omega\tau - 1}{1+\omega^2\tau^2}Ake^{-\frac{t}{\tau}} \tag{1.6}$$

$$= E^*\varepsilon(t) + \frac{i\omega\tau - 1}{1+\omega^2\tau^2}\varepsilon(0)Ee^{-\frac{t}{\tau}}. \tag{1.7}$$

And thus we obtain the Debye relations for the storage and the loss modulus

$$E' = E\frac{\omega^2\tau^2}{1+\omega^2\tau^2} \qquad\qquad E'' = E\frac{\omega\tau}{1+\omega^2\tau^2}. \tag{1.8}$$

Comparing eqs. (1.5) and (1.8) two important facts can be observed. First, the frequency dependency in the KV model comes only from the loss modulus. This makes sense, because as we have seen before E does not contribute to the time dependency of $\sigma(t)$. Second, for the MW model both E' and E'' are frequency dependent and E'' has a resonance at

$$\omega_r = \frac{1}{\tau}.$$

This resonance is characteristic of the material's properties and gives a significant, i.e. characteristic, timescale for the material relaxation (cf. eq. (1.7)).

For more complex materials one can combine the springs and dashpots arbitrarily to design the appropriate behaviour. The simplest realistic solid polymer material is described in this way by the so called standard-linear solid (SLS) where a spring E_∞ is in parallel to a Maxwell module with a spring E_M and viscosity η. This material has the advantage that it neither exhibits the artefacts of the KV model, i.e. instantaneous deformation can take place, nor does it show the artefact of the MW material, i.e. it is not a fluid. Moreover, the SLS gives the MW model in the limit of $E_\infty \to 0$ and the KV model for $E_\mathrm{M} \to \infty$. The storage and loss modulus are then given by

$$E' = E_\infty + E_\mathrm{M}\frac{\omega^2\tau^2}{1+\omega^2\tau^2} \qquad\qquad E'' = E_\mathrm{M}\frac{\omega\tau}{1+\omega^2\tau^2}. \tag{1.9}$$

The resonance of this material is the same as for the Maxwell model.

At this point I will not cover the mathematical description of the more complicated viscoelastic materials (this will be done in chapter 4), but it should be mentioned that the most general model for linear viscoelastic materials is the generalised MW model, which consists of an array of MW elements. Such a material can be realised as liquid (fig. 1.6d) or as solid (fig. 1.6e). For plastic deformation, it is always necessary that the material displays fluid-like behaviour at a certain timescale and stress. Such a behaviour is called viscoplastic. This is relevant for plant growth. However, this does not exclude that viscoelastic responses occur at other timescales.

1.3 Multiscale – Continuum Mechanics Versus Molecular Mechanisms

The behaviour of an object depends on the spatial and temporal scales at which it is observed. For many applications we are interested in the behaviour of macroscopic

quantities, such as cellular or organ growth in the plant context or in spring elongation or the deformation of a crystal in the material context. However, to understand the mechanism behind a macroscopic observation we need a description at a smaller level. In the case of a spring it could be the level of the coils and the diameter of the spring and the material the spring is made of; for the behaviour of the material one has to go down to the atomic level. The same is true for the deformation of crystals, where one can describe the linear elasticity with a mechanism at the atomic scale. To make this a little bit clearer we have a closer look at both examples I have given above. Both the spring and the crystal display linear elasticity for sufficiently small deformation (section 1.2). From this behaviour we only know that the deformation of the material is linear with an applied force but the equations do not explain any mechanism behind this phenomenon. In the case of the crystal it is fairly easy to show an atomic mechanism which explains the phenomenon observed on the macroscopic scale.

The periodicity of a crystal makes this relatively simple. The energy of a crystal is given by a combination of attractive potentials $U_a = -ACe^2/r$ and repulsive potentials $U_r = B/r^n$ thus we have

$$U = -\frac{ACe^2}{r} + \frac{B}{r^n}.$$

For small deformations every ion will be near equilibrium which is at

$$(f)_{r=r_0} = \nabla\, U\Big|_{r=r_0}$$
$$r_0 = \left(\frac{nB}{ACe^2}\right)^{\frac{1}{n-1}}.$$

Now for a point force $\sigma = F = \frac{f}{r_0}$ and with the true strain $\mathrm{d}\varepsilon = \frac{\mathrm{dr}}{r_0}$ we obtain the Young's modulus

$$E = \left.\frac{\mathrm{d}\sigma}{\mathrm{d}\varepsilon}\right|_{\varepsilon\to 0} = \frac{1}{r_0}\left.\frac{\mathrm{d}f}{\mathrm{d}r}\right|_{r\to r_0}.$$

and we obtain

$$E = \frac{(n-1)\,ACe^2}{r_0^4} \tag{1.10}$$

(Keating, 1966; Roylance, 2000). As the example shows, the microscopic behaviour scales differently from the macroscopic behaviour ($\sigma = E\varepsilon$ for the macroscopic level), and depends strongly on the interaction, i.e. the equilibrium distance r_0. More importantly, the derivation from interatomic forces provides an understanding of the mechanism behind the relation between deformation and material properties, for small deformations. The appearance of the interatomic distance r_0 in eq. (1.10) also explains immediately why materials exhibit different mechanical properties. For example the CMFs occur as triclinic and monoclinic crystal structures, which both have different lattice constants in all three dimensions. Although the principle of multiscale behaviour is now clear, a closer look at the behaviour of the ideal spring shows the scaling behaviour at a mesoscale. The spring constant contains the whole information about the spring, i.e. Mischke and Shigley (2001)

$$k = \frac{Gd^4}{8n(D-d)^3}$$

with the wire diameter d, the coil diameter D, and the number of active coils

n, and the shear modulus $G = E/(2(1+\nu))$. This already shows the underlying mechanism, namely that the spring behaviour is determined by its structure on a mesoscale, i.e. the wire and the coils, and the structure at the microscale given by the material elasticity E and deformational anisotropy (Poisson's ratio) ν.

For more complex materials like polymers this simplistic approach is not possible anymore and one has to go via a thermodynamic approach, which means averaging over a number of conditions. As statistical physics or thermodynamics has shown before, averaging over many microstates can lead to a description of macroscopic quantities and it can also give an understanding of the microscopic mechanism behind a process. For example temperature (of an ideal gas) is the average kinetic energy $3k_BT/2 = \langle mv^2 \rangle /2 = \langle E_{\text{kin}} \rangle$ and this shows that temperature is the mere jiggling of particles (Feynman, 1965).

This can also be applied to the mechanics of polymers. The work of the deformation of a polymeric material is given by

$$\mathrm{d}W = F\mathrm{d}L = \mathrm{d}U - T\mathrm{d}S$$

and thus the force to deform the material is given by

$$F = \frac{\partial W}{\partial L} = \frac{\partial U}{\partial L} - T\frac{\partial S}{\partial L}.$$

For a perfect rubber (small deformations of the polymer and spatially fixed cross-links) the change in internal energy U is negligible and the force is purely determined by the temperature T and the entropy S. For an ideal polymer (long chain and no self-avoidance) the end-to-end distance of the polymer chain displays a probabilistic behaviour which shows a Gaussian distribution. It can be shown that in such a

scenario the stress for an incompressible rubber consisting from n strands per unit volume and relative extension in x-direction is given by (Rubinstein and Colby, 2003, chapter 7)

$$\sigma = nk_BT\left(\lambda - \frac{1}{\lambda^2}\right). \tag{1.11}$$

$\lambda = x/x_0$ is the relative elongation of the rubber. The relation between strain and relative elongation is given as $\lambda = \varepsilon + 1$. The shear modulus of such a rubber is given by $G_{\text{rubber}} = nk_BT$

For a more realistic polymer the cross-links are not fixed in space and therefore, the resulting elasticity decreases. Such a material can be described by the phantom network model and its shear modulus is (Rubinstein and Colby, 2003, chapter 7)

$$G_{ph} = nk_BT(f-2)/f = G_{\text{rubber}}(f-2)/f \tag{1.12}$$

where f is the coordination number of a cross-link, i.e. how many chains are connected by a cross-link.

This description can be further refined for polymer gels and topological entanglements of the polymer network. Because the detailed theory of those models is not required in this thesis it will not be explained here. Nevertheless, it should be mentioned that, although entanglement affects the pure elasticity, the main effect will be at modulating dynamic processes. This should be kept in mind, because the main experimental method of this thesis will be dynamic AFM methods, but it is not known how far topological knots play a role in plant CW architecture.

This brief overview demonstrates how macroscopic (continuous) behaviour can be derived from microscopic discrete quantities (e.g. ions or monomers). From both

deterministic and probability descriptions, we can learn something about the underlying mechanisms behind the phenomena. This is very useful because, although one can use macroscopic quantities for a description or modelling on the scale of plant development, by using the physics of thermodynamics it is possible to understand their behaviour from first or hierarchical principles. The hierarchical phenomena were demonstrated with the examples of spring and rubber elasticity, which show that we can understand behaviour on a mesoscale and can see how this leads to the macroscopic behaviour. But those derivations do not only show how one can understand those phenomena, they also demonstrate which approximations have been done and, consequently, it is possible to understand in which regimes these approximations are valid. In terms of understanding plant development, the mesoscale is the cellular level, which must be understood as well as the subcellular level, to explain organ growth. In this thesis, however, the main focus will be on investigating how the molecular architecture at the nm scale influences the continuum mechanical properties at a subcellular level.

1.4 Plant Growth

Plant growth is a highly complex phenomenon, which happens on several length- and timescales. In this section I will introduce the biophysical and biochemical processes occurring during wall expansion and then I will introduce three mathematical models of plant growth.

The most general definition of growth is the irreversible increase of mass over time. Typical quantities of interest in plant growth are biomass, height, or more generally volume. Those are parameters which are sufficient for a macroscopic description of growth but, for a microscopic one more detailed information is necessary. For our purposes the local CW density $\rho(x, y, z)$ and the total CW volume V are interesting,

thus one could obtain the total biomass $\mathcal{M}$ by

$$\mathcal{M} = \int_V \rho(x, y, z) \mathrm{d}V.$$

Notice that V can be any CW volume of interest, e.g. the CW volume of the whole plant, an organ, a single cell, or even of a section of the wall. The advantage of such a definition is that one can distinguish between either biomass or sole volume growth and the integral gives the total biomass. The reason why this is important is because we can only measure the mechanical properties of growth if we have an idea of which properties, that influence growth, contribute to the mechanical properties. These can be factors like the material density $\rho(x, y, z)$, the $\mathrm{pH}(x, y, z)$, or the cross-linking density $\chi(x, y, z)$, in other words, $E \equiv E(\rho, \mathrm{pH}, \chi, \dots)$ where we can obviously only consider any growth factors that influence viscoelasticity.

As an example lets consider a cylindrical cell of thickness d with uniform density $\rho(x, y, z) = \rho_0$. The volume is then given by the length l and the inner and outer radius R_i and R_o, respectively, with $d = R_o - R_i$:

$$\begin{aligned} V &= 2\pi \left(l \left(R_o^2 - R_i^2 \right) + 2R_o^2 d \right) \\ &= 2\pi d \left(l \left(2R_i + d \right) + 2 \left(R_i + d \right)^2 \right). \end{aligned}$$

The mass $\mathcal{M}$ is then simply given by $\mathcal{M} = V\rho_0$

In plant development, however, the volume growth of the cell is the interesting parameter, which can be described in general by a simple linear differential equation (Lockhart, 1971)

$$\frac{\mathrm{d}V}{\mathrm{d}t} = \Phi^* V,$$

or for unidirectional growth

$$\frac{\mathrm{d}l}{\mathrm{d}t} = \Phi^* l,$$

with the CW extensibility Φ^*. This definition will be the most useful one for this thesis. Therefore, we define plant growth for the purposes of this thesis in terms of cellular growth:

'Cellular growth is the irreversible change of cell volume over time.'

1.4.1 Growth Factors

The ability of a plant to grow will depend on the environmental conditions. Lockhart (1965b) defined as 'growth factor' any physical conditions or chemical components which have a direct influence on plant growth. Lockhart distinguishes between external and internal growth factors. External growth factors are substances which have to be provided by the environment, such as water and radiation but also nutrients. Water is important to maintain the internal turgor pressure, the driving force of growth, but also to keep the transport and the chemical reactions in the plant alive. Radiation is crucial for photosynthesis to guarantee the energy supply of the plant. And nutrients are important to produce internal growth factors, which are the ones which can be synthesised by the organism itself. For example the synthesis of the CW polysaccharides but also the growth hormone auxin, and the protein α-expansin

and enzymes, such as the family of the xyloglucan endotransglucosylase/hydrolase (XTH), and cellulases (endo-(1,4)-β-D-glucanases). Auxin influences plant growth on all scales, from the cellular level to the whole plant. It induces downstream pathways, which I will not introduce here, that promote growth and with this it influences cytokinesis, morphogensis and new organ initiation. Expansins are wall loosening agents which are active during acidic growth. They act on the hydrogen bonds between XGs and cellulose and in this way a less cross-linked network is created which has the ability to extent plastically. Xyloglucan endotransglucosylase (XET), a member of the XTH family are CW remodelling enzymes which are involved in wall loosening, strengthening and the incorporation of newly synthesised XGs into the CW (Cosgrove, 2005). The cutting and reintegration of XGs might be crucial to prevent a formation of knots during the extension of the wall. Cellulases also act on XGs and it is proposed that they release XGs entrapped in CMFs (Ohmiya et al., 2000). Unlike XGs, they show only wall loosening properties and improve the extensibility of treated walls.

1.4.2 Cell Growth: A Conceptual Description

With the knowledge about the network-forming properties of CW polysaccharides and the growth factors, we can consider the conceptual mechanism of plant growth and CW extension. The mathematical models of this phenomenon will be considered after this phenomenological description.

The driving force of plant growth is the internal turgor pressure which is a hydrostatic pressure and therefore isotropic throughout a cell (Hamant et al., 2010). This induces a mechanical stress, which relaxes with time and spreads the CW polysaccharides. This gives space to incorporate newly synthesised material, which has to be produced at least at a sufficient pace so that the CW does not become thinner, because that would lead eventually to the rupture of the wall. The stress relaxation

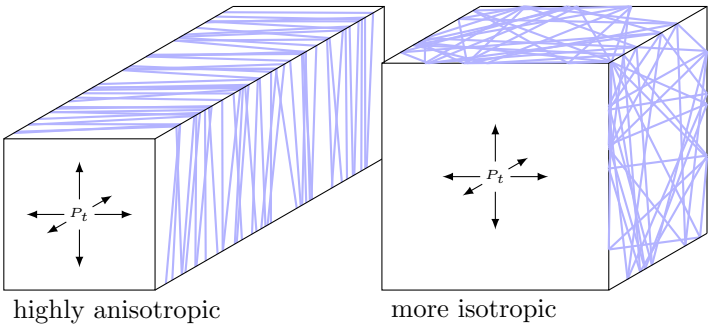


Figure 1.7: Cellular growth. The isotropy of the turgor pressure P_t requires CW anisotropy to enable unidirectional growth. In this case the CMFs (blue lines) are wound around the cell and therefore inhibit radial extension and promote axial growth (left cell). On the other hand, more isotropically oriented CMFs allow the same amount of growth in all directions (right cell).

happens through the breakage of cross-links, e.g by expansins. The connections have a certain life-time that decreases with increasing wall stress. To control this process of removing cross-links, plants use internal growth factors to modify the CW architecture.

At a cellular level the isotropy of the turgor pressure implies that the growth directionality of a cell can only be influenced by the overall mechanical isotropy of the wall. Therefore, a structural anisotropy of the wall leads to more unidirectional growth perpendicular to the alignment of the CMFs, while an isotropic wall gives the cell an isotropic shape (fig. 1.7) (Hamant et al., 2010). The alignment of the CMFs happens with the guidance of the cortical microtubules (MTs) which guide the CESA complexes during the synthesis of cellulose. For unidirectional growth the CMFs are winded around the cell and in this way radial extension is inhibited and axial growth promoted. During unidirectional growth the CMFs are aligned towards growth direction and consequently the older layers of CMFs have a different, more axial, orientation than the newly deposited CMFs. The concept of anisotropic wall properties for anisotropic growth works also with more complex cellular structures, such as the pavement cells in leaves, where the CMFs are denser at positions with high internal stress Sampathkumar et al. (2014). While the arrangement of the CMFs

is a long term investment, biochemical alterations can promote or inhibit growth on the short term but also over longer timescales.

It should be noted that, in a tissue, cells are restricted to their position, i.e. they cannot migrate. This implies that for an appropriate stress relaxation between neighbouring cells local a modification of the wall properties is necessary. Furthermore, there is evidence from finite element modelling (FEM) simulations that the epidermal cells are the most relevant for the direction of plant growth (Dyson et al., 2014) but this finding has been challenged by experimental (only structural and no mechanical investigation was done) results in the *A. thaliana* hypocotyl (Crowell et al., 2011).

1.4.3 Mathematical Models of Cellular Growth

The mathematical modelling of plant growth can be approached at many different levels, such as the plain elongation of cells, the change of the relative growth rate ξ, or even the explicit description of growth factors. Independent of the level of the description it seems that the consensus over the last six decades is that the relative growth rate ξ obeys the time evolution of the true (logarithmic) strain (Lockhart, 1965a; Dyson et al., 2012; Ortega, 1985; Pietruszka, 2009b; Ray et al., 1972)

$$\xi(t) = \frac{1}{l(t)} \frac{\mathrm{d}l(t)}{\mathrm{d}t} = \frac{\mathrm{d}}{\mathrm{d}t} \ln(l(t)). \tag{1.13}$$

The reasoning behind the assumption in eq. (1.13) is that plant growth appears to be slow compared to CW remodelling and thus equilibrium is achieved again after only small increments. This seems to be in good agreement with experimental data Lockhart (1971). One consequence of eq. (1.13) is that plant growth happens exponentially, i.e

$$l(t) = l_0 \exp\left(\int_{-\infty}^{t} \xi(t')\mathrm{d}t'\right). \tag{1.14}$$

1.4.3.1 The Lockhart Model

One of the first descriptions of $\xi(t)$ which incorporated growth factors was the work of Lockhart who derived an expression for $\xi(t)$ at the cellular level. In this model he considered the plant cell as a cylindrical osmometer where the plant CW resembles a Bingham fluid with yield a threshold Y (Lockhart, 1965a)

$$\xi(t) = r\Phi(P_t - Y) = \frac{2K_w r\phi(\Delta\Pi - Y)}{2K_w + r^2\phi}. \tag{1.15}$$

K_w is the water permeability per unit surface area of the cell membrane. The geometry of the cell is assumed to be cylindrical with radius r and length l. $\Delta\Pi$ is the osmotic pressure in the cell and $\phi = \Phi/2h$ is the CW extensibility with the CW thickness h and the cell extensibility Φ. If the water influx is not limiting eq. (1.15) reduces to

$$\lim_{K_w\to\infty} \xi(t) = \lim_{K_w\to\infty} \frac{2K_w r\phi(\Delta\Pi - Y)}{2K_w + r^2\phi} = r\phi\left(\Delta\Pi - Y\right). \tag{1.16}$$

The cell length follows from eqs. (1.14) and (1.15) and is

$$l = l_0 \exp\left(\frac{2K_w r\phi\Delta\Pi}{2K_w + r^2\phi}t\right). \tag{1.17}$$

This describes a forever exponentially growing cell. To obtain a realistic descrip-

tion of cell length, the growth has to cease. With the assumption that $\Delta\Pi$ does not decrease to zero it follows that ϕ must decrease. Lockhart assumed $\phi(t) = \phi_0 - ct$, where c is the rate of how fast the extensibility goes to zero, which leads to the expression

$$l(t) = l_0 \exp\left(\frac{2K_w}{r}\Delta\Pi\left[t + \frac{2K_w}{r^2 c}\ln\left(\frac{\phi_0 - ct + 2K_w/r^2}{\phi_0 + 2K_w/r^2}\right)\right]\right). \tag{1.18}$$

Although eq. (1.18) considers some growth factors, it still provides no explanation for the origin of the decrease in ϕ. Note that ϕ is a material property which depends on the molecular structure of the polymeric network of the CW. The structure of the network can change due to the deformation induced by stresses in the wall or it can be actively remodelled by hormonal or enzymatic activity.

1.4.3.2 The Dyson, Band, Jensen Model

One approach for a molecular explanation of the tethered network model at the CW level, including expansins and XTHs activity as well as deposition of newly synthesised material, was done by Dyson, Band, and Jensen (2012).

While Lockhart was looking at the change of $\xi(t)$ under the influence of stress, Dyson et al. (2012) consider how stress and extensibility change under a certain strain rate ξ. The assumptions in their derivation are that

(i) the flux of the newly synthesised CW materials maintains $h = \text{const.}$

(ii) the deposited material has always the same density distribution and is homogeneous

(iii) $h \ll R$, with the cell radius R

(iv) the CMFs are cross-linked by XG and strongly embedded into the pectin matrix

Furthermore, the XG cross-links are assumed to behave like a Gaussian chain and the rate of breaking cross-links κ_{off} in absence of enzymatic activity is assumed to be

$$\kappa_{\text{off}} = \kappa_0 \exp\left(\beta^2 \frac{U(L)}{k_B T}\right). \tag{1.19}$$

β is a parameter which characterises the cross-link energy landscape. $k_B T$ is the thermal energy with the Boltzmann constant k_B and the absolute temperature T. The energy of the stretched cross-link $U(L)$ is given by

$$U(L) = \frac{k_{\text{bond}}}{2} (L - L_0)^2 . \tag{1.20}$$

k_{bond} is the spring-constant of the bond, L_0 the length of the bond in the relaxed state, and L the length of the bond in an elongated state.

Finally, the number density of cross-links n is described by a Smoluchowski equation

$$\frac{\mathrm{d}n}{\mathrm{d}t} - \xi y \frac{\mathrm{d}n}{\mathrm{d}y} = -\kappa_{\text{off}} n. \tag{1.21}$$

Notice that y is the direction of the coordinate system in the direction of CW thickness, with $y = 0$ at the extracellular side of the wall and $y = h$ at the intracellular side of the wall (fig. 1.8).

In the case of enzymatic activity an additional degradation term for n is added. Dyson et al. (2012) describe this for xyloglucan endohydrolase (XEH) and XET by the relative degradation factors g_{XEH} and g_{XET} and eq. (1.21) becomes

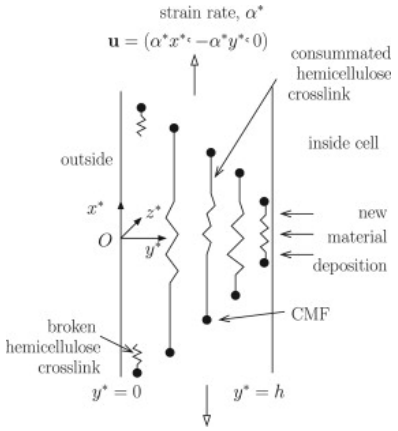


Figure 1.8: This figure is taken from Dyson et al. (2012). A cross-section of the CW, where the CMF are represented as black circles and lie perpendicular to the page, showing the movement of hemicellulose crosslinks through the CW.

$$\frac{\mathrm{d}n}{\mathrm{d}t} - \xi y \frac{\mathrm{d}n}{\mathrm{d}y} = -\kappa_{\mathrm{off}} n - \kappa_0 \left(g_{\mathrm{XEH}} + g_{\mathrm{XET}}\right) n. \tag{1.22}$$

Similarly, the activity of expansins can be described by a rate g_{EXP} which describes a change in L_0 by

$$\frac{\mathrm{d}L_0}{\mathrm{d}t} = g_{\mathrm{EXP}} \left(L - L_0\right). \tag{1.23}$$

This changes n and the wall stress Σ, which is given by

$$\Sigma(t) = \int_0^h n(t,y) k_{\mathrm{bond}} \left(L(t,y) - L_0\right) \mathrm{d}y + \frac{\xi}{\Phi_m} \tag{1.24}$$

The final term in eq. (1.24) is the contribution from the pectin matrix which has an extensibility $\Phi_m = 1/(4\mu h)$, where μ is the shear viscosity of the matrix.

This is a highly sophisticated model, which incorporates elements of continuum

mechanics, polymer physics, and considers (bio-)chemical reaction rates. Furthermore, the fact that this is a description of the tethered network model is not a limitation of the model, because the behaviour of the cross-links, which introduce the yielding behaviour in this model, can be adapted to describe the real CW architecture. However, so far this hypothesis was not tested experimentally, due to a lack of suitable experimental methods.

1.4.3.3 The Veytsman-Cosgrove Model

A purely thermodynamic approach for plant CW extension was chosen by Veytsman and Cosgrove (1998). They distinguish between the pure extension and biosynthesis of the CW. The extension can be promoted by biochemical reactions and happens on a short timescale, while new biosynthesis is a long-term phenomenon. Their model aims to describe the short timescale behaviour, whereby they assume that the CW composition is not changing. Similarly to Lockhart's approach, they consider a long cylindrical cell of radius r, length l, and wall thickness h, with the conditions $h \ll r$ and $r \ll l$. They use the free energy $\mathcal{A}$, which determines the internal wall stress σ by

$$\sigma = \frac{1}{2\pi r h} \frac{\partial \mathcal{A}}{\partial l}. \tag{1.25}$$

Furthermore, they derive Lockhart's equation (eq. (1.16)) via the work done by the wall and the water uptake under the consideration of energy dissipation and they find

$$\frac{\mathrm{d} \ln l}{\mathrm{d}t} = \frac{K_1 K_2}{K_1 + K_2} \left(P_t - \frac{2h}{r} \sigma \right), \tag{1.26}$$

where P_t is the turgor pressure, K_1 is the hydraulic conductance of the wall, and K_2 is the wall yielding coefficient. The yield threshold Y is then given by $Y = 2h/r\sigma$. The wall stress σ is then given by the free energy (eq. (1.25)), which is determined by the specific assumptions about the polymer network in the wall. In this model the assumptions are that

1. Cross-links are only between cellulose and HCs and pectins are only a filler.
2. Water does not contribute to the wall stress.
3. The contribution from the van der Waals bonds is neglected, which they justify because it will not change with wall extension.
4. Hydrogen bonds between CMFs and XGs and between water molecules are considered but not between water and cellulose and XGs. The latter can be included if an effective constant for the hydrogen bonds between CMFs and XGs is measured in a water environment.

The free energy is then given by the free energy of the elastic part of the macromolecules in the wall $\mathcal{A}_{el}$ and by the free energy of the hydrogen bonds $\mathcal{A}_h$ by

$$\mathcal{A} = \mathcal{A}_{el} + \mathcal{A}_h. \tag{1.27}$$

The free energy for the polymers is given from polymer physics by

$$\mathcal{A}_{el} = \frac{k_B T \pi^2 b^2 \mathcal{N}}{6} \left(\frac{1}{l^2} + \frac{1}{h^2} + \frac{1}{2\pi r^2} \right), \tag{1.28}$$

with the Kuhn length b, the thermal energy $k_B T$ and the number of Kuhn segments $\mathcal{N}$. Finally, they calculate the free energy for the hydrogen bonds by a mean field

approach. To do this they introduce cellulose 'stickers' (potential binding sites) $\mathcal{C}$ and glucan 'stickers' $\mathcal{G}$ on M XG threads. Furthermore, they consider free, not bound, stuck strands of N pairs. The free strands have $l_1, l_2, \ldots, l_N$ stickers and the stuck strands $s_1, s_2, \ldots, s_N$ and with $\mathcal{L} = \sum_{i=1}^{N} l_i$ and $\mathcal{S} = \sum_{i=1}^{N} s_i$, which leads to the total number of glucans

$$\mathcal{G} = \mathcal{L} + \mathcal{S}. \tag{1.29}$$

This gives the free energy

$$\begin{aligned}\mathcal{G}_h = k_B T N \ln\left(\frac{V(z_g-1)N^2}{(N-\mathcal{L})(\mathcal{S}-N)(\mathcal{S}-N-\mathcal{C})v_g z_n^2}\right) \\ + \mathcal{L}\ln\left(\frac{\mathcal{L}-N}{\mathcal{L}(z_g-1}\right)\mathcal{S}\ln\left(\frac{(\mathcal{S}-N)(\mathcal{S}-N-\mathcal{C})ev_g}{K\mathcal{S}(\mathcal{S}-\mathcal{C})}\right) \\ + \mathcal{C}\ln\left(\frac{\mathcal{S}-\mathcal{C}}{\mathcal{S}-N-\mathcal{C}}\right) - M\ln\left(\frac{Mv_g}{V}\right)\end{aligned} \tag{1.30}$$

where K is the equilibrium constant of the hydrogen bond formation, V the CW volume, v_g the volume of a glucan segment, z_g and z_n are related to the flexibility of the glucan chains (see Veytsman and Cosgrove (1998) appendix), e is Euler's number.

With eqs. (1.25), (1.27), (1.28) and (1.30) this leads to a wall stress

$$\sigma = -k_B T \frac{\pi^2 b^2 \mathcal{N}}{3Vl^2} + k_B T \frac{N}{V} - k_B T \frac{M}{V}. \tag{1.31}$$

The reason that this stress depends only on the wall volume and not on the wall shape is due to the sole contribution of hydrogen bonds to wall stress, which only describes a liquid like disordered material. For a derivation of the anisotropic

Table 1.1: Mechanical properties from literature. * means that the cells were plasmolysed during the experiment.

Organism	E[MPa]	Method	Reference
A. thaliana hypocotyl	16–22	Microtensile stretch	Cavalier et al. (2008)
A. thaliana hypocotyl	30–50	Microtensile stretch	Saxe et al. (2016)
L. esculentum (tomato)	2300	Micro manipulators (compression) + FEM	Wang et al. (2004)
A. thaliana SAM*	0.05–0.6	AFM, 1 µm bead	Peaucelle et al. (2011)
A. thaliana SAM*	0.06 and 0.36	AFM, 1 µm and 5 µm bead	Braybrook and Peaucelle (2013)
A. thaliana hypocotyl*	0.2	AFM, 1 µm bead	Peaucelle et al. (2015)
A. thaliana SAM	1–14	AFM, cone 10 nm	Milani et al. (2011)
A. thaliana leaves	2–10	AFM	Sampathkumar et al. (2014)
N. tabacum suspension (BY-2)	91–591	CFM + FEM	Weber et al. (2015)
A. cepum (onion)	100	CFM + FEM	Routier-Kierzkowska et al. (2012)
A. thaliana leaves	66	Triboscope, 2.5 µm bead + FEM	Forouzesh et al. (2013)
A. thaliana leaves	28–70	AFM	Hayot et al. (2012)
A. cepum (onion)	1–30	AFM, cone 10 nm	Zhang et al. (2017)

contribution from the CMFs see Dyson and Jensen (2010).

The maximum of eq. (1.31), with respect to the volume, gives the yield threshold Y from a thermodynamic origin. It should be emphasised that this equation does not consider the contribution of pectins and any stress induced by concentration differences in CW material throughout the thickness of the wall since the mean field approach averages over the whole wall and therefore it cannot infer any local changes. However, this approach could also be done for only a fraction of the wall where local changes could be inferred.

The three models I introduced here do not cover the complete literature of the mathematical descriptions, but these are the models which give the most interesting insights into the molecular mechanism underpinning the mechanical behaviour of the plant CW. Other models, like the ones from Pietruszka's group, give a more advanced theory (tensor description) for anisotropic behaviour and the response to external stimuli (Pietruszka and Lewicka, 2007; Pietruszka, 2009b; Lewicka and Pietruszka, 2010) and despite their interesting results they are beyond the scope of this thesis.

1.5 Experimental Determination of Plant Cell Wall Mechanics

In the previous sections we defined basic material properties, learned about their molecular origin and introduced how a plant grows. Moreover, three simple experiments to measure viscoelastic properties, were presented, namely creep, stress relaxation, and oscillatory experiments. In this section I will lay out different experimental approaches in the past and evaluate their pros and cons. Table 1.1 shows a summary of the most relevant elastic measurements. The design of those experiments depends strongly on the length- and timescale of interest. I will start with the organ level and go down towards the subcellular level.

On a macroscopic scale a sample can be clamped and then stretched with micro manipulators to obtain a constant stress or strain (Burgert et al., 2003). With this microtensile test Cavalier et al. (2008) measured the extensibility of XG deficient *A. thaliana* hypocotyls and obtained mechanical properties of 16 MPa–22 MPa. Similar measurements were done by (Saxe et al., 2016) to measure the mechanical properties of *A. thaliana* hypocotyls at different ages. They found slightly higher values of 30 MPa–50 MPa. In both cases, these values describe not the elastic modulus of the wall but the volumetric modulus, a combination of the mechanical properties of intra- and extracellular spaces, of the whole tissue. This includes a combination of CW mechanics, cell geometry, and hydrodynamics. The latter arises from the cytoplasm and the turgid state of the cells. With the same experimental setup Park and Cosgrove (2012b) looked at the extensibility of XG deficient petioles in *A. thaliana*. However, with these experiments the mechanical properties were not quantified but rather relaxation rates and qualitative differences in the extension-time curves were determined.

Cosgrove (1985) measured, on a cellular level in peas (*Pisum sativum*), the me-

chanical quantities Φ and Y, which characterise Lockhart's growth model, in a combination of osmotic treatment and cell elongation measurements. An extensibility of $\Phi \approx 0.084\,\mathrm{MPa}^{-1}\,\mathrm{h}^{-1}$ and a yield threshold of $Y \approx 0.29\,\mathrm{MPa}$ were found. While this method provides important information about cellular growth, it is not suitable to obtain mechanical properties with local information at a subcellular level. Because the models of Veytsman and Cosgrove (1998) and Dyson et al. (2012) make assumptions about local CW behaviour, spatial resolution is needed to confirm them, and also to investigate the evolution of tissue stresses during plant development. In another study Wang et al. (2004) compressed tomato (*Lycopersicon esculentum*) suspension cells with micromanipulators. In a combination with FEM they found a Young's modulus for the CW of $E \approx 2.3\,\mathrm{GPa}$.

In recent years, nanoindentation has become a popular technique to obtain *in vivo* mechanical properties of the primary plant CW with spatial resolution. Those indentation experiments can provide local information about an object but the contact area, i.e. indenter geometry and three-dimensional sample properties, are crucial to obtain quantitatively correct mechanical values. For an elastic, isotropic infinite half-space, which represents an elastic, homogeneous, isotropic, infinitely thick material, the measured force differs for various indenter geometries (Sneddon, 1965)

$$F(\delta) = 2R\pi\tilde{E}\delta \qquad \text{(for flat end of a cylinder of radius } R\text{)} \tag{1.32}$$

$$F(\delta) = \frac{2}{\pi}\tan(\alpha)\tilde{E}\delta^2 \qquad \text{(for a cone of half-opening angle } \alpha\text{)} \tag{1.33}$$

$$F(\delta) = \frac{4\sqrt{R}}{3}\tilde{E}\sqrt{\delta^3} \qquad \text{(for a sphere of radius } R\text{)} \tag{1.34}$$

$$F(\delta) = g\tilde{E}\delta^\gamma \qquad \text{(general case w/ geometrical factor } g \text{ and exponent } \gamma\text{).} \tag{1.35}$$

$\tilde{E} = E/(1-\nu^2)$ takes into account the three-dimensional behaviour, by considering Poisson's ratio. Poisson's ratio describes the compressibility of a material and is in the range $-1 < \nu < 0.5$. A Poisson's ratio $\nu = 0.5$ means the material is incompressible, $\nu = 0$ means perfect compressibility (e.g. cork), and $\nu < 0$ means a material which when stretched becomes thicker in radial direction (referred to as an auxetic material). For example, Poisson's ratio for the primary plant CW is not known and might change for different developmental stages. Most nano-indentation studies assume an incompressible CW and, therefore, the choice is $\nu = 0.5$ (Milani et al., 2011; Braybrook and Peaucelle, 2013; Weber et al., 2015; Peaucelle et al., 2015).

Various implementations of nanoindentation experiments can be realised, such as AFM, CFM, and triboscopes. In fact all three instruments have been used to determine the elastic modulus of the plant CW. Peaucelle et al. (2011) and Braybrook and Peaucelle (2013) measured the mechanical properties during organ initiation of the shoot apical meristem (SAM) in *A. thaliana* with beads of a diameter of 1 µm and 5 µm. The experiments were performed on plasmolysed cells and with that they found a Young's modulus of 0.05 MPa–0.6 MPa. In a similar experiment in which the

cells were deformed by about 10 % of their diameter Peaucelle et al. (2015) reported values for the anticlinal walls of about $E \approx 0.2\,\mathrm{MPa}$.

In experiments on turgid cells the reported values for Young's modulus are usually about one to two orders of magnitude larger than in the case of plasmolysed cells. The reason for this discrepancy is the prestressed wall and additional resistance of the hydrostatic pressure during the measurements. Under those conditions Milani et al. (2011) report elastic moduli for the SAM of $E \approx 1\,\mathrm{MPa}$–$14\,\mathrm{MPa}$ and Sampathkumar et al. (2014) reported for pavement and guard cells in leaves values of about $E \approx 2\,\mathrm{MPa}$–$10\,\mathrm{MPa}$.

One problem with *in vivo* AFM measurements is the contribution of the bending modulus of the walls to the elastic modulus. Therefore, larger cells appear to be softer than smaller ones. To overcome this matter, several studies combined nanoindentation experiments with FEM. In those studies the indentation experiment is modelled and the mechanical properties in those simulations are adapted to fit the experimental result. With the CFM, an instrument which was developed for the purpose of nanoindentation on cells, Routier-Kierzkowska et al. (2012) reported for the peeled walls of onion (*Allium cepum*) epidermis, that the Young's modulus should be about $E \approx 100\,\mathrm{MPa}$. Using the same experimental setup Weber et al. (2015) reported for tobacco (*Nicotiana tabacum*) cell suspension (BY-2 cells), values of $E \approx 91\,\mathrm{MPa}$–$591\,\mathrm{MPa}$. One important result in this study is the consideration of mechanical anisotropy in longitudinal, radial, and circumferential direction. The cells were modelled with low moduli in longitudinal direction and higher ones in radial and circumferential orientation to account for the nearly unidirectional growth of the cells. A similar result as for the onion epidermis was obtained by Forouzesh et al. (2013) who applied a triboscope with a Berkovich indenter for nanoindention on leaves. In combination with FEM they found that the elastic modulus should be about $E \approx 66\,\mathrm{MPa}$.

In another study Hayot et al. (2012) measured the viscoelastic properties of *A. thaliana* leaves by using an oscillatory approach in combination with AFM nanoindentation. They found a storage modulus of $E' \approx 28\,\text{MPa}$–$70\,\text{MPa}$ and a loss modulus of $E'' \approx 4.0\,\text{MPa}$–$5.8\,\text{MPa}$. They further used FEM, which suggested that the CW in their experiments must have a true storage modulus of $E' \approx 292\,\text{MPa}$ if the CW thickness is $t \approx 500\,\text{nm}$ and the turgor pressure is $P_t \approx 0.2\,\text{MPa}$.

Zhang et al. (2017) studied the CW expansion in isolated onion (*A. cepum*) epidermis. To do this the CW was chemically extracted and a strip of the wall was attached to a movable stage. AFM nanoindentation experiments were performed to obtain the mechanical properties in the relaxed state and during extension. The effect of internal growth factors was also tested in these experiments. The elastic values reported in this work are about $E \approx 1\,\text{MPa}$–$30\,\text{MPa}$. Surprisingly, these values show a large discrepancy to the values obtained in combination with FEM, whereas the measurements of the isolated wall should give the geometry independent Young's modulus. In fact, this study neglected the BECC correction for thin samples (Gavara and Chadwick, 2012) and therefore, the reported values should even overestimate the true Young's modulus.

To summarise the results of mechanical measurements on the primary plant CW, the reported mechanical values span a large range and depend strongly on various length-scales in the experimental design. Furthermore, there are only a few reported viscoelastic or differently obtained time-dependent measurements fo viscoelastic properties and none of the reported values provides spatial resolution at the subcellular level. This time dependence is crucial to describe plant development correctly and to provide experimental evidence for existing mathematical models.

A promising method for viscoelastic mapping with high spatial resolution are dynamic AFM methods. In particular, the method developed by Raman et al. (2011) was successfully applied to measure viscoelastic properties of fibroblasts, red blood

cells and bacteria (*Escherichia coli*). This method was advanced to account for hydrodynamic corrections (Cartagena and Raman, 2014) and to use feedback on the deflection instead of the amplitude. The link between the cantilever observables, amplitude A_1, phase ϕ_1 and is given by Cartagena-Rivera et al. (2015)

$$E'_{1D} = F_{\mathrm{mag}} \left(\frac{\cos(\phi_1)}{A_1} - \frac{\cos(\phi_1^{\mathrm{near}})}{A_1^{\mathrm{near}}} \right) \tag{1.36}$$

$$E''_{1D} = F_{\mathrm{mag}} \left(\frac{\sin(\phi_1)}{A_1} - \frac{\sin(\phi_1^{\mathrm{near}})}{A_1^{\mathrm{near}}} \right), \tag{1.37}$$

with $F_{\mathrm{mag}} = \frac{k_c A_1^{\mathrm{far}}}{Q_1^{\mathrm{far}}} \sqrt{1 - \frac{1}{4Q_1^{\mathrm{far}2}}}$ being the force brought into the system by the magnitude of the cantilever oscillation. k_c is the spring constant of the cantilever, A_1^{far} is the oscillation amplitude of the cantilever far away from the surface and Q^{far} is the quality factor of the cantilever. The terms with the phase ϕ_1^{near} and the amplitude A_1^{near} close to the surface account for the hydrodynamic correction which is necessary to obtain correct mechanical values. This can be translated to a three-dimensional modulus by applying a Taylor series expansion to the model in eq. (1.35) (see section 4.2).

The difficulty of applying this method to plants will be that so far it has only been applied to isolated cells and not to tissues. Moreover, plant cells are much stiffer than mammalian cells and even stiffer than bacteria. Another challenge will be the application to plant development, because current models of plant growth use descriptions in terms of the MW model, while the method of Cartagena-Rivera et al. (2015) is based on the KV model. Therefore, a first challenge will be to apply this technique to plant tissues and obtain correct mechanical properties. In a second step the theory must be extended to link these measurements to physiologically relevant growth properties. The final part will include the application to living plants with altered physiological conditions.

In this thesis I will approach these problems in two parts. The first part focusses on the development of the technique. This will include accurate imaging, i.e. the identification of potential imaging artefacts caused by the complex topography of tissues and how they can be avoided. After the imaging conditions are well established the theoretical and experimental foundations will be built. This involves the integration of an appropriate viscoelastic model and the experimental evidence for its validity. In the second part the theoretical description which connects the viscoelastic properties to plant development will be derived. On this basis, the connection between plant growth and the viscoelastic properties the wall will be investigated. Finally, well targeted chemical interventions will provide information about the viscoelastic contribution of CMFs and pectins. This will be applied to test if viscoelastic measurements can be used as an analytic tool for an investigation of plant CW deficiencies.

Chapter 2

Materials and Methods

2.1 Plant Material and Sample Preparation

2.1.1 Wildtype Seedlings

All plants used during this project were *A. thaliana* from the ecotype columbia (Col-0). The wild type plants were grown on $2.2\,\mathrm{g\,L^{-1}}$ Murashige and Skoog growth medium (Murashige and Skoog, 1962) with and addition of 1 % sucrose, 0.8 % BactoAgar, and 0.05 % MES hydrate. The pH was adjusted to 5.70 ± 0.01.

The spacing between the seedlings was at least 5 mm to prevent the seedlings to get into physical contact before the experiments. The seedlings were always left for 3 d in the cold room at 4 °C before they were transferred to the tissue culture room as reported previously (Peaucelle, 2014). There they grew for 48 h–60 h before the experiment was conducted. Dark grown plants were wrapped in two layers of aluminium foil after (7 ± 2) h light exposure of an intensity $I \approx (100 \pm 10)\,\mathrm{\mu mol\,m^{-2}\,s^{-1}}$ to induce germination.

For the atomic force microscopy (AFM) experiments the seedlings were attached to magnetic metal plates with a diameter of 15 mm, which are the sample holders from the Cypher AFM (Asylum Research, Santa Barbara, CA). For the attachment the



Figure 2.1: *A. thaliana* seedling on AFM sample holder.

medical adhesive Hollister 72 was used (Gjetting et al., 2012). The medical adhesive was sprayed into a small glass vessel where it has a liquid state. One drop of the adhesive was evenly distributed on the metal plate by the use of a toothpick, which was dipped into the bottle to obtain the right amount of adhesive. The seedlings were transferred from the Petri dish, using sharp bent tweezers, which were gently slid under the apical hook. To place the seedlings as even as possible onto the sample holder they were pressed gently into the adhesive using a 22 mm × 50 mm cover slip. The medical adhesive had to dry for about 15 min. To prevent the seedlings from drying out, during the hardening of the adhesive, they were left in a closed Petri dish with a wet tissue, which maintains a sufficient humidity in these chambers. The Petri dish was covered by aluminium foil for dark grown seedling to avoid physiological changes by light response.

After 15 min a drop of about $\sim$ 50 ml pure water (or other liquid if for the experiment required) was used to cover the seedling. Another 5 min–10 min are required for the adjustment of the osmotic/turgor pressure, before the experiment can be started.

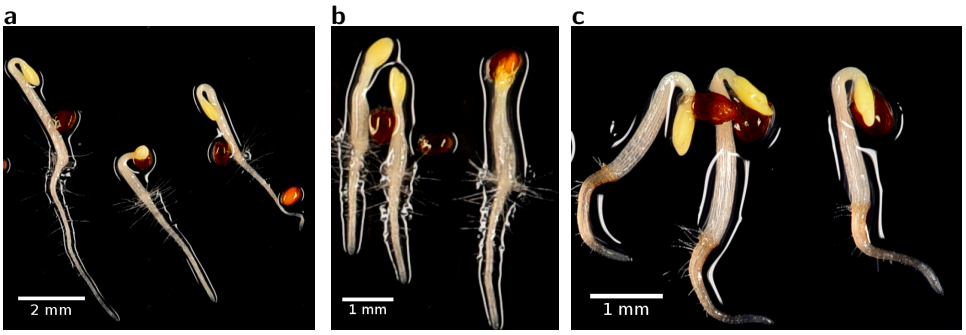


Figure 2.2: Comparison between WT (a) and IXB (b) and ECG (c) treated 3 d dark grown seedlings.

2.1.2 Pharmacological Interventions

In this thesis three different pharmacological interventions were used to change the material properties of the primary plant cell wall. All chemicals were dissolved in dimethyl sulfoxide (DMSO) whose amount was chosen so that the stock concentration was thousandfold the final concentration, i.e. DMSO was thousandfold diluted when added to the growth medium. Although this keeps the effect of the DMSO to a minimum, growth medium containing DMSO was used for the control experiments. All plants were germinated and grown on a growth medium which contains the chemical for the corresponding treatment. This was to avoid any potential influence which can arise through a transfer of the seedlings.

Cellulose synthase inhibition reduces the total cellulose content of the plant cell wall. With pharmacological treatments this can be achieved by the use of the drug isoxaben (IXB) (Heim et al., 1990). With a concentration series we found that a concentration of 3 nM generates a strong phenotype with reduced growth and cell swelling. This concentration was chosen to measure the influence of cellulose content on the mechanical properties of the cell wall (CW).

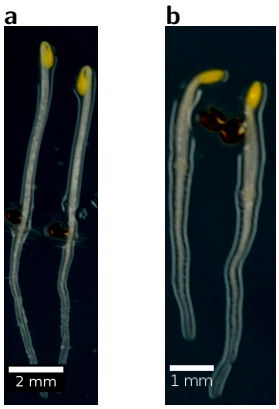


Figure 2.3: Comparison between RAB-E1d_DN DMSO (a) and DEX (b) treated 3 d dark grown seedlings.

Demethylation of pectin alters the architecture of the matrix in the CW. This can be inhibited by the drug epicatechin gallate (ECG) or epigallocatechin gallate (ECGC) (Lewis et al., 2008). For all experiments a final concentration of 200 µM were used as reported by Mravec et al. (2014) and Lewis et al. (2008). We also found in a dilution series that the phenotype is not very pronounced at lower concentrations.

Induced mutations grow like a wild type plant under environmental conditions but with certain drugs a malfunction is induced and a phenotype occurs. In this project the dominant negative mutant RAB-E1d_DN was used. RAB-E1d is part of the family of RAB GTPases, which are involved in vesicle fusion to the membrane. In particular, RAB-E1d is involved in trafficking from the Golgi to the plasma membrane (PM). Dominant negative mutants lose their function by an interference with the binding sites of the original protein. In the case of RAB-E1d_DN, the mutation can be induced by the drug dexamethasone (DEX), which was used in this project at a dosage of 1 µM.

2.2 Preparation of Hypocotyl Casts and Moulds

To investigate topographical contributions during the mechanical mapping (chapter 3) it is useful to create replicas of the sample as a control, made from less complex materials in order to asses the contribution of the topography alone. The existing protocols Dumais and Kwiatkowska (2002) turned out to not being useful for the application of viscoelasatic mapping, because dental waxes are too stiff for the investigation of dynamic mechanical properties. Instead we used a polymorphic plastic compound from ThermoMorph® to create the mould. The plastic was purchased via amazon.co.uk.

The Thermomorph was heated in water to 70 °C. In this state this substance was soft enough to be deformed easily by the seedlings. For a high quality cast the plastic must be spread evenly on a substrate. It was important to achieve a smooth surface and at the same time the compression of the material should not create domains in deeper layers because this causes a resistance when the seedling is pressed into the material. To avoid these artefacts the plastic is formed to a small ball of a diameter $d \approx 5\,\mathrm{mm}$ using thumb and index finger. The exact size depends on the size of the seedling. In this project seedlings of an age of about 3 d after transfer to the culture room were used.

The plastic ball is then compressed between two glass slides into a thin layer and after the layer had the desired dimensions the top slide was removed and the seedling was pressed into the layer using a slide. After the material became rigid the slides and the seedling were removed. During the whole process it was useful to keep the hydration layer of the plastic. This helped when removing the slides and the seedling which are hydrophilic whereas the plastic is hydrophobic.

The cast was filled with liquid moulding latex from the Vesey gallery in Birmingham, UK. The amount required depended on the size of the seedling. However, it was important that not only the cast was filled but also that a little bit of the smooth

surface was covered. This made it easier to remove the mould from the cast and attach it to a sample holder after the latex dried. If it was difficult to separate cast and mould from each other the cast could be covered in a layer of sunflower oil or any other surfactant. But the droplet formation of the surfactant could create artefacts in the mould and therefore a uniform monolayer must be achieved.

Before the mould could be attached to the sample holder, unnecessary parts were removed with a razor blade. This made it easier to find the replica on the latex surface. The mould can be attached with any adhesive to the holder. We used the medical adhesive, which was also used to attach the seedlings.

2.3 Atomic Force Microscopy

The majority of the experiments were performed with the Cypher ES$^{\text{TM}}$ (Asylum Research, Santa Barbara CA). Images with dimensions $> 30\,\mu\text{m}$ were acquired with the MFP-3D Classic$^{\text{TM}}$ (Asylum Research, Santa Barbara CA) because of the larger range of the stages.

All experiments were conducted in a liquid environment. To avoid air bubble formation between the probe holder and the probe, it is useful to not only place a drop of the liquid on the sample but also on the probe holder.

2.3.1 Dynamic Mechanical Mapping

The cantilevers used in these experiments were from Nanosensors$^{\text{TM}}$ PPP-NCLAuD. A cantilever with a nominal spring constant of $k = 48\,\text{N}\,\text{m}^{-1}$ with a range of $21\,\text{N}\,\text{m}^{-1}$–$98\,\text{N}\,\text{m}^{-1}$ and a nominal frequency of $f_1 = 190\,\text{kHz}$ with a range of 146 kHz–236 kHz. The spring constant was calibrated in air in the beginning of every experimental day using the Sader method (Sader et al., 2016). The dimensions of the cantilever are given by the manufacturer with length $l = (225 \pm 10)\,\mu\text{m}$, width $w = (38 \pm 8)\,\mu\text{m}$,

and thickness $d = (7 \pm 1)\,\mu\text{m}$. However, the length and width of the cantilevers were measured before each experimental day with the optical microscope of the Cypher ES to use these values for the calibration. The height of the conical probes is given with a range $h = 10\,\mu\text{m}$–$15\,\mu\text{m}$ and the tip radius is specified as $r < 7\,\text{nm}$. Additionally these cantilevers are gold coated at the detector side, which is important to enhance the effect of the photothermal excitation.

Several methods exist to image the dynamic mechanical properties. Our experiments are based on the method of Cartagena-Rivera et al. (2015). For this technique, the feedback for the cantilever is on the deflection, while the cantilever is oscillating at the same time. The imaging in liquid requires direct actuation of the cantilever for which we used the photothermal excitation (Ramos et al., 2006), which is implemented in the Cypher ES$^{\text{TM}}$ with the blueDrive$^{\text{TM}}$. To combine both the feedback on the deflection and the cantilever actuation by the blueDrive$^{\text{TM}}$ it was required to operate the microscope in the DART contact resonance mode. Yet, this technique is not used but in any other mode the blueDrive$^{\text{TM}}$ turns of automatically for security reasons when the feedback is set to the deflection. This also means the resonance frequency of the cantilever must be tuned in tapping-mode and not in PFM-mode where it would find the contact resonance of the system cantilever sample.

The experiments were conducted with a set point for the deflection of $d = 0.3\,\text{V}$. Lower deflections do not allow a reliable feedback and larger deflections increase the probability of cutting the CW. The integral gain was $g_i \approx 150$ and proportional gain g_p and differential gain g_d were set to zero. The blue laser power was set to $P_{\text{blue}} = 8\,\text{mW}$ for the first eigenmode. To achieve this high laser power, we used the blue filter, i.e. no laser attenuation.

For multifrequency experiments, the cantilever was driven at the first and second eigenmode simultaneously. The settings for the first eigenmode were as described above. For the second eigenmode, the resonance frequency was about $f_2 \sim 530\,\text{kHz}$

and this mode was driven with a laser power of $P_{\text{blue}} = 1\,\text{mW}$.

2.3.2 Force-Volume Measurements

Force-volume measurements were used in this thesis mainly for the calibration of the dynamic modulus. For this purpose, the scanned z-range should be as large as possible. The distance was chosen to 3 µm (the height of the z-stage is 5 µm). To avoid viscoelastic responses influencing the deformation process, the indentation speed was chosen to $6\,\mu\text{m}\,\text{s}^{-1}$ and the sampling rate during this process was 16 kHz. The trigger point of the force curve was set to 1 V, to obtain information about the indentation behaviour around the set point of the mechanical scan (0.3 V, see above).

2.4 Photographs

Photographs of the seedlings were taken by John Baker. Bright field images were acquired at various zoom levels with a Nikon D700 and a 60 mm macro lens. For each zoom level a scale bar for calibration was imaged.

2.5 Confocal Microscopy

2.5.1 Determination of Cell Wall Thickness

The epidermal CW of the *A. thaliana* hypocotyl is, with a thickness $d > 200\,\text{nm}$, thick enough to be determined by confocal microscopy. The major problem is to get a dye into the hypocotyl or the CW of the hypocotyl. For this reason the hypocotyl was cut with a razor blade near the desired location for measurement. The part of interest was then placed into a dilution of calcofluor white for 90 min with a concentration of $50\,\text{mg}\,\text{mL}^{-1}$ and Nile red for 30 min with a concentration of $0.1\,\text{mg}\,\text{mL}^{-1}$ on a standard microscopy slide and a cover slip was put on top with two layers of tape between the

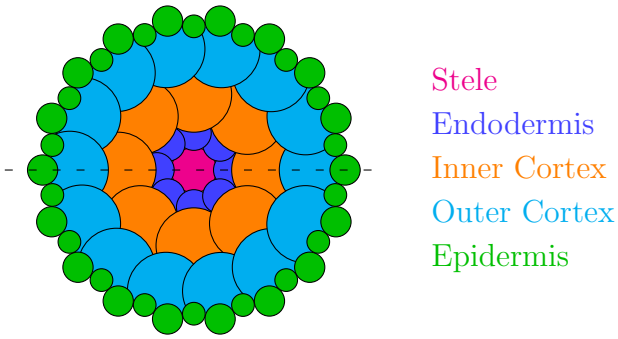


Figure 2.4: Illustration of measured cross section of confocal measurements. The circles represent cells in a cross section of a cylindrical hypocotyl. The dashed line shows the height at which the CW thickness was measured.

cover slip and the slide. The calcofluor white is supposed to stain the CW (Greenspan et al., 1985), while the Nile red stains the hydrophobic parts of the cell, i.e. cuticle, PM, and cytosol (Herth and Schnepf, 1980). The images were taken with a Zeiss LSM 510 Meta confocal microscopy, which was operated in sequential mode with a 4 line average and an excitation with two lasers. The wavelength of the first laser was at $\lambda_{1,e} = 405\,\text{nm}$ to excite the calcofluor white and the emitted light was collected in a range of $\lambda_{1,c} = 435\,\text{nm}$–$585\,\text{nm}$. The excitation of the Nile red with the second laser was at a wavelength $\lambda_{2,e} = 543\,\text{nm}$ and the light was collected at wavelength $\lambda_{2,c} \geq 585\,\text{nm}$. The pinholes were set to a diameter of $d_1 = 21\,\mu\text{m} \mathrel{\widehat{=}} 0.5\,\text{Airy units}$ and $d_2 = 36\,\mu\text{m} \mathrel{\widehat{=}} 0.9\,\text{Airy units}$ for the first and second laser, respectively. Since only a few cells near the section were dyed, the non-damaged cells near the section were imaged with steps of $x \times y \times z = 110\,\text{nm} \times 110\,\text{nm} \times 500\,\text{nm}$. The magnification was $40\times$ with a C-Apochromate ($1.2\ NA$) water immersion lens.

To obtain a higher resolution than this is possible with the z resolution, the stacks were measured at about half way through a hypocoyl section at the epidermis as illustrated in Figure 2.4.

2.6 Data Analysis

The AFM data was entirely analysed with Python3.5 for which I was using my own library that I coded completely. The code is published under `https://github.com/jcbs/ForceMetric`. The only exception from that is the analysis of the plant growth.

2.6.1 AFM Library

To read the IgorPro '.ibw' files it is possible to use the binarywave package from the python igor library. However, using this package the data is not brought into an appropriate format, where the metadata and the data can be accessed easily. Figure 2.5 shows a summary of the classes which build up an easily accessible data format suitable to describe AFM data. Additionally, there are classes which create the framework for static and dynamic mechanical analysis.

In a first step, I translated the data structure as read from the igor.binarywave package into the `Wave` structure, where the metadata can be easily accessed by a dictionary structure. This is implemented in the `Header` class. Furthermore, the data can be accessed in the `Wave` class through the `getData` function. The `Wave` class is then used to create the `AFMScan` class to represent the structure and useful functions for AFM scans. Similarly, I created a data structure for force-volume measurements that contains the class `FDIndices` and `FDData`. The first class only contains the indices at which sampling point the trace, dwell time, and retrace start and end. The second class returns the appropriate data in separate arrays for trace, retrace, and dwell time. In another step an object for static force measurements was created that includes calculating the contact point (class `ContactPoint`) and the Young's modulus (class `StaticYoung`). These two classes create in combination with the classes `Wave` and `FDData` the class ForceCurve, which provides the structure to analyse any kind of quantity vs distance data, including phase, amplitude,



Figure 2.5: Representation of the programmed AFM library showing hierarchy and dependencies of the python classes as well as the underlying functions of the individual classes.

deflection, indentation, and force, with a focus on mechanical analysis. Finally, a structure for the analysis of dynamic mechanical analysis was created, represented by the class `DynamicViscoelastic`, and the translation of these one-dimensional values into three dimensional quantities, given by the class `DynamicYoung`. These two class create in combination with the class `AFMScan` the class `DynamicMechanicAFMScan`, which is suitable to translate amplitude and phase and appropriate calibration values into maps of dynamic mechanical properties.

2.6.2 Hydrodynamic Calibration

The contact point of the force-volume measurements was determined with the force indentation variation (FIV) method (see chapter 3). With the knowledge of the contact point the phase ϕ^{near} and the amplitude A^{near} near the surface were determined at an indentation $\delta \approx -10\,\text{nm}$, which corresponds to a distance of 10 nm above the surface, for the first and second eigenmode. Furthermore, the quantities ϕ^{far}, A^{far}, and d_0 were determined with an average over the first twenty data points of the force-volume curve, which was usually at a distance $\delta \approx -2\,\mu\text{m}$. d_0 represents the initial deflection, i.e. the deflection without any force applied to the cantilever. This deflection is usually set to zero but thermal equilibration can cause a change of this value. An accurate knowledge of the initial deflection is crucial to obtain the correct quantitative mechanical values. Finally, the relaxation modulus E_0 was determined by fitting 20 %–80 % of the applied force range to the Sneddon model (see chapter 1).

2.6.3 Computational Extraction of Cell Walls

For unidirectional growth three different kinds of cell walls can be distinguished, which are the periclinal walls, and the anticlinal walls, transverse and parallel to growth direction. For a detailed analysis of the mechanical properties, the different walls have to be considered separately. Moreover, it is also important to distinguish between

walls of the same kind. For example a single epidermal cell has two longitudinal and two transverse anticlinal walls and two periclinal walls. For the latter ones only the outer wall can be measured. If the cells under consideration are in a tissue, they share their longitudinal and transverse walls. The tiling of tissues causes that, in most cases, the longitudinal walls of one cell belong at least to two other cells. Because of the shared nature of the anticlinal walls but also because of their different orientation and growth relevance, they must considered separately.

If we consider the anticlinal walls on the surface topography of the epidermis, the walls longitudinal to growth direction have the significant feature of being the local minimum of the cross section, which is taken orthogonal to the wall. However, if the position of the wall is not known it is not possible to determine the line orthogonal to the wall. For automatic computation of these walls we used the fact that the slope of the periclinal walls changes its sign between adjacent cells. This change was detected by calculating the gradient and with the application of a canny edge filter to its absolute value the longitudinal walls were detected. Different longitudinal walls were determined by the choice of corresponding regions of interest (ROIs).

In contrast, the transverse anticlinal walls are 'saddles' and usually they are the shortest connection between the cell's two longitudinal walls. The restriction of the microscopy stages, however, made it rarely possible to measure the whole wall. Therefore, a computational implementation to determine these walls automatically was too difficult to implement. Instead, the walls were determined manually with lines of three to four nodes.

The periclinal walls were determined last and were defined as everything which is neither longitudinal nor transverse wall. Since the transition of the mechanical properties of the walls must be smooth, but only the differences between the walls and not their transition regime is of interest, a margin of 20 px around the anticlinal walls was applied.

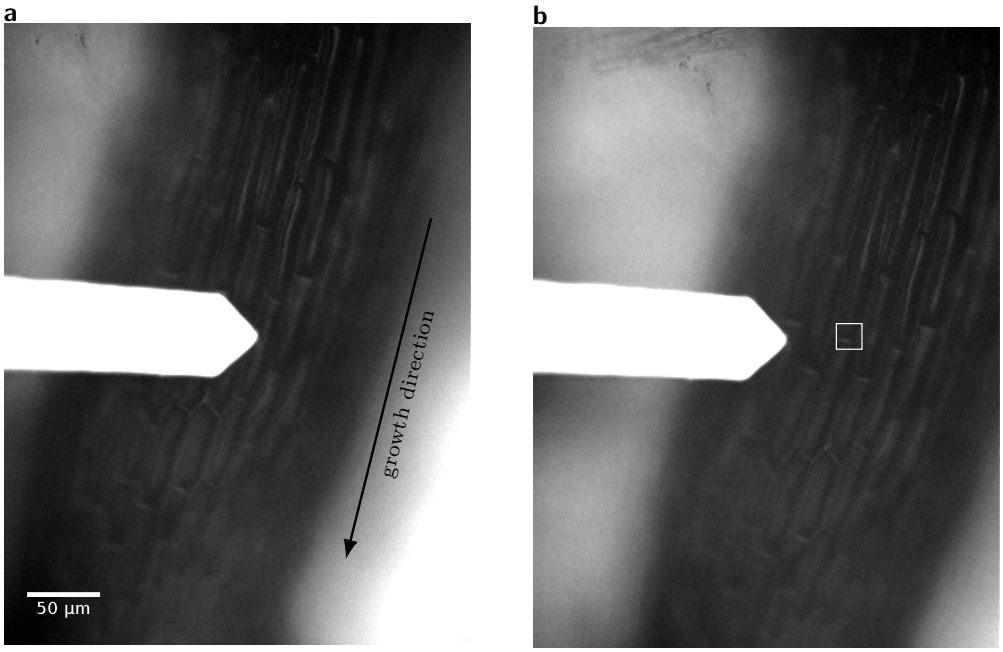


Figure 2.6: Cell length measurements. (a) shows the photograph directly after the scan, when the cantilever is above the imaged region. (b) shows the imaged region, which is indicated by the white rectangle.

2.6.4 Statistical Analysis and Data Representation of the Mechanical Properties

The mechanical properties were extracted for the different walls as described in section 2.6.3. To avoid artefacts which arise from the z-stage when it moves into its limits, all values which were acquired within 200 nm from the limits, were discarded for the analysis. All walls were considered separately and their mean was considered as quantity for this specific wall. For statistical significance Welch's t-test was used implemented in the scipy stats package with the ttest_ind function. All represented errors are the standard errors (SE) of the mean achieved by bootstrapping with $n = 1000$ iterations and a confidence interval $ci = 95\,\%$ as it is implemented in the seaborn package from python.

2.6.5 Cell Length and Growth Velocity

To measure the cell length, the seedlings were photographed directly after AFM imaging with the cantilever over the last imaging position. For the photograph the internal optical microscope of the Cypher^{TM} at 2 $\times$ magnification and the video panel of the AFM software were used. A second image was acquired after the cantilever was moved aside to see the whole cell (fig. 2.6). The images were opened with the Fiji (ImageJ) imaging software and every cell was measured in length several times, where images from different imaging positions were used. This gives the length of individual cells (not only the ones which were measured with the AFM) and an approximate error of 5 %.

A population average of these cell lengths was used to calculate a growth velocity, because mechanical measurements initiate physiological changes (Braam, 2005). The population average of the length measurements at different time-points introduces the problem that outliers or differences in germination times can lead to negative growth velocities. However, from the definition of plant growth it is known plant growth that they display only monotonic growth behaviour. To reduce the artefacts of negative growth the data points were fitted with an polynomial of degree two and the analytical derivative of this fit was used to determine the velocity.

2.6.6 Hypocotyl Length

The hypocotyl length was measured with segmented lines in fiji from photographs of the seedlings. The statistical analysis was performed in Python with the usage of the function ttest_ind from the the scipy.stats package was used.

2.6.7 Measuring Cell Wall Thickness from Confocal Microscopy Slices

To obtain the CW thickness from the confocal images, the slices were opened with ImageJ 1.51s (fiji) using the bio formats plugin. Only healthy cells were chosen and a line profile of the fluorescence intensity was measured at the z-slice were the wall section was the thinnest. The reasoning behind this is that the CW has roughly the same thickness within one cell and the thinnest section is the undistorted cross-section. For example if the cross-section is measured at a curved section of the CW the wall appear thicker than it actually is because the section is not planar. The line profile was measured over an average of 50 px, which corresponds to 5.5 µm, to obtain a good statistical average. Another advantage of the averaging is that it reduces artefacts, which can arise if the hand-drawn line is not orthogonal to the cell faces. This averaged profile was saved for both channels (calcofluor white and Nile red) for further analysis in Python3.5. For each cell at least two profiles were measured and the manual analysis was repeated three times. No significant differences were obtained for the different analysis and therefore, only the example of one data extraction is shown in section 5.2.1.

With the two dyes there are two different methods to determine the CW thickness. On the one Hand, calcofluor white is supposed to stain only the CW and therefore, the full width at half maximum (FWHM) was used to determine the wall thickness. To reduce artefacts of a small sample size per profile, the peaks were fitted to a Gaussian distribution, using a least square minimization, and its analytical FWHM was used. This is given by the relation $\mathrm{FWHM} = 2\sqrt{2\ln(2)}\sigma$, with the variance of the Gaussian σ. On the other hand, Nile red stains only the cuticle and the PM/cytosol and therefore, a dip in intensity appears at the position of the CW. This and the vacuolated state of the plant cell enables the possibility of measuring the peak to peak distance between the cuticle and the cytosol and use this as CW

thickness. Additionally, the resolution of small structures depends on the point spread function (PSF) of the focussed laser beam, whereas the measurement of the peak to peak distance is not affected by this. Therefore, the peak to peak distance is more accurate.

Part I

Development of AFM Based Techniques and Theory for Quantitative Mapping of Live Tissues of *A. thaliana*

This first part of the thesis focusses on the development of a suitable technique for viscoelastic mapping on plant tissues. In a first step the ideal imaging conditions are identified. This includes the detection of possible imaging artefacts and how they can be avoided. For this, contact mode, tapping mode, and force-volume measurements are considered independently, because all methods display characteristic imaging artefacts. To improve the qualtity of the images a few simple theoretical considerations are provided.

In a second step, an existing theory for viscoelastic mapping is extended to match the requirements for the use of viscoelastic dynamic AFM mapping to investigate plant development. In the beginning we develop a mathematical description to link the generalised Maxwell (MW) model to the cantilever observables. To obtain three dimensional material properties we demonstrate that the contact behaviour of the probe during the indentation follows the Sneddon model. In this framework we demonstrate the viscoelastic mapping on epidermal cells of living *A. thaliana* hypocotyls and compare the elastic component with previously reported results. Furthermore, we provide a new method to test which viscoelastic description is most appropriate for the plant cell wall. With the knowledge of the viscoelastic models obtained from the dynamic modulus we show that it is possible to extract more detailed viscoelastic properties, such as k_{M}, τ, η, and k_{∞}, which are required for physiological investigations of the plant CW and to link the mechancis to polymer physics theory.

Chapter 3

Accurate Imaging With AFM on *Arabidopsis* Hypocotyl Tissues

Atomic force microscopy (AFM) requires a carefully fine-tuned experimental design to achieve high resolution and quantitative high data quality. The optimal setup depends strongly on several properties of a sample, such as the topography, the size of the region of interest, and mechanical properties, i.e. visco- and poro-elasticity. In the case of a tissue with the curvature of the hypocotyl, the topography and stiffness are of special interest, because they can introduce significant imaging artefacts and, therefore, they need to be taken into account in the optimal choice of AFM cantilevers.

It should be emphasised that AFMs were historically developed for high resolution measurements on surfaces. Consequently, the stages are usually very small to suppress noise in the measurements. Therefore, most AFMs are not designed to measure large scale tissues such as the *A. thaliana* hypocotyl. For example the Cypher AFM from Asylum research has a z-stage of 5 µm and the x-y-stage has a range of 30 µm. It is obvious that such a microscope cannot measure whole cells of a length of $l \sim 80$ µm. But even microscopes designed for biological applications, such as the Nanowizard® 4 BioScience from JPK instruments (`www.jpk.com`) has a range of only 100 µm in all

three dimensions and this means that even with this microscope a hypocotyl with a diameter $d_h \approx 200\,\mu m$ cannot be measured as a whole and it will be even difficult to have several cells of the size mentioned above in one frame. Nonetheless, it has been shown that AFMs are extremely useful for biological measurements of cells, tissues, and plants *in vitro* and *in vivo* (Peaucelle et al., 2012; Perrault et al., 2015; Milani et al., 2011; Braybrook et al., 2012; Raman et al., 2011) but one has to be aware of restrictions that apply to experiments conducted at larger samples.

This chapter discusses the difficulties, which can arise during the imaging of tissues in general and of the hypocotyl in particular. In the beginning contact mode is discussed, because the artefacts occurring here are more obvious and can also occur in tapping mode. The artefacts in tapping mode are subtler and some of them are only relevant for quantitative mechanical measurements.

3.1 Contact Mode – Stiffness And Topography And Cantilever Design

3.1.1 Basic Imaging And Artefacts

3.1.1.1 Topography Artefacts

In contact mode several major artefacts can be found, which can arise from an inappropriate cantilever shape and size. First, I will discuss the effect of the probe geometry. Geometrical artefacts are already known from smaller structures (Haugstad, 2012) but they are less studied in the case of tissues.

With a given sample topography $h(x, y)$ the measured topography $z(x, y)$ depends on the probe geometry $g(x, y)$. At any given point (x', y') the measured topography is given by the first contact point with the sample subtracted from the initial probe height. For a well designed experiment this contact point should be the tip of the

probe. The tip position of the probe is given by $g(x_0, y_0)$ and can be set to zero without any restriction of validity. This can be brought into the mathematical form

$$z(x, y) = g(x_0, y_0) - \min_{x,y}(g(x - x', y - y') - h(x', y')). \tag{3.1}$$

To simplify this, from now on we consider everything on line profiles, i.e. $z(x, y) \to z(x)$, $g(x, y) \to g(x)$, and $h(x, y) \to h(x)$. For example we look at the measured topography given by the simple topography of a step measured with a conical indenter of half-opening angle α. The step of height h_0 can be represented by the Heaviside step function $\theta(x) = \begin{cases} 1 & x > 0 \\ & \\ 0 & x < 0 \end{cases}$, as $h(x) = h_0\theta(x)$. The shape of the conical indenter is given by $f(x) = m|x|$ with a slope $m = \tan(90° - \alpha)$. The measured result is then given by

$$z(x) = \begin{cases} 0 & x < x_c \\ m|x - x_c| & x_c < x < 0 \\ h_0 & x > 0 \end{cases} \tag{3.2}$$

and the critical point x_c is given by $x_c = -h_0/m$. The result is plotted in fig. 3.1a. From the plot we can immediately see that every feature below the slope of the cone from the critical point until the height of the step is reached, cannot be resolved. In other words, if the slope of the probe is shallower than the slope of the feature, it creates an imaging artefact. This means even with the knowledge of the tip geometry we lose information. This effect becomes more pronounced the smaller the features are until the feature cannot be resolved any more (fig. 3.2), because the noise is larger than the deviation in the trajectory of the measurement. A similar problem occurs

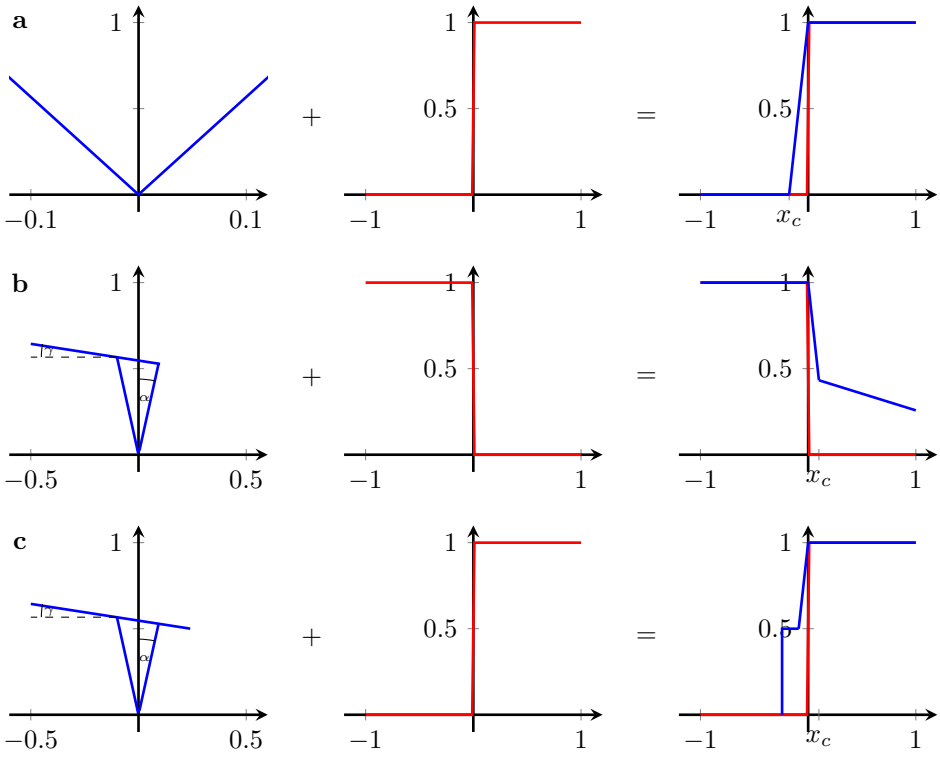
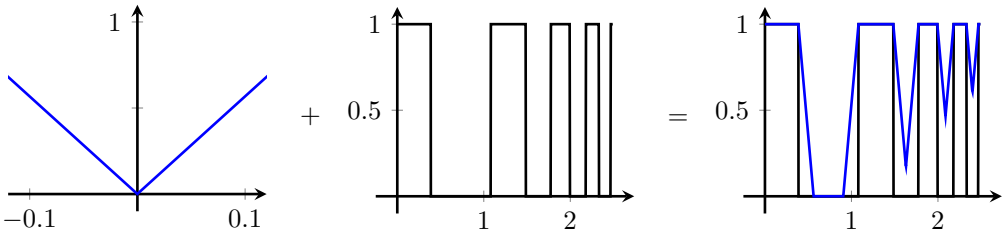
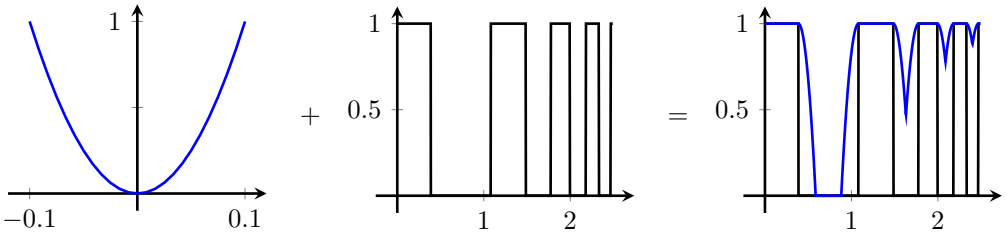


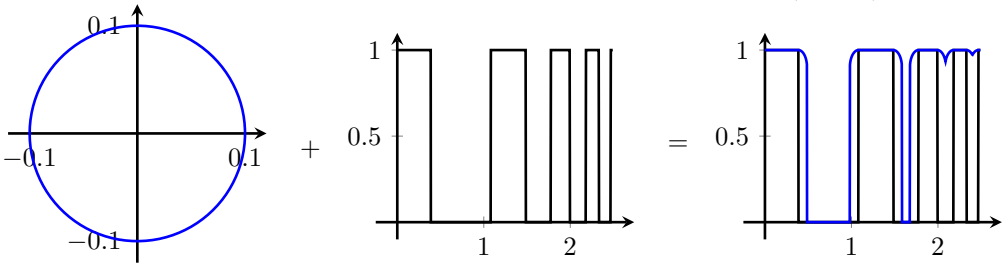
Figure 3.1: Topography of a step function measured with a cone (a) and a cone attached to a cantilever (b, c). In all three cases the shape of the step is given by the slope of the probe. If the slope is shallower than the slope of the step this creates an artefact, otherwise the real slope can be measured. In the case of the cantilever attached to the cone (b, c), the cantilever creates an artefact if the height of the probe is smaller then the height of the step. (b) shows the measured profile if the cantilever hits the sample because the probe is too short. (c) shows a cantilever design where the probe is not at the end of the cantilever and in this case the cantilever hits the step first. The jump occurs when the cantilever is above the step and the probe starts to hit the sample. The half-opening angle of the tip is $\alpha = 10°$ and the inclination of the cantilever is $\gamma = 11°$.



(a) Conical indenter with half-opening angle $\alpha = 10°$



(b) Paraboloidal indenter with apical radius $R_0 = \left(\frac{\mathrm{d}^2 f(x)}{\mathrm{d}x^2}\right)^{-1} = 0.02$



(c) Spherical indenter with radius $R = 0.1$

Figure 3.2: Measured topography for features of different sizes and different tip geometries. The blue line in the resulting (right image in every line) measured topography.

if a cantilever is attached to the probe and the height of the probe is smaller than the height of the step. In this case the cantilever introduces an additional artefact since it hits the step because the probe is too short to touch the sample (fig. 3.1b). In some cantilever designs the probe is not attached at the end of the cantilever but a little bit before (fig. 3.1c first graph). This leads to the fact that the cantilever hits the step before the probe does and images the real step until the cantilever is above it. This leads to a 'jump' of the cantilever until the probe hits the sample (fig. 3.1c third graph) and this part is probed as in fig. 3.1a.

Figure 3.2 shows how the resolution changes for features of different sizes and for different probes. It clearly shows that the smaller the feature the worse the resolution.

Furthermore, it can clearly be seen that the behaviour for a conical (fig. 3.2a) and a parabolic (fig. 3.2b) indenter is very similar but the resolution of a cone is better than the one of a parabola. The worst resolution is achieved by a spherical indenter (fig. 3.2c). Moreover, the sphere has the additional problem that only small step heights can be resolved with a high resolution, since a cantilever must be attached to the probe as well, which leads to the artefacts described above. More generally, a spherical probe is not designed for scanning experiments but a good choice for indentation experiments.

From these considerations and eq. (3.1) it can be conducted that the contact angle between two cells must be smaller than opening angle 2α of the tip (if we assume a conical tip) to resolve all features.

While the features considered so far arise in the area of the measured image, they are easy to recognise. More difficult artefacts can be found in the case of curved (or even more complex) tissues, because the origin of the artefacts can be outside of the region which was imaged with the AFM. The cause for these artefacts originates usually not from the tip but is caused by the cantilever itself. If we consider a step with a step size larger than the tip length, the cantilever will start 'sampling' the step, once the tip is below the step height (fig. 3.1). This process continues until the lever drops off the step. If the tissue has a complicated structure, such as a hypocotyl with an idealised regular structure of epidermal cells, we can observe the influence of the topography. If, for example the right-most cell in fig. 3.3 is measured, the artefacts originate from previous cells which are not in the measured image. This is very likely to occur, since a typical cantilever has a length of about $l \sim 100\,\mu\text{m}$–$250\,\mu\text{m}$ and the dimensions of a typical AFM scan are $20\,\mu\text{m} \times 20\,\text{um}$ to $100\,\mu\text{m} \times 100\,\mu\text{m}$. Therefore, the best cantilever choice is a long lever with a high aspect ratio probe. Moreover, the tip should be longer than the height of the largest feature, that can disturb the measurements.

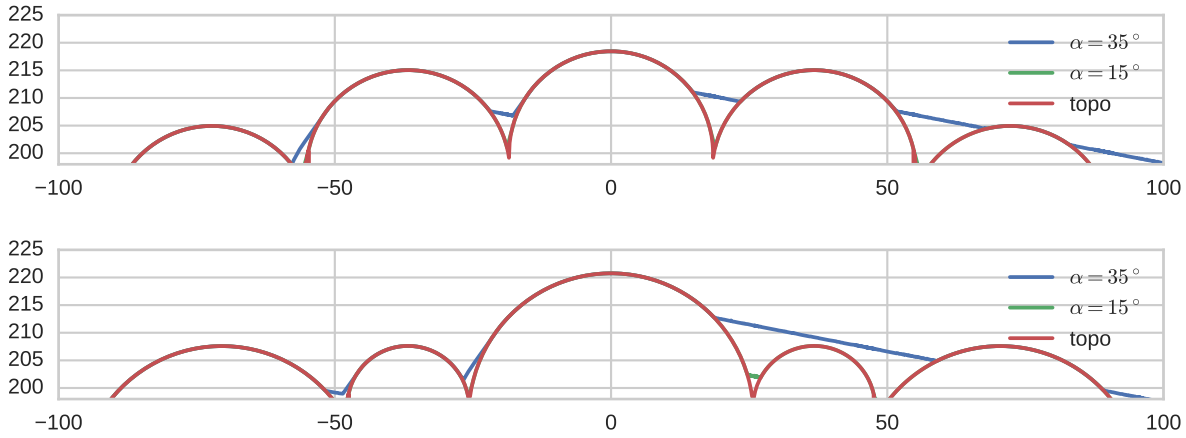


Figure 3.3: Ideal hypocotyl surface with 34 epidermal cells. Surface topography simulated data for an AFM imaging experiment for cantilevers with half-opening angles $\alpha = 15°$ and 35° and a maximum tip width of 8 µm just below the cantilever. As the images clearly show a cantilever with $\alpha = 35°$ is not appropriate.

It is possible to see those artefacts when looking at real data. This can be done by calculating the gradient of the raw data of the height image[1], i.e. the slope m, in direction of the cantilever (in our case x, fig. 3.4). From the gradient the angle β of the slope can be obtained by $\beta = \arctan(m)$.

The Asylum Research AFMs have a typical cantilever slope of $\gamma \approx (-11 \pm 1)°$[2]. Note that the minus sign comes from the orientation of the coordinate system which, in this case, is in the same orientation as the cantilever coordinate system. With this knowledge we can compare the extracted angles from the data with the typical cantilever angle (the range of the angle is indicated by the dashed lines in fig. 3.4a). This, however, must be done carefully, because not all the angles in this range indicate that the cantilever was in contact with the sample. It could simply be that this is the slope of the sample. In the case of the hypocotyl the knowledge about the surface can be used. The gradually changing topography suggests, that every constant slope of

[1]It is very important that the raw data is used and not a flattened or plane subtracted image. It is worth mentioning that the default settings of some AFM softwares is save corrected images and in those corrected images the real information of the slope is lost and it is not possible to find the correct angle, which is significant to the cantilever.

[2]I got this information directly from Asylum Research

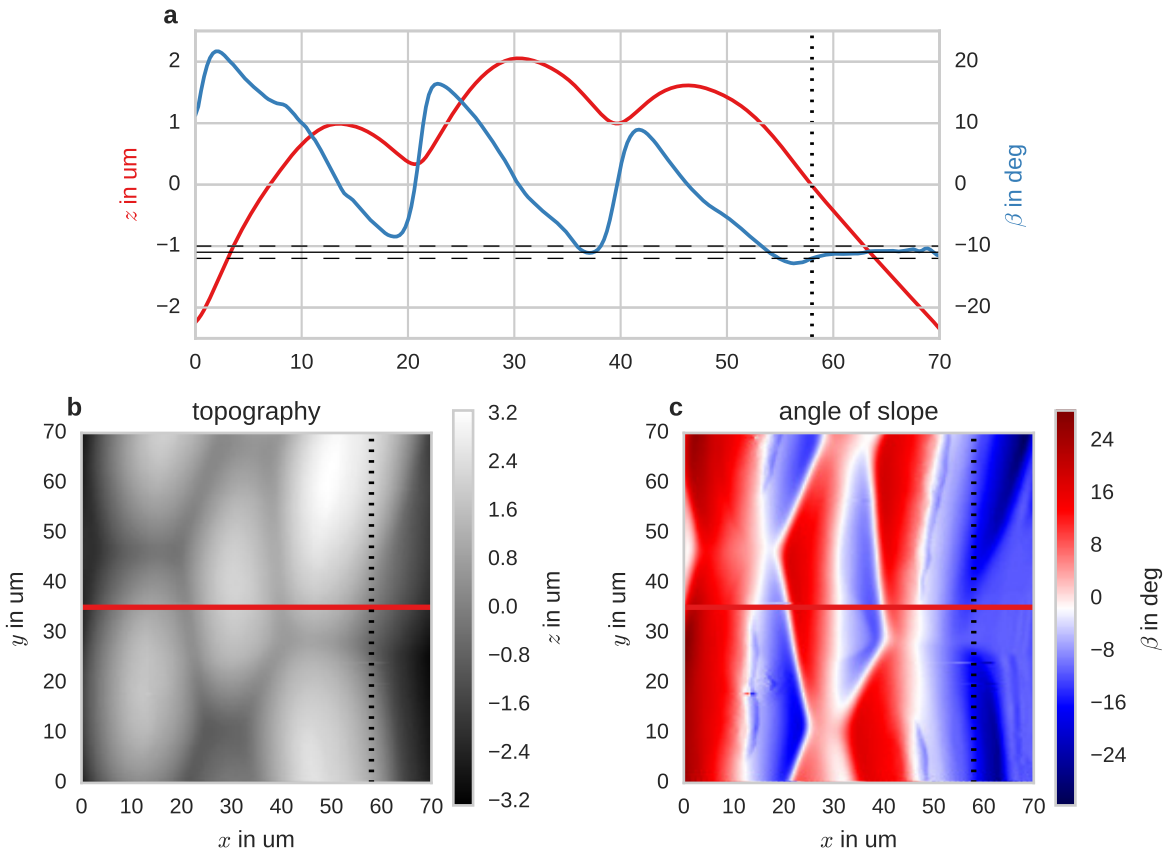


Figure 3.4: Topographical data from an *A. thaliana* hypocotyl. (a) shows the topography profile and its corresponding angle of the slope for an *A. thaliana* hypocotyl. (b) shows the topography of a whole AFM scan and the red line indicates the position of the line plot shown in (a). (c) shows the angle of the slope of a whole AFM scan and the red line indicates the position of the line plot shown in (a). The dashed lines in (a) indicate the range of the cantilever angle given by the manufacturer. The dotted vertical line in all three images is an aid for the eye to indicate the region with the artefacts.

approximately $-11°$ originates from the cantilever. This means for example that in the profile in fig. 3.4a all values at the right hand side of the dotted line are artefacts. However, this could not be true for other sections as it can be seen in fig. 3.4c, the angle changes gradually for other x-sections. From this data we infer that a cantilever with a long probe is required, as already suggested by the generated artificial data in fig. 3.3.

Artefacts can be minimised by minimizing the area of the cantilever over the sample. In the case of a unidirectionally growing tissue, the cantilever should be placed orthogonal to growth direction. In fact, a cantilever oriented parallel to growth direction can even hit the tissue with the cantilever chip. This interaction introduces more difficult artefacts and in many cases it is impossible to acquire an image because the sample is moved by the cantilever chip.

3.1.2 Sample Artefacts

Further problems can arise, which are not imaging artefacts in the classical understanding, but rather originate from the sample itself. Yet they are sometimes difficult to recognise. Two examples I will discuss here are cell damage and loose, i.e. not properly attached, samples.

Cell damage is an artefact, because the cell is in an unphysiological state. Those artefacts can originate from two phenomena. First, they can originate from a poor sample preparation, e.g. the sample dried out before water was added or mechanical damage happened during mounting. Second, mechanical damage can happen during imaging. This is the case, if the tip is too sharp and at the same time the applied force too large. The pressure can pierce the wall during the approach of the probe or, when scanned in contact mode, the wall can be cut. The difference between piercing and cutting the cell wall is, that in the first case the rupture of the wall is caused only by forces normal to the sample forces, whereas in the second event the

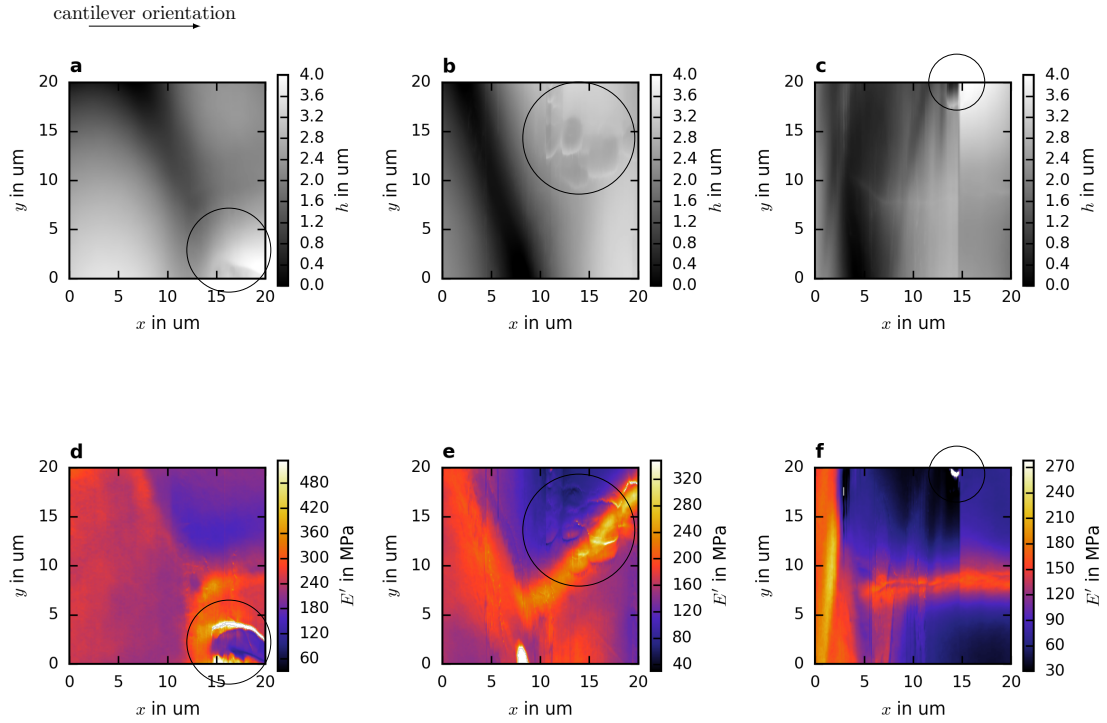


Figure 3.5: Cell damage. (a) and (d) show a damage where a layer of the CW was removed and the damage changes the mechanics. (b) and (e) show a damage where parts of the CW were removed as well but in this case the damage does not change the mechanical properties. (c) and (f) show a cell which was pierced during the scan. It can clearly be seen that the cell deflated and the mechanical properties change with the deflation. The y was the fast scanning axis and x the slow scanning axis. The scanning direction was from right to left.

rupture is predominantly caused by shear forces. Under typical imaging conditions the damage is more likely to occur through the shear than through the normal forces. Moreover, it is possible that only certain layers of the cell wall (CW) are damaged, which ultimately might change the mechanical properties of the wall.

3.1.2.1 Cell Damage During Data Acquisition

Artefacts of cell damage are easy to recognise if the cell geometry is well known. Figure 3.5 shows topography images with three different cases of mechanical damage

that occurred during the measurement, plus the corresponding maps of the storage modulus E'. Figure 3.5a shows damage where a part of the CW was removed during the scan and fig. 3.5d shows that in this particular case the mechanical properties change because of the damage. Figure 3.5b shows an example where the damage is again removal of CW material but as fig. 3.5e shows it hardly affects the mechanical properties. Finally, fig. 3.5c shows an example of a cell which was pierced during the scan and immediately lost its turgor pressure. The topography image shows a very sharp transition from a well defined topography towards a more blurry deflated one. Moreover, fig. 3.5f shows that not only the topography is affected but also the mechanical properties changed after the damage occurred. The origin of the changes of the mechanical properties is explained in detail in chapter 5. In general, cell damage can be reduced by the use of blunt probes, i.e. a truncated cone, which can either be bought or created by using sharp tips for other experiments before they are used for the measurement of cell mechanics.

3.1.2.2 Artefacts During Sample Preparation

The problem of poor sample preparation is that the sample is pushed down towards the substrate during the approach of the cantilever towards the surface. However, during the experiment the buoyancy of the seedling causes it to float which usually results in a blurry image and the cell appears much softer than it actually is. Eventually the z-piezo will run into the limits of its stages because the buoyancy of the seedling will cause it to rise further up. With little experience these artefacts are sometimes very difficult to spot because the buoyancy of the seedling varies and the change in position can happen very slowly. An easy test to spot this problem is to activate the feedback loop (without any scan) and watch if the position of the z-piezo is changing. If this is the case the sample is most likely floating. Alternatively, the system is not in thermal equilibrium which also is not a good imaging condition.

3.1.3 Force Volume Measurements

In contact mode we make the assumption that our sample is not deformed during the measurements. This assumption is only true if the cantilever is much softer than the sample. However, if the mechanical response of a sample should be measured the cantilever must have a similar stiffness to the sample and consequently the sample will be deformed. To find the mechanical properties of a sample it can be deformed by indenting it with the probe and measuring the force response as a dependent variable of the distance. This kind of experiment is called a force volume measurement. During force volume measurements not only the same artefacts as in contact mode appear but also additional ones caused by the deformation. For an isotropic linear elastic material those artefacts can be easily spotted by looking at the deviation of the indentation from the theoretical prediction. However, most materials, such as the plant cell wall, are neither isotropic nor linear elastic. The difficulty is to distinguish between artefacts and non-linear or non-isotropic behaviour.

First, it is important to recognise that the artefacts can occur at any point during the deformation. Here, I will only discuss the most common artefacts for experiments on curved tissues. Second, I note that not all apparent artefacts are real. Some are caused by incomplete theory which is beyond the scope of this thesis.

3.1.3.1 Derivation of the Hertz Model for a Conical Indentation of an Inclined Half-Space

One major problem of curved tissues is that the indentation is usually not normal to the surface but occurs at an angle. The classical indentation theory from Hertz (1882) and its modifications assume the orthogonal indentation δ of an infinitely thick isotropic half-space. A correction for the contribution of the substrate for thin samples was introduced by Gavara and Chadwick (2012). Corrections exist also for the effect of a slope and they account for the fact that the force is not acting normal to the

surface (Routier-Kierzkowska et al., 2012). However, this is not sufficient, because the detected force depends on the projected contact area A_c between indenter and sample. For a conical indenter on an inclined isotropic half-space or on a flat anisotropic half-space, the contact area becomes elliptical (because it is an oblique cone section). This part is a theoretical consideration of the indentation of an inclined half-space by a conical indenter. The inclination of the half-space can be described by the inclination angle β and the cone is characterised by the half-opening angle α (fig. 3.6). With this considerations of the contact area A_c we proceed with the approach of Vlassak et al. (2003), who considered the convolution of an indentation with an elliptical cylinder and an axisymmetric cone.

Consider the axisymmetric cone $\mathcal{C}$ with half opening angle α and the tip C. The aim is to determine A_c for which it is necessary to determine the half axes a and b for a section of a distance h to the tip C, where h is on the central axis of the cone. If the angle β of a virtual cone section fulfils the condition $0 < \beta < \pi/2 - \alpha$, the section is elliptical. The other cases are not interesting for an indentation experiment since this implies the indentation is not happening with the tip of the probe. It is easy to show that for the small half-axis $b = r_{\mathcal{C}}(h) = h \cot \alpha$ is obtained. For the axis a we calculate the intersection between cone and plane. Let's consider the cone in projection with the origin $\mathcal{O}$ of the coordinate system at the position of the tip C (fig. 3.6). Thus, we seek the intersection between the triangle (ABC) and a line $g_1(x) = m_1 x + h$ with slope $m_1 = \tan \beta$. The triangle can also be parametrised by lines $g_i(x) = m_i x, i = 2, 3$ with slopes $m_3 = -m_2 = \cot \alpha$. The x-coordinates of the intersection are then given by

$$g_i(x) = m_i x \stackrel{!}{=} m_3 x + h = g_3(x). \tag{3.3}$$

This leads to the intersections $x_{i,s} = \frac{h}{m_i - m_1}$. If we substitute these into g_i we get the y-coordinate $g_i(x_{i,s}) = y_{i,s} = \frac{m_3 h}{m_i - m_3} + h$. Now the large half-axis a is given by

$$a = \frac{1}{2} |\mathbf{s_2} - \mathbf{s_3}|, \tag{3.4}$$

with $\mathbf{s_i} = (x_{i,s}, y_{i,s})^T$. Now replace m_3 by $-m_2$ and we get $a = \frac{h m_2}{m_2^2 - m_1^2} \sqrt{1 + m_1^2}$ and it follows with the definitions of $m_2 = \cot\alpha$ and $m_1 = \tan\beta$

$$a = \frac{h \cot\alpha}{\cot^2\alpha - \tan^2\beta} \frac{1}{\cos\beta}. \tag{3.5}$$

The eccentricity e of the ellipse is then given by $e = \sqrt{1 - \frac{b^2}{a^2}}$ and this is independent of h for constant α and β, as expected, namely

$$e^2 = 1 - \left[\cos\beta \left(1 - \frac{\tan^2\beta}{\cot^2\alpha}\right)\right]^2. \tag{3.6}$$

3.1.3.2 The Force Response of an Axisymmetric Cone Indenting an Inclined Half-Space

With these geometrical considerations, the force response of the sample can now be determined. Vlassak et al. (2003) showed that the force response for a cone with an elliptical contact area is

$$F(a, b) = \pi p_0 ab (2U - \cot\alpha a E(e)) \tag{3.7}$$

$$p_0 = \frac{\mu}{(1 - \nu) bK(e)} \tag{3.8}$$

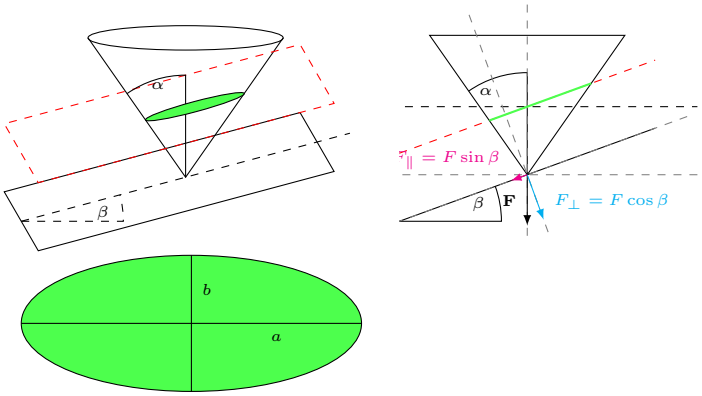


Figure 3.6: Schematic projection of cylinder and inclined half-space.

with the half axis a, b and the half-opening angle α of the ellipse. U refers to the solid body displacement and p_0 to the zero pressure of an elliptical flat cylinder. The mechanical property is given by the rigidity (Lamé modulus) μ which is related to Young's modulus by $E = 2(1+\nu)\mu$, where ν is Poisson's ratio. Since we have an elliptical contact area it is also not surprising that the complete elliptical integrals of first $K(e)$ and second $E(e)$ kind appear in the equations. Minimizing the force in eq. (3.7) with respect to a we obtain $U = \cot(\alpha) a E(e)$ and with eq. (3.8)

$$F(a,b) = \pi \frac{\mu}{(1-\nu)K(e)} a^2 \cot\alpha E(e) \tag{3.9}$$

$$= \pi \frac{\mu}{(1-\nu)K(e)} \frac{\tan\alpha}{E(e)} U^2 \tag{3.10}$$

Now we consider the case of an orthogonal indentation, i.e. $e \stackrel{!}{=} 0$, and eq. (3.10) reduces to

$$F(a,b) = \frac{4}{\pi} \frac{\mu}{(1-\nu)} \tan\alpha U^2 \tag{3.11}$$

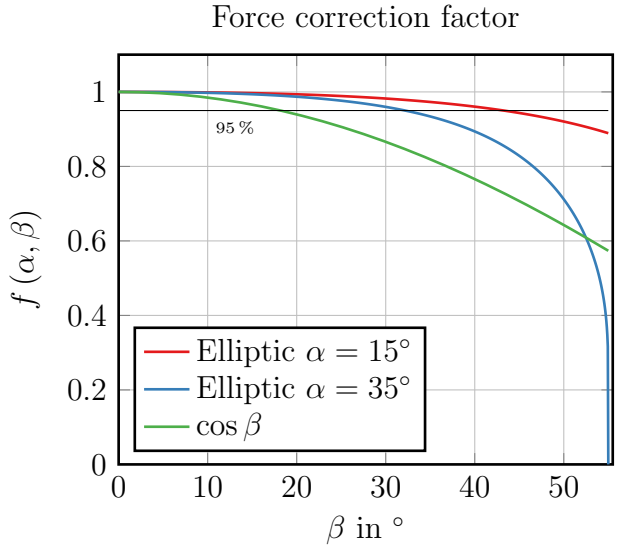


Figure 3.7: Attenuation factor $f(\alpha, \beta)$ for an inclined half-space. The red and the blue line show the behaviour of the attenuation factor in eq. (3.13) for a typical conical indenter with $\alpha = 15°$ and $35°$ for the inclined half-space. The green curve shows the behaviour if only the normal indentation for the inclined half-space is used, i.e. $f(\alpha, \beta) = \cos\beta$.

Notice that $K(e = 0) = E(e = 0) = \pi/2$. Comparing this to the result of Sneddon (1965) we find that the solid body displacement equals the indentation δ, i.e. $U = \delta$.

We can now rewrite eq. (3.10) as

$$F(a, b, e) = F_{\text{Sneddon}} \cdot f(\alpha, \beta) \tag{3.12}$$

$$f(\alpha, \beta) = \frac{\pi^2}{4} \frac{1}{K(e)\, E(e)} \tag{3.13}$$

It should be emphasised, that $e \equiv e(\alpha, \beta)$.

Figure 3.7 shows the behaviour of $f(\alpha, \beta)$ for a conical indenter with typical half-opening angles $\alpha = 15°$ and $35°$ and the behaviour if only the normal direction for the indentation is used, i.e. $f(\alpha, \beta) = 1/\cos\beta$. The graph shows two important relations. First, the contribution of the force parallel to the surface can only be neglected if $\beta \lesssim 5°$ but for larger angles this is not a good approximation. Second, the attenuation has a singularity at $\alpha + \beta = 90°$ because in that case the indentation

is not caused by the tip anymore but by the side slope of the cone. This implies only that eq. (3.12) is not valid for those angles and not that the force reduces to zero. The reason that the force in this case apparently reduces to zero is that the cone has an infinite height and hence an infinitely long side area. However, in such an event the conical indenter probes a huge area of the half-space and a local investigation is not possible. Hence, this case is not interesting for a nano-indentation experiment. Moreover, fig. 3.7 shows that for the indentation of inclined half-spaces a cantilever with a high-aspect ratio, i.e. small α, is preferred, since this reduces the effect of the inclination. This implies that for small enough α it is possible to neglect the effect of the inclination for increasing β.

As a final remark, I want to emphasise that eq. (3.13) considers neither friction nor anisotropy of the material. The latter can be included with the approach of Vlassak et al. (2003) but introduces further complications and requires numerical considerations of the problem and, therefore, this case is not considered in this thesis. However, it is useful to notice that the inclination of the tissue may be neglected if high aspect ratio cantilevers are chosen. This shows that the findings above not only reduce the imaging artefacts for topography imaging but also for force imaging.

3.1.4 Determination of the Contact Point: Force-Indentation Variation (FIV)

For an accurate determination of Young's modulus from indentation experiments, it is not only important to use the correct contact model but also to exactly determine the contact point (Gavara, 2016). The problem with contact point determination is that it is very often based on models, such as the goodness of fit (GOF) model, or on numerical approaches, such as the ratio of variances (ROV) model. On the one hand, GOF is inadequate because in real experiments the force-indentation curves follow rarely the predicted model behaviour exactly which consequently results in an

inaccurate determination of the contact point. On the other hand, ROV is strongly dependent on the interval over which the variance is determined and this interval must be adjusted to sampling density, noise level, and indentation depth. Therefore, this method is very slow and not well suited for automatised data analysis. Here we present an analytical solution to determine the contact point, which has neither of the mentioned restriction.

We start with the general form of an indentation experiment for an arbitrarily shaped indenter (eq. (1.35)). The problem in an indentation experiment is that the coordinate system given by the stage is usually not set up in a way that $F(\delta = 0) = 0$ but rather has an arbitrary offset for the indentation, denoted by δ_0, and the force, f_0. This can be written as

$$F(\delta - \delta_0) = \begin{cases} g(\delta - \delta_0)^\gamma - f_0 & \text{for } \delta > \delta_0 \\ -f_0 & \text{else.} \end{cases} \tag{3.14}$$

For an ideal experiment, i.e. no virtual deflection, no hydrodynamic effects, and no noise, f_0 would be the value of the baseline and δ_0 would be the last value at the baseline. In a real experiment this method is not possible, because of the noise in the data and, therefore, many different methods have already been developed. Here we are going to use the knowledge that eq. (3.14) is a piecewise defined function. To find δ_0 and f_0 we add an arbitrary offset δ' and f' and we obtain

$$F(\tilde{\delta}) = \begin{cases} g(\tilde{\delta} + \delta_0 + \delta')^\gamma - \tilde{f} & \text{for } \tilde{\delta} > \delta_0 + \delta' \\ -\tilde{f} & \text{else.} \end{cases} \tag{3.15}$$

with $\tilde{\delta} = \delta - \delta_0 - \delta'$ and $\tilde{f} = f_0 + f'$. Now we multiply eq. (3.15) by $\tilde{\delta}$ and

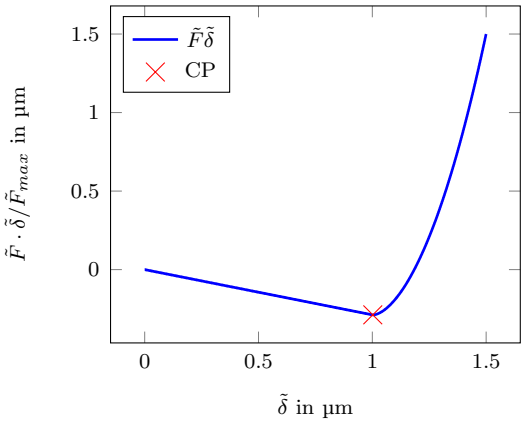


Figure 3.8: Graphical representation of the determination of the contact point using the FIV method, for $f' = (\max(F) - \min(F))/2$ and $\delta' = \delta - \min(\delta)$ for 1.5 µm Hertzian indentation of 150 MPa and $R = 10$ µm.

determine the minimum which gives (fig. 3.8)

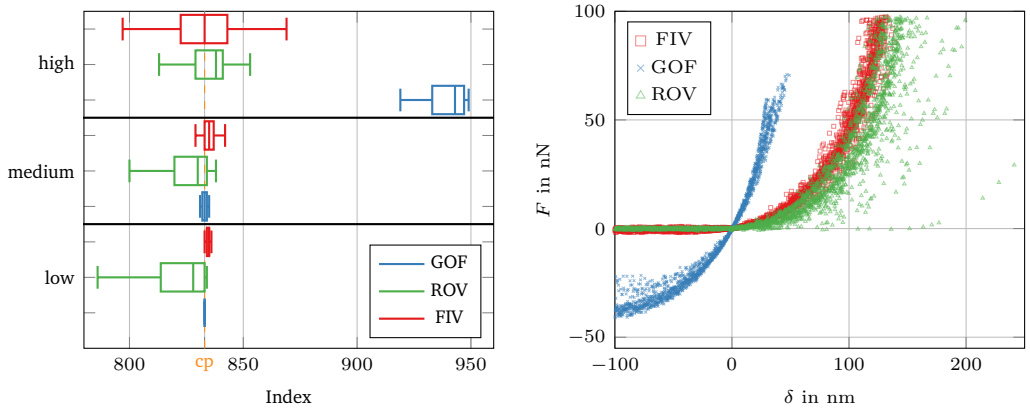
$$\frac{\partial(F(\tilde{\delta})\tilde{\delta}}{\partial\tilde{\delta}} \stackrel{!}{=} \underbrace{-\tilde{f}}_{l.h.s} = \underbrace{g\left(\tilde{\delta}+\delta_0+\delta'\right)^{\gamma} + g\gamma\left(\tilde{\delta}+\delta_0+\delta'\right)^{\gamma-1} - \tilde{f}}_{r.h.s} \tag{3.16}$$

The reason that the left-hand side (l.h.s) is not zero for the minimum is that an arbitrary offset was introduced in eq. (3.15). Furthermore, $F(\tilde{\delta})\tilde{\delta}$ is continuously differentiable and, therefore, the condition l.h.s = right-hand side (r.h.s) must be fulfilled, which implies

$$\tilde{\delta}_{\min} + \delta_0 + \delta' \stackrel{!}{=} 0 \Leftrightarrow \tilde{\delta}_{\min} + \delta' = -\delta_0. \tag{3.17}$$

Since δ' was chosen and $\tilde{\delta}_{\min}$ can be determined from the data this method gives δ_0.

In order for the method to work it is necessary to chose δ' and f' in a way that eq. (3.15) has a minimum. It turns out empirically that $f' = 0.5(\max(F_{\exp}) - \max(F_{\exp}))$ and $\delta' = 0.6(\max(\delta) - \min(\delta))$ are good values to determine the contact



(a) CP accuracy for simulated data. **(b)** methods applied to noisy data.

Figure 3.9: Contact point (CP) data. (a) shows the distribution of the CP for 0.004 %, 0.04 % and 0.4 % (low, medium, high) signal to noise ratio with respect to the maximal applied force for GOF, ROV and FIV. (b) shows the application of the three methods to experimental indentation data with a spherical indenter in pure water.

point accurately. However, if these values are not accurate enough these can be varied. Moreover, it should be emphasised, that this method determines the first point of cantilever deflection. This implies, that any surface effect, such as hydrodynamic effects, will be detected as contact point, if the cantilever is deflected. However, if a theory for such a deflection is known, this effect can be subtracted and the method can be applied again to determine the contact point which causes the sample deformation.

3.1.5 The Effect of Noise on the Determination of the Contact Point

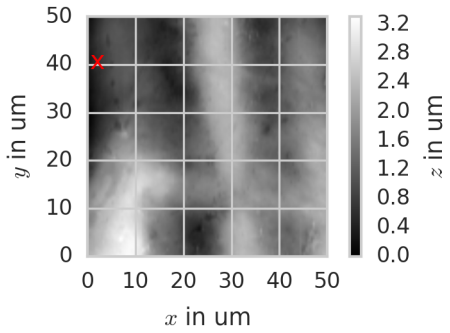
To determine the effect of noise on the accuracy of the method, we simulated a force indentation curve with Hertzian contact geometry. The sample size of the curve was $n = 1000$ and the contact point was at sample $n = 833$. We added to this curve a Gaussian noise with amplitudes of 0.004 %, 0.04 % and 0.4 % (low, medium, high) relative to the maximal applied force. We analysed this data with the GOF, ROV, and force indentation variation (FIV) algortihms for 100 curves.

Figure 3.9a shows that for low and intermediate noise GOF is the most accurate

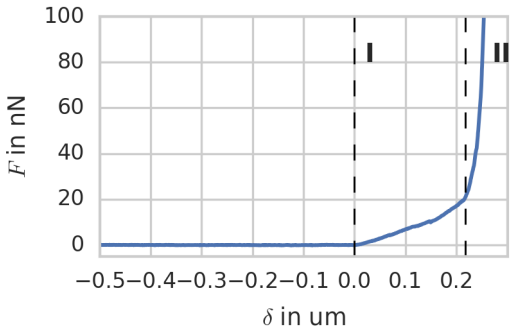
of the three methods but it is rather useless at high noise levels. Moreover, GOF works only reliably if the geometric exponent of the model (eq. (1.35)) matches the experimental one, which is rarely the case. At the high noise levels ROV is the most accurate method, which can be explained by the fact that this method considers the noise level when the contact point is determined. On the other hand, it is the least favourable at lower noise levels, which might be a numerical problem that occurs for divisions by small numbers. For none of the noise levels is FIV the most favourable method. However, it performs well across all noise levels; indeed almost as accurately as the best method for each level. Furthermore, like ROV, this method is not based on an indentation model, and is therefore favourable to GOF.

To investigate strengths and weaknesses of the FIV method we applied it to an experimental data set during which we indented polycaprolactone (PCL)[3] with a spherical indenter of radius 20 µm in pure water. The large spherical indenter was chosen because for larger indenters the samples obey better to the Hertzian contact mechanics. This reduces the disadvantage of GOF, for which a correct contact model is crucial. We did 100 indentations at one point, where each curve had 1000 ± 15 samples. Figure 3.9b shows the 100 curves plotted for the analysis with GOF, ROV, and FIV, where $\delta = 0.0$ represents the contact point. It shows clearly that in this experiment GOF leads to the narrowest distribution of the curves after the contact point. But we can clearly see that the model was wrong since the baseline is below the level $F = 0$. Both the ROV and FIV methods show that the baseline is around $F = 0$, which suggest that they determined the contact point rather accurately. While ROV shows a narrower distribution around the baseline, FIV shows a narrower distribution of the curves after the contact point. Since the indentation of the material was on the same position we would expect that the curves would look rather similar. This, and the fact that at low and intermediate noise levels FIV determines the contact point

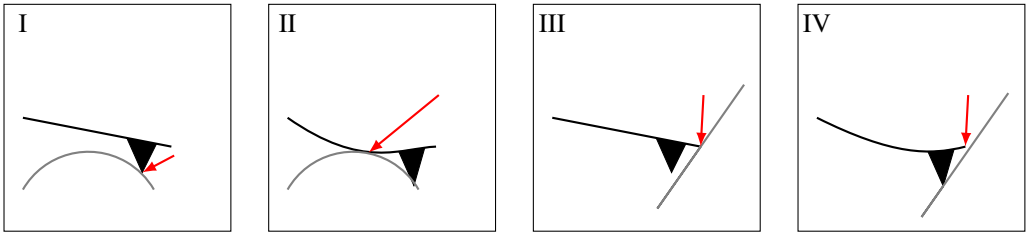
[3]Provided by Andrea Bonilla-Brunner.



(a) ThermoMorph replica



(b) indentation tip artefact.



(c) indentation tip artefact.

Figure 3.10: Indentation artefacts.

better than ROV, suggest, that it performs better than ROV. In fact the noise SNR in the experiment is 0.03 %, which is within the intermediate noise level and hence we obtain the better result for FIV as expected from the simulations.

3.1.6 Cantilever Artefacts

Another kind of artefact that can arise directly from the cantilever during the indentation in a similar way to the artefacts encountered in contact mode. First, it can happen that although the tip is indenting the sample (fig. 3.10c I), during the indentation the probe is too short for the amount of the deformation and, consequently, the cantilever touches the cell (fig. 3.10c II). This creates a significant artefact in a force-distance curve: two different exponents in eq. (1.35) appear with a very sharp transition (fig. 3.10b). The reason for this discontinuity is that effectively the indenter changes from a conical indentation to an indentation with a flat beam. Furthermore,

the point at which the force acts is different, which is indicated by the red arrows in fig. 3.10c I and II. This phenomenon is in principle the same artefact as the one which occurs during contact mode measurements of topography, where the cantilever rather than the tip samples the topography. As we have seen before these artefacts occur only if the changes in the topography are larger than the size of the tip and therefore they can be reduced again by changing the cantilever design towards an enhanced probe length.

Another problem occurs only for cantilever designs where the probe is not directly at the end of the cantilever as indicated in the pictograms in fig. 3.10c. In this case a steep slope of the sample causes the cantilever to hit the sample first. During the indentation the cantilver will bend further and at some point the tip starts indenting the sample. This can again be recognised by the fact that two, clearly distinct, regimes during the indention appear (fig. 3.10b). A similar artefact for cellular indentation was reported previously by Harris and Charras (2011) who observed that even on flat cells the indentation will be affected by the tip, since at a certain indentation depth the tip will start hitting the cell. In a sense of categorization, however, this is more similar to the artefact, which is shown in fig. 3.10cI and II, in the sense that the indentation happens with the tip first and the artefact occurs just at a certain depth. While in this case the first part of the indentation curve, where the tip indents, can still be used for analysis, this is not possible if the cantilever touches the sample first and the indentation with the tip happens after certain amount of bending.

The major problem with both of these artefacts is that they are difficult to distinguish from non-linear material behaviour with depth, for example the different material properties in layered materials (Lee et al., 2009), or the indentation of thin shells, which also does not follow the Hertzian indentation model (eq. (1.35)) (Vella et al., 2011). However, one main difference is that in most cases the actual material behaviour shows smooth transitions and not abrupt ones. Additionally, a good knowl-

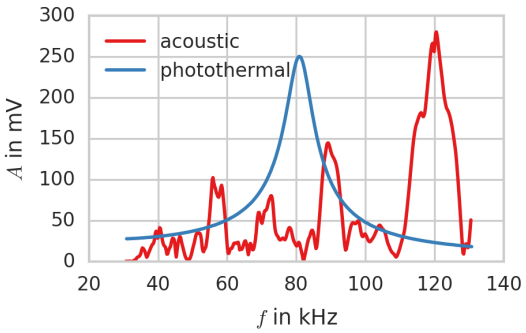
edge of the topography and the cantilever geometry make it possible to calculate if an artefact can arise from such problems or if it is more likely to be caused by pure material behaviour.

3.2 Tapping Mode – Topography And Hydrodynamic Interactions

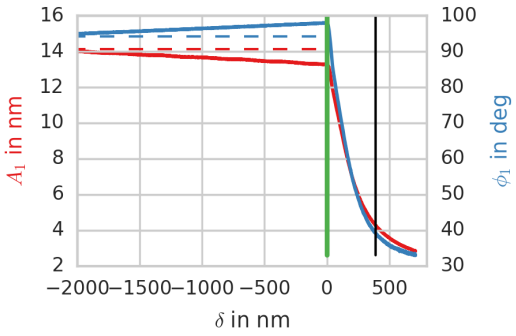
In tapping mode I will discuss two kind of artefacts. Both are only relevant for mechanical imaging and not for basic topography. The first artefact I will discuss is the contribution of liquid and the second is the problems that can arise from cantilever stiffness and attractive forces.

3.2.1 Hydrodynamic effects

In basic tapping mode imaging the hydrodynamics can be used to advantage in imaging with high resolution (Voïtchovsky et al., 2010). In contrast, it can cause problems for quantitative mechanical imaging. The general problem is an additional coupling between cantilever and surface. This connection arises from the cantilever oscillation, which simultaneously excites a water column which reflects from the surface and interacts with the cantilever. In the following I call this interaction hydrodynamic coupling. With acoustic excitation a much larger amount of water is excited than with direct actuation of the cantilever such as photothermal excitation (Ramos et al., 2006). This results from the significantly larger area of the chip compared to the cantilever. This additional excitation makes the hydrodynamic coupling strong and hence very difficult to predict. On the other hand, with photothermal excitation, the water coupling is weak and results in a minor shift of the resonance when the cantilever approaches the surface (cf. fig. 3.11). This coupling can be described by an effective cantilever spring constant $k_c^{\text{eff}} = k_c + k_w(d)$, where $k_w(d)$ accounts for the coupling of



(a) Resonance frequencies for photothermal and acoustic cantilever actuation.



(b) A_1 and ϕ_1 for an oscillating cantilever vs δ.

Figure 3.11: The effect of the hydrodynamic coupling on the oscillating cantilever. (a), data of acoustic and photothermal cantilever actuation shows the difference in the resonance peaks. The hydrodynamic effect is very severe in acoustic actuation mode, which introduces new resonances, whereas the direct photothermal actuation leads only to a small coupling which still preserves the resonance of the cantilever. (b), shows the amplitude A_1 and phase ϕ_1 vs indentation depth. It clearly shows that the coupling is weak and can be approximated by a linear function. The red and blue dashed lines indicate the values of A_1^{far} and ϕ_1^{far}, the calibration values for amplitude and phase, respectively, far from the surface. The green line indicates the contact point and the black vertical line indicates the indentation depth during the scanning experiments.

the water, which depends on the distance d to the surface. With this approach, the resonance frequency $\omega_0 = \sqrt{k_c/m}$ becomes $\omega_{0,w} = \sqrt{(k_w(d) + k_c)/m} \approx \omega_0(1+k_w(d)/k_c)$. From fig. 3.11b it can be seen that the coupling of the water, i.e. the change of A_1 and ϕ_1 for negative δ, is much weaker than the change during the indentation, i.e. $\delta > 0$. This means that the hydrodynamic effect can be corrected and the dynamic interaction can lead to mechanical properties.

Moreover, the linear and small change in A_1 and ϕ_1 indicate that the topography of the sample will have no significant effect on the mechanical measurements.

This hypothesis was tested using a latex replica of the hypocotyl (cf. chapter 2). If the characteristic distribution in the mechanical mapping in fig. 3.12 (a) is caused by the topography, the mechanical profile of the replica (cf. fig. 3.12 (c)) should qualitatively have the same distribution. However, this is not the case and suggests that the hydrodynamic effect is not responsible for the mechanical behaviour of the

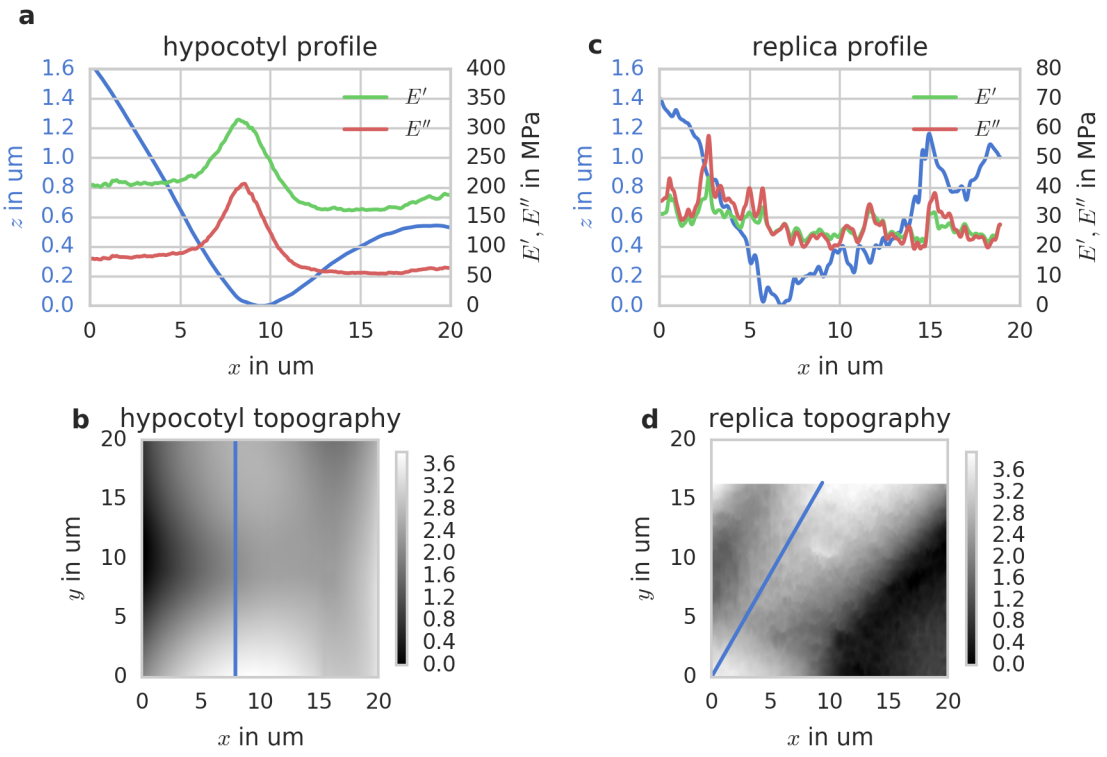


Figure 3.12: Comparison of the mechanical properties of an *A. thaliana* hypocotyl and a latex replica of an *A. thaliana* hypocotyl. (a) shows the line profile of the topography of the seedling, which is indicated by the blue line in (b), and the corresponding mechanical properties. (c) shows the line profile of the topography of the replica, which is indicated by the blue line (d), and the corresponding mechanical properties.

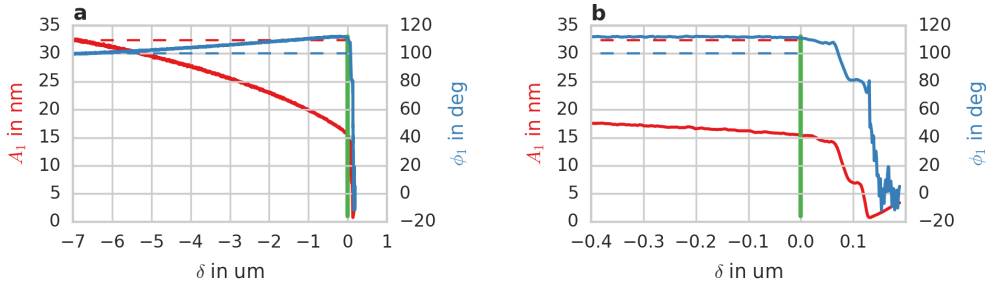


Figure 3.13: The hydrodynamic coupling for a short lever. (a) shows amplitude and phase plotted vs distance. (b) shows a zoom into the contact region of (a). The green line indicates the contact point and the red and blue dashed lines indicate the free amplitude and phase, respectively.

plant samples at the cell junctions but it is caused by differences in the mechanical properties or wall internal stresses.

Above we already discussed that the hydrodynamic coupling is a function of the distance between the lever and the surface. This causes problems during measurements with shorter probes because during these measurements, the cantilever is closer to the surface than if the tip is longer. As already discussed in section 3.1 this can cause the cantilever to have physical contact with the sample, which obviously causes artefacts of this type as well. But even if the cantilever is not in physical contact with the sample, it will be very close to it, which increases the hydrodynamic coupling significantly.

Figure 3.13a shows an example of the behaviour of A_1 and ϕ_1 with distance for a short and soft cantilever. It shows clearly that especially the amplitude changes very significantly and the change cannot be approximated by a linear function. The reason for this is the relative strength of the hydrodynamic coupling which is larger than for a stiff lever but also the shorter tip which causes the absolute strength of the coupling to increase. The extent of this effect can be seen in fig. 3.13b in the contact regime (to the right of the green line where $\delta > 0$), where the phase becomes negative and very noisy and the amplitude increases after a certain indentation, which is caused by the water coupling. This effect would be reduced in a softer sample since a stiff

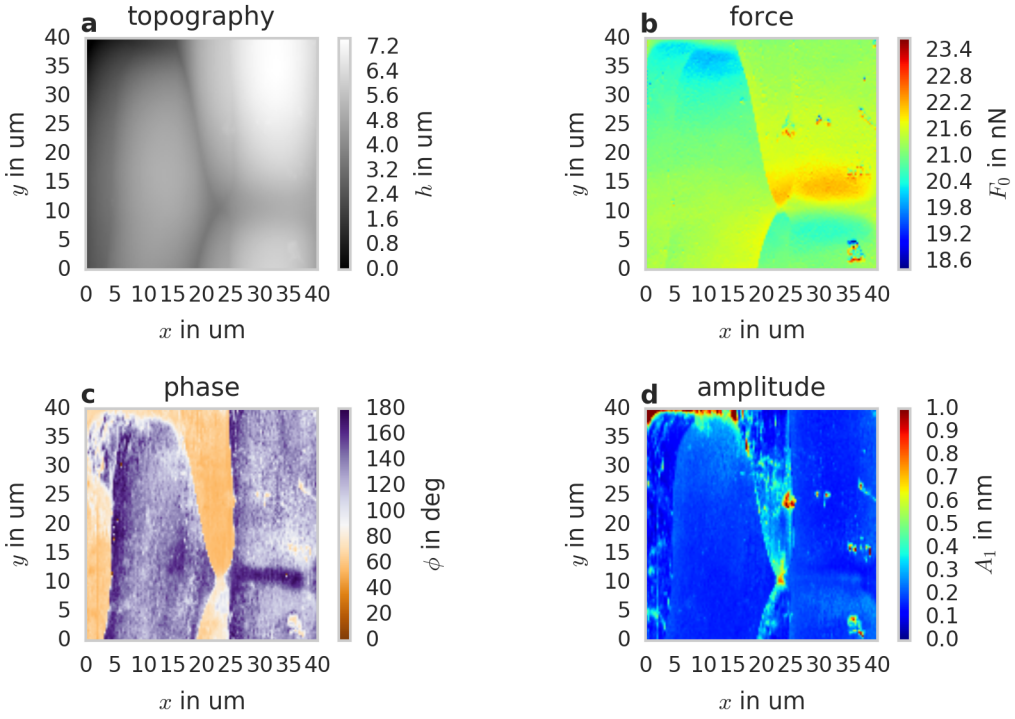


Figure 3.14: Topographic artefacts for a short lever during a dynamic AFM scan. (a) shows the topography, (b) the force, (c) the phase, and (d) the amplitude of the dynamic AFM scan.

surface reflects the water better than a soft one. Furthermore, the hydrodynamic coupling can cause the phase to be larger than 90° (fig. 3.13), which suggests that the experiment is conducted in the attractive regime, which would not probe the mechanical properties of the sample but rather the surface potential.

These effects cause problems during a dynamic AFM scan. Figure 3.14 shows the relevant quantities (F_0, A_1, ϕ_1) to calculate the mechanical properties from a dynamic AFM scan. The topography image in fig. 3.14a shows the artefact described in fig. 3.10c III at $x = 5\,\mu m$ and $25\,\mu m$, where the end of the lever hits the sample because of the steep slope of the cell. While the force image (fig. 3.14b) shows no significant artefacts, the phase image (fig. 3.14c) shows that at the majority of the scan the values are above 90°. In fact, only the positions where the cantilever end rather than the probe hits the sample, the values are below 90° (orange regions

in fig. 3.14c). The amplitude image (fig. 3.14d) shows the same artefacts as the phase image. Moreover, the contact amplitude is very small, which suggests that the cantilever is too soft to transmit a significant amount of energy into the CW. The motion, which results in the amplitude, is in this case most likely caused by the hydrodynamic coupling rather than by the response of the cell wall. Although a correction for the hydrodynamic effect is technically possible (Cartagena and Raman, 2014), in the case of the stiff plant CW most of the energy dissipation will be caused by the motion in the liquid and therefore the result of the viscoelastic properties will not be reliable. As we have seen above this problem can be avoided by the choice of a stiffer cantilever with a longer probe.

3.2.2 Reproducibly of AFM Measurements

One very important question is the reproducibility of the AFM measurements under hydrodynamic conditions. To asses that we measured the same position twice including calibration curves. The important quantities for the mechanical measurements are A_1, ϕ_1, F_0 for which we find ratios of the two subsequent measurements of 1.02 ± 0.05, 1.0 ± 0.2 and 1.0 ± 0.3, respectively, for four positions. Calculating the mechanical properties as shown in the next chapter, we obtain the ratios 0.98 ± 0.05 and 0.98 ± 0.06 for E' and E'', respectively. This shows that the mechanical measurements are fairly reproducible. In fact the differences between the measurements are not only caused by noise during the measurements but also due to drifts of the sample, i.e. the 'same' position is slightly shifted. Moreover, the scanning in contact mode can remove a tiny layer of the cuticle (fig. 3.5) and therefore, this slightly alters the mechanical properties.

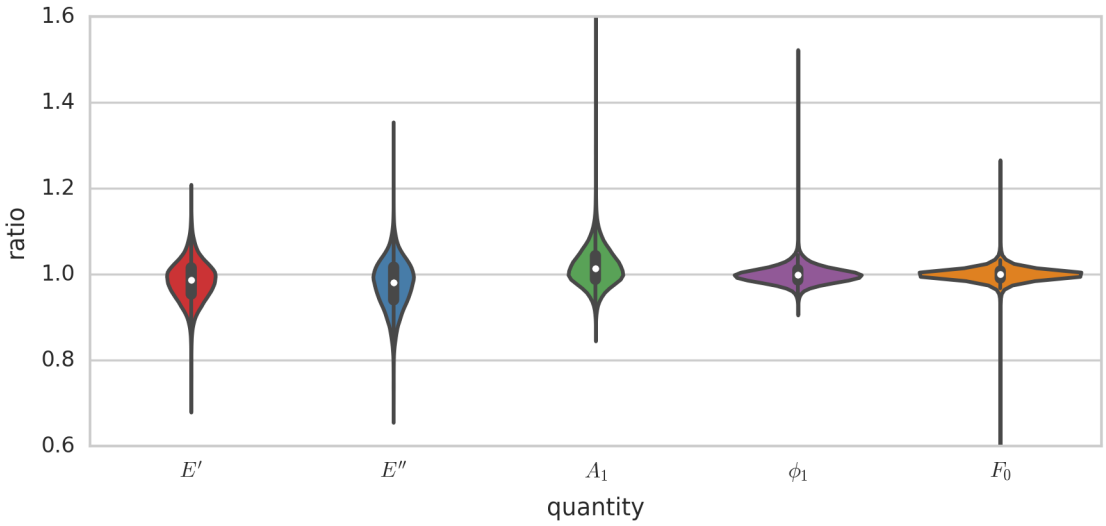


Figure 3.15: Reproducibility of a dynamic AFM scan.

3.3 Summary

In this chapter we investigated the origin of imaging artefacts on cells in tissues. We have seen that in several circumstances cantilevers with short probes are more likely to introduce imaging artefacts. In contrast, longer probes reduce the restrictions given by the topographical variation. Furthermore, the force that is introduced by the hydrodynamic coupling is weaker in the case of long probes. In addition, we have seen that for mechanical measurements on sloped surfaces, high aspect ratio probes are more desirable, because they reduce the effect of the inclination on the force. Ultimately, high aspect ratio probes give a higher resolution but their sharpness might introduce cell damage by destroying the cell or only removing CW material. Nevertheless, high aspect ratio probes are favourable for dynamic mechanical measurements, because they not only reduce imaging artefacts but also reduce hydrodynamic coupling.

Chapter 4

Quantitative Mechanical Properties Mapping With AFM

The mechanical imaging technique which was used in this thesis relies on the method described by Cartagena-Rivera et al. (2015). The Cartagena method is a kind of contact resonance imaging were the atomic force microscopy (AFM) feedback is on the deflection and at the same time the cantilever is driven at one or two oscillatory eigenmodes. However, this method is only applicaple in the case where the material can be described by the Kelvin-Voigt (KV) model, which is not accurate for the description of complex composite materials as the theory of the stress-relaxation and the creep experiments show (section 1.2). The most general linear viscoelastic material can be described by the generalised Maxwell (MW) model which accounts for the behaviour of materials whose relaxation occurs on several timescales (fig. 1.6d). This chapter will provide new theory that I have developed, which links the cantilever observables A_0, ϕ_1, and A_1, for a sinusoidal actuation to the generalised MW model. This can be reduced to the KV, MW, and standard-linear solid (SLS), which I will discuss in detail in this chapter. Finally, an approach to obtain the quantities k_i (stiffness), τ_i (relaxation time), η_i (viscosity) from the general MW model is developed

and presented.

To obtain a relation between the cantilever observables and the mechanical properties three steps will be followed. (i) the cantilever motion is described by a driven harmonic oscillator with damping to which an external force is applied. (ii) the external force will be determined by the material parameters, which implies that the force, exerted by an oscillating generalised MW material, will be determined. (iii) the cantilever motion will be linked to an appropriate indentation model.

4.1 A Model for Dynamic AFM Mapping of Linear Viscoelastic Materials

The Cartagena method uses the approximation of a driven harmonic oscillator moving in an external force field $F_{\text{ext}}(t)$ the following equation is obtained

$$\frac{1}{\omega_0^2}\ddot{q} + \frac{1}{\omega_0 Q}\dot{q} + q = \frac{F_{\text{osc}}\sin(\omega t)}{k_c} + \frac{F_{\text{ext}}(t)}{k_c}. \tag{4.1}$$

The cantilever motion is characterised by its trajectory $q(t)$, resonance frequency ω_0, spring constant k_c and quality factor Q. The driving force oscillates with a force F_{osc} and a frequency ω. To solve this problem for a generalised MW material $F_{\text{ext}}(t)$ must be the resulting force on such a material. In the following derivation the external force will be denoted by F instead of F_{ext}.

The steady state solution for $q(t)$ in eq. (4.1) is given by the following expression

$$q(t) = A_0 + A_1\sin(\omega t - \phi_1). \tag{4.2}$$

Every arm in the generalised MW material is characterised by its spring constant

k_i and its timescale $\tau_i = \eta_i/k_i$, with the viscosity η_i. Furthermore, in the generalised MW model the total strain δ must be the same as the strain $\delta_i, i = 1 \dots N$ in every arm, i.e. $\delta_i = \delta_j \equiv \delta, \forall i, j$. The total force F is given by the sum of the forces f_i in every arm and a relaxation, steady state, force f_∞ by

$$F = f_\infty + \sum_{i=1}^{N} f_i. \tag{4.3}$$

The force f_i for the MW model is given by the partial differential equation (PDE) (eq. (1.2))

$$k_i \frac{\partial \delta_i}{\partial t} = k_i \left(\frac{\partial \delta_{\text{dashpot}}}{\partial t} + \frac{\partial \delta_{\text{spring}}}{\partial t} \right) = \frac{1}{\tau_i} f_i + \frac{\partial f_i}{\partial t}. \tag{4.4}$$

In the real space the PDEs cannot be simply summed but such an expression can be found in the Laplace domain, in which eq. (4.4) has the form

$$\hat{f}_i(s) = \frac{s k_i}{s + \frac{1}{\tau_i}} \hat{\delta}_i(s). \tag{4.5}$$

The Laplace transform of a function $g(t)$ is denoted by $\hat{g}(s) = \mathcal{L}(g(t))(s)$, where s is the free parameter in the Laplace domain. Because of the linearity of the Laplace transform, the total F can be written in the Laplace domain as

$$\hat{F}(s) = \hat{f}_\infty + \sum_{i=1}^{N} \hat{f}_i(s) = \left(\frac{\hat{f}_\infty}{s} + \sum_{i=1}^{N} \frac{s k_i}{s + \frac{1}{\tau_i}} \right) \hat{\delta}(s). \tag{4.6}$$

The last equality is true because $\delta_i = \delta, \forall i = 1 \dots N$. With the approximation of

the cantilever motion as a driven harmonic oscillator, the material stimulation can be expected to be sinusoidal. This is the case in the steady state oscillation of the driven harmonic oscillator (eq. (4.2)). From this assumptions the deformation $\delta(t)$ is of the form

$$\delta(t) = \delta_0 + A_1 \sin(\omega t - \phi_1). \tag{4.7}$$

In fact, in an AFM experiment the relation between the cantilever motion $\delta(t)$ and $q(t)$ is given by

$$\delta(t) = -\left(Z + q(t)\right) \tag{4.8a}$$

$$\delta_0 = -\left(Z + A_0\right) \tag{4.8b}$$

with the position of the z-piezo Z, the deflection of the cantilever A_0.

The Laplace transform of eq. (4.7) is

$$\hat{\delta}(s) = \frac{\delta_0}{s} + \frac{\omega}{s^2 + \omega^2} A_1 \cos(\phi_1) - \frac{s}{s^2 + \omega^2} A_1 \sin(\phi_1). \tag{4.9}$$

Substituting eq. (4.9) into eq. (4.5) and applying the inverse Laplace transform we obtain

$$
\begin{aligned}
f_i(t) = &\left(k_i\delta_0 - A_1 k_i \frac{1}{1+\omega^2\tau_i^2}\left(\omega\tau_i\cos(\phi_1) + \sin(\phi_1)\right)\right) e^{-\frac{t}{\tau_i}} \\
&+ A_1 k_i \frac{\omega^2\tau_i^2}{1+\omega^2\tau_i^2}\sin(\omega t - \phi_1) \\
&+ A_1 k_i \frac{\omega\tau_i}{1+\omega^2\tau_i^2}\cos(\omega t - \phi_1).
\end{aligned} \tag{4.10}
$$

From eq. (4.10) an initial modulus $\epsilon_{0,i}$, the storage modulus ϵ_i', and the loss modulus ϵ_i'' can be found as in the literature for the MW model (Doi, 2013)

$$
\epsilon_{i,0} = k_i - \frac{1}{\delta_0\omega\tau_i}\left(\epsilon_i'\cos(\phi_1) + \epsilon_i''\sin(\phi_1)\right) \tag{4.11a}
$$

$$
\epsilon_i' = A_1 k_i \frac{\omega^2\tau_i^2}{1+\omega^2\tau_i^2} \tag{4.11b}
$$

$$
\epsilon_i'' = A_1 k_i \frac{\omega\tau_i}{1+\omega^2\tau_i^2}. \tag{4.11c}
$$

With eq. (4.11) we can rewrite eq. (4.10) as

$$
\begin{aligned}
f_i(t) &= \epsilon_{0,i}\delta_0 e^{-\frac{t}{\tau_i}} + \epsilon_i' A_1\sin(\omega t - \phi_1) + \epsilon_i'' A_1\cos(\omega t - \phi_1) \\
&\overset{\text{eq. (4.7)}}{=} \epsilon_{0,i}\delta_0 e^{-\frac{t}{\tau_i}} + \epsilon_i'(\delta(t) - \delta_0) + \frac{\epsilon_i''}{\omega}\dot{\delta}(t).
\end{aligned} \tag{4.12}
$$

Using eqs. (4.6) and (4.10) and the linearity of the Laplace transform the total

force for the generalised MW model with a relaxation spring constant k_∞ is

$$F(t) = k_\infty \delta_0 + k_\infty(\delta(t) - \delta_0) + \sum_{i=1}^{N} \left(\epsilon_{0,i}\delta_0 e^{-\frac{t}{\tau_i}} + \epsilon_i'(\delta(t) - \delta_0) + \frac{\epsilon_i''}{\omega}\dot{\delta}(t) \right) \tag{4.13a}$$

$$= \left(k_\infty + \sum_{i=1}^{N} \epsilon_{0,i} e^{-\frac{t}{\tau_i}} \right) \delta_0 + \left(k_\infty + \sum_{i=1}^{N} \epsilon_i' \right) (\delta(t) - \delta_0) + \left(\sum_{i=1}^{N} \epsilon_i'' \right) \frac{\dot{\delta}(t)}{\omega} \tag{4.13b}$$

$$= E_0(t)\delta_0 + E'(\delta(t) - \delta_0) + E''\frac{\dot{\delta}(t)}{\omega}. \tag{4.13c}$$

In eq. (4.13c) the total relaxation modulus E_0, storage modulus E' and loss modulus E'' are given by the following equations:

$$E_0(t) = k_\infty + \sum_{i=1}^{N} \epsilon_{0,i} e^{-\frac{t}{\tau_i}} \tag{4.14a}$$

$$E' = k_\infty + \sum_{i=1}^{N} \epsilon_i' \tag{4.14b}$$

$$E'' = \sum_{i=1}^{N} \epsilon_i''. \tag{4.14c}$$

Equation (4.14) is well known and implemented in most finite element modelling (FEM) softwares, such as ABAQUS. With the solution in eq. (4.13) as external force in eq. (4.1) we obtain

$$\frac{1}{\omega_0^2}\ddot{q} + \frac{1}{\omega_0 Q}\dot{q} + q = \frac{F_{\text{osc}}\sin(\omega t)}{k_c} + \frac{E_0(t)\delta_0 + E'(\delta(t) - \delta_0) + E''\frac{\dot{\delta}(t)}{\omega}}{k_c}. \tag{4.15}$$

The interaction will only happen when the cantilever is close to the surface, and therefore the quantities in eq. (4.1) must be near the surface, which will be denoted by the subscript 'near'. Substituting the steady state solution from eq. (4.2) into eq. (4.15), using the relations in eq. (4.8) and adding in the driving force to the frequency the phase $\phi_1 - \phi_1$, i.e. $F_{\text{drive}} = F_{\text{osc}} \sin(\omega t + \phi_1 - \phi_1)$, we obtain

$$-\frac{\omega^2}{\omega_{\text{near}}^2} A_1 \sin(\omega t - \phi_1) + \frac{\omega}{Q_{\text{near}}\omega_{\text{near}}} A_1 \cos(\omega t - \phi_1) + A_1 \sin(\omega t - \phi_1) + A_0 \quad (4.16a)$$

$$= \frac{F_{\text{osc}}}{k_c} \left(\sin(\omega t - \phi_1)\cos(\phi_1) + \cos(\omega t - \phi_1)\sin(\phi_1)\right)$$

$$+\frac{1}{k_c} \left(E_0(t)\delta_0 - E' A_1 \sin(\omega t - \phi_1) - E'' A_1 \cos(\omega t - \phi_1)\right). \quad (4.16b)$$

Comparing now terms with $\sin(\omega t - \phi_1)$ and $\cos(\omega t - \phi_1)$ we get the relations between the observables k_c, A_1, ϕ_1 and the material properties

$$k_c A_0 = E_0(t)\delta_0 \quad (4.17)$$

$$E' = F_{\text{osc}} \frac{\cos(\phi_1)}{A_1} - k_c \left(1 - \frac{\omega^2}{\omega_0^2}\right) \quad (4.18)$$

$$E'' = F_{\text{osc}} \frac{\sin(\phi_1)}{A_1} - k_c \frac{\omega}{Q\omega_0}. \quad (4.19)$$

From Cartagena-Rivera et al. (2015) we obtain the relations

$$F_{\text{osc}} = \frac{k_c A_{\text{far}}}{Q_{\text{far}}} \sqrt{1 - \frac{1}{4Q^2}} \quad (4.20)$$

$$1 - \left(\frac{\omega}{\omega_{\text{near}}}\right)^2 = \frac{F_{\text{osc}}}{k_c} \frac{\cos(\phi_{1,\text{near}})}{A_{1,\text{near}}} \quad (4.21)$$

$$\frac{\omega}{\omega_{\text{near}} Q_{\text{near}}} = \frac{F_{\text{osc}}}{k_c} \frac{\sin(\phi_{1,\text{near}})}{A_{1,\text{near}}}, \quad (4.22)$$

which we can substitute into eq. (4.16) and the final result is

$$F_0 = k_c A_0 = E_0(t)\delta_0 \tag{4.23a}$$

$$E' = F_{\text{osc}} \left(\frac{\cos(\phi_1)}{A_1} - \frac{\cos(\phi_{1,\text{near}})}{A_{1,\text{near}}} \right) \tag{4.23b}$$

$$E'' = F_{\text{osc}} \left(\frac{\sin(\phi_1)}{A_1} - \frac{\sin(\phi_{1,\text{near}})}{A_{1,\text{near}}} \right). \tag{4.23c}$$

In our experiments, we measured the quantities $A_{1,near}$ and $\phi_{1,near}$ near the surface, at about $\sim 10\,\text{nm}$ above the sample surface. This is needed to correct for hydrodynamic effects of the liquid (Cartagena and Raman, 2014, see chapter 3 for details). F_0 is the force which is applied through the cantilever indentation and is measured by the cantilever spring constant and deflection $k_c A_0$. Equations (4.23b) and (4.23c) show the same relations between the cantilever observables and mechanical quantities as obtained by Cartagena-Rivera et al. (2015) but the quantities $E_0(t)$, E', and E'' are different for the different models. The reason that the relations between the mechanical properties and the cantilever observables do not change, is that E' quantifies the stored energy in the system and is related to the displacement, while E'' is a measurement of the dissipated energy and is proportional to the velocity. Therefore, the left-hand side (l.h.s) in eq. (4.23) will depend on the viscoelastic model applied to describe the material, whereas the right-hand side (r.h.s) is universal for all viscoelastic models.

For the SLS model $N = 1$ and the three moduli are given as

$$E' = k_\infty + k_1 \frac{\omega^2 \tau_1^2}{1 + \omega^2 \tau_1^2} \tag{4.24}$$

$$E'' = k_1 \frac{\omega \tau_1}{1 + \omega^2 \tau_1^2} \tag{4.25}$$

$$E_0(t) = k_\infty + \left(k_1 - \frac{A_1}{\delta_0 \omega \tau_1} \left((E' - k_\infty) \cos(\phi_1) + E'' \sin(\phi_1) \right) \right) e^{-\frac{t}{\tau_1}}. \tag{4.26}$$

This is in agreement with the result from the literature as it was introduced in chapter 1 (eq. (1.9)).

The final contribution of the individual terms in eq. (4.26) depends, eventually, on the scan speed v (although v is not directly involved in eq. (4.26), it determines the time t the cantilever spends at a pixel), the initial indentation δ_0, and the oscillation amplitude A_1. Usually the term with $A_1/\delta_0\omega\tau_1$ is negligible, because the assumption for the derivation was $A_1 \ll \delta_0$ and for a polymer we expect that $\omega\tau_1 \sim \mathcal{O}(1)$. Furthermore, v is usually that small that the time spend at a pixel $t_p \gg \tau_1$ and therefore the material is in the relaxed state and we obtain

$$E_0(t) \approx k_\infty. \tag{4.27}$$

4.2 Choosing the indentation model

To link the viscoelastic values from the one dimensional standard linear solid model, which was used in the derivation above, to three dimensional moduli an appropriate indentation model has to be chosen. This can be very complex since the plant cell wall is an intricate composite material. However, we can assume that at small scales, such as the size of the volumes at which the indentation takes place, the sample behaves isotropically. Additionally, the wall is much thicker than the oscillatory indentation

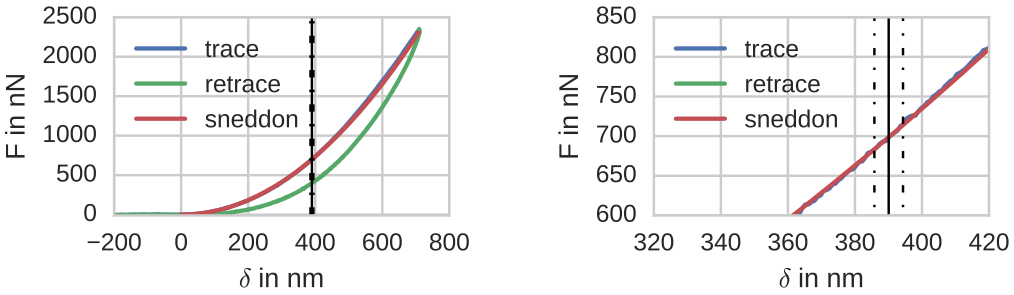


Figure 4.1: The indentation curve justifies the choice of the Sneddon model as the fit shows. The image on the r.h.s. shows a zoom from the l.h.s. image. The solid black line shows the indentation depth and the dashed line show the oscillation amplitude.

depth, which is about $\sim 5\,\mathrm{nm}$, that we can assume that the major contribution comes from indenting the material rather than bending it. With the assumptions of local isotropy and having an infinitely thick material all the models from indentation theory can be used. For linear elasticity that implies

$$F = g\frac{E}{1-\nu^2}\delta^\gamma, \tag{4.28}$$

where ν is the Poisson ratio of the sample and E the corresponding Young's modulus, and g and γ are geometrical coefficients specific to the indenter geometry (eq. (1.35)).

For the Sneddon model as used in the fit, which is shown in fig. 4.1 $g = 2\tan(\alpha)/\pi$ with $\alpha \approx 15°$ being the half opening angle, which is given by the manufacturer of the cantilever (cf. fig. 4.2) and $\gamma = 2$ (Sneddon, 1965).

From this model the three dimensional (3D) moduli can be determined by following the approach of Raman et al. (2011) and Cartagena-Rivera et al. (2015). With a Taylor series expansion of the indentation model in eq. (4.28) we obtain

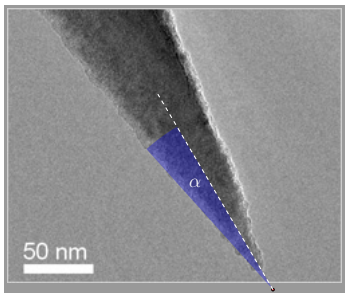


Figure 4.2: Half opening angle α of a Nanosensors PPP-NCAuLD tip. The angle has to be measured for a virtual tip, which is outside the real probe since the real tip size is finite. However, the fit in fig. 4.1 demonstrates that the experiment behaves according to this simplified model, justifying the choice of the model.

$$F(\delta) = F(\delta_0) + \frac{\partial F}{\partial \delta}(\delta - \delta_0) + \frac{\partial F}{\partial(\omega\delta)}\dot{\delta} \tag{4.29}$$

$$= g\frac{E_0(t)}{1-\nu^2}\delta_0^{\gamma} + \gamma g\frac{E'_{3D}}{1-\nu^2}\delta_0^{\gamma-1}(\delta - \delta_0) + \gamma g\frac{E''_{3D}}{1-\nu^2}\delta_0^{\gamma-1}\frac{\dot{\delta}}{\omega}. \tag{4.30}$$

The introduction of E'_{3D} and E''_{3D} is reasoned by the knowledge we deduced from the one dimensional (1D) derivation that E' is related to the displacement $(\delta(t) - \delta_0)$ and E'' is related to the velocity $\dot{\delta}(t)$ (eq. (4.13)).

Comparing eq. (4.30) with eq. (4.13) we find

$$F(\delta_0) = F_0 = g\frac{E_0(t)}{1-\nu^2}\delta_0^{\gamma} \tag{4.31a}$$

$$E'_{1D} = \gamma g\frac{E'_{3D}}{1-\nu^2}\delta_0^{\gamma-1} \tag{4.31b}$$

$$E''_{1D} = \gamma g\frac{E''_{3D}}{1-\nu^2}\delta_0^{\gamma-1}. \tag{4.31c}$$

From here the three 3D moduli can be obtained by

$$\delta_0 = \sqrt[\gamma]{\frac{F_0}{E_0}\frac{1-\nu^2}{g}} \tag{4.32a}$$

$$E'_{3D} = \frac{E'_{1D}}{\gamma}\sqrt[\gamma]{\frac{1-\nu^2}{g}}\sqrt[\gamma]{\frac{E_0}{F_0}}^{\gamma-1} \tag{4.32b}$$

$$E''_{3D} = \frac{E''_{1D}}{\gamma}\sqrt[\gamma]{\frac{1-\nu^2}{g}}\sqrt[\gamma]{\frac{E_0}{F_0}}^{\gamma-1}. \tag{4.32c}$$

E_0 can be determined from the quasi-static indentation as shown in fig. 4.1 and with the assumption of eq. (4.27) E_0 is the relaxation modulus, which we assume to be constant for the whole sample. We then obtain F_0, E'_{1D}, E''_{1D} from the AFM scan. Furthermore we assume the cell wall (CW) is an incompressible material and therefore $\nu = 0.5$. Moreover, fig. 4.1 shows that our indentation follows the Sneddon model (left panel), i.e. $\gamma = 2, g = \frac{2}{\pi}\tan(\alpha)$, and that the experiment was done in the limit of small oscillations where the linear approximation fits very well (right panel). With this experimental evidence we obtain from eq. (4.32)

$$E'_{3D} = \frac{E'_{1D}}{2}\sqrt{\frac{1-\nu^2}{\tan(\alpha)}\frac{\pi}{2}\frac{E_0}{F_0}} \tag{4.33a}$$

$$E''_{3D} = \frac{E''_{1D}}{2}\sqrt{\frac{1-\nu^2}{\tan(\alpha)}\frac{\pi}{2}\frac{E_0}{F_0}}. \tag{4.33b}$$

It is important to highlight, that Cartagena-Rivera et al. (2015) chose E'_{3D} instead of E_0 because they use the KV model. This approach overestimates the material stiffness because it neglects the relaxation which happens throughout the scan in contact mode. Comparing the mathematical expressions from eq. (4.33) with the result of

Cartagena-Rivera et al. (2015) $E'_{3D} = \pi(1-\nu^2)E'^2_{1D}/(8\tan(\alpha)F_0)$, demonstrates that in the overestimation of the KV is given by a factor

$$\frac{E'^{\mathrm{GMW}}_{3D}}{E'^{\mathrm{KV}_{3D}}} = \sqrt{\frac{1-\nu^2}{\tan(\alpha)}\frac{\pi}{2}}\frac{E'_{1D}}{\sqrt{F_0 E_0}} \approx 1.3\frac{E'_{1D}}{\sqrt{F_0 E_0}}.$$

The same relation can be found for the loss modulus. With a relaxation modulus of $E_0 \approx 30\,\mathrm{MPa}$ and an applied force of $F_0 \approx 750\,\mathrm{nN}$ and $E'_{1D} \approx 40\,\mathrm{N\,m^{-1}}$ the KV model provides values which are about a factor 4.25 larger than the generalised MW model.

To summarise, in order to obtain dynamic viscoelastic maps the following conditions and experimental order must be fulfilled:

- $A_0 \gg A_1 > A_2$ to ensure linearisation of the problem, i.e. contact area does not change significantly during oscillation (see also fig. 4.1)
- The experiment must take place in the repulsive regime, i.e. $\phi_1 < 90°$ and $\phi_2 < 90°$
- Force-volume curves must be obtained after every scan and record the parameters A_0, A_1, ϕ_1, and if measured in the experiment also higher eigenmodes. The calibration quantities near the surface should be measured at about 10 nm above the surface and the quantities far from the surface should be measured at least 2 µm above the surface. This curve is also important to determine the contact model, i.e. exponent γ in eq. (4.28).
- With the scan and the calibration quantities E'_{1D} and E''_{1D} can be calculated.
- With the contact model and the fitted Young's modulus E_0 from this model and the one dimensional quantities E'_{3D} and E''_{3D} can be determined

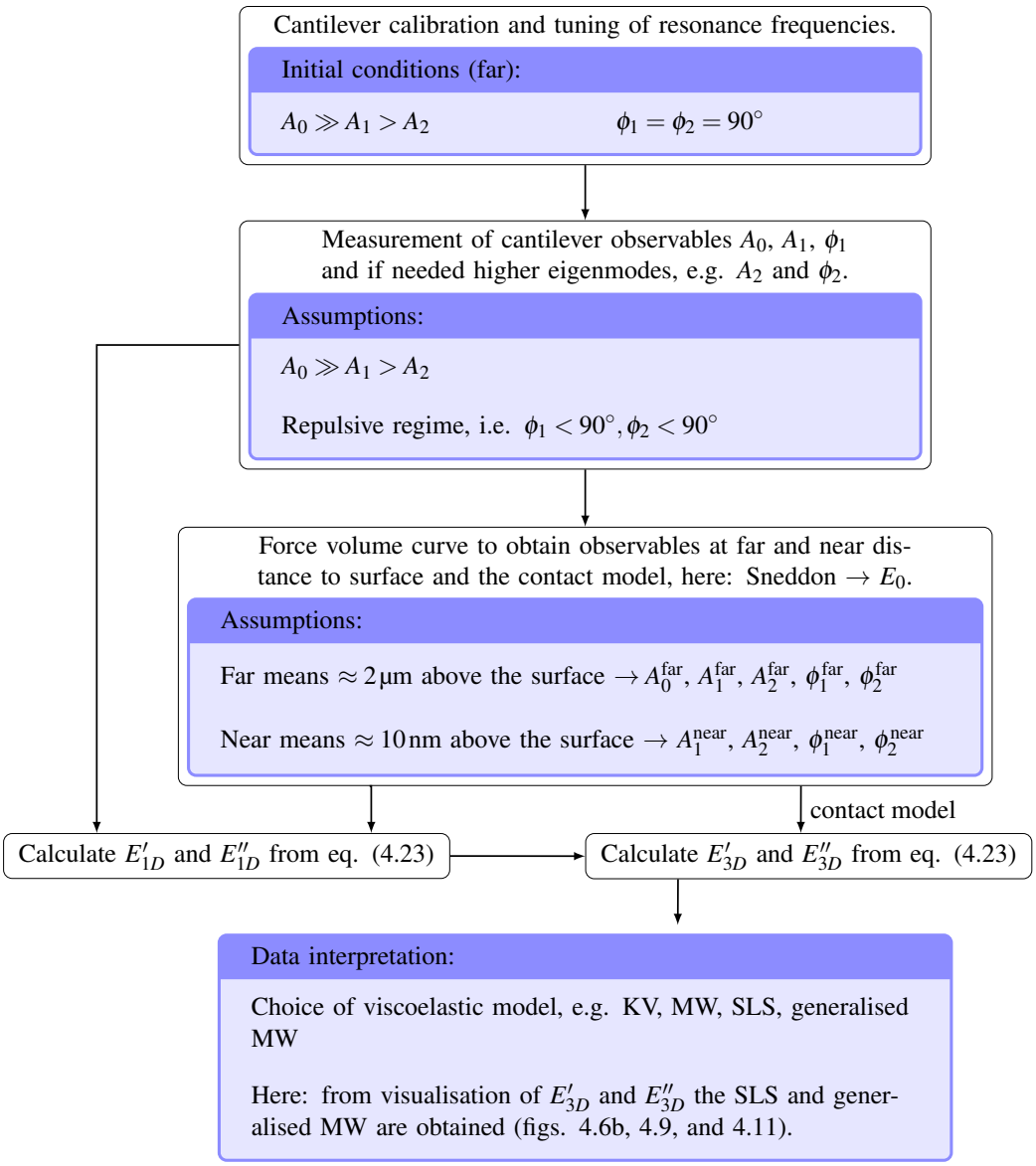


Figure 4.3: Assumptions and order of dynamic AFM experiment and data analysis.

.

The choice of the viscoelastic model, e.g. MW, KV, SLS, is important for the data interpretation but not for the experiment.

Figure 4.3 summarises these assumptions and experimental settings as flowchart.

4.3 The Maxwell Approximation

One problem with the approach as it is chosen above is that the SLS model has three parameters of interest (k_{M}, τ, k_{∞}), but the AFM experiment gives only two observables of the mechanical properties (E', E''). Furthermore, it can be shown (see section 5.1) that the plant CW extensibility is related to the viscosity ($\eta = k_{\mathrm{M}}\tau$). For these reasons it is useful to have an approximation of the SLS model as an MW one.

From eqs. (4.24) and (4.25) we obtain

$$\frac{E'}{E''} = \frac{\kappa}{\omega\tau} + (1+\kappa)\omega\tau \equiv \Theta(\kappa, \omega\tau). \tag{4.34}$$

We call $\Theta(\kappa, \omega\tau)$ the time response function and we introduced $\kappa = k_{\infty}/k_{\mathrm{M}}$. For the MW model we obtain the relations for k_{M} and η

$$k_{\mathrm{M}} = \frac{E'^2 + E''^2}{E'} \tag{4.35a}$$

$$\eta = \frac{1}{\omega}\frac{E'^2 + E''^2}{E''}. \tag{4.35b}$$

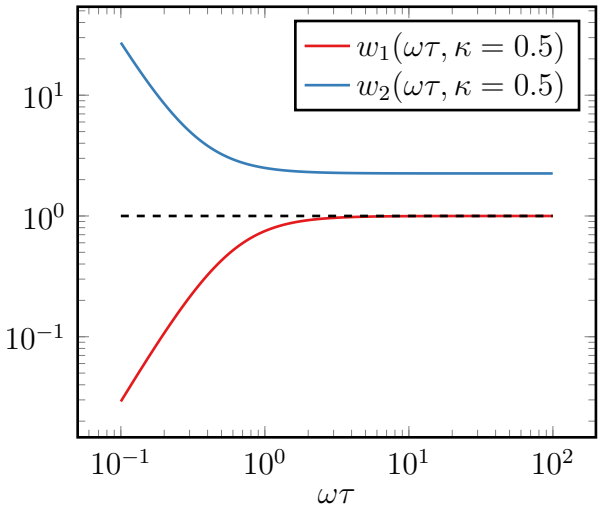


Figure 4.4: Behaviour of w_1 and w_2 in eq. (4.37).

Using the approach at the r.h.s of eq. (4.35) for the SLS model we obtain

$$\begin{aligned}
\frac{E'^2 + E''^2}{E'} &= E' + \frac{E''}{\Theta(\kappa, \omega\tau)} \\
&= k_0 - k_{\text{M}} + k_{\text{M}} \frac{\omega^2\tau^2}{1 + \omega^2\tau^2} + k_{\text{M}} \frac{\omega\tau}{1 + \omega^2\tau^2} \frac{1}{\Theta(\kappa, \omega\tau)} \\
&= k_0 - k_{\text{M}} \left(1 - \frac{\omega^2\tau^2}{1 + \omega^2\tau^2} \left(1 + \frac{1}{\Theta(\kappa, \omega\tau)\omega\tau}\right)\right) \\
&\equiv k_0 - k_{\text{M}} \left(1 - w_1(\kappa, \omega\tau)\right) \qquad (4.36a) \\
\frac{1}{\omega} \frac{E'^2 + E''^2}{E'} &= E'' \left(1 + \left(\frac{E''}{E'}\right)^2\right) \\
&= \eta \frac{1 + \Theta(\kappa, \omega\tau)^2}{1 + \omega^2\tau^2} \equiv \eta w_2(\kappa, \omega\tau), \qquad (4.36b)
\end{aligned}$$

where we introduced the weight factors $w_1(\kappa, \omega\tau), w_2(\kappa, \omega\tau)$

$$w_1(\kappa, \omega\tau) = \frac{\omega^2\tau^2}{1+\omega^2\tau^2}\left(1 + \frac{1}{\Theta(\kappa, \omega\tau)\omega\tau}\right) \tag{4.37a}$$

$$w_2(\kappa, \omega\tau) = \frac{1+\Theta(\kappa, \omega\tau)^2}{1+\omega^2\tau^2}. \tag{4.37b}$$

Both w_1 and w_2 depend on the significant timescale $\omega\tau$ but $w_1 \in [0, 1]$ introduces a reduction of $k_0 = k_\infty + k_\mathrm{M}$ by a percentage of k_M, whereas $w_2 \geq 1$ introduces an additional resistance which arises from the presence of k_∞, which can be seen by the consideration of the equality, where we find $w_2 = 1 \Leftrightarrow \kappa = 0 \Rightarrow k_\infty = 0$.

4.4 Quantitative Viscoelastic Properties Mapping of Primary Plant Cell Walls Using Dynamic AFM

Our derivation linking the generalised MW model to the cantilever observables relies on the model of Cartagena-Rivera et al. (2015). We therefore apply their dynamic AFM method, with the feedback on the deflection (instead the amplitude), in our experiments to image the topography and map the viscoelastic properties of epidermal cells of the hypocotyl of whole, living *A. thaliana* seedlings which are immersed in water and attached to a solid support. We image the sample using feedback on the deflection of the AFM cantilever while the first mode of the lever is simultaneously excited. The hypocotyl is the embryonal part of the stem that grows mainly unidirectionally and where cell divisions rarely occur, which are useful properties for the investigation of pure plant growth. The imaged seedlings were germinated under

dark grown conditions and grown for 60 h previous to the experiment. Dynamic AFM is used to map the junctions between three (or more) cells, in order to capture the topography and mechanical behaviour of the three different types of walls, namely transverse and longitudinal radial (anticlinal) walls, and azimuthal (periclinal) walls. Figure 4.5a shows a photograph of an *A. thaliana* seedling at the age of 60 h and a schematic which shows the cellular structure of the hypocotyl and a typical frame of a cellular junction, including all three wall types. A topography image for a typical 3 cell junction is shown in fig. 4.5b; the corresponding A_1 and ϕ_1 were simultaneously obtained (not shown). With the latter two quantities, we can determine $E'$and E'', using eqs. (4.23b) and (4.23c), and project them on the topography, as shown in figs. 4.5c and 4.5d. The pixel size in these experiments is 78 nm.

Statistical analysis over every pixel of images for 86 cells on 4 seedlings, were used to obtain the mean values of E' and E'' resulting in, $E' = (191 \pm 12)$ MPa, (150 ± 7) MPa and (129 ± 7) MPa, for transverse, longitudinal, and periclinal walls, respectively (fig. 4.5e). Analogously we obtained mean values of $E'' = (103 \pm 8)$ MPa, (75 ± 4) MPa and (50 ± 4) MPa , for the transverse, longitudinal, and periclinal walls respectively (fig. 4.5f). The growing periclinal and longitudinal walls are significantly different from the non-growing transverse walls with $p < 0.01$ for E' and $p < 0.001$ for E'', with p being the p-value of Welch's t-test. Furthermore, there is a significant difference between the longitudinal and periclinal walls with $p < 0.05$ for E' and $p < 0.001$ for E''. The reason for the difference in both growing walls is probably caused by the fact that these walls have a different orientation with respect to the indentation direction. The periclinal walls are probed in transverse direction, whereas the longitudinal walls are probed in axial direction.

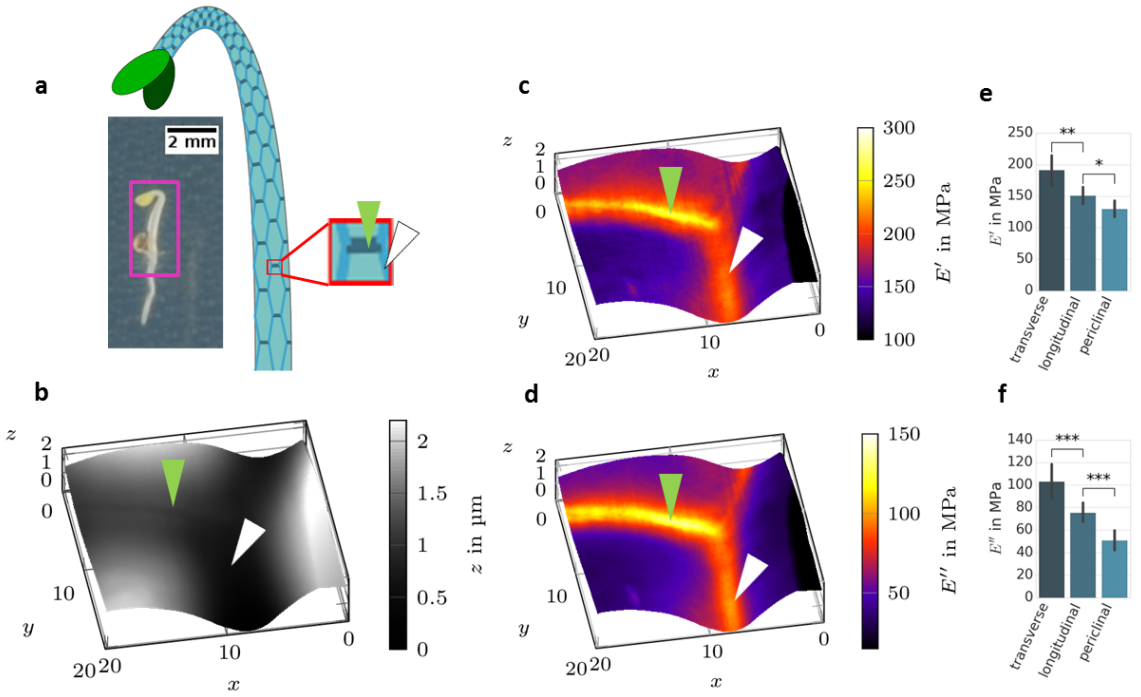


Figure 4.5: Dynamic AFM 20 µm × 20 µm images of a junction between three cells in an *A. thaliana* hypocotyl. (a), shows a photograph of the seedling before imaging and a schematic which resembles the cell structure at the hypocotyl. The frame in the photograph highlights the part which is shown in the schematic below. The red frame in the schematic shows (a) structural example of the part we imaged in an experiment, as an example of the topography of such a frame is given in (b). The colour coding for the different wall types in the schematic is the same as in (e) and (f). Maps of storage E' and loss E'' moduli projected on the topography are given in (c) and respectively. The walls transverse to growth direction are marked by green arrowheads and longitudinal walls are marked by white arrowheads. The walls which are not intersections are periclinal. E' and E'' show significant differences between different walls (e, f). (e) and (f) show the statistical distributions of E' and E'' obtained from dynamic AFM maps of 86 cells and 4 seedlings (i.e. 86 periclinal, 65 longitudinal anticlinal, and 32 transverse anticlinal walls) Statistical significance is obtained by Welch's t-test and $*$ means that the p-value $p < 0.05$, $**$ $p < 0.01$ and $***$ $p < 0.001$. Both growing walls (longitudinal and periclinal) are significantly different from the non-growing transverse walls but also show statistical significance in direct comparison with each other.

4.5 Comparison with Previously Reported Values of Elastic Modulus

A common criticism for quasi-static AFM indentation experiments of plant CWs is that they report values that are orders of magnitude smaller than those obtained with other techniques, which for example use macroscopic stretching of tissues or osmotic pressure measurements (Cosgrove, 2016). A detailed study combining quasi-static indentation, osmotic treatment, and finite element modelling by Weber et al. (2015) reported both a radial modulus in the range of $E_r = 200\,\text{MPa}$–$750\,\text{MPa}$ and an axial modulus of about $E_a = 120\,\text{MPa}$–$220\,\text{MPa}$, in tobacco suspension cells Our results agree qualitatively with other quasi-static indentation experiments in that the longitudinal walls have lower E' values than the transverse walls (Peaucelle et al., 2015). In our experiments, the indentation is in the radial direction for the periclinal walls and in the axial direction for the radial walls, therefore we assume that the main contribution comes from the radial modulus which means that our results agree with Weber et al. (2015) and are one to three orders of magnitude larger than the Young's moduli reported using quasi-static AFM nano-indentation (Milani et al., 2011; Peaucelle et al., 2015; Sampathkumar et al., 2014; Hayot et al., 2012). Comparing our values to the mechanical properties of the components of the plant CW, we find that they are below the range of the Young's modulus of cellulose microfibrils, as previously demonstrated from molecular dynamic (MD) simulations and x-ray diffraction studies ($E_{\text{transverse}} = 5\,\text{GPa}$–$50\,\text{GPa}$, $E_{\text{axial}} = 50\,\text{GPa}$–$220\,\text{GPa}$) (Moon et al., 2011). This suggests that the contribution of cellulose to elasticity in our experiments is reduced by the compliance that is introduced by the pectin matrix. This is in agreement with the current view, that cellulose has the role of resisting stress elastically and pectins contribute the viscose, plastic, component (Cosgrove, 2005; Zhang et al., 2016). The discrepancy with previous AFM quasi-static nanoindentation experiments can be ex-

plained by the fact that our cantilevers are excited at 80 kHz, hence the measurement is mainly due to the CW's component that dominates the response of the material at that frequency. Our results seem to indicate that in this case, the dominant contribution comes from cellulose microfibrils (CMFs). Slow/quasi-static indentation experiments can be expected to capture the response of CW components with slower time response (such as pectin) which would explain the small reported values. Hayot et al. (2012) found values, from nanoindentation experiments (without spatial resolution), for E' and E'' on leaves of *A. thaliana*, using the KV model, which are about one order of magnitude smaller than ours, which is the same deviation as in other AFM nano-indentation experiments. This can be explained by the different timescale in their experiment, which was three orders of magnitude smaller than in ours.

4.6 The Relevant Timescale of The Cell Wall Response Can Be Used to Understand the Underlying Mechanism of Cell Growth

In plant growth, the relevant timescale τ of the material relaxation is the parameter that can be used to relate the material properties of the cell wall to mathematical models of growth. As we show below it is possible to extract the significant timescale from our experiments using the experimental E' and E''. It can be easily seen from eqs. (4.23b) and (4.23c), that for the MW model ($k_\infty = 0$) the inverse loss tangent $E'/E'' = \omega\tau$ gives the significant timescale τ. Similarly, for the KV model $E'/E'' = 1/\omega\hat{\tau}$, where $\hat{\tau} = \eta/k_\mathrm{V}$ is the KV timescale. For the SLS the expression is $E'/E'' = \kappa/\omega\tau + (\kappa+1)\omega\tau$, with $\kappa = k_\infty/k_\mathrm{M}$ (eq. (4.34)). The first term represents the contribution of the KV ($\tau/\kappa = \hat{\tau}$) and the second term represents the MW regime. Figure 4.6 shows the variation of E'/E'' with $\omega\tau$ for the SLS model for different

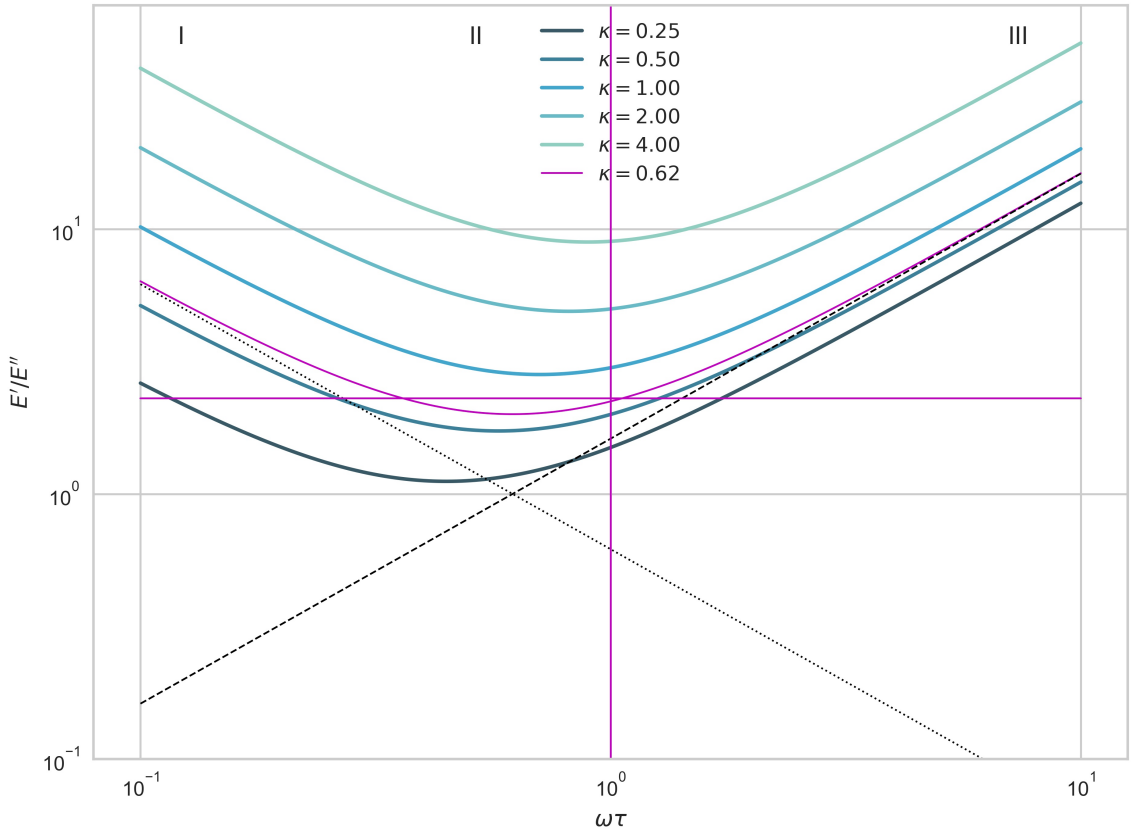


Figure 4.6: Behaviour of the inverse loss tangent E'/E'' with respect to the significant timescale $\omega\tau$ in the SLS model for different ratios of $\kappa = k_\infty/k_\mathrm{M}$. Systems with large κ are KV-like and systems with small κ are MW-like. The dotted and dashed lines show the KV (regime I) and MW (regime III) behaviour, respectively, for $\kappa = 0.62$. The transition regime (regime II) is where the curve for $\kappa = 0.62$ is neither on the dotted nor the dashed line. The magenta horizontal and vertical lines indicate the experimental results of the inverse loss tangent and the timescale, respectively. The magenta curve for $\kappa = 0.62$ indicates the behaviour of the plant CW in our experiments

κ values. Three regimes can be found, namely the KV regime (fig. 4.6I), the MW regime (fig. 4.6III), and a mixed regime (fig. 4.6II). For comparison, the dotted and dashed lines show the behaviour of the KV and MW model respectively for $\kappa = 0.62$. Moreover, fig. 4.6 shows that the mixed regime is only present for one order of magnitude of $\omega\tau \in [0.2, 5.0]$. This implies that if the excitation is quick with respect to the timescale, i.e. $\omega\tau \gg 1$, the material shows MW behaviour, and if the excitation is slow with respect to τ, i.e. $\omega\tau \ll 1$ the material displays KV behaviour. Furthermore, the inversion of the timescale implies that the choice of the model is crucial for understanding the relaxation time of the material. If plant growth is explained using the MW model – as it is usually done – only one timescale exists, which is given by the growth rate. In our experimental case the oscillation is $\omega\tau = 2\pi f = 502\,\mathrm{radkHz}$ (where f is the driving frequency of the cantilever) and a relative growth rate (GR) of $GR = 61\,\mu\mathrm{Hz}$ (Crowell et al., 2011) the difference is ten orders of magnitude and hence we expect to be in the quick indentation regime. If we compare absolute velocities, for the oscillation $v_o \approx 100\,\mathrm{nm\,s^{-1}}$ and for growth $v_g \approx 5\,\mathrm{nm\,s^{-1}}$, which is still a difference of two orders of magnitude and therefore the expectation is still to be in the quick indentation regime. However it is also reasonable to hypothesise that plant growth is a macroscale emerging phenomenon in which the dependence on local, nanoscale polymer dynamics cannot be directly extrapolated from the cellular scale (Dyson et al., 2012; Crowell et al., 2011) , hence different time-responses could in principle be expected both in the micron and the nm-scales and hence the inverse loss tangent could be found in all three regimes for $\omega\tau$. In the following two sections we will use these considerations to (i) develop a test for the validity of the viscoelastic models applied to explain the material properties of the CW using dynamic AFM mapping and (ii) obtain high spatial resolution maps of the local relaxation time, the initial stiffness and the viscosity of CWs.

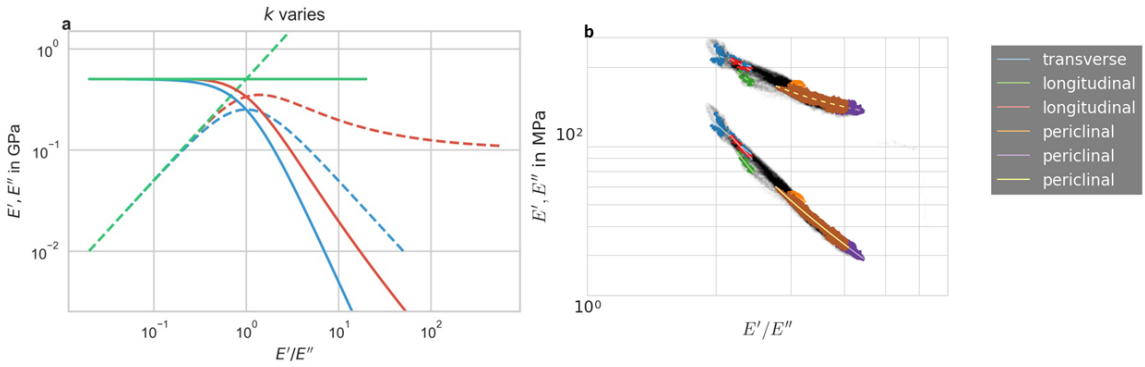


Figure 4.7: Local distribution of material properties. (a), Plot of E' and E'' vs the inverse loss E'/E''tangent if only k changes for the KV (green), MW (blue), and SLS (red) model (notice that the k in the KV and MW model are different, in the SLS model we change k_{M}). (b), displays a scatter plot of the distribution of E' and E'' vs E'/E'' for the experimental values from figs. 4.5c and 4.5d. The lines in (b) show the fit to the SLS model for constant η and changing k_{M} (dashed E', solid E'')

4.7 Local Distribution of Material Properties to Test the Validity of the Viscoelastic Model

While the determination of the viscoelastic model is straight forward in stress-strain experiments, so far there is no available method to determine the material behaviour in dynamic AFM experiments. Here we propose to use the local distribution of the viscoelastic properties of the material to determine the validity of the viscoelastic model. The idea is to plot E' and E'' against the inverse loss tangent E'/E'' for every pixel. In the KV and MW model this corresponds to a plot against the inverse and direct timescale, respectively. In the SLS model this is a plot against the timescale behaviour as shown above in fig. 4.6. The assumption for this approach is that the material properties are continuous in adjacent pixels and hence every pixel follows the same model and consequently has a fixed relation between E' and E'', e.g. for the SLS $E' = k_\infty + E''\omega\tau$. This premise can be justified by the fact that adjacent pixels are coupled to each other and therefore contribute also to the measurements of their neighbours and the behaviour is observed to be rather smooth. Figure 4.7a shows the

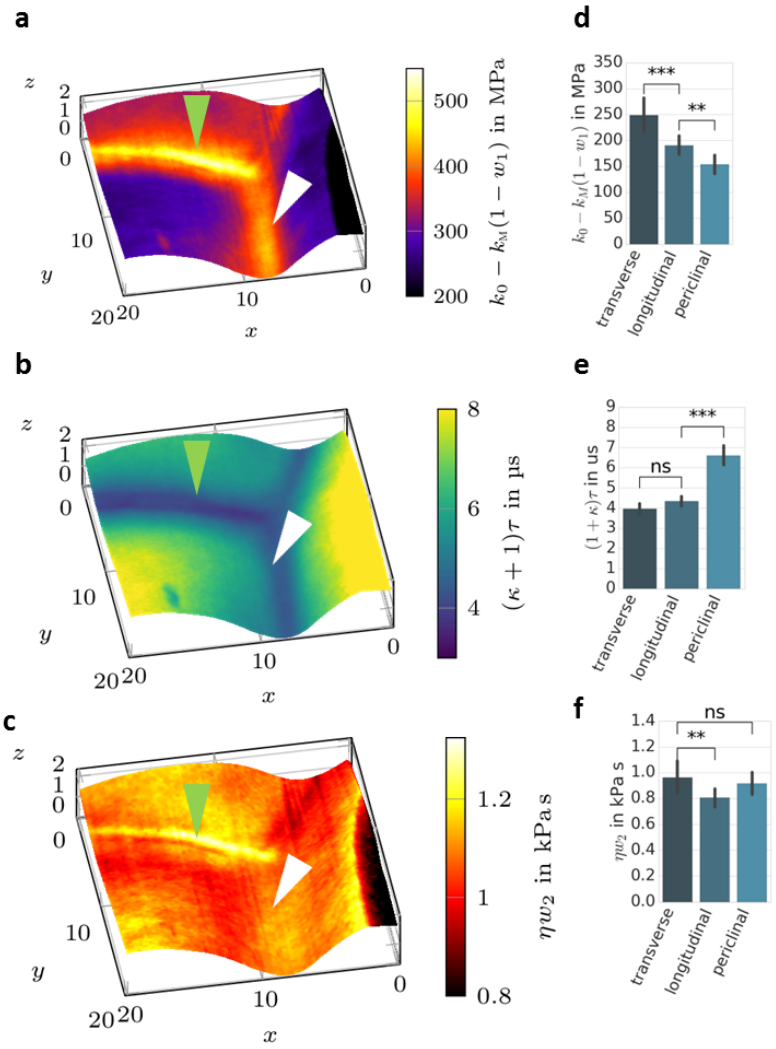


Figure 4.8: Material maps the initial stiffness k_0, timescale $(\kappa{+}1)\tau$, and viscosity $(\kappa{+}1)2\eta$ calculated in the quick indentation limit. (a)-(c) show maps of each these three quantities overlaid on the topography of the three cell junction shown in fig. 4.5. The walls transverse to growth direction are marked by the green arrowheads and longitudinal walls are marked by the white arrowheads. (d)-(f) show the statistical distribution of k_0, $(\kappa{+}1)\tau$, and $(\kappa{+}1)2\eta$ for 86 cells from 4 seedlings. Statistical significances in d-f were obtained by Welch's t-test where ns means not significant, $**$ means that the p-value is < 0.01 and $***$ the p-value is < 0.001. The statistical significance in d is between the non-growing transverse walls and the growing longitudinal and periclinal walls and also among the growing walls. The statistical significance in e is between the walls at the junctions (transverse and longitudinal) and the periclinal walls, which are not at junctions. There is no statistical significance between transverse and longitudinal walls. The statistical significance in f is only between transverse and longitudinal walls but not between transverse and periclinal

expected behaviour for the KV, MW, and SLS models if k varies (notice that the k in the KV and MW model are different, in the SLS model we change k_{M}). Figure 4.7b displays experimental data, in a scatter plot using E' and E'' values obtained from figs. 4.5c and 4.5d plotted against E'/E''. The different colours indicate different CWs. The lines are the fit to the SLS model for varying k_{M} (dashed lines for E' and solid lines for E''). The fitted parameters are the same for E' and E''.

From the fits we can obtain mean values of $k_{\mathrm{M}} = (226 \pm 19)\,\mathrm{MPa}$, $(170 \pm 12)\,\mathrm{MPa}$ and $(110 \pm 10)\,\mathrm{MPa}$ for transverse, longitudinal and periclinal walls, respectively, and $\kappa = 0.38 \pm 0.03$, 0.43 ± 0.02 and 0.86 ± 0.04 for transverse, longitudinal and periclinal walls, respectively. We also obtain values for the relaxation times $\tau_{\mathrm{fit}} = (2.36 \pm 0.17)\,\mu\mathrm{s}$, $(2.57 \pm 0.13)\,\mu\mathrm{s}$ and $(2.40 \pm 0.10)\,\mu\mathrm{s}$ for transverse, longitudinal and periclinal walls, respectively. This leads to $\omega\tau \approx 1.3$, which suggests, that the timescale of our experiments is still relevant for the material behaviour. This is in agreement with theory from polymer physics, which suggest a continuous contribution of significant timescales for macromolecular materials (Doi and Edwards, 1986). Comparing these relaxation times with the timescale of growth, which is $\tau_g \approx 16\,393\,\mathrm{s}$, the discrepancy is indeed ten orders of magnitude. Figure 4.7 shows that the fits present an excellent agreement with the SLS model and from the timescales we can see that we are in the MW regime. Moreover, the fact that the plant cell wall behaves like an SLS at the nm scale implies that there is at least one timescale which contributes to the material relaxation, besides the growth relaxation. This indicates that the theoretical prediction made by Dyson et al. (2012), that plant growth follows a MW-like behaviour at the subcellular level, is valid. Although for a complete confirmation of the theory further experiments, which link the material properties directly to growth, are required. It is remarkable that the plant CW behaves linearly on all these different scales, the subcellular, the cellular, and organ level (Lockhart, 1965a; Ortega, 1985; Cosgrove, 1985; Dyson and Jensen, 2010; Dyson et al., 2012). The local

distribution of E' and E'' is a powerful tool for dynamic AFM methods to test the validity of viscoelastic models. Furthermore, the fits provide additional information about the individual quantities in the model, i.e. $k_{\mathrm{M}}, k_{\infty}, \tau$ and they indicate whether the experiment takes place in the slow, quick or intermediate indentation regime.

The MW approximation can be used to obtain high-resolution spatial maps of the local relaxation time, the initial stiffness, and the viscosity of the plant's CWs. In order to identify areas where stress accumulates during growth due to locally slower relaxation times, it is useful to obtain a spatial map of τ. This can be obtained – with the MW approximation – using the relation $(1+\kappa)\omega\tau = E'/E''$. The error of this approximation is given by the ratio of the KV term and the MW term from the inverse loss tangent, which is given by $\kappa/(\kappa+1)\omega^2\tau^2 < 1$ for our experiments this error is approximately 15 %.

Moreover, relations for the initial spring constant $k_0 = k_{\infty} + k_{\mathrm{M}} = (\kappa+1)k_{\mathrm{M}}$ and viscosity η can also be found, and k_0 is given by eq. (4.36a). In this case k_0 is reduced due to relaxation during the measurements. In our experiment $w_1(\kappa, \omega\tau) \approx 0.85$ and hence k_0 is reduced by about $0.15k_{\mathrm{M}}$. The viscosity is obtained by eq. (4.36b) which increases η, caused by the resistance of k_{∞}, i.e. $w_2(\kappa, \omega\tau) = 1 \Leftrightarrow \kappa = 0$. Our results yield $w_2(\kappa, \omega\tau) \approx 2.1$ (for details see supplementary section 4.3). Figures 4.8a to 4.8c show spatial maps of $k_0 - k_{\mathrm{M}}(1 - w_(\kappa, \omega\tau))$, $(\kappa+1)\tau$, and $\eta w_2(\kappa, \omega\tau)$ projected on the topography of the 3 cell junction, shown in figs. 4.5a and 4.5b. Figures 4.8d to 4.8f show the statistical distribution obtained from 86 cells from 4 seedlings. The mean timescales obtained from these distributions are $(1+\kappa)\tau = (3.96 \pm 0.14)\,\mu\mathrm{s}$, $(4.34 \pm 0.12)\,\mu\mathrm{s}$ and $(6.58 \pm 0.25)\,\mu\mathrm{s}$ for transverse, longitudinal, and periclinal walls, respectively.

The spatial map of τ in fig. 4.8b indicates that the areas of the cell junctions, where more stress accumulates during growth, have the ability to relax more quickly, and thus release tissue stress faster than the purely growing regions of the periclinal walls.

From the images we also obtain the mean initial stiffness $k_0 - k_{\mathrm{M}}(1 - w_1(\kappa, \omega\tau)) = (248 \pm 17)\,\mathrm{MPa}$, $(191 \pm 9)\,\mathrm{MPa}$ and $(154 \pm 9)\,\mathrm{MPa}$, for transverse, longitudinal, and periclinal walls, respectively. This is in agreement with the axial modulus of Weber et al. (2015), who measured only the relaxed value in their experiments. Finally, we can obtain the averaged viscosity $\eta = (0.96 \pm 0.06)\,\mathrm{kPa\,s}$, $(0.80 \pm 0.04)\,\mathrm{kPa\,s}$ and $(0.91 \pm 0.05)\,\mathrm{kPa\,s}$, for transverse, longitudinal, and periclinal walls, respectively. This result is in agreement with the finding above, namely that it is mainly the elasticity that changes, while the viscosity remains constant throughout the tissue. To conclude, the MW approximation provides high-resolution maps of the local distributions of the relaxation timescale, initial stiffness, and viscosity.

4.8 Reconstruction of the Generalised Maxwell Model in the Plant Cell Wall Using Stress Gradients

So far the mechanical properties of the plant CW were determined by an average over all pixels resulting in the average mechanical properties of the individual walls. However, it would be desirable to obtain the viscoelastic information for the individual pixels of one wall to extract spatial information of mechanical response. This would be straight forward if the underlying model was the MW model and the relaxation time would be given by $\omega\tau = E'/E''$. In the case of the SLS model this is much more difficult as we have seen above we had to use an average over all pixels and some approximations to get some useful values from the experiment. However, it makes sense to consider the pixels as individual elements, which have their own mechanical properties and we can use the spatial information to obtain more information about the system.

Obviously adjacent pixels are mechanically related because the pixel size is of the size of the indenter. Furthermore, the oscillatory indentation of the CW excites

adjacent pixels since a mechanical wave is propagating through the material, which is caused by shaking the CW through the oscillations. Additionally, it can be assumed that the plant CW is a smooth continuous material, i.e. it has no singularities, and therefore we can assume that adjacent pixels follow the same viscoelastic model. With these assumptions and the approximation of a standard linear solid model we can express E' as a function from E'' and obtain from eqs. (4.24) and (4.25)

$$E' = k_\infty + E''\omega\tau. \tag{4.38}$$

The timescale can now be obtained from the gradient of E' with respect to E''

$$\tau = \frac{1}{\omega}\frac{\partial E'}{\partial E''}. \tag{4.39}$$

A similar approach for a quantum mechanical phenomenon was chosen by Miyahara et al. (2017), who calculated a quantum mechanical tunneling rate for the atomic orbitals in quantum dots from a conservative and a dissipative quantity.

Equation (4.39) uses the spatial information to determine the relevant timescale of the material but the numerical derivative of E' with respect to E'' cannot be performed straight forwardly but instead they have to be done independently with respect to the spatial dimensions. This assumes that the relevant timescale of the sample depends on the location, i.e. $\tau \equiv \tau(\mathbf{r})$, with $\mathbf{r} = (x, y)^T$ pointing to the

location of the sample. Using this approach we obtain with eqs. (4.24) and (4.25)

$$\frac{\partial E'}{\partial \omega\tau} = \boldsymbol{\nabla} E' \frac{\partial \mathbf{r}}{\partial \omega\tau} = k_{\mathrm{M}} \frac{2\omega\tau}{\left(1+\omega^2\tau^2\right)^2} \tag{4.40a}$$

$$\frac{\partial E''}{\partial \omega\tau} = \boldsymbol{\nabla} E'' \frac{\partial \mathbf{r}}{\partial \omega\tau} = k_{\mathrm{M}} \frac{1-\omega^2\tau^2}{\left(1+\omega^2\tau^2\right)^2}, \tag{4.40b}$$

with the Nabla operator $\boldsymbol{\nabla} = \partial/\partial\mathbf{r}$. Dividing now eq. (4.40a) by eq. (4.40b), we obtain

$$\frac{\frac{\partial E'}{\partial \omega\tau}}{\frac{\partial E''}{\partial \omega\tau}} = \frac{2\omega\tau}{1-\omega^2\tau^2}. \tag{4.41}$$

This can be brought into a quadratic equation and finally we obtain a solution for τ, which is given by

$$\tau = \frac{1}{\omega}\left(-D \pm \sqrt{D^2+4}\right), \tag{4.42}$$

with $D = (\frac{\partial E'}{\partial \omega\tau}/\frac{\partial E''}{\partial \omega\tau})^{-1}$. The negative part of the solution can be neglected, because the relaxation time must be positive.

Sampathkumar et al. (2014) reported that the mechanical properties follow local geometric stress patterns, therefore, it is important to look at the gradient images of E' and E'' with respect to the topography z. If the gradient of the mechanical properties follows the gradient of the topography it is very likely that this differences arise from geometrical stress patterns, whereas if this is not the case, the changes in the mechanical properties have a molecular origin. In this way we can see if the gradient can lead to additional information of the mechanical properties or if we only

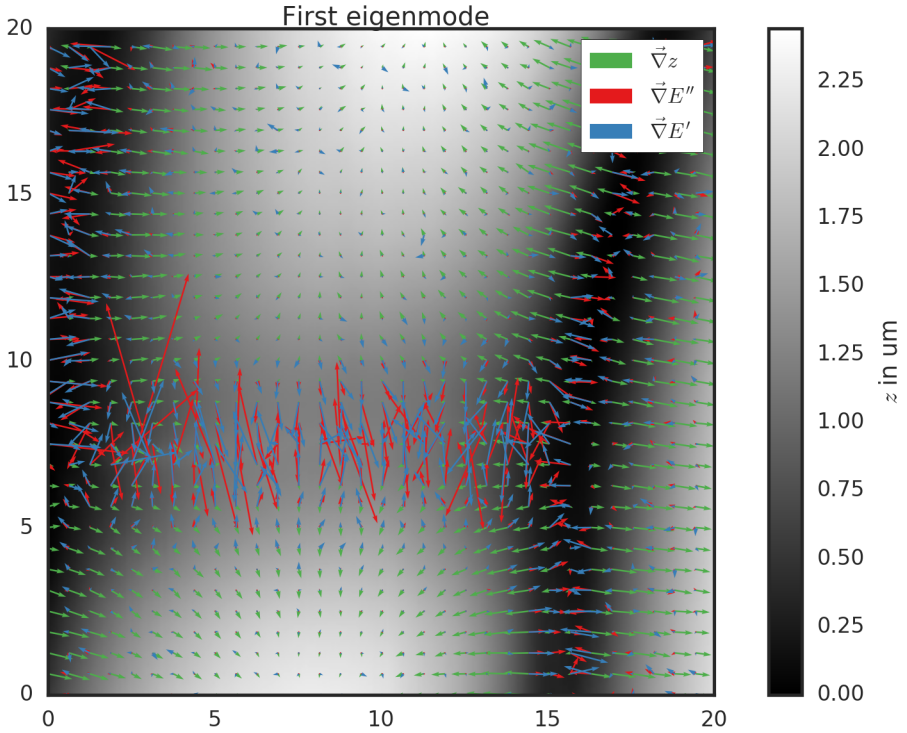


Figure 4.9: Mechanical gradients of the first eigenmode. The figure shows the gradient of the topography z, the loss modulus E'' and the storage modulus E''. At positions of large geometrical stress (green arrows are long), as in the r.h.s of the image, the mechanical gradients follow the geometrical stress patterns (red and blue arrows are anti parallel to green arrows). Additionally, at those positions E'' and E' are closely related, i.e. are nearly parallel. At the cell junctions, however, the mechanical gradient is enhanced and the directions of energy dissipation seem to differ from those of stored energy.

obtain differently represented geometrical information.

Figure 4.9 shows the gradient of z, E', and E'', which were obtained by a dynamic mechanical AFM scan as described above. It can be clearly seen that some regions, as the majority of the r.h.s of the image, follow the stress patterns of the geometry, i.e. the gradient (green) arrow of the topography is in opposite direction to the arrow of both moduli (red for E'' and blue for E'). However, most parts show a very different behaviour, that it could be imagined that these regions might still be influenced by the geometric stress but the data reveals more information about the mechanical properties of the plant CW. The deviation from the geometric stress patterns is particularly large at the cell junctions. These should be the positions where most

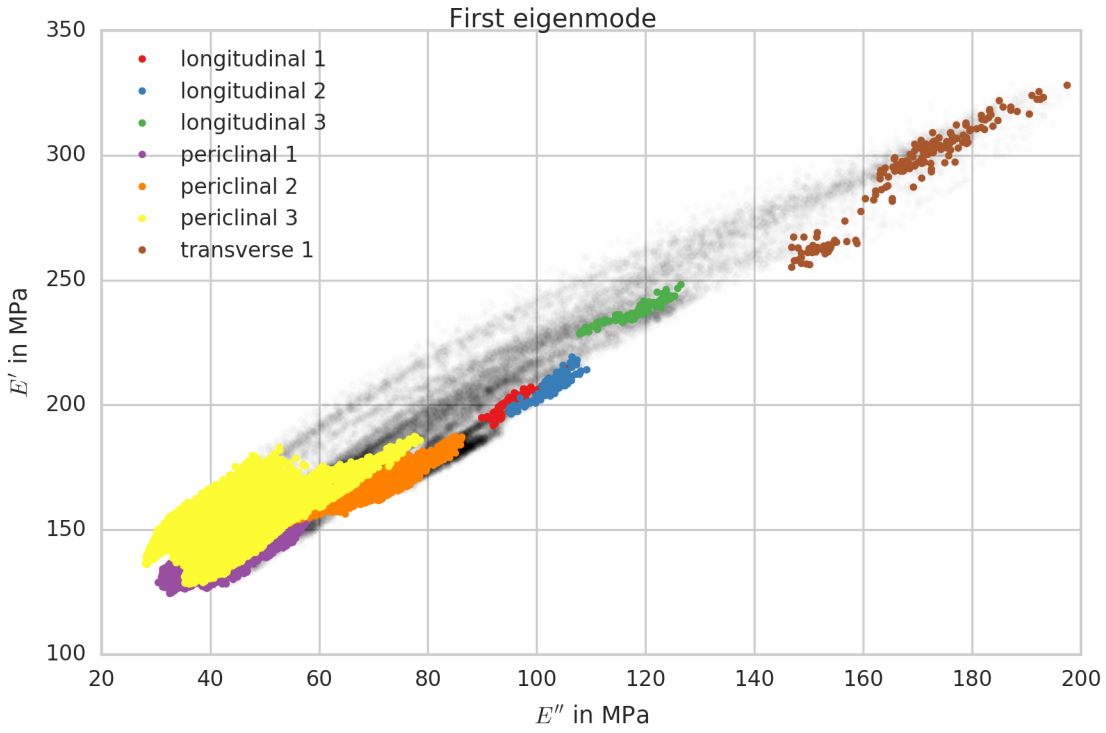


Figure 4.10: SLS behaviour of measurements with the first eigenmode. The relation between E' and E'' is an indicator of which viscoelastic model the material follows. The grey dots in the plot represent all data points from a dynamic AFM scan for E' plotted against E''. The coloured dots represent the different walls. All dots which are not coloured, were neglected during the analysis to obtain a sharp separation of the different walls and they belong mostly to periclinal walls. If the average of the pixels, i.e. the majority of the pixels, follows a linear function then eq. (4.40) is valid, which implies the SLS is the appropriate viscoelastic model. For the first eigenmode, which corresponds to a frequency of $f_1 \approx 78\,\mathrm{kHz}$, as shown in this figure, the SLS is a good approach.

stress accumulates, because the cells are attached to each other and they have to adapt their growth rate to the adjacent cells, since they cannot migrate. And indeed, the longer arrows confirm that these regions are positions where the mechanical properties change more rapidly and this indicates that more stress accumulates there. However, this is not a geometric stress in the sense of a bent wall and therefore the directions of the mechanical gradients deviates on the junctions more from the topographical gradient than on the faces.

Figure 4.10 shows a plot of the relation between E' and E''; the plot confirms that eq. (4.38) is a good approach for the plant cell wall because the relation between E'

and E'' is nearly linear. In fact the Pearson correlation coefficients for the pixels of the different walls of the image shown in fig. 4.9 are 0.96 for the transverse, 0.92, 0.91 and 0.94 for the longitudinal, and 0.89, 0.91 and 0.71 for the periclinal walls. The small deviations from a perfect correlation between E' and E'' in the anticlinal walls show again that the SLS model is a good approach but even the larger deviations in the periclinal walls should not be a problem, because even the generalised MW model can be always described with an first order approximation of the SLS model. Having now shown that the approach in eq. (4.39) is reasonable, we can now obtain k_∞, k_M, and η, using the following equations:

$$k_\infty = E' - E''\omega\tau \tag{4.43a}$$

$$k_\mathrm{M} = E''\frac{1+\omega^2\tau^2}{\omega\tau} \tag{4.43b}$$

$$\eta = \tau k_\mathrm{M}. \tag{4.43c}$$

Figures 4.11a and 4.11b show E'' and E' for the image shown in fig. 4.9 and we can see that the patterning and the mechanical values are similar as in fig. 4.5. From eqs. (4.39) and (4.43), we can derive k_M, k_∞, τ, and η from the standard linear solid model, which are schown in figs. 4.11c to 4.11f. In those images we can clearly see that the anticlinal walls are better visible than they were in the E' and E'' maps. The reason for this is that E' and E'' reflect also the internal wall stresses, which have to be continuous and therefore the transitions in those images resemble the stress transition between the walls, which is not necessarily the case for the derived quantities. With a pixel size of 78 nm and an estimated thickness of the anticlinal CW of 100 nm–200 nm (Derbyshire et al., 2007) the increased values in k_M, τ, and η seem to accurately reproduce the actual positions of those walls. Another interesting fact is

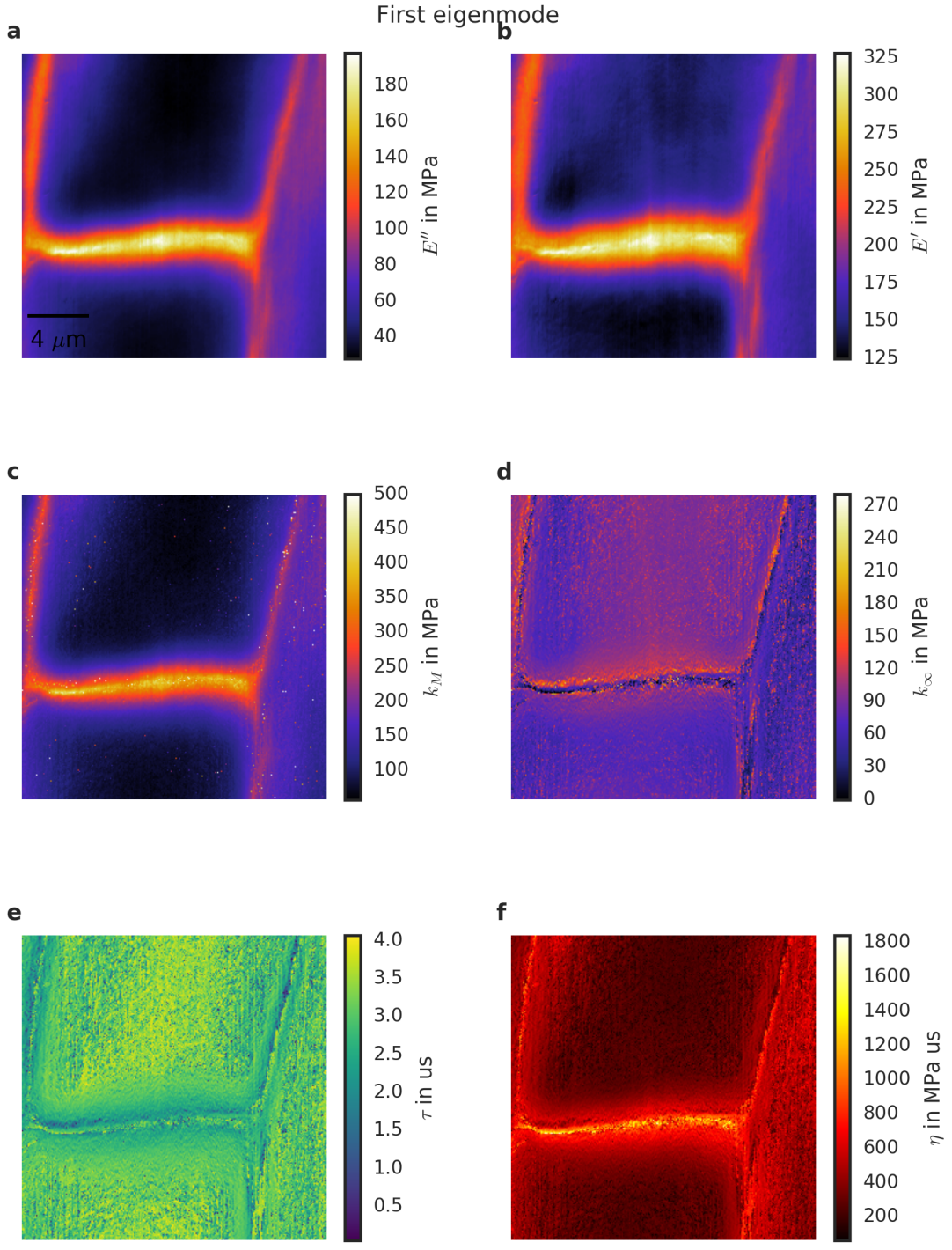


Figure 4.11: Derived SLS quantities for the first eigenmode. (a) and (b) show E'' and E' for the scan which is already shown in figs. 4.9 and 4.10. (c), (d), (e), and (f) show the derived SLS quantities, k_{M}, k_∞, τ, and η, respectively. The quantities were determined according to eqs. (4.42) and (4.43).

that in this data representation not only the actual walls become visible but also other structures appear. This can be seen particularly well in figs. 4.11e and 4.11f. That these structures represent the exact molecular structure of the CW is very unlikely considering that the pixel size is 78 nm and the CMFs are about 5 nm in diameter and the matrix molecules have even smaller widths. However, it is to expect that this represents a projection of the mechanical properties over a penetration depth of the indentation depths and the mechancial wave, which is sent into the material by the cantilever oscillation. While the indentation depth is known from the quasi-static indentation and it is about $\sim$ 300 nm, the penetration depth λ_p can be estimated by the oscillation velocity $\langle v_o \rangle = 1/2 A_1 \omega_1$ and the relaxation time τ_1, which gives $\lambda_p = \langle v_o \rangle \tau_1 \approx 1.3\,\text{nm}$. The small value caused by the oscillation compared to the initial indentation makes this contribution negligible and the mechanical properties of a pixel comes mainly from the area which is in contact with the probe. Finally, we can compare the derived τ and k_{M} with the fitted values from the approach above where these quantities were obtained from the average. Here we obtain a mean ($\pm$ SD) value of $(2.9 \pm 0.5)\,\mu\text{s}$, which is very close to the values obtained from the collective above which where $\tau_{fit} = 2.36\,\mu\text{s}$–$2.57\,\mu\text{s}$. For k_{M} we obtain $(144 \pm 73)\,\text{MPa}$ for the mean value for the local map and $k_{\text{M}} = 110\,\text{MPa}$–$226\,\text{MPa}$. With these results we can say that the collective behaviour of the spatial maps is in agreement with the average behaviour obtained by the fits of the data.

To complete the generalised MW model from the SLS approximation with the missing values of the higher orders, it is possible to do measurements at different frequencies to penetrate MW arms with a different relaxation time. If we assume two MW arms with the stiffnesses k_1 and k_2 and the relaxation times $\tau_1 = \eta_1/k_1$ and $\tau_2 = \eta_2/k_2$, with the viscosities η_1 and η_2 in arm one and two, respectively, we obtain

a model, where E' and E'' are given by eq. (4.14) for $N = 2$

$$E' = k_\infty + k_1 \frac{\omega^2 \tau_1^2}{1 + \omega^2 \tau_1^2} + k_2 \frac{\omega^2 \tau_2^2}{1 + \omega^2 \tau_2^2} \tag{4.44a}$$

$$E'' = \quad k_1 \frac{\omega \tau_1}{1 + \omega^2 \tau_1^2} + k_2 \frac{\omega \tau_2}{1 + \omega^2 \tau_2^2}, \tag{4.44b}$$

with the relaxed stiffness k_∞. Without loosing generality we assume $\tau_1 > \tau_2$. In this case there is an excitation frequency ω_1 where mainly the arm containing τ_1 contributes to E' and E'', because the arm with τ_2 relaxes too quickly to be relevant. This was the assumption we did in the previous discussion for the first eigenmode. This assumption with two discrete timescales makes the most sense if the material of interest is a composite one were the different components display very different viscoelastic behaviour. This is the case in the plant CW, where the matrix polymers display a much more fluid response than the CMFs, which show a rather elastic behaviour. However, even for polymeric materials made from only one kind of polymers these measurements are useful, since shorter timescales are associated with with shorter lengthscales (Kachman et al., 2017).

Performing the experiment now at ω_1, which is in our case the first eigenmode of the cantilever, we can obtain $E'(\omega_1)$ and $E''(\omega_1)$ from which we can determine τ_1, k_1, k_∞ and η_1 as described in eqs. (4.42) and (4.43). With the Cypher ES$^{\text{TM}}$ it is possible to excite two eigenmodes at the same time and therefore the measurements for the higher frequency ω_2 can be performed parallel to the first one. This gives the moduli $E'(\omega_2)$ and $E''(\omega_2)$ from which we can subtract the quantities from the first scan to obtain a quantity from which we can determine τ_2, k_2 and η_2. This gives reduced

moduli $E'_r(\omega_2)$ and $E''_r(\omega_2)$

$$E'_r(\omega_2) = E'(\omega_2) - k_\infty - k_1 \frac{\omega_2^2\tau_1^2}{1+\omega_2^2\tau_1^2} = k_2 \frac{\omega_2^2\tau_2^2}{1+\omega_2^2\tau_2^2} \tag{4.45a}$$

$$E''_r(\omega_2) = E''(\omega_2) - k_1 \frac{\omega_2\tau_1}{1+\omega_2^2\tau_1^2} = k_2 \frac{\omega_2\tau_2}{1+\omega_2^2\tau_2^2}. \tag{4.45b}$$

It should be emphasised that the moduli, which where obtained from the first eigenmode were extrapolated to the second eigenmode by the multiplication $\omega_2\tau_1$ and consequently, the errors made by the approximation from the first calculation propagate to the second eigenmode. With these reduced moduli we can now perform the same procedure as above and obtain the quantities, k_2, τ_2, and η_2, in the second arm again by eqs. (4.42) and (4.43).

Here, we used the second eigenmode of the cantilever which was at $f_2 \approx 531\,\mathrm{kHz}$. Figure 4.12 shows in a scatter plot the relation between $E'(\omega_2)$ and $E''(\omega_2)$ of the scan, which is shown in fig. 4.11 for the first eigenmode. A very interesting result here is the fact that $E''(\omega_2) > E'(\omega_2)$, whereas this was the other way around for the first eigenmode. This implies that in the case of the second eigenmode the energy dissipation dominates the indentation process, which means that the indentation disrupts molecular bonds before they can relax into the equilibrium position, which would happen when $E' > E''$. That bonds are breaking at the second eigenmode is not very surprising given the fact that $k_2 \approx 7998\,\mathrm{N\,m^{-1}} \approx 46k_1$. Moreover, we observe that the relation between $E'(\omega_2)$ and $E''(\omega_2)$ does not follow the simple SLS model any more, in fact the Pearson correlation is now 0.39 for the transverse, 0.38, -0.22 and 0.61 for the longitudinal, and 0.11, 0.74 and -0.42 for the periclinal walls. This result is to expect if the plant CW displays a more complicated material relaxation at this higher frequency. For a composite material with the very distinct components

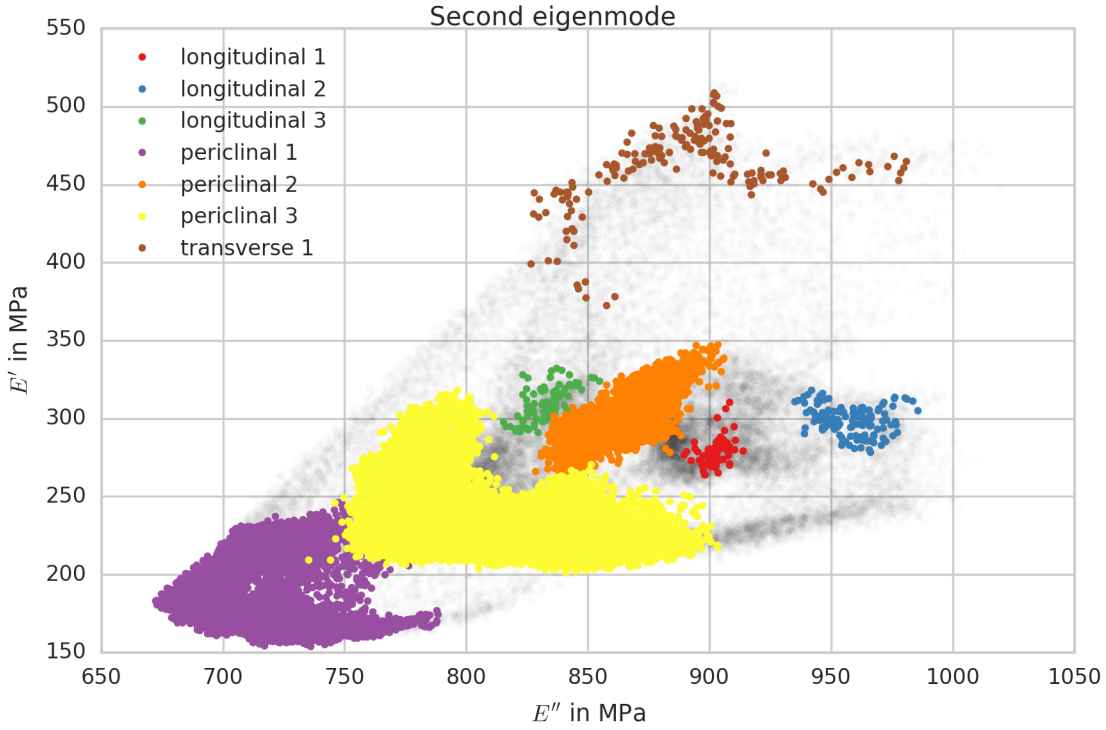


Figure 4.12: Stored and dissipated energy relation of measurements with the second eigenmode of the cantilever. The relation between E' and E'' is an indicator, of which viscoelastic model the material follows. The grey dots in the plot represent all data points from a dynamic AFM scan for E' plotted against E''. The coloured dots represent the different walls. All dots which are not coloured were neglected during the analysis to obtain a sharp separation of the different walls and they belong mostly to periclinal walls. If the collective, i.e. the majority of the pixels, follows a linear function then eq. (4.40) is valid, which implies the SLS is the appropriate viscoelastic model. For the second eigenmode, which corresponds to a frequency of $f_2 \approx 531\,\mathrm{kHz}$, as shown in this figure, the SLS is obviously not good approach and a more complicated viscoelastic model must be chosen.

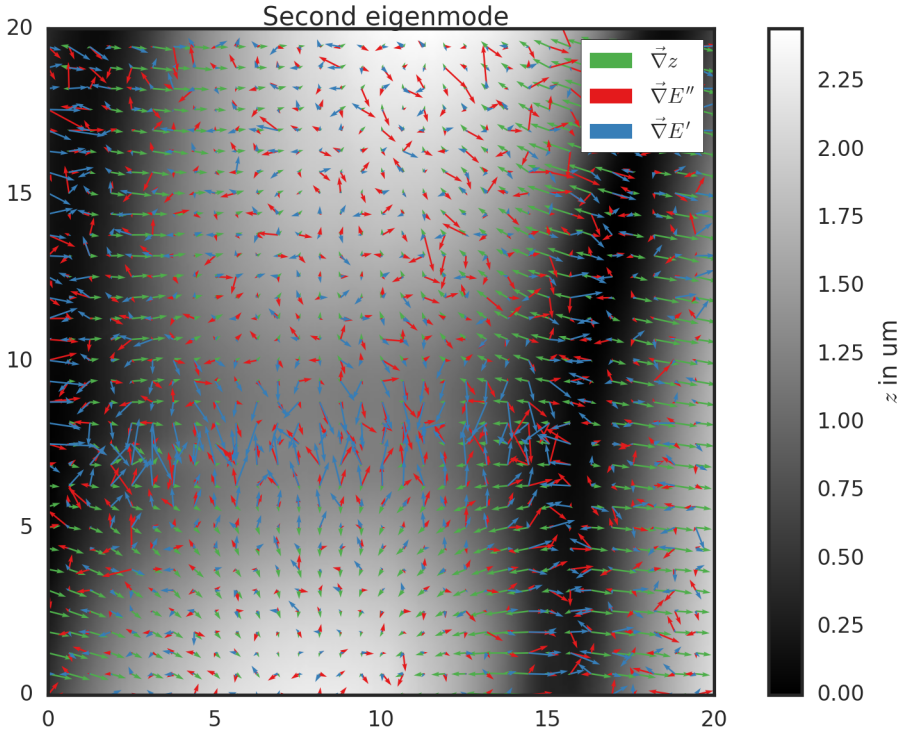


Figure 4.13: Mechanical gradients of the second eigenmode. The figure shows the gradient of the topography z, the loss modulus E'' and the storage modulus E''. Unlike for the first eigenmode (fig. 4.9, at positions of large geometrical stress (green arrows are long), as in the r.h.s of the image, the mechanical gradients do not follow the geometrical stress patterns (red and blue arrows are anti parallel to green arrows means they follow the geometrical stress). Additionally, at almost all positions E'' and E' are not related at all, i.e. are not parallel. At the cell junctions, however, the mechanical gradient is still enhanced but the directions of energy dissipation seem to differ from those of the stored energy in almost all positions.

of a matrix and fibre this should happen at a frequency which is above a certain threshold as this is apparently the case for the second eigenmode in this experiment.

Even more interesting is that the gradients of $E'(\omega_2)$ and $E''(\omega_2)$ show now almost no agreement with the geometric stress patterns, which is caused by the bending of the wall, while the stress at the cell junctions is still increased (fig. 4.13). Yet there is still a minimal agreement between those patterns near the cell junctions where presumably the accumulated stress is maximised (Kirchhelle et al., 2016). This suggests that at this timescale the penetrated molecular bonds are not aligned into the direction of the maximal wall stress but they rather show an intrinsic behaviour of the CW.

Moreover, at almost all positions there is no agreement between the directions of the gradients of $E'(\omega_2)$ and $E''(\omega_2)$. This suggests that there are different paths along which deformation energy is dissipated and stored. This is in agreement with the hypothesis that most of the CMFs bear most of the elastic energy, while the matrix, the cross-links in particular, dissipate energy. With the knowledge about the stress relaxation at this timescale the derived quantities k_2, τ_2, and η_2 for the second eigenmode become very interesting.

Combined with the result of the first eigenmode, which followed the SLS model very nicely (fig. 4.10), and the finding that the second eigenmode follows neither the the SLS model (fig. 4.12), nor does it represent the geometric stress patterns, we performed the approach with the two arm model as described by eqs. (4.44) and (4.45) and obtained the spatial distribution for the quantities k_2, η_2, and τ_2, which are shown in fig. 4.14. Figures 4.14a and 4.14b show the spatial distribution of $E''(\omega_2)$ and $E'(\omega_2)$ from fig. 4.12. Despite that $E'(\omega_2)$ and $E''(\omega_2)$ do not follow the geometric stress pattern of the wall, the values of both moduli are still increased at the anticlinal walls. This suggests that these walls are most likely stiffer not because of an increased stress at the cell junctions but rather because of the different orientation of those walls compared to the periclinal ones. Moreover, the values of both moduli are increased significantly with the higher frequency and as already discussed above it is to expect for $E'(\omega_2)$ to be increased compared to $E'(\omega_1)$ but this is not a necessity for the loss moduli. This large increase suggests that the stiffness of the second eigenmode causes a significant amount of bonds to break. Alternatively it could be that the deformation is far from the adiabatic limit and therefore more energy is dissipated during the non-adiabatic relaxation process.

Figure 4.14c shows the derived value for k_2, which is increased compared to k_1 and is in the GPa range. This makes sense because stiff structures have shorter relaxation times, which are probed with the higher frequency as fig. 4.14d shows. In the context

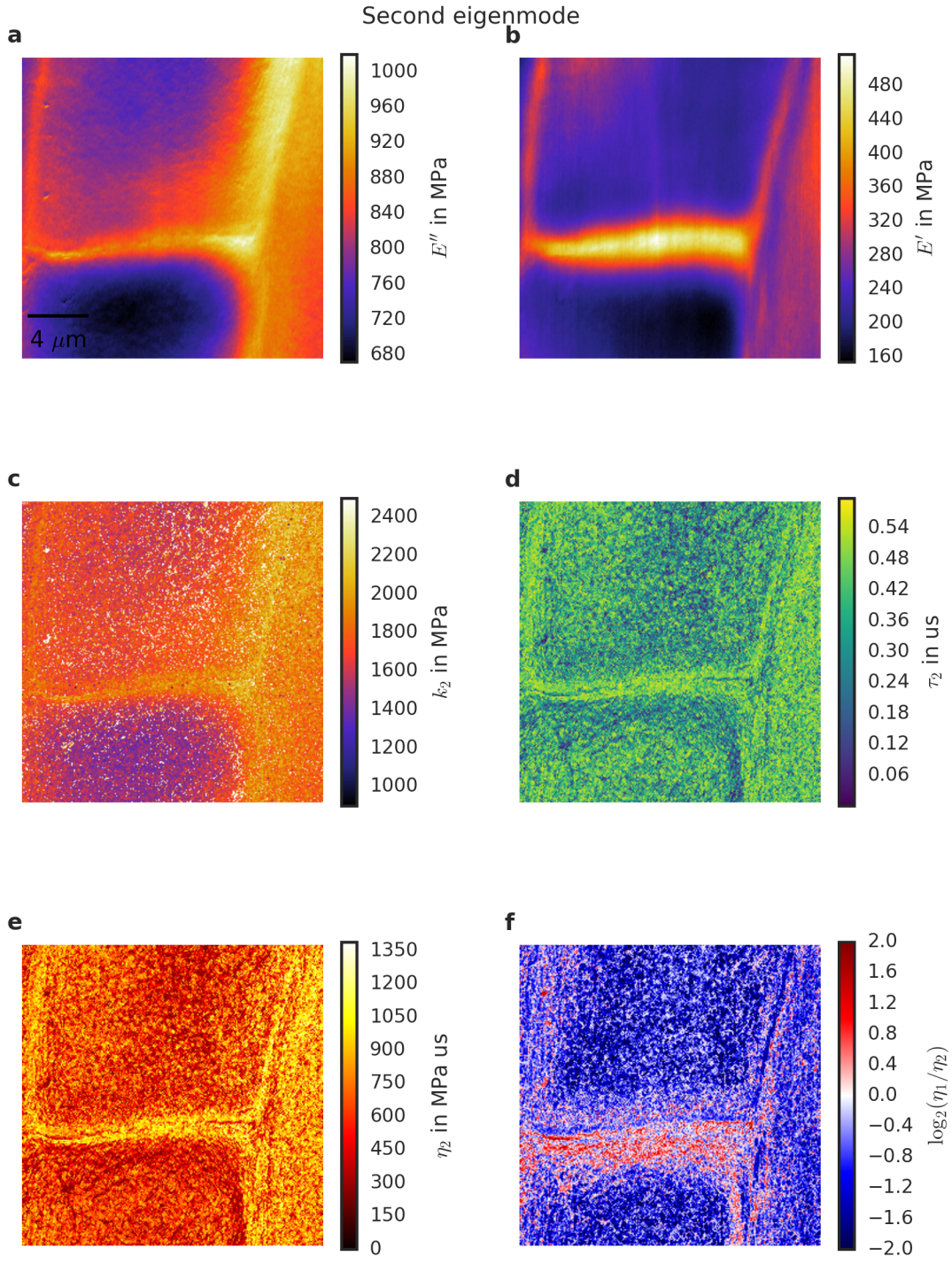


Figure 4.14: Derived SLS quantities for the second eigenmode. (a) and (b) show E'' and E' for the scan which is already shown in figs. 4.12 and 4.13. (c), (d), and (e) show the derived generalised MW quantities, k_2, τ_2, and η_2, respectively. The quantities were determined according to eqs. (4.42) and (4.43). (f) shows the $\log_2$ ratio of η_1 (fig. 4.11f) and η_2 (e). Red values indicate $\eta_1 > \eta_2$, white pixels indicate $\eta_1 \sim \eta_2$ and blue values indicate $\eta_1 < \eta_2$.

of the plant CW this suggests that either the glassy behaviour of the polymer network is the cause of the values measured in our experiments, which appears to be of the order of 3 GPa (Rubinstein and Colby, 2003), or that the increased stiffness comes from the contribution of the CMFs, which have a larger contribution at the shorter timescales. In fact the median of the ratio of the timescales $\tau_1/\tau_2 \approx 7.6$ is almost the same as the ratio between the frequencies, which is $\omega_2/\omega_1 \approx 6.8$. This is consistent with the behaviour of a polymeric material which displays relevant responses at almost all timescales because of the excitation of different modes of the polymer chains (Doi and Edwards, 1986). This continuity of the timescales is of course contradictory to the approach made before, that we have only discrete relevant timescales for the material relaxation. And indeed for a full mechanical spectral analysis of the CW, an investigation at continuous timescales is necessary. However, the small discrepancy between the ratios of the timescale and of the frequencies show that this approach works reasonably well. Furthermore, even at the second eigenmode the structure visible in the timescale image shows distinct properties between cell faces and cell junctions and the contrast of the positions of the anticlinal walls is enhanced as already seen for the first eigenmode. Finally, fig. 4.14e shows the viscosity, which can be related to the CW extensibility (see section 5.1). It represents a resistance to flow and its strength depends on τ_2 and k_2 and it cannot be predicted what the expectations for a higher frequency are. In the case of the *A. thaliana* hypocotyl it looks like η_1 and η_2 are very similar from its values. The ratio η_1/η_2 is shown in a logarithmic representation in fig. 4.14f. White pixels mean the ratio is one, blue pixels mean $\eta_1 < \eta_2$, and red pixels show values with $\eta_1 > \eta_2$. Interestingly, for the majority of the pixels $\eta_1 < \eta_2$ and only at the cell junctions $\eta_1 > \eta_2$ but the values are always close to a ratio of one. On the one hand, this suggests, that not only the stiffness but also the viscosity in the plant CW is stress dependent, which is somehow surprising because the viscosity in a typical fluid should not increase if already a certain force is

exerted on the material. One explaination for this might be that the viscosity arises also from the Xyloglucan (XG) cross links and as described by Dyson et al. (2012) their life-time depends on their amount of extension (eq. (1.19)). This shows that although the plant CW is treated like a viscose fluid, the viscosity originates not only from the properties of the polymer network but also from the breakage of cross-links. This is a further confirmation of the model of Dyson et al. (2012) and in general the current view of plant cell growth. On the other hand, the small deviation of the ratio from one, indicates that the extensibility of the plant CW is similar on different time- and lengthscales, which would enable steady and smooth growth across those scales.

4.9 Summary

In this chapter we introduced a theoretical framework to link the most universal linear viscoelastic model, the generalised MW model, to the cantilever observables A_1, ϕ_1, and d_0. When the relaxation time is important to describe a biological process then the underlying viscoelastic model for the material of interest is crucial to explain its behaviour accurately. We then demonstrated that this method can be applied successfully to the epidermal cells of *A. thaliana* hypocotyls. To test the underlying viscoelastic models we introduced a visual method for dynamic mechanical AFM measurements which is used to validate the viscoelastic behaviour, which the material displays. With this method we showed that at a excitation frequency of $f \approx 78\,\mathrm{kHz}$, the plant CW behaves like a SLS. We then used this knowledge to determine the quantities, which describe the SLS from the averaged values of all pixels of one scan. We further introduced a second method, which uses the spatial information of the scan, to determine the characteristic SLS quantities with spatial resolution. If we compare the values obtained from the second method with the values obtained from the fits of the average CW behaviour we get a reasonable agreement. The consistency

of the two methods enables us to obtain high resolution maps of the local relaxation timescale as well as of the local material stiffness. Finally, we can apply our technique at several frequencies; doing this we can not only obtain values for E' and E'' at the higher frequency but we can also use these measurements in combination with the lower frequency to start reconstructing the total relaxation modulus of the plant CW. Furthermore, with the higher frequency we can show that the plant CW has a similar extensibility at different timescales, which probably enables smooth and continuous growth. Additionally, we can confirm that the viscosity is influenced by how much the cross-links in the wall are stretched, which supports the theory of Dyson et al. (2012).

Part II

Biophysics of Plant Growth

In this part I aim to test the biological relevance of viscoelastic properties during plant development from a physics perspective. First, we demonstrate the universality of the Lockhart model, by deriving it for the first time from non-equilibrium thermodynamics, using the Onsager principle. In this way we show that the plant behaves like a thermodynamic system out of equilibrium. In a second step we show that viscoelastic dynamic atomic force microscopy (AFM) mapping is sensitive to different physiological conditions of the plant cell wall (CW). In particular we establish that this method is capable of quantifying mechanical differences caused by an alteration of CW composition, which can be induced by directed pharmacological interventions. Third, I show that the CW mechanics can be linked to cellular growth by the Lockhart model at different length- and timescales. Finally, I use the dynamic AFM method as an analytical tool to investigate an *A. thaliana* mutant, that exhibits an altered phenotype in the hypocotyl, caused by a disturbance in a membrane trafficking pathway.

Chapter 5

Hypocotyl Growth: Cell Wall Properties Link to Cellular Growth

The plant, like any living organism, is a thermodynamic system, that exists away from equilibrium. Therefore, it is sensible to derive a model for plant growth from non-equilibrium thermodynamics. In the past, the growth equations were derived from empirical mechanical principles, fluid dynamics, and near equilibrium thermodynamics. In this chapter, I use for the first time a more general approach, the 'Onsager principle', which applies for systems where frictional forces exceed inertia forces. Plant growth seems to be the perfect system to apply this concept because of its slow time evolution. However, it is possible that this is a good formulation for many dynamic systems in biology besides plant growth. Here we use Onsager's principle to derive Lockhart's equation. In particular we describe a growth model for a cylindrical, unidirectionally growing plant cell, using the viscoelastic properties of the wall.

5.1 Deriving the Growth Equations for Plant Growth from First Principles

The Onsager principle is a variational principle which describes dynamic thermodynamic systems out of equilibrium by the principle of minimal energy dissipation (Doi, 2016). Key features of this method are that it is derived from first principles from statistical mechanics and that its simplicity makes it a perfect approach for multiscale problems. In the past the Onsager principle was used to derive fundamental time evolution equations in physics, such as the diffusion equation, particle flow-diffusion coupling, the Smoluchowski equation, gel dynamics, and the Ericksen-Leslie equation Doi (2011).

Although Onsager's method is based on first principles, the following approximations must be fulfilled to justify its application:

(O1) $l(t)$, the variable in which time-evolution we are interested, is changing much slower than the other variables. $l(t)$ is called a slow variable and the other variables are called fast variables.

(O2) The fast variables are near equilibrium.

(O3) The relaxation time of the fast variables is much shorter than the one of the slow variables.

(O4) The slow variables change slower than the random forces, such as thermal forces.

In principle Onsager's approach is based on the concept of minimal energy dissipation, which can be expressed by the minimisation of an energy flow which is determined by the Rayleighian $\mathcal{R}$. $\mathcal{R}$ is given by the time derivative of the free energy $\mathcal{A}$, i.e. the rate change of the free energy, and by a dissipation function $\mathcal{D}$ as

$$\mathcal{R} = \frac{\partial \mathcal{A}}{\partial t} + \mathcal{D}. \tag{5.1}$$

In order to apply the Onsager principle to plant growth consider a cylindrical cell of length l and inner and outer radius r_i and r_o, respectively. In this case the wall has a thickness $d = r_o - r_i$. For such a body $\mathcal{A}$ is given by the energy of P_t pressing on the inner area of the cell. Here, we consider only a unidirectionally, along the axis of the cylinder, growing cell and thus only the two faces at the top and the bottom of the cylinder contribute to this energy, which is given by

$$\mathcal{A}_P = -\pi r_i^2 P_t l. \tag{5.2}$$

Additionally, there is a retracting force which is given by the energy of the stretched wall with an internal stress σ_w, which is written as

$$\mathcal{A}_\sigma = 2\pi dr \sigma_w l. \tag{5.3}$$

The factor $2\pi dr$ gives the cross sectional area of the wall A_w. This is given

$$\begin{aligned} A_w &= \pi \left(r_o^2 - r_i^2\right) = \pi \left(r_o - r_i\right)\left(r_o + r_i\right) \\ &= 2\pi dr. \end{aligned}$$

Notice that $d = r_o - r_i$ and the radius $r = \left(r_o + r_i\right)/2$ gives the neutral, unstressed, plane of the cylinder. From eqs. (5.2) and (5.3) we obtain

$$\mathcal{A} = \pi \left(2dr\sigma_w - r_i^2 P_t\right) l \tag{5.4}$$

$$\frac{\partial \mathcal{A}}{\partial t} = \dot{\mathcal{A}} = \pi \left(2dr\sigma_w - r_i^2 P_t\right) \dot{l}. \tag{5.5}$$

The over dots signalise time derivatives. Radial growth and changes in wall thickness can be included easily, by considering d and r as time dependent as well but for the purpose of deriving Lockhart's equation we omit that. Note that if the radial growth should be included the term for the side walls of the cylinder must be included in eq. (5.2).

$\mathcal{D}$ will be proportional to the internal viscosity η and the squared velocity $\dot{l}$, i.e. $\mathcal{D} = \Lambda\eta\dot{l}^2/2$ (Doi, 2013). Λ is a significant length scale at which energy is dissipated and has to be found for the system. It is to be expected that the energy is given by the cross section of the cell wall A_w. However, this is an area and has to be divided by a length scale. If we assume that $\eta/\Delta l$ is dissipated per length element Δl we obtain a total energy dissipation for the length of the cylinder which is proportional to η/l. The last step follows from the fact that viscose elements in series add inversely, i.e. $1/\eta_{\text{total}} = \sum_{i=1} N1/\eta_i$ and if $\eta_i = \eta_j = \eta \;\forall\; i, j$ we obtain $1/\eta_{\text{total}} = N/\eta$. With these assumptions we obtain $\Lambda = 2\pi tr/l$ and the energy dissipation is now given by

$$\mathcal{D} = -2\pi dr \frac{\eta}{2} \frac{\dot{l}^2}{l} \tag{5.6}$$

and the Rayleighian by

$$\mathcal{R} = \pi \left(2dr\sigma_w - r_i^2 P_t\right) \dot{l} + 2\pi dr \frac{\eta}{2} \frac{\dot{l}^2}{l}. \tag{5.7}$$

We minimise this function now for $\dot{l}$ and obtain

$$\frac{\partial \mathcal{R}}{\partial \dot{l}} = \pi \left(2dr\sigma_w - r_i^2 P_t\right) - 2\pi dr\eta \frac{\dot{l}}{l} \stackrel{!}{=} 0. \tag{5.8}$$

We can rewrite this as

$$\frac{1}{l}\frac{\mathrm{d}l}{\mathrm{d}t} = \frac{1}{\eta}\left(\frac{1}{2dr} r_i^2 P_t - \sigma_w\right) = \frac{r_i^2}{2dr}\frac{1}{\eta}\left(P_t - \frac{2dr}{r_i^2}\sigma_w\right).$$

If we compare this with the Lockhart equation

$$\frac{1}{l}\frac{\mathrm{d}l}{\mathrm{d}t} = \Phi\left(P_t - Y\right) \tag{5.9}$$

we find how the extensibility Φ and the yield threshold Y are related to the material properties σ_w and η

$$\Phi = \frac{r_i^2}{2dr}\frac{1}{\eta} \tag{5.10}$$

$$Y = \frac{2dr}{r_i^2}\sigma_w. \tag{5.11}$$

It is important to note that σ_w is the internal wall stress at growth equilibrium, i.e. uniform growth for the time interval Δt at which σ_w is considered. This means that before the wall yields the internal wall stress increases until the internal frictional force equals the counteracting elastic force of the material. In the simplest case the wall stress is given by a step function but a more realistic case is a sigmoid function. In general any function which saturates at the applied pressure P_t could describe

the behaviour and the exact function has to be found experimentally. However, the theoretical expression derived by Dyson et al. (2012) or by Veytsman and Cosgrove (1998), which describe the yield of the plant cell wall as a biochemically active, thermodynamic material, might be a good approach. The advantage of using this expression (eqs. (1.24) and (1.31)) is that it includes the molecular mechanism of how the cell wall resists the extension. Moreover, eqs. (5.10) and (5.11) give the same results as found by the thermodynamic approach from Veytsman and Cosgrove (1998), if $t \ll r$ (eq. (1.26)). Similarly, the extensibility is similar to the result from Veytsman and Cosgrove (1998), with the only difference that they also considered the hydraulic conductance of the wall, which could be included in the model as well. Although the final results in eqs. (5.10) and (5.11) were found previously (Veytsman and Cosgrove, 1998), the derivation from the Onsager principle has important implications. First, the successful implementation of a non-equilibrium thermodynamics approach implies that plant growth can indeed be described by this fundamental theory and hence the plant is a thermodynamic system out of equilibrium. Second, the derivation shows that the Lockhart model is valid at any timescale at which the conditions (O1) to (O4) are fulfilled.

This second implication is a very important finding, because it suggests that the application of the dynamic AFM method we introduced above, is capable of measuring viscoelastic material properties of the CW that are related to cell growth. This will be tested below.

5.2 The Effect of Cell Geometry on the Measurements of Mechanical Properties

The derivation above of the Lockhart equation and previous results, showed that plant growth is very sensitive to geometrical parameters, such as t, r, and l. Furthermore,

previous finite element modelling (FEM) simulations showed that nano-indentation experiments measure the bending modulus of the wall, which depends on cell size, rather than the Young's modulus (Hayot et al., 2012). Although our results suggest that more realistic mechanical properties are obtained (chapter 4), it is important to test how much the measurements are influenced by geometric factors.

5.2.1 Estimation of the Cell Wall Thickness

Above we derived an expression for Y and Φ, which are both strongly dependent on the geometric parameters r_i, r_o, and t. From eqs. (5.10) and (5.11) we can see that t, r_i, and r_o contribute nearly equally to the growth properties ($r_i \approx r_o \approx r$ for $t \ll r$). However, it is known that under physiological conditions r is much more stable than t Gendreau et al. (1997); Derbyshire et al. (2007) and hence the latter is the most relevant parameter as its effect is almost two orders of magnitude larger, as shown in fig. 5.1, while, for constant thickness, the radius is not changing Y and Φ by more than a factor two. Because of this and the fact that Derbyshire et al. (2007) report a changing CW thickness in the hypocotyl, we tried to find an estimate for the thickness of the wall using confocal microscopy.

We used two dyes to determine the thickness of the CW (fig. 5.2). First, we stained the cellulose with calcofluor white to determine the CW thickness directly from the full width at half maximum (FWHM) of the fluorescence peak. Second, we used the hydrophobic dye Nile red to stain the cuticle and the plasma membrane (PM)/cytosol and we measured the gap between the two with the peak to peak distance (fig. 5.2a).

It turns out that the results for the two methods are very different for thin walls, but become more similar for thicker ones (fig. 5.2b). For Nile red, we obtain a thickness of $d = 0.72\,\mu\text{m}$, $0.79\,\mu\text{m}$ and $1.50\,\mu\text{m}$ and for calcofluor white $d = 1.18\,\mu\text{m}$, $1.49\,\mu\text{m}$ and $1.55\,\mu\text{m}$ for basal, medial, and apical sections, respectively. While the values obtained by Nile red are in the expected range of $0.2\,\mu\text{m}$–$1.2\,\mu\text{m}$, this is

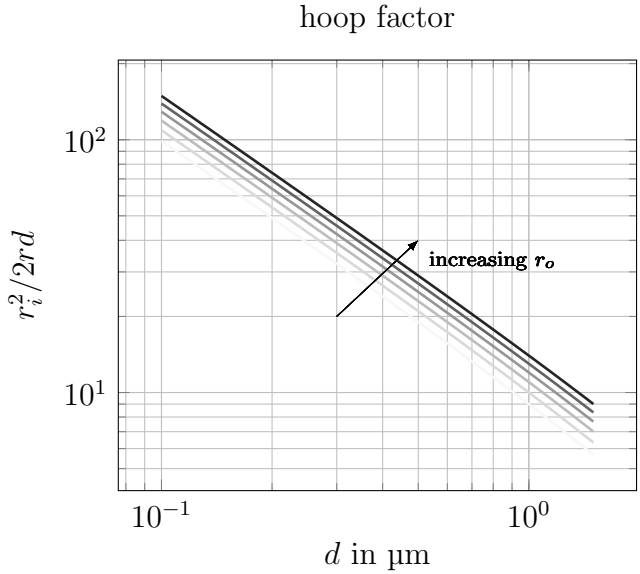


Figure 5.1: The change of the hoop factor $r_i^2/2rd$ with thickness d for a constant outer radius $r_o = 10\,\mu\text{m}$–$15\,\mu\text{m}$, with increments of $1\,\mu\text{m}$. The thickness is in the range of $d = 0.1\,\mu\text{m}$–$1.5\,\mu\text{m}$ as reported in the literature.

not the case for calcofluor white. The reason for this is that peak to peak distance is more reliable than the FWHM, which is overestimating the CW thickness if the dye is saturating or dying other compartments of the cell as well. It should be emphasised, that this is only a rough estimate, because the confocal resolution in the x-y plane is at best 200 nm but most likely a little bit worse. Furthermore, it seems that for both dyes the walls near the apical hook are very thick. This can have two reasons. First, the walls at the hook are indeed very thick, or second, the sections are not orthogonal to the cell wall extension. This is caused by the higher curvature of the cells, which makes it very difficult to find an orthogonal section. The fact, that Derbyshire et al. (2007) do not report a difference of wall thickness at different positions at the hypocotyl, but rather with age, suggests a thickness of the epidermal walls of $d \approx 800\,\text{nm}$. However, it could well be that the values obtained by the CW stain are more accurate and that the wall is thicker than $1\,\mu\text{m}$, which would be in agreement with the larger value at the apical section obtained from both measurements. Although this is not in agreement with previously reported values for wall thickness

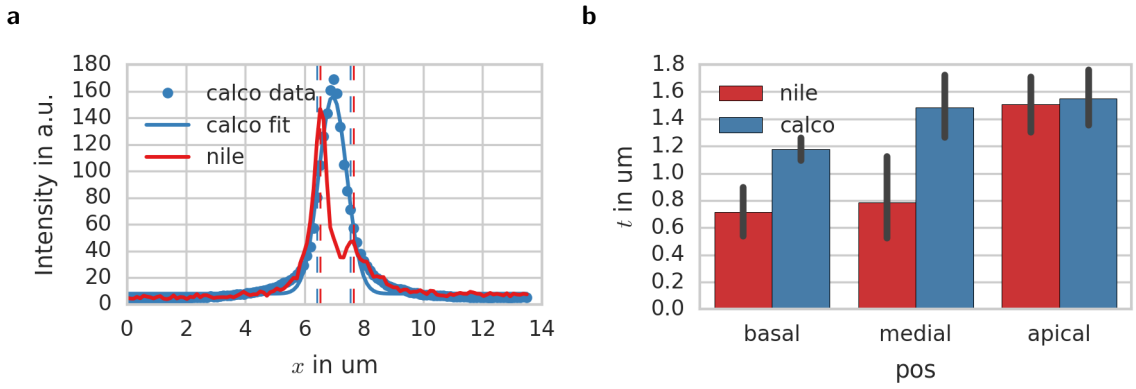


Figure 5.2: CW thickness determined by confocal microscopy. Two different methods are used to obtain the wall thickness. First, the cellulose stain calcofluor white (in blue) staining the CW directly and second, the hydrophobic stain Nile red (in red) to stain the cuticle and the PM to measure the gap between the two (for details see chapter 2). (a) shows an example profile how the CW thickness is determined by both methods. The dashed lines show the thickness obtained for this particular example. (b) shows the CW thickness for sections at different positions of the hypocotyl.

it might be possible that the sections from fixed CW material, obtained by scanning electron microscopy (SEM), underestimate the thickness. This would be the case if the CW was swelling under hydrated conditions. However, this seems unlikely as it implies that the fixed material shrinks before or after fixation. In fact values up to 1.6 µm for the CW thickness of dark grown hypocotyls were reported by Derbyshire et al. (2007), but at a different growth stage. Moreover, Derbyshire et al. (2007) only report values around 0.2 µm for older dark grown hypocotyls, which could not be detected with the CW stain. On the other hand, with the hydrophobic stain this should not be a limitation, because a gap is detected which is less dependent on the beam geometry, e.g. point spread function (PSF), than the actual width.

Although this discrepancy requires a more accurate determination of the CW thickness, this is sufficient for the crude estimate of Y possible by population averages and a deeper investigation would be beyond the scope of the thesis. Moreover, the wall thickness, estimated with the method described above, shows that the indentation during our AFM experiments is still smaller than the wall thickness. Yet, it is still

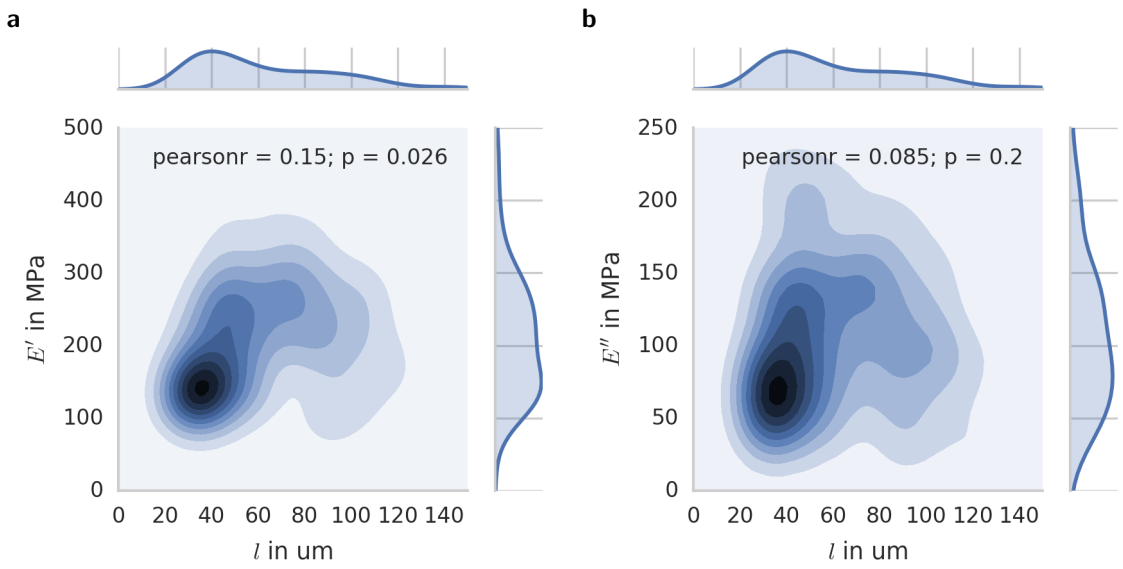


Figure 5.3: Relation between viscoelastic properties of the plant CW and cell length.

possible that the wall is bending significantly during the indentation. This implies an underestimation of E_0 and consequently, an underestimation of E'_{3D} and E''_{3D}. The one dimensional moduli E'_{1D} and E''_{1D}, however, are not affected by the bending, because their measurement takes place with small oscillations, which causes no relevant change of the state of the material.

5.2.2 Cell Length and Mechanical Properties

From the Lockhart equation it is known that growth velocity depends on cell length and therefore the mechanical properties have to change with increasing cell length to cease growth. However, the bending modulus of the CW also depends on the length of the cell and thus the question rises of how the cell length affects the measured result of the mechanical properties. This can be investigated with a very simple experiment: to measure the mechanical properties and cell lengths for different growth stages, i.e. ages or different positions, of hypocotyl cells. With the assumption that the CW thickness at a certain age is constant along much of the hypocotyl we chose to measure cells at different positions along the hypocotyl, which uses the growth gradient that

occurs along the hypocotyl (Gendreau et al., 1997; Crowell et al., 2011). In this case the hypocotyl will have cells of the same length in growing and non-growing regions, which should display different viscoelastic properties. Figure 5.3 shows E' and E'' plotted against cell length for four different seedlings at the age of 54 h. It clearly shows that the viscoelastic properties of the cells can be very different for cells of the same length. The centred maximum at $l \approx 30\,\mu\text{m}$ is caused by the distribution of cells of certain lengths along the hypocotyl. Many of the non-growing shorter, i.e. stiffer, cells are located after the apical hook and these are much more difficult to measure and therefore, more cells of this length were measured in the growing than in the non-growing regime as shown in fig. 5.3.

5.3 Determination of the Yield Threshold From Plasmolysis Experiments

So far we showed that the measurements are independent of the mechanical properties and that the dynamic AFM method is capable of measuring the material properties, that are relevant to growth. Here we want to determine the yield threshold Y from plasmolysis experiments with the assumption of a linear elastic stretching behaviour of the cell during its inflation.

With the assumption of a linear elastic CW we can replace $\sigma_w = E_{\text{eq}}\Delta l/l_0 = E_{\text{eq}}\varepsilon_0$ with an elastic modulus E_{eq} in growth equilibrium and the extension of the cell $\Delta l = l_t - l_f$ and the engineering strain $\varepsilon_0 = \Delta l/l_f$. Notice that ε_0 is the relative extension of the CW compared to equilibrium, i.e. the difference between the length of the flaccid cell l_f and the turgid cell l_t, and is assumed to be constant during growth.

The internal wall stress σ_w can now be estimated from plasmolysis experiments with the assumption that both flaccid and turgid cells follow Hooke's law. For the

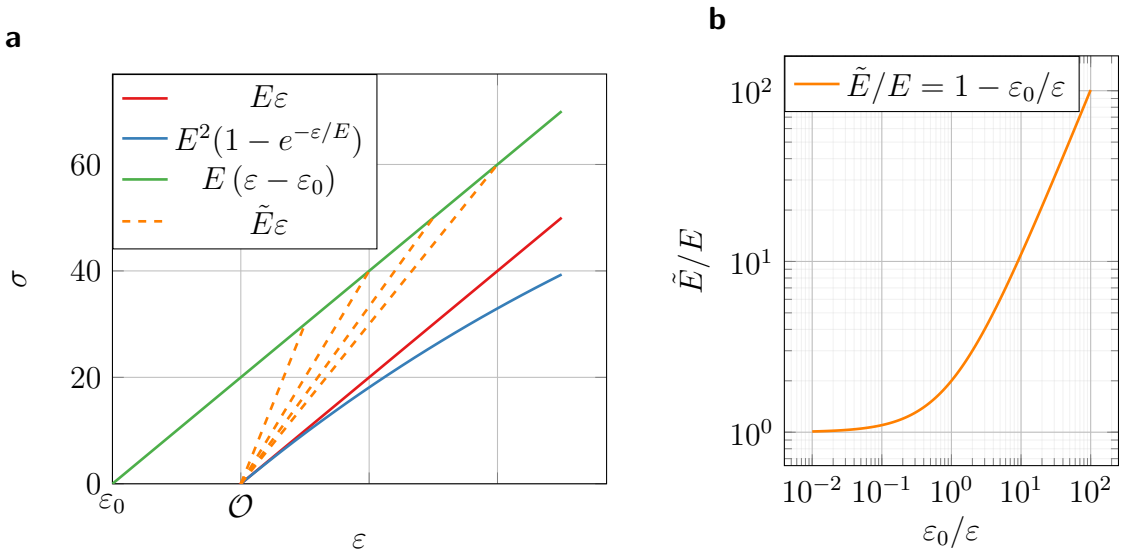


Figure 5.4: Strain stiffening for a linear elastic material. (a) shows a linear elastic material with (green) and without (red) pre-stress and a non-linear elastic material with strain softening (blue). The orange dashed lines show the stiffness obtained when the system is pre-stress but the additional stress is not taken into account. (b) shows the apparent strain stiffening for a linear elastic material if the pre-stress is not taken into account when the stiffness of the material is measured.

turgid cell, however, an offset ε_0 must be considered, caused by the tension through the turgor pressure, giving

$$\sigma_w = E(\varepsilon - \varepsilon_0). \tag{5.12}$$

In the whole derivation of the mechanical properties we have not considered any offset caused by an internal stretch of the wall and therefore we obtain a larger Young's modulus $\tilde{E}$ for the turgid cells than for the flaccid ones. The change in the modulus can be found by considering the following relation

Table 5.1: Relative extension and yield threshold for $\delta \approx 300\,\text{nm}$. The outer cell radius was assumed to be $R_o = 10\,\mu\text{m}$ and the thickness of the CW was assumed to be $t \approx 1\,\mu\text{m}$.

Wall	Zone	ε_0[%]	Y[MPa]
transverse	1	10.51	0.55
	2	5.22	0.58
	3	3.08	0.57
	4	2.78	0.82
longitudinal	1	2.15	0.07
	2	1.00	0.10
	3	1.00	0.15
	4	1.36	0.29
periclinal	1	3.15	0.06
	2	1.67	0.09
	3	1.80	0.17
	4	2.31	0.34

$$\sigma_w = E(\varepsilon - \varepsilon_0) = \tilde{E}\varepsilon$$
$$\Rightarrow \tilde{E} = E\left(1 - \frac{\varepsilon_0}{\varepsilon}\right).$$

Notice that $\varepsilon_0/\varepsilon < 0$. The offset can now be determined by

$$\varepsilon_0 = \left(1 - \frac{\tilde{E}}{E}\right)\varepsilon. \tag{5.13}$$

This is seemingly a strain softening (fig. 5.4b): the material appears to soften with increasing strain. This arises because no initial stress is considered, while in reality the increasing strain only approaches the true stiffness (fig. 5.4a), i.e. the orange lines approach the green line in fig. 5.4. Another way of strain softening is represented by the function $\sigma = E^2(1 - \exp(-\varepsilon/E))$, which leads to an actual decreasing stiffness with strain, which is given by $E(\varepsilon) = E\exp(-\varepsilon/E)$. For example the model from

Dyson et al. (2012) with the stretching dependent life time of cross-links describes a mechanistic behaviour for such a description. However, this implies energy dissipation and therefore, it is not a purely elastic model anymore.

For the indentation experiment ε can be approximated by δ/l_p, where l_p can be measured for the different zones and indentation depth δ is estimated by E' and the Sneddon contact model. With an approximated indentation of $\delta \approx 300\,\mathrm{nm}$ the relative extension caused by turgor is about $\varepsilon_0 \approx 1\,\%$–$10\,\%$ (table 5.1), which is in agreement with the literature (Hong et al., 2016). This gives an estimate for the yield threshold $Y \approx 0.06\,\mathrm{MPa}$–$0.34\,\mathrm{MPa}$, for longitudinal and periclinal walls, which is in agreement with yield threshold measurements previously reported by Cosgrove (1985). The transverse walls display a much higher value $Y \approx 0.55\,\mathrm{MPa}$–$0.82\,\mathrm{MPa}$. With a typical turgor pressure of $P_t \approx 0.5\,\mathrm{MPa}$ the longitudinal and periclinal walls are able to extend, while the transverse walls cannot grow. In fact the values for the transverse walls most likely do not represent the yield threshold, because the walls are not yielding and consequently the wall stress σ_w is not in growth equilibrium. Therefore, the estimation of Y is not valid and underestimates the true yield threshold.

5.4 Comparison of The Viscoelastic Properties of Different Cell Types

Plants consist of about 35 cell types Cosgrove (2005). These cell types serve various functions in the organism and therefore they can be expected to have different mechanical properties. In fact elastic mechanical measurements were performed on epidermal hypocotyl cells (Peaucelle et al., 2015), guard and pavement cells in leaves (Sampathkumar et al., 2014; Hayot et al., 2012), and embryonic cells in the shoot apical meristem (Milani et al., 2011; Peaucelle et al., 2011; Braybrook and Peaucelle, 2013). We show in this section a comparison between growing hypocotyl cells with

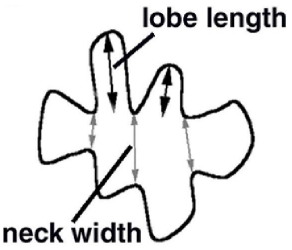


Figure 5.5: Schematic of a pavement cell (Graphic from Fu et al. (2005)).

stomatal guard cells and pavement cells in the cotyledons.

Figure 5.6a shows the topography of a typical structure of pavement cells (a schematic of this cell type is shown in fig. 5.5) from a cotyledon of a 4 d old *A. thaliana* seedling. Significant for this cell type is the jigsaw-puzzle like pattern of the cells, which created additional stress patterns at regions of concave curvature of the cell (arrowheads). These geometric stress patterns can also be seen in the viscoelastic properties E' and E'' as shown in figs. 5.6b and 5.6c respectively. In chapter 4, we discussed that these stress patterns occur in the hypocotyl cells. Furthermore, Sampathkumar et al. (2014) found with quasi-static indentation measurements that the elastic modulus at those positions is increased. This confirms the fact that the dynamic measurement is sensitive to geometrical stress as well as to actual material properties. If we compare E' and E'' from the measurements on the hypocotyl with the pavement cells, we can see that both $E' \approx (70 \pm 23)\,\mathrm{MPa}$ (Mean $\pm$ SD), and $E'' \approx (26 \pm 20)\,\mathrm{MPa}$, are about one order of magnitude smaller than at the hypocotyl and thus are two to four times larger than the values reported previously by Hayot et al. (2012) and Sampathkumar et al. (2014). Only at stressed locations near the cell junctions the values are in agreement with the ones at the hypocotyl. This could have several causes. First, it might be that at the hypocotyl we only measured regions which are under geometrical stress but this seems very unlikely because we usually measured the cells across at least half of their width and no major decrease in the mechanical properties was observed. Second, it is possible that the

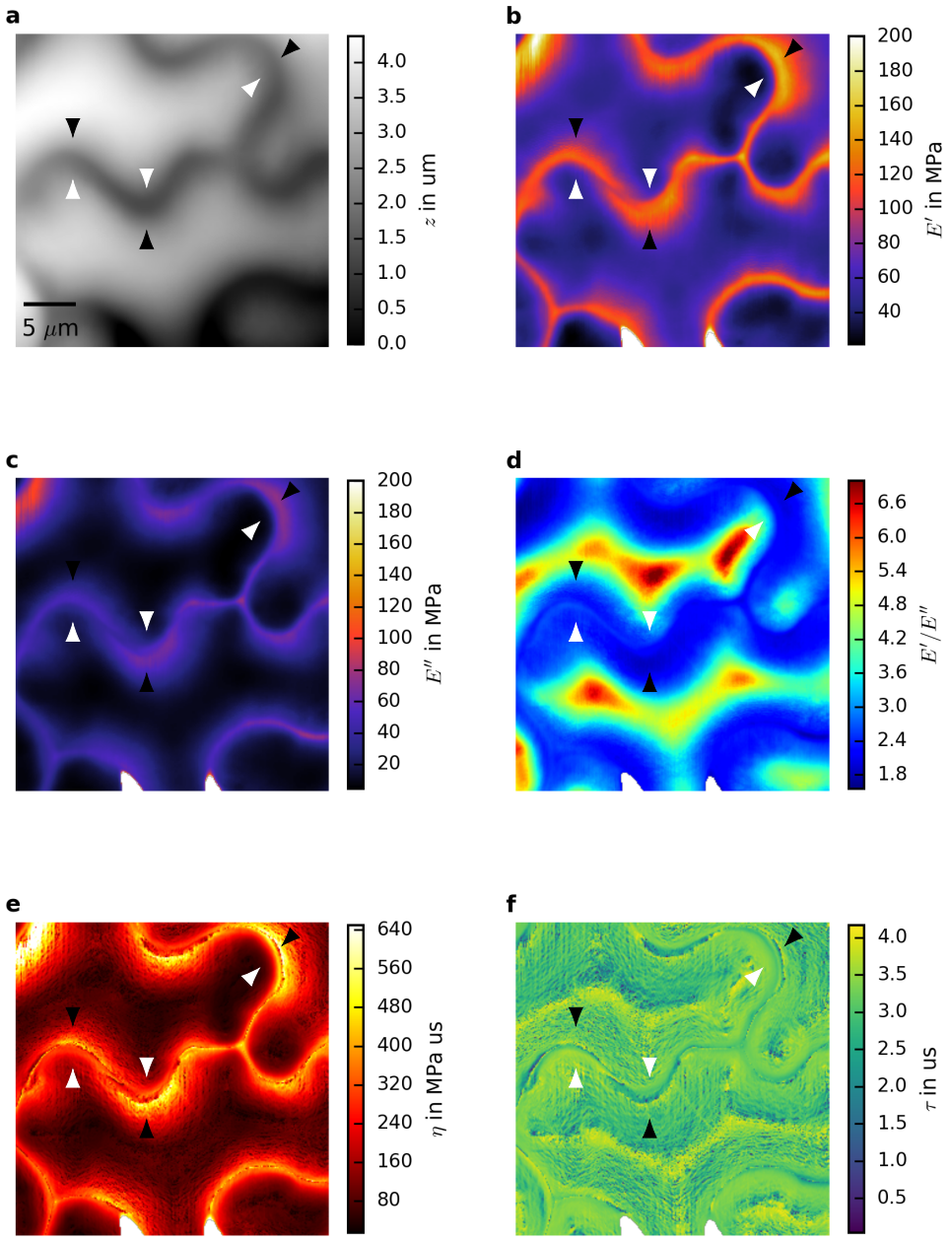


Figure 5.6: Viscoelastic properties of pavement cells. The jigsaw-puzzle patterned topography (a) shows different stress patterns at concave and convex curvatures in the storage (b) and loss (c) moduli. The inverse loss tangent (d) shows that at both concave and convex curvature display a similar elastic to viscose ratio, independently of stress patterns. The differences in viscosity (e) indicate that the viscosity depends on the amount of extension of cross-links. The homogeneous timescale (f) behaviour suggest continuous distribution of timescales as expected from polymer networks.

fast growing hypocotyl cells are under a particularly high stress. The third explanation is that, because the hypocotyl is vital for the plant, its cells need increased stability and consequently they possess both higher E' and E''. A fourth scenario is that more isotropic wall properties result in a softer CW. The reason for this could be for example that the cellulose microfibrils (CMFs) cannot be as densely packed as they can be if they were all aligned. Another interesting observation in the pavement cells is that the ratio E'/E'' is slightly increased ($(E'/E'')_{\text{hypo}} \approx 2.5 \pm 1.0$, $(E'/E'')_{\text{pavement}} \approx 3.2 \pm 1.0$, Mean $\pm$ SD) compared to the hypocotyl. Differences in development might account for this – the young cell's need to grow causes them to display a more viscose behaviour than maturer cells, which display more elastic material properties. In contrast to the individual moduli, E'/E'' is very similar at concave and convex curvatures of the cells, which suggests that the molecular behaviour at those geometrically very different positions is the same. As a reminder $E' > E''$ implies a more elastic behaviour and $E' < E''$ implies that the viscose behaviour dominates. Figure 5.6e shows the viscosity of the pavement cells. With $(176 \pm 80)\,\text{MPa}\,\mu\text{s}$ it is smaller than the one for the hypocotyl, which is $(408 \pm 180)\,\text{MPa}\,\mu\text{s}$. Yet this does not imply that the pavement cells are more extensible than the hypocotyl cells because the extensibility depends strongly on the cell geometry (section 5.1). Furthermore, the different values of the viscosity at the differently stressed positions are in agreement with the proposed behaviour, that the necks are inhibited in growth, while the lobes promote growth (Fu et al., 2005; Yang, 2008; Sampathkumar et al., 2014). With the assumption that eq. (1.19) is valid, this implies that the cross-links at the lobes are under tension and they are more relaxed at the neck positions. If we assume that all cross-links are about the same length, eq. (1.19) makes sense, because the CMF density is much higher than at the lobes as inferred from microtubule (MT) patterning (Sampathkumar et al., 2014). The reasoning is as follows: at concave curvatures the cross-links are more relaxed and therefore the viscosity is increased, i.e.

extensibility decreased. Conversely, at convex curvatures the cross-links are under tension and consequently the viscosity is decreased, i.e. extensibility increased. It should be highlighted that in this interpretation the viscosity only arises from the breakage of cross-links as described by eq. (1.19) and thus is only a measure for the resistance against plastic deformation during growth. However, the intrinsic viscosity of the polymer network cannot be explained by the behaviour of the cross-links and requires separate consideration.

Figure 5.6f shows that the relaxation time $\tau_1 \approx (3.1 \pm 0.5)\,\mu s$ of the pavement cells, which are also measured at the first eigenmode, i.e. $f_1 \approx 78\,kHz$, is very similar to the one obtained in the hypocotyl ($(2.9 \pm 0.5)\,\mu s$). This must be the case if the assumption is that the plant CW shows the response of a polymer network and consequently has almost a continuous distribution of relaxation times.

Another interesting case is that of the guard cells, which display a sophisticated mechanical mechanism. During the opening and closing procedure they can change rapidly from a flaccid to a turgid state and back. With inflation, the guard cells have to push the pavement cells away, which are always turgid and, therefore, they invade the space of the flaccid guard cells. From this consideration it can be expected that guard cells show a mechanical anisotropy between the side which faces the pore and the side which faces the pavement cells.

Figure 5.7a shows the typical topography of a pore on a cotyledon (of a 5 d old *A. thaliana* seedling), which is surrounded by two guard cells (white arrowhead for the pore and red arrowheads for the guard cells), which are embedded into pavement cells. Both the cell size of the guard cells and the cellular structure of the pavement cells suggest that these cells are not fully developed. A mature pore, including guard cells, can have a diameter of up to 30 µm, while the one presented here is only about $\sim 15\,\mu m$ in diameter. Furthermore, the shape of two small cells on the top of fig. 5.7a (black arrow heads) indicates an early developmental stage, because this pattern

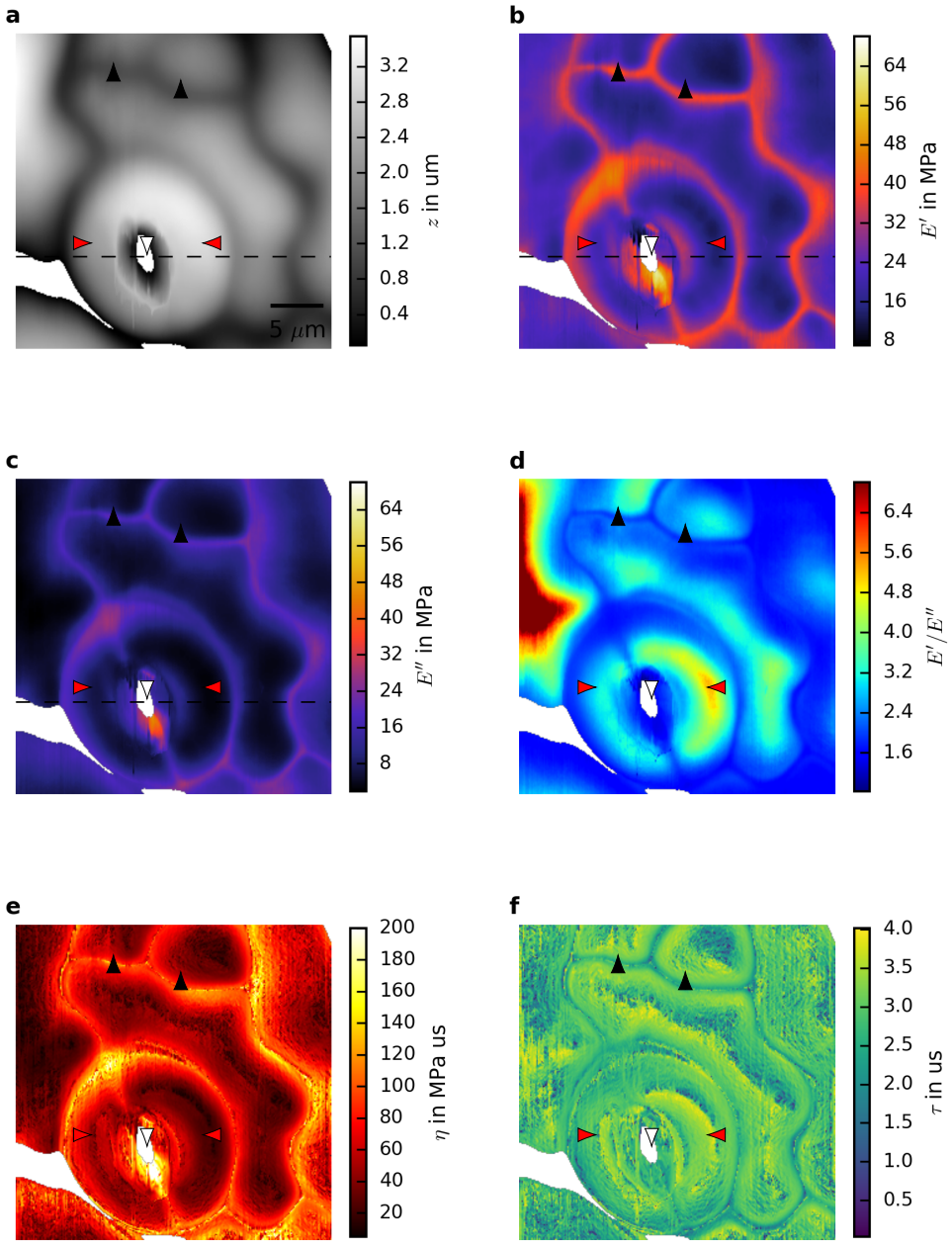


Figure 5.7: Viscoelastic properties of turgid guard cells (open pore). (a) shows the topography of a pore embedded in young pavement cells (white arrow head points to the pore and red arrowheads to the guard cells). The dashed line indicates the location of the profile which is plotted in fig. 5.8. Storage (b) and loss (c) moduli show a mechanical asymmetry between the pore inner and outer walls. The increased inverse loss tangent (d) at the apex of the guard cells suggests a particular high elasticity, which might be required for the mechanical performance of the cells. The viscosity (e) in the guard cells indicates no particular growth behaviour. The homogeneous timescale (f) behaviour indicates continuous relaxation times as it is expected from a polymer network.

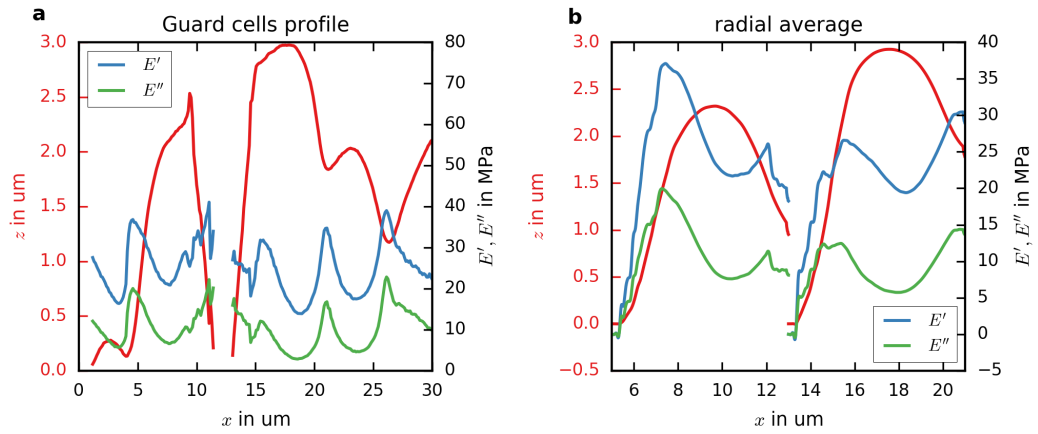


Figure 5.8: Mechanical asymmetry in guard cells. Profile of topography and dynamic moduli of the guard cells in fig. 5.7. (a) shows the profile for the dashed line in fig. 5.7. (b) shows the average profile for each guard cell with the pore being in the centre.

appears during the formation of guard cells. Indeed, E' and E'', which are shown in figs. 5.7b and 5.7c, respectively, show smaller values for the pavement cells than the ones shown in fig. 5.6. In particular the values $E' \approx (25 \pm 8)\,\mathrm{MPa}$ are surprisingly close to the values obtained previously from quasi-static ($E' \lesssim 10\,\mathrm{MPa}$) and dynamic ($E' \approx 27\,\mathrm{MPa}$–$38\,\mathrm{MPa}$) indentation experiments (Sampathkumar et al., 2014; Hayot et al., 2012). Moreover, the loss modulus here of $E'' \approx (11 \pm 7)\,\mathrm{MPa}$ is also very close to the result from Hayot et al. (2012). The differences might arise from the fact that we measured several cells with spatial resolution and averaged over all pixels, while Hayot et al. (2012) made only one measurement at the centre of each cell, and averaged over several of those measurements. Additionally, they had different growth conditions, did not use cotyledons, and performed their measurements at different frequencies and different indentation depth. Furthermore, the results from the hypocotyl suggest that our results are closer to the true material properties and, therefore, it is very likely that cotyledons are much softer than maturer leaves.

Figure 5.7d shows the ratio E'/E'', which for the presumably younger cells in this measurement is indeed smaller than for the mature pavement cells in fig. 5.6d. From the values of the E'/E'' it seems that only the cell in the upper left in fig. 5.7d seems

to be at a similar age as the cells in fig. 5.6d. These differences in E'/E'' for cells of various developmental stages suggest that this quantity is a good indicator for the growth potential of a cell. One advantage of E'/E'' is that probably all geometric contributions will be cancelled out because geometric factors are multiplicative in the same way in E' and E''. The viscosity, which is shown in fig. 5.7e, confirms the assumption that the E'/E'' is a good indicator for the growth potential because its value is $\eta \approx (62 \pm 32)\,\mathrm{MPa\,\mu s}$, which is about one order of magnitude smaller than for the older cells.

Figure 5.7f shows the relaxation time, which is $\tau \approx (2.8 \pm 0.5)\,\mu\mathrm{s}$, and is again in agreement with the previously measured relaxation times at the first eigenmode. It is very important to confirm that for every cell type at any developmental stage the relaxation time for the same experimental frequency is similar, because it confirms a nearly continuous distribution of relaxation times.

Figure 5.8 shows a profile for topography, E', and E'' from the images in fig. 5.7. From the radial average it can be clearly seen that the cells display a mechanical asymmetry (fig. 5.8b), which is in agreement with the observation of an asymmetric structure of the open cells.

5.5 Physiological Relevance of Viscoelasticity

So far we looked only at cells with an intact CW, however, it would also be interesting to use the method as a diagnostic tool and eventually test different mathematical models to unravel the thermodynamic behaviour of this intricate polymer network. To see if the technique is sensitive enough to measure changes in the CW composition, we performed chemical manipulations on the seedlings during growth.

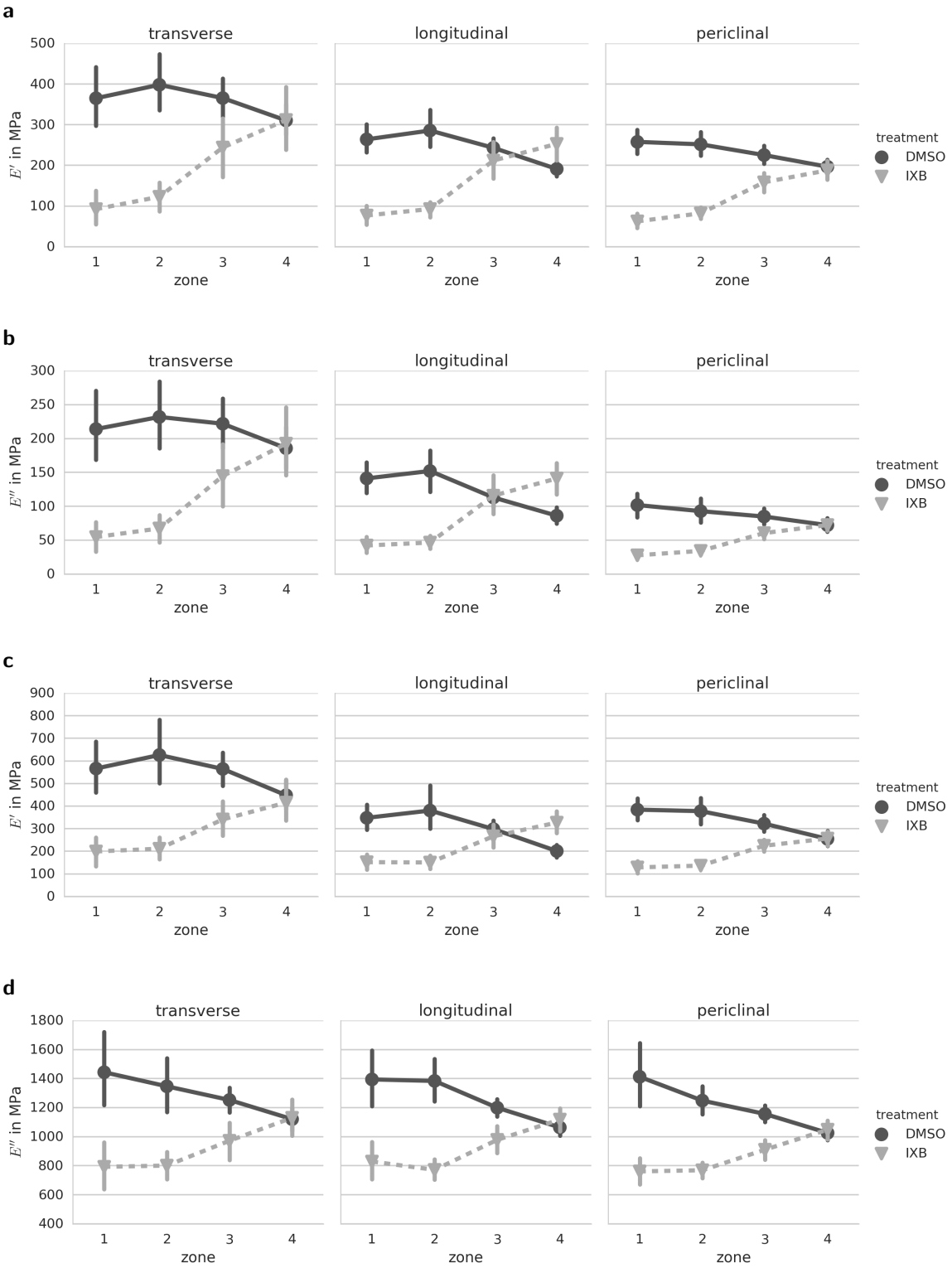


Figure 5.9: Viscoelasticity of IXB treated seedlings. Maps of storage (a) and (c) and loss (b) (d)moduli at first and second eigenmode respectively.

5.5.1 Cellulose Reduction

First we asked how the cellulose content of the CW changes its mechanical properties. To achieve this we added 3 nM isoxaben (IXB) to the growth medium on which the seedlings germinated and grew them for 3 d, as described in chapter 2. IXB inhibits cellulose synthase complexes and therefore the total amount of cellulose in the wall is reduced (Heim et al., 1990). The hypocotyls show a phenotype of severe cell swelling and reduced organ growth (fig. 2.2b). Although the phenotype reduces from the basal part towards the apex of the hypocotyl, the IXB treated seedlings do not form an apical hook. The swelling presumably originates from increased material isotropy and the more isotropic growth leads to a reduced hypocotyl length. With reduced cellulose content one would not only expect the cells to swell but also a reduction in their elastic modulus. Figure 5.9 shows E' and E'' for 9 IXB treated and 6 dimethyl sulfoxide (DMSO) treated control seedlings. The dots represent the mean values of 224 and 176 cells for treatment and control, respectively, including 77 and 58 transverse, 150 and 116 longitudinal, and 224 and 176 periclinal walls. The error bars represent the 1000 fold bootstrapped error of the mean with a 95 % confidence interval. The different zones are counted from the base (1) towards the apical hook (4) of the hypocotyl to create an average over several cells of the same seedling. Figure 5.9 shows clearly, that after IXB treatment, both E' and E'' are reduced at the basal cells and as the chemically induced phenotype becomes less pronounced towards the apex the difference between treated and control seedlings decreases.

The resulting ratios (fig. 5.10) are $E'/E'' = 1.76 \pm 0.05$, 1.92 ± 0.04 and 2.44 ± 0.05 for the IXB treatment and $E'/E'' = 1.75 \pm 0.04$, 2.15 ± 0.04 and 2.98 ± 0.07 for the DMSO seedlings at the first eigenmode. The larger ratio of the DMSO suggests that it relaxes more strongly than the IXB treated seedlings. Considering that CMFs contribute significantly to the elastic behaviour of the CW this behaviour is as expected. Similarly, at the second eigenmode we obtain $E'/E'' = 0.30 \pm 0.01$, 0.23 ± 0.01 and

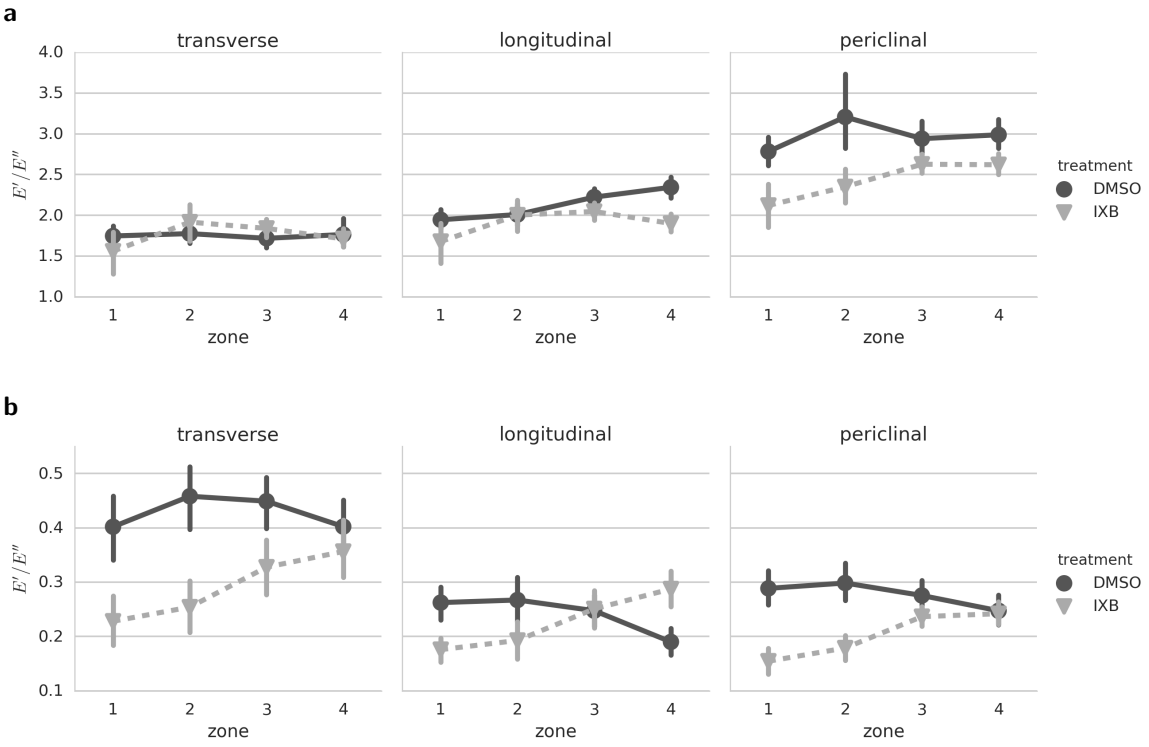


Figure 5.10: IXB treated seedlings ratio of E'/E'' for first (a) and second (b) eigenmode.

0.21 ± 0.01 for the IXB treatment and $E'/E'' = 0.43 \pm 0.01$, 0.24 ± 0.01 and 0.28 ± 0.01 for the control. The lower cellulose content of the IXB treated seedlings is consistent with the view that dissipate more energy at the second eigenmode, i.e. $(E'/E'')_{\mathrm{IXB}} < (E'/E'')_{\mathrm{DMSO}}$ as this we believe measures the properties of the CMF component of the wall.

One important question is how the viscosity of the wall changes in response to IXB. This is because IXB influences not only the cellulose content but also changes the amount of rhamnose, mannose, and uronic acids (Manfield et al., 2004). The viscosity is shown in fig. 5.11 and it is at the first eigenmode $\eta = (643 \pm 65)\,\mathrm{MPa\,\mu s}$, $(506 \pm 34)\,\mathrm{MPa\,\mu s}$ and $(336 \pm 16)\,\mathrm{MPa\,\mu s}$ for IXB and for the control seedlings $\eta = (1166 \pm 54)\,\mathrm{MPa\,\mu s}$, $(704 \pm 28)\,\mathrm{MPa\,\mu s}$ and $(585 \pm 22)\,\mathrm{MPa\,\mu s}$ and at the second eigenmode $\eta = (970 \pm 50)\,\mathrm{MPa\,\mu s}$, $(899 \pm 34)\,\mathrm{MPa\,\mu s}$ and $(811 \pm 21)\,\mathrm{MPa\,\mu s}$ for IXB and $\eta = (1425 \pm 52)\,\mathrm{MPa\,\mu s}$, $(1270 \pm 41)\,\mathrm{MPa\,\mu s}$ and $(1152 \pm 27)\,\mathrm{MPa\,\mu s}$ for the DMSO.

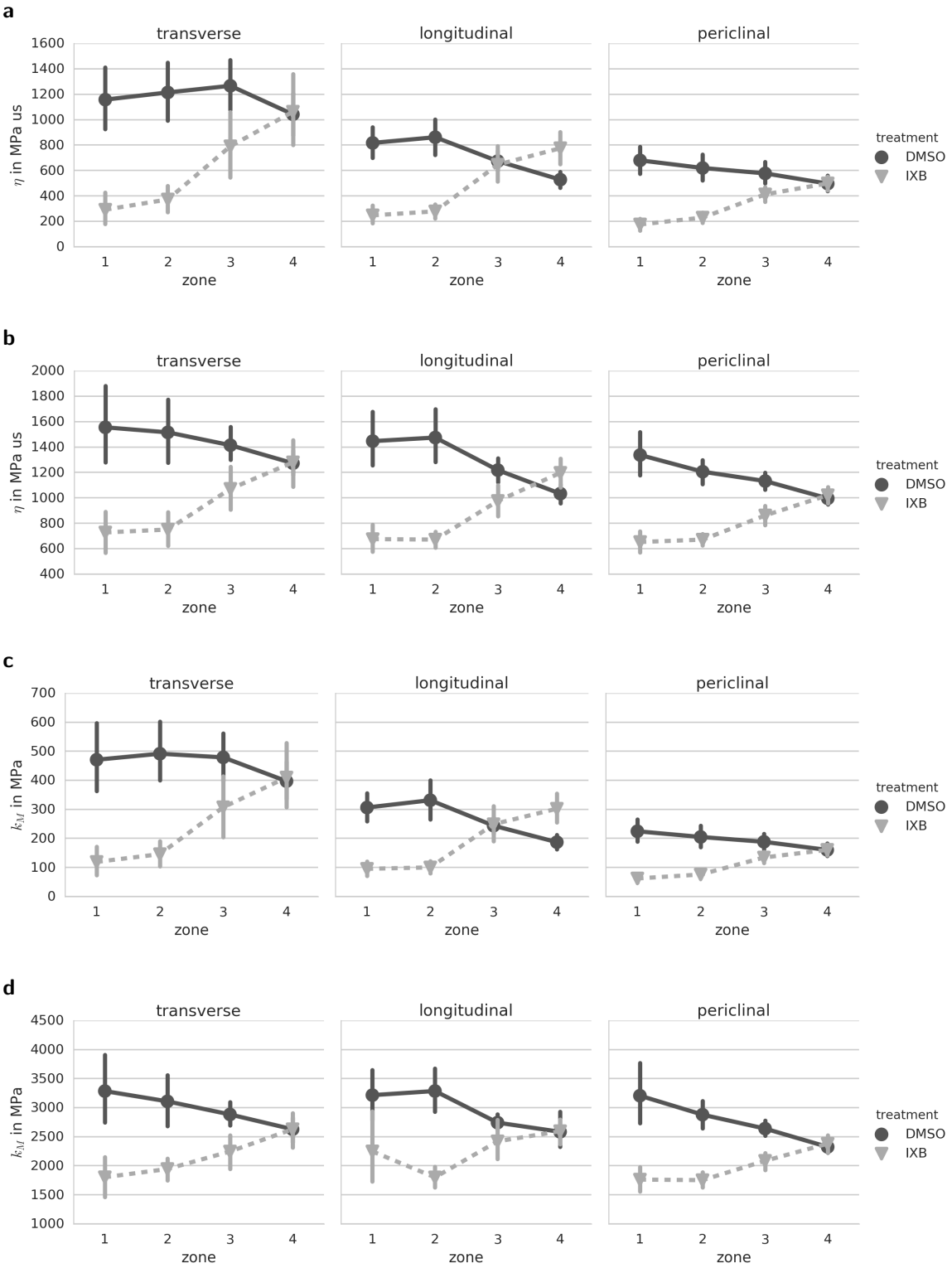


Figure 5.11: Effect of IXB treatment η viscosity of treated seedlings for first (a) and second (b) eigenmode as well as local elasticity k_{M} for first (c) and second (d) eigenmode.

The lower values for the IXB treated seedlings at both eigenmodes are in agreement with the hypothesis that the CMFs make a major contribution to the elasticity of the plant CW. While it may seem counter-intuitive that if the viscosity is related to cell extensibility, the smaller IXB treated seedlings have a smaller viscosity, these cells are more swollen than the DMSO ones and could indeed have an increased extensibility. In fact, Manfield et al. (2004) found that in cell suspension both the total cell size and the wall thickness increases with IXB treatment, where the latter influences the extensibility as well as the viscosity (eq. (5.10)). With the assumption that the CW of suspension cells behave similarly those of *A. thaliana* hypocotyl cells, this result makes sense. Additionally, there is experimental and theoretical evidence that reduced cellulose content indeed causes an increased extensibility (Ali and Traas, 2016), this is equivalent to a decreased viscosity.

The last component of the standard-linear solid (SLS) model is k_{M}, which should decrease, because of the cellulose deficiency. Indeed, the stiffness shows exactly this behaviour with $k_{\mathrm{M}} = (251 \pm 26)\,\mathrm{MPa}$, $(194 \pm 14)\,\mathrm{MPa}$ and $(110 \pm 5)\,\mathrm{MPa}$ for IXB and $k_{\mathrm{M}} = (456 \pm 24)\,\mathrm{MPa}$, $(260 \pm 12)\,\mathrm{MPa}$ and $(191 \pm 8)\,\mathrm{MPa}$ for the DMSO at the first eigenmode. Furthermore, the convergence towards the apex is in agreement with the macroscopic behaviour, where the phenotype is less severe at the apex than that at the base. At the second eigenmode the stiffness is $k_{\mathrm{M}} = (2171 \pm 82)\,\mathrm{MPa}$, $(2286 \pm 94)\,\mathrm{MPa}$ and $(2010 \pm 45)\,\mathrm{MPa}$ for the reduced cellulose content and $k_{\mathrm{M}} = (2942 \pm 99)\,\mathrm{MPa}$, $(2919 \pm 88)\,\mathrm{MPa}$ and $(2722 \pm 70)\,\mathrm{MPa}$ for the control seedlings at the second eigenmode. The difference for this higher frequency is clearer than for the first eigenmode, which supports the hypothesis that the higher eigenmode probes stiffer, more crystalline, structures, such as the CMFs. This does not exclude the hypothesis that the second eigenmode displays the glassy behaviour of the polymer network, because in IXB treated seedlings not only the cellulose content but also the glucan content is reduced (Manfield et al., 2004) and, therefore, there is certainly an

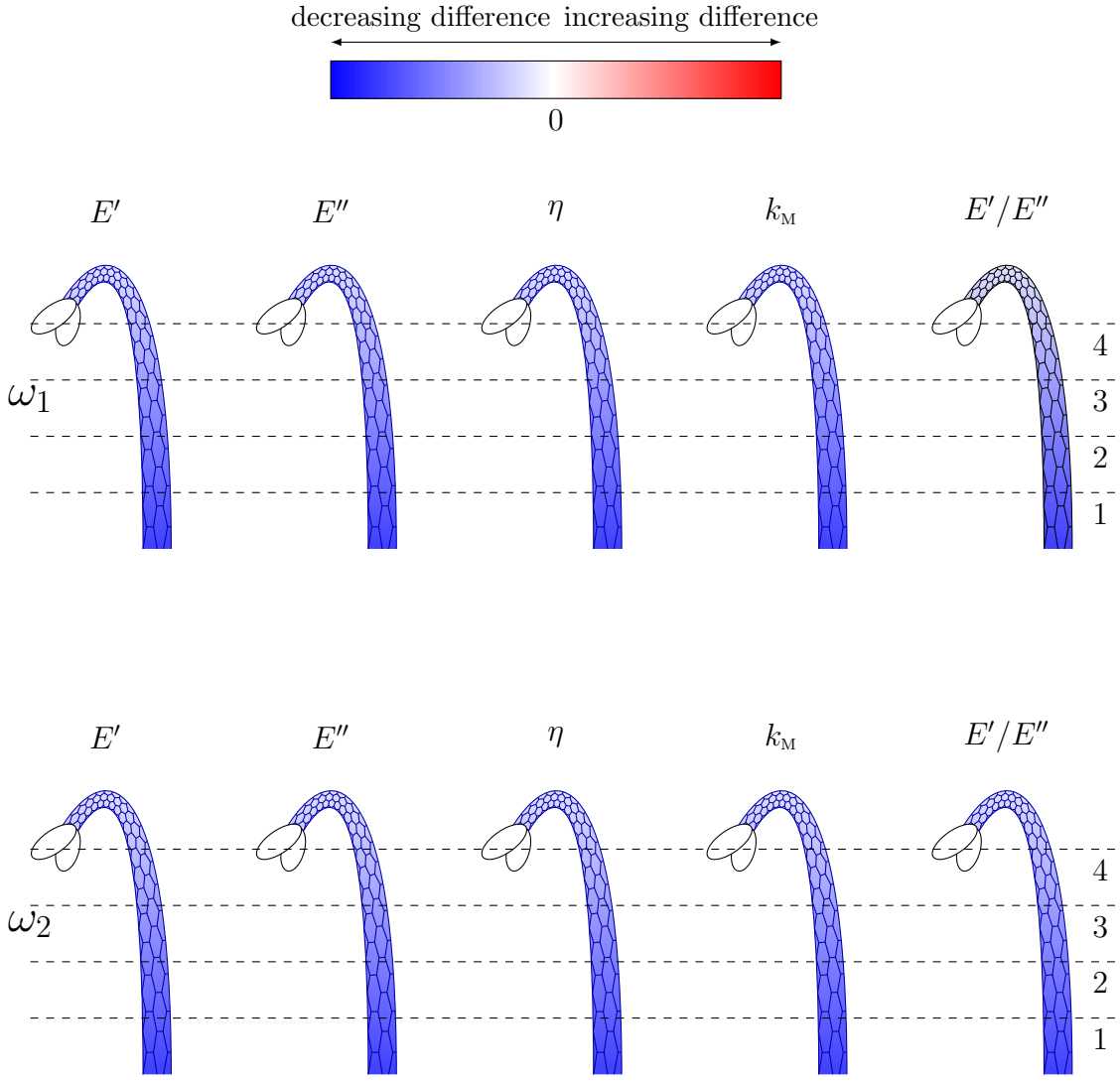


Figure 5.12: Differences between IXB treated seedlings with respect to the wild type. After IXB treatment all viscoelastic properties are reduced for both eigenmodes. The colour gradient indicates that the reduction is less severe closer to the apex. The blue colour represents a reduction of the properties, while a red colour would show an increase of the properties. White indicates no significant changes. The black radial walls indicate no changes in the properties.

alteration of the matrix.

In summary, the reduction of cellulose leads to an increased isotropy and all mechanical properties shown in figs. 5.9 to 5.11 are decreased as summarised in fig. 5.12.

5.5.2 Pectin Matrix Alteration

Next, we looked at the contribution of the integrity of the pectin matrix. This polymer network can be strengthened by ionic Ca^{2+} cross-links, which bind at demethylesterified positions of the homogalacturonan (HG) backbone. The activity of pectin methyl esterases (PMEs) can be inhibited by the green tea extract epicatechin gallate (ECG) (Lewis et al., 2008). The reduced cross-link density with decreasing PME activity is thought to lead to softening of the plant (Pelloux et al., 2007). This hypothesis is challenged by the findings of Milani et al. (2011), Peaucelle et al. (2011), Braybrook et al. (2012) and Peaucelle et al. (2015), where the last authors found that PMEs are involved in breaking the mechanical symmetry of embryonic cells in the *A. thaliana* hypocotyl. The other authors found reduced organ initiation in the shoot apical meristem (SAM), caused by wall stiffening. They used quasi-static AFM nano-indentation experiments to measure the CW mechanical properties and found that reduced PME activity leads to a stiffening of the walls. For this unexpected behaviour they provide several explanations. First, they argue that demethylesterification does not necessarily result in a more cross-linked network because the cross-linking density depends on the Ca^{2+} concentration which is unknown in the apoplast, the extracellular domain. Second, they suggest that demethylesterification could result in increased acidification in the apoplast, which in turn would activate cell wall loosening agents. Third, demethylesterification supports pectin degradation which could decrease the elastic modulus. Last, the hydrolysis of HG might generate oligogalacturonides (OGAs), which are known to act as messengers and thus might modify the CW.

Here we tested how the viscoelastic properties will change in response to a sup-

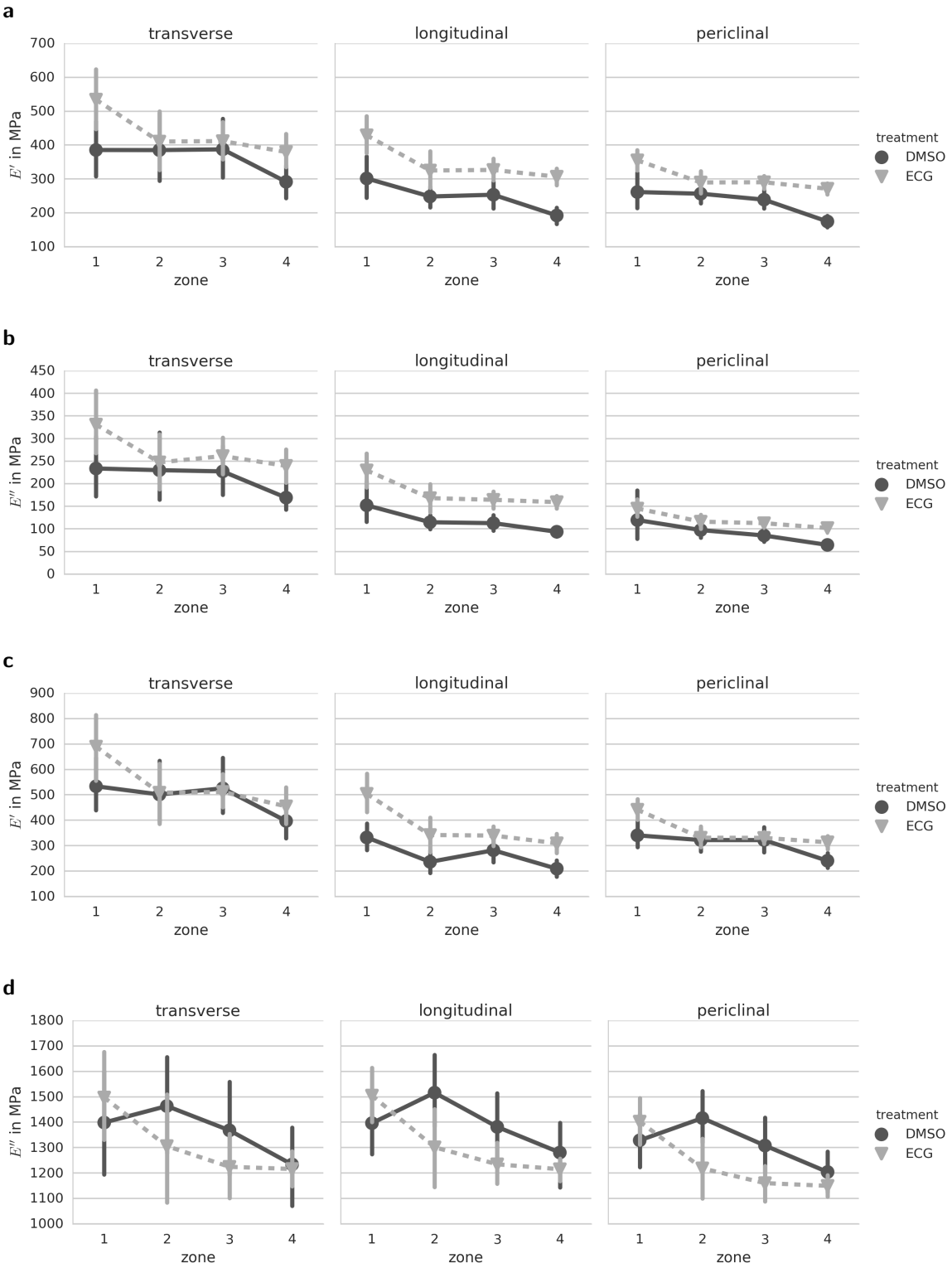


Figure 5.13: Viscoelasticity of ECG treated seedlings. Maps of storage (a) and (c) and loss (b) (d)moduli at first and second eigenmode respectively.

pressed PME activity. To obtain a biologically significant aberrant phenotype we germinated the seedlings on growth medium with 200 µM ECG and measured the seedlings 3 d after transfer to the culture room. The treated seedlings showed reduced growth in both root and hypocotyl (fig. 2.2c). The AFM measurements were performed at the first and second eigenmode simultaneously to obtain different time responses. Furthermore, during the penetration at the second eigenmode we observed an increased viscosity (chapter 4), which one would expect to change if the cross-linking density in the matrix is reduced because the entropic component of the viscosity increases due to longer free, non cross-linked, chains.

Figure 5.13 shows E' and E'' for the first (a and b) and second (c and d) eigenmode. The different zones represent again a summary over cells in a certain growth region, as for the IXB treatment. For the first eigenmode we observed increased values for the ECG treatment for both moduli E' and E''. From 8 (74 transverse, 156 longitudinal, 213 periclinal walls, of 213 cells) ECG treated and 8 (63 transverse, 128 longitudinal, 197 periclinal walls, of 197 cells) DMSO control seedlings we obtain $E' = (431 \pm 19)$ MPa, (345 ± 11) MPa and (299 ± 7) MPa (Mean ± SE) and $E' = (362 \pm 22)$ MPa, (250 ± 12) MPa and (231 ± 9) MPa, respectively, and $E'' = (268 \pm 14)$ MPa, (179 ± 7) MPa and (117 ± 4) MPa and $E'' = (215 \pm 15)$ MPa, (119 ± 7) MPa and (91 ± 8) MPa for ECG and DMSO respectively. For both moduli we obtain a main effect with $p < 0.001$ calculated by a multivariate analysis (see chapter 2 for details). If we look at the second eigenmode we see an increase relative to the first eigenmode in E' for both treated and control plants to $E'_{\mathrm{ECG}} = (536 \pm 27)$ MPa, (370 ± 15) MPa and (350 ± 9) MPa and $E'_{\mathrm{DMSO}} = (489 \pm 27)$ MPa, (266 ± 12) MPa and (305 ± 12) MPa as expected but also E'' increases significantly to $E''_{\mathrm{ECG}} = (1305 \pm 39)$ MPa, (1307 ± 27) MPa and (1225 ± 22) MPa and $E''_{\mathrm{DMSO}} = (1362 \pm 48)$ MPa, (1392 ± 35) MPa and (1310 ± 27) MPa. This is the type of behaviour which was observed for the DMSO in chapter 4. The question now arises

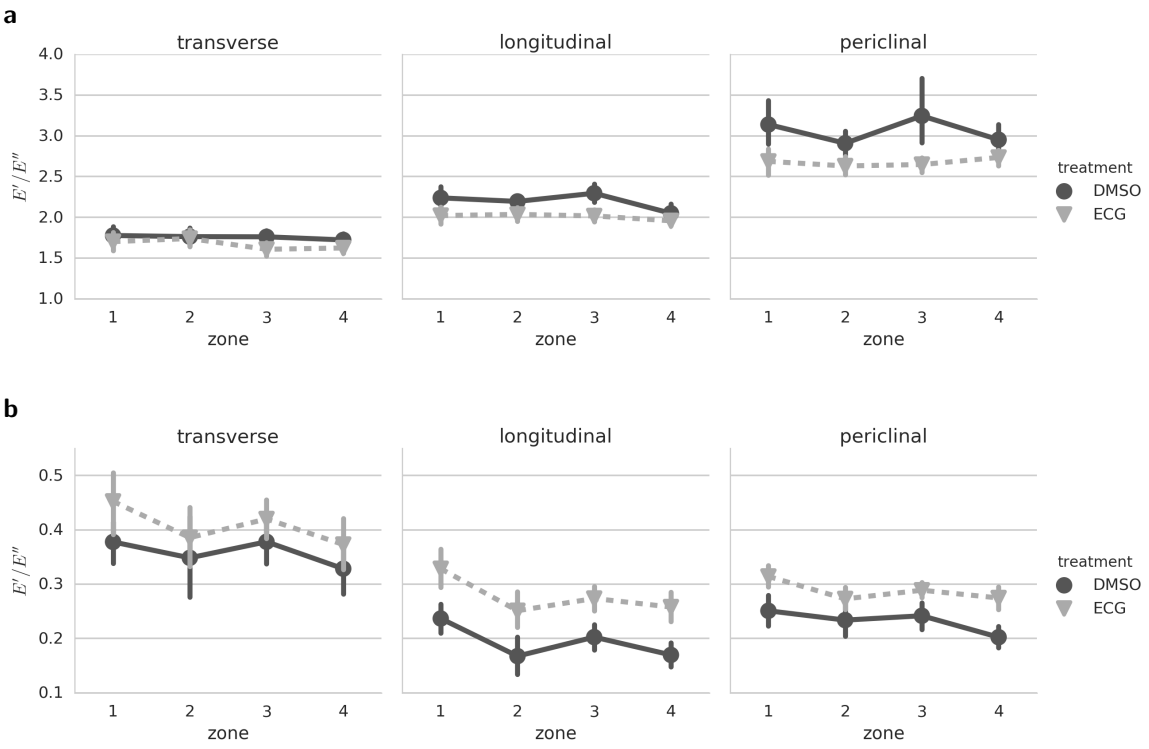


Figure 5.14: ECG treated seedlings ratio of E'/E'' for first (a) and second (b) eigenmode.

about the relation between stored and dissipated energy, which is given by the ratio E'/E''.

Figure 5.14 shows E'/E'' for the first and second eigenmode. The values for the first eigenmode (Mean $\pm$ SE) for treated seedlings are $E'/E'' = 1.67 \pm 0.02$, 2.01 ± 0.02 and 2.68 ± 0.03, while the values for the control seedlings are 1.76 ± 0.03, 2.20 ± 0.03 and 3.07 ± 0.07, for transverse, longitudinal, and periclinal walls, respectively, with a main effect where $p < 0.05$. For the second eigenmode for the treated seedlings we obtain 0.41 ± 0.01, 0.28 ± 0.01 and 0.290 ± 0.004 and for the controls we get 0.36 ± 0.01, 0.20 ± 0.01 and 0.23 ± 0.01, with a main effect where $p < 0.001$. This shows two interesting outcomes. First, the DMSO shows a more elastic behaviour at the first eigenmode ($(E'/E'')_{\mathrm{DMSO}} > (E'/E'')_{\mathrm{ECG}}$). Higher elasticity can be explained by an increased cross-linking density eq. (1.11) and thus the data suggests that the matrix of the DMSO treated seedlings may have a higher cross-linking den-

sity than the ECG treated ones. At the second eigenmode we see for both treatments $E' < E''$ suggesting that more cross-links break than recover their position. Interestingly, there is a change in behaviour between the different treatments. While at the first eigenmode $(E'/E'')_{\mathrm{DMSO}} > (E'/E'')_{\mathrm{ECG}}$, at the second eigenmode we observe $(E'/E'')_{\mathrm{DMSO}} < (E'/E'')_{\mathrm{ECG}}$. This suggests that more cross-links break down with an excitation at the second eigenmode for DMSO compared to ECG treatment, which is a consistent result, given the fact that the cross-linking density is increased for the untreated seedlings. However, this result also suggests that the treated CW is less extensible than the untreated one, because more cross-links can break in the DMSO, which gives more ability to control permanent deformation. This is indeed what we observe macroscopically and it supports the notion that $E'/E'' < 1$ gives an indication of CW extensibility.

Given the above, it makes sense to look at the viscosity, which is related to the cell extensibility, derived by eq. (4.43), which is shown in fig. 5.15. Here we find for the first eigenmode that the ECG treated seedlings indeed display a higher viscosity than the DMSO intervention, namely $\eta_{\mathrm{ECG}} = (1399 \pm 67)\,\mathrm{MPa\,\mu s}$, $(1019 \pm 34)\,\mathrm{MPa\,\mu s}$ and $(793 \pm 23)\,\mathrm{MPa\,\mu s}$ and $\eta_{\mathrm{DMSO}} = (1154 \pm 73)$, (729 ± 39) and $(587 \pm 36)\,\mathrm{MPa\,\mu s}$, for transverse, longitudinal, and periclinal walls respectively. This is in agreement with the smaller extensibility of the ECG treated seedlings, confirming that the microscopic measurements are in agreement with the macroscopic behaviour. At the second eigenmode the viscosity is slightly increased for the treated seedlings $\eta_{\mathrm{ECG}} = (1565 \pm 55)\,\mathrm{MPa\,\mu s}$, $(1428 \pm 34)\,\mathrm{MPa\,\mu s}$ and $(1297 \pm 24)\,\mathrm{MPa\,\mu s}$ compared to the untreated ones $\eta_{\mathrm{DMSO}} = (1583 \pm 62)\,\mathrm{MPa\,\mu s}$, $(1311 \pm 36)\,\mathrm{MPa\,\mu s}$ and $(1234 \pm 27)\,\mathrm{MPa\,\mu s}$. This increase of the viscosity in both moduli is similar for treated and DMSO plants and therefore suggests that the methyl esterified CWs have a smaller extensibility than the DMSO.

The next parameter of interest is the stiffness k_{M}, which is shown for the first

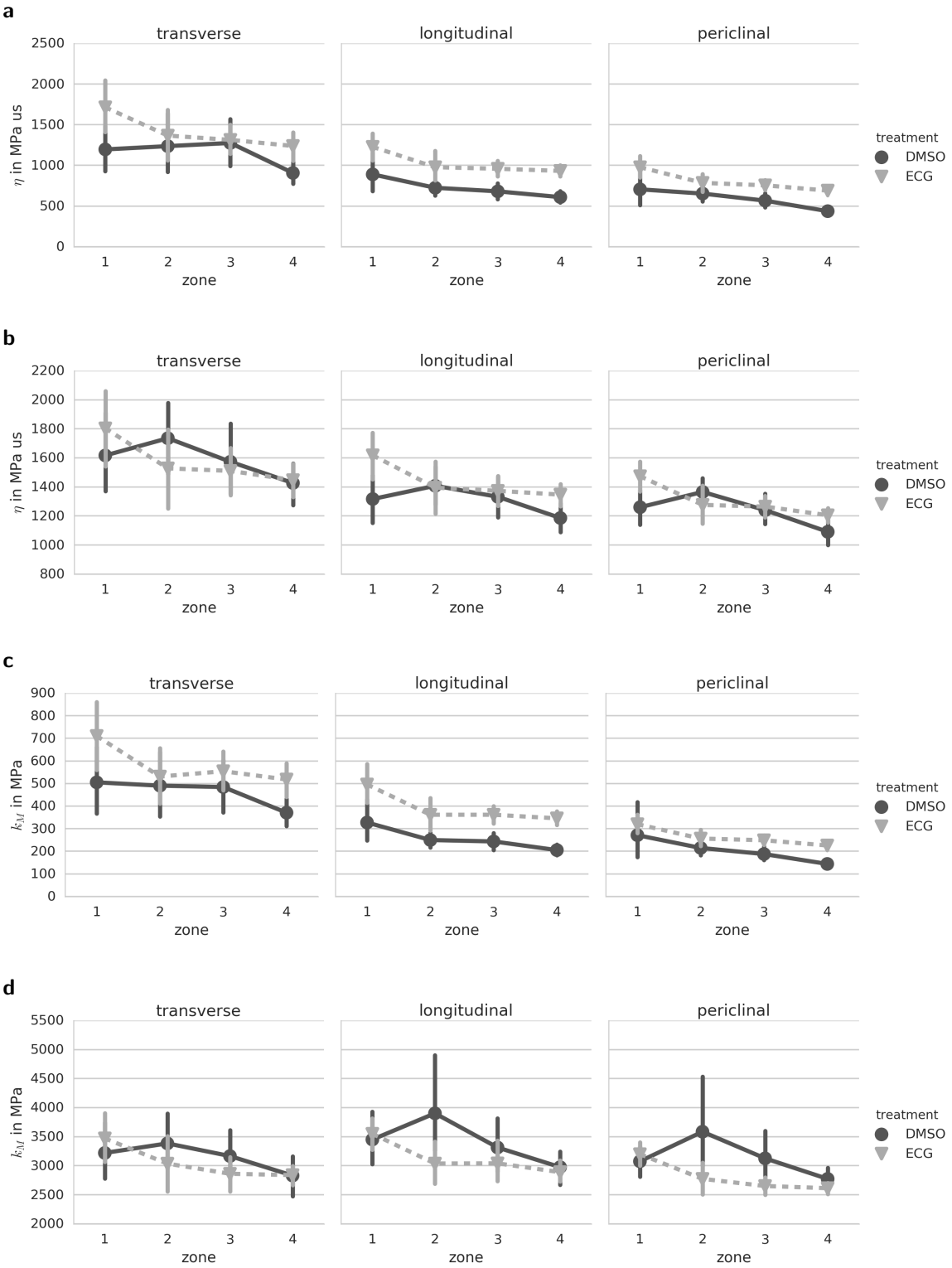


Figure 5.15: ECG η viscosity of treated seedlings for first (a) and second (b) eigenmode as well as local elasticity k_{M} for first (c) and second (d) eigenmode.

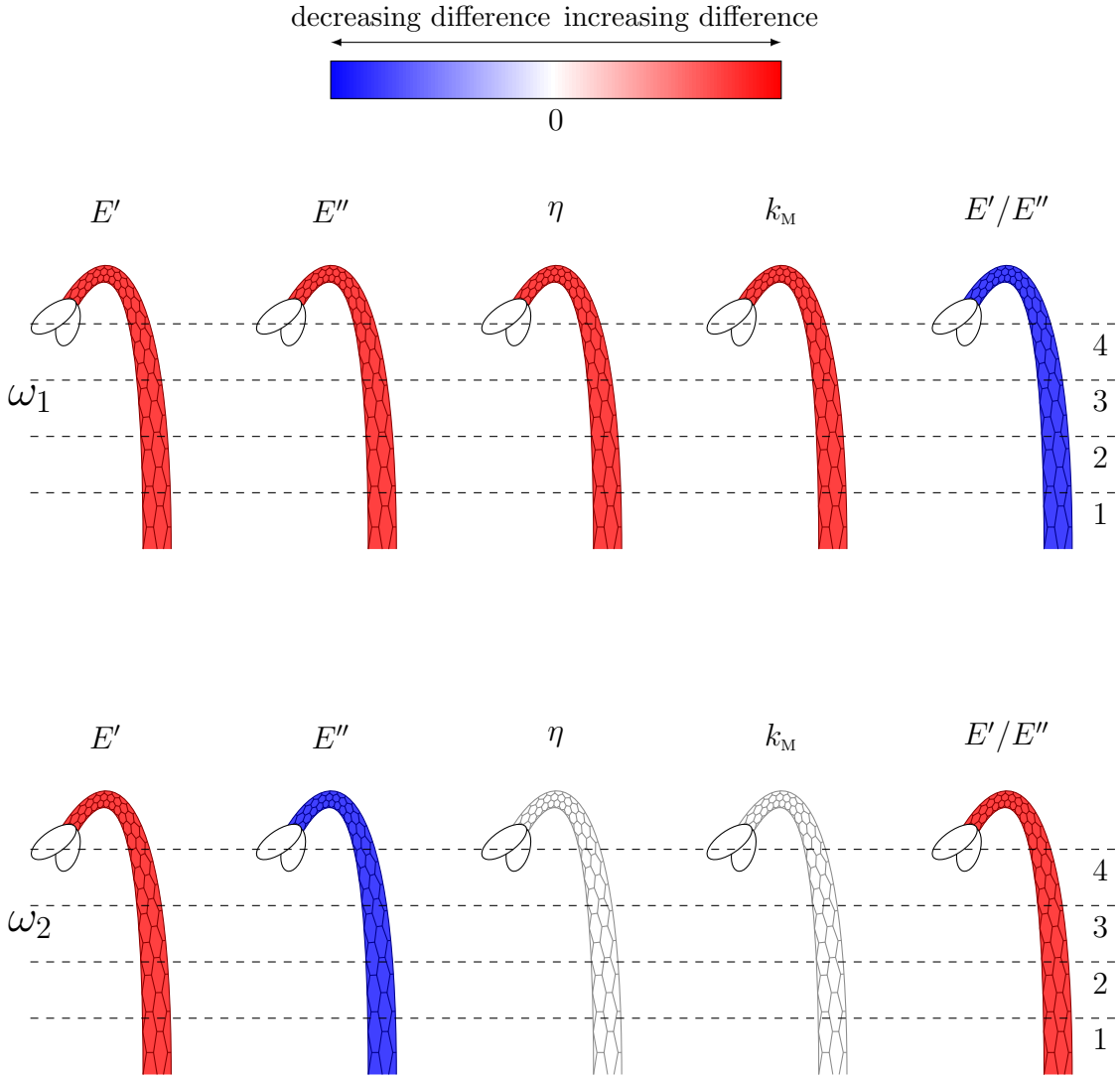


Figure 5.16: Mechanical differences of ECG treated seedlings with respect to the wild type. After ECG treatment most viscoelastic properties are increased for the first eigenmode. The blue colour represents a reduction of the properties, while a red colour would show an increase of the properties. White indicates no significant changes of the properties.

and second eigenmode in fig. 5.15 (c and d for first and second eigenmode respectively). What changes can be expected from the demethylation? On the one hand, the stiffness should be decreased with an decreased cross-linking density in the presence of ECG, because from rubber elasticity we obtain that the shear modulus is $G = nkT/V = \rho RT/M$ (eq. (1.11) and Rubinstein and Colby (2003)). On the other hand, the phantom network model gives a shear modulus $G_{ph} = RT\rho/M(1 - 2/f)$ (eq. (1.12)). This implies that cross-links with high coordination number f, such as the pectin in the demethylesterified state approach the rubber elasticity and networks with smaller f appear softer. (As a reminder for the reader, the model for rubber elasticity implies spatially fixed cross-links and a polymer chain is considered a polymer between the cross-links. The phantom network model also considers a polymer chain between nodes but cross-links can move in space and, therefore, the coordination number reduces the effective stiffness of the individual chains.) Furthermore, demethylesterified HG is also targeted by pectin degrading enzymes (Pelloux et al., 2007) which can lead to shorter chains. *In vitro* rheological studies of HG show indeed, that acetyl and methyl groups hinder its dimerization (Ralet et al., 2003; Hocq et al., 2017; Oosterveld et al., 2000). According to the worm-like chain (WLC) (Rubinstein and Colby, 2003) model shorter chains appear stiffer for the same absolute extension and, therefore, it might well be that the wall becomes stiffer. The values for k_{M} for the treated seedlings are $k_{\mathrm{M}} = (575 \pm 30)\,\mathrm{MPa}$, $(389 \pm 16)\,\mathrm{MPa}$ and $(260 \pm 8)\,\mathrm{MPa}$, which is an increase compared to the DMSO with $k_{\mathrm{M}} = (462 \pm 33)\,\mathrm{MPa}$, $(258 \pm 15)\,\mathrm{MPa}$ and $(203 \pm 18)\,\mathrm{MPa}$. This indicates that the pectin matrix behaves like a phantom network model. Alternatively, it could represent simple rubber elasticity if, with a reduction in PMEs, the absolute chain length of HG reduces. For the second eigenmode we observe $k_{\mathrm{M}} = (3038 \pm 93)\,\mathrm{MPa}$, $(3117 \pm 79)\,\mathrm{MPa}$ and $(2791 \pm 49)\,\mathrm{MPa}$ for the ECG treated seedlings and $k_{\mathrm{M}} = (3143 \pm 111)\,\mathrm{MPa}$, $(3407 \pm 141)\,\mathrm{MPa}$ and $(3123 \pm 121)\,\mathrm{MPa}$ for the DMSO seedlings. The difference between ECG and DMSO

is not significant ($p > 0.05$) and therefore, suggests a similar behaviour at short length scales. Whether this is due to the CMFs or to glassy behaviour is not clear yet.

To conclude, an alteration of the pectin matrix results in an increase of most mechanical properties shown in and all mechanical properties shown in figs. 5.13 to 5.15 at the first eigenmode. However, a characteristic behaviour for matrix alteration could be the fact that the ratio E'/E'' is decreased at the first and increased at the second eigenmode, suggesting a characteristic timescale and therefore length-scale response. The results of the ECG treatment are summarised in fig. 5.16.

5.6 The Relation Between Plant Growth And Viscoelastic Properties

Above we show that the dynamic mechanical AFM measurements are sensitive to the composition of important CW polysaccharides and that the response is different for an alteration of the matrix polymers than for a change of the load bearing components. With this potential we want to look how mechanical properties change for various growth stages. To test this, the *A. thaliana* hypocotyl is an ideal test organ, because it displays a growth gradient from the base towards the apex (Gendreau et al., 1997; Crowell et al., 2011).

Figure 5.17a shows the normalised inverse growth velocity, of 60 h old *A. thaliana* hypocotyls, which was obtained from the cell length in Gendreau et al. (1997). This can be compared to the viscoelastic properties, namely, E', E'', the inverse loss tangent E'/E'', η, and k_{M}, which are shown in Figure 5.17. The graphs show clearly that the mechanical values are inversely related to the growth velocity. The faster the growth (zone 1 is the fastest) the softer the material and conversely, slower growth correlates with stiffer material properties (zone 4 displays the slowest growth). In section 5.1 we show that for the Lockhart model $1/\eta \propto \Phi \propto \frac{\mathrm{d}l}{\mathrm{d}t}/l$. With this finding

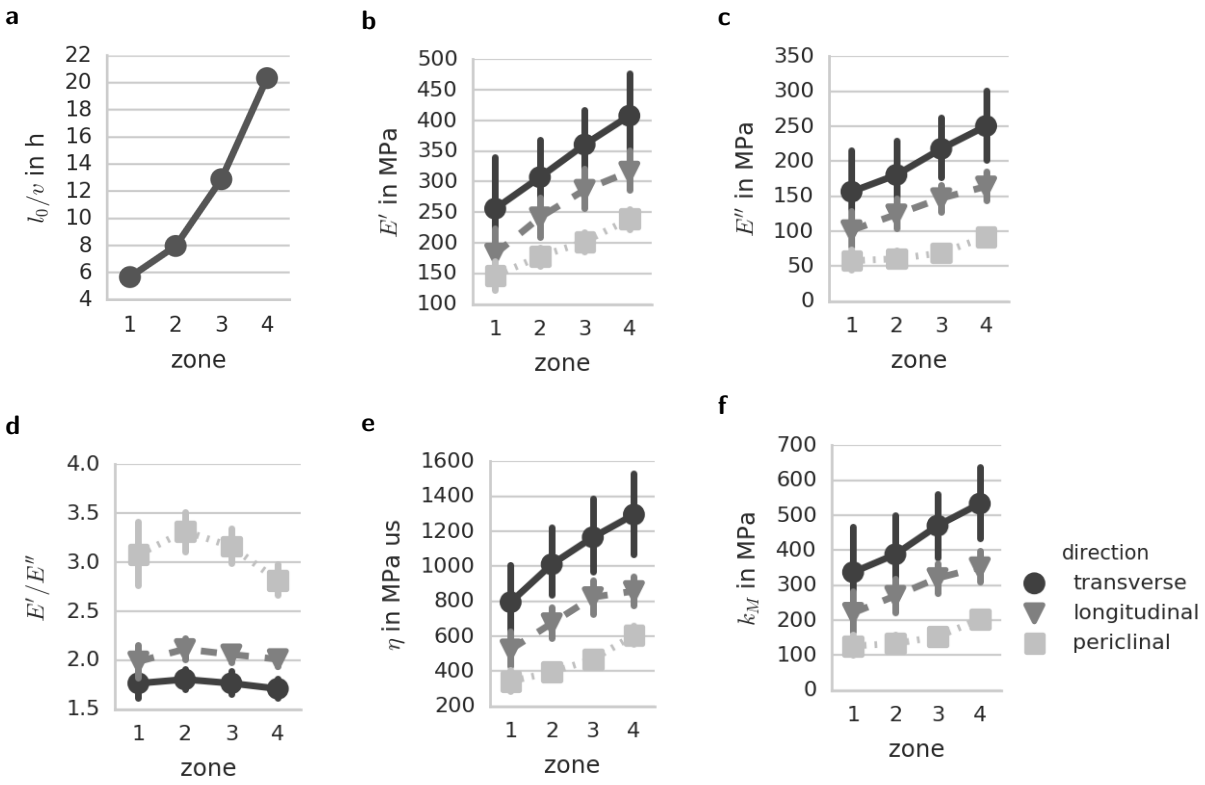


Figure 5.17: Mechanical properties and growth gradient along the hypocotyl. The *A. thaliana* hypocotyl shows a growth gradient (Data taken from Gendreau et al. (1997)). The inverse growth rate, or normalised velocity, shows (a) that the hypocotyl is growing slower at the base (zone 1) than towards the apex (zone 4). The storage (b) and loss (c) moduli evidently correlate with the growth gradient, while the ratio of elasticity and viscosity, represented by the inverse loss tangent (d), does not display such a correlation. The wall viscosity (e) and (f) stiffness, on the other hand, follow the tendency of storage and loss moduli.

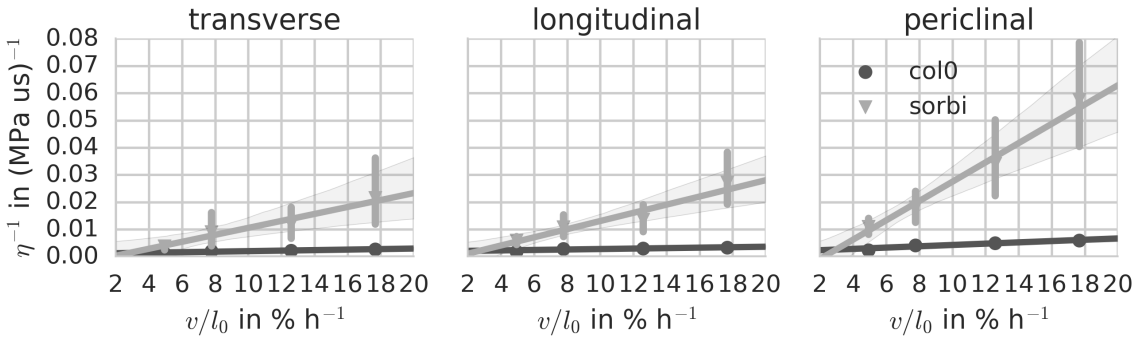


Figure 5.18: Hypocotyl growth. The relation between growth rates and extensibility $\Phi \propto \eta^{-1}$ demonstrated by a linear regression for the different wall types. The graph shows a comparison between pressurized (col0) and sorbitol (sorbi) treated seedlings.

it is resonable to test if there is a linear relationship between $1/\eta$ and the normalised velocity (or growth rate) v/l_0.

Figure 5.18 shows a linear regression, for the viscosity in fig. 5.17e and the viscosity obtained from plasmolysed data in section 5.3, versus growth rates. The data shows great agreement ($p < 0.001$) with the linear behaviour predicted by the Lockhart model. The slope of the fit relates to the effective pressure $P^* = P_t - Y$, for which we obtain for turgid cells $(0.14 \pm 0.01)\,\mathrm{MPa}$ for transverse, longitudinal, and periclinal walls with the assumption that the cells have a radius of $r = 10\,\mu\mathrm{m}$ and a wall thickness of $t = 1\,\mu\mathrm{m}$. For the plasmolysed cells we find $P^* = (0.15 \pm 0.01)\,\mathrm{MPa}$ for all three orientations. The reason that P^* can also be found for flaccid cells, is given by the thermodynamic theory from Veytsman and Cosgrove (1998) and Dyson et al. (2012), which predicts a smooth transition from the elastic towards the yielding behaviour of the wall so points close to either side of Y are similar. From a physical point of view, this continuous transition makes more sense. It should be emphasised, that these estimates of P^* strongly depend on the CW geometry. For example doubling the cell radius or reducing the wall thickness by 50 % would already result in a twofold increase in P^*.

Experimentally relating the growth gradient of the hypocotyl to the mechanical properties at a cellular level is a big achievement in understanding how mechanical

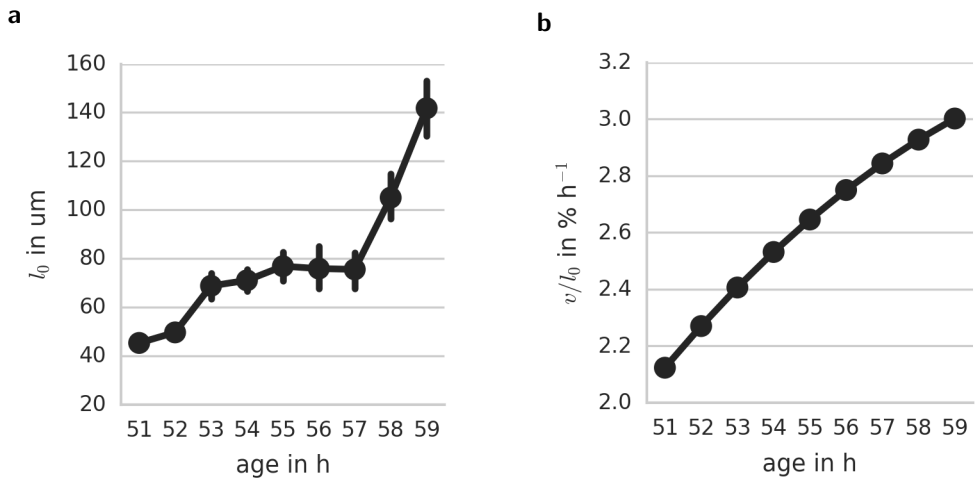


Figure 5.19: Cell length and growth rate. Average cell length (a) and normalised growth velocity (b) for unidirectionally growing cells (# 4–8).

properties are related to plant growth. The Lockhart model applies only to single cell growth, therefore, it is important to test if his theory (eq. (5.9)) is valid at the subcellular scale. To test this hypothesis we measured 27 seedlings over a period of 9 h starting with an initial age of 1 h and time increments of 1 h. We did this for 3 seedlings for each age. For every seedling we measured between 6–9 cells, corresponding to cells 3–12 at the hypocotyl (numbered from the base). Since Lockhart's model applies only to unidirectionally growing cells, we dismissed cells at the apical hook. For the younger seedlings those cells can already appear at cell number 9. Therefore, we only consider cells 4–8, over which we averaged.

The averaging is necessary, because neighbouring cells in adjacent files can be of a different cell number. However, for unidirectional growth it is important that those neighbouring cells extend with the same speed because otherwise the resulting elongation would result in a bent organ (Zieschang et al., 1997). Furthermore, Lockhart uses true (logarithmic) strain for the elongation, which states that not only the individual cell but any arbitrary two points should follow this equation, assuming continuum mechanics. With this in mind we can state that the dimensions of cells

are natural but arbitrary marks and thus the averaging over several cells leads to an averaging over these marks and ,therefore, resembles the true strain better than the consideration of individual cell numbers.

Additionally, it is not possible to measure the mechanics of growth over time in the same seedling, because light exposure and mechanical stimulation inhibits growth. This leads to the need to measure population averages of cell length. Furthermore, variable initial seedling age is caused by a variability in germination time of about 3 h (Peaucelle et al., 2015, supplementary material). The cell length of the hypocotyls was measured from images, that were acquired with the optical microscope of the Cypher$^{\mathrm{TM}}$. Figure 5.19a shows the cell length l plotted against the plant age. The cell length is very variable with age and should follow a monotonically increasing function. However, fig. 5.19a shows clearly that at certain time points the cell length apparently decreases, which implies a shrinking of the cells. This reduction in length is not possible according to the definition of growth (section 1.4, page 24). To avoid artefacts for the growth velocity from this noisy data, we fit the data with an analytical function, and its derivative is used to determine the growth velocity. It should be mentioned that the choice of the analytical function already implies an assumption about the growth behaviour. To avoid over fitting we used a polynomial of degree two. For the normalised velocity we fitted the logarithm of the length to a polynomial of second order, because $\frac{\mathrm{d}\ln(f(t))}{\mathrm{d}t} = \frac{1}{f(t)}\frac{\mathrm{d}f(t)}{\mathrm{d}t}$. The result is shown in fig. 5.19b.

Figure 5.20 shows a plot of η versus v/l_0 for the time-lapse experiment with a slope $P^* = (0.13 \pm 0.01)\,\mathrm{MPa}$ for all three walls. This is similar to the value of 0.14 MPa for the growth gradient along the hypocotyl fig. 5.18. Given the fact that the seedlings are at a similar age (60 h vs 51 h–59 h), it makes sense that the cells show a similar effective driving force.

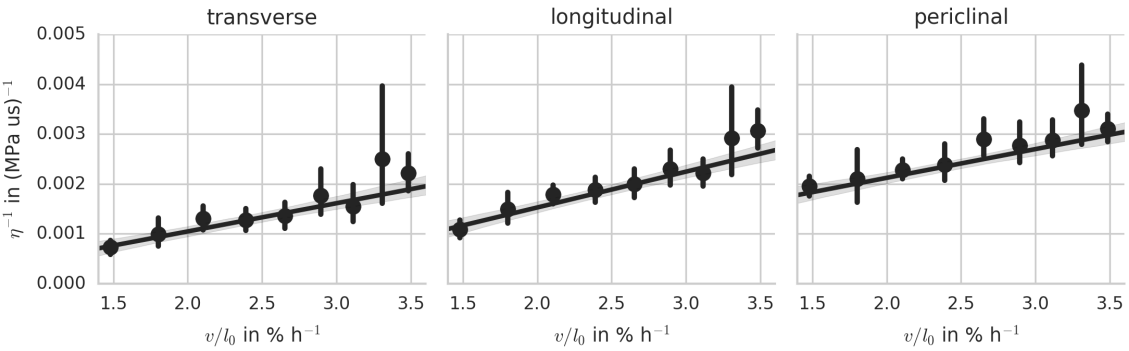


Figure 5.20: Growth mechanics. Regression plot of $1/\eta$ vs velocity v normalised by cell length l_0.

5.7 Change of Viscoelastic Properties at Dark-Light Transitions

It is well known that the *A. thaliana* hypocotyl ceases to grow when transferred from the dark to the light. This mechanism is important because when the seedling is in the soil it grows heterotrophically and it has to reach the light as quickly as possible, so that it can unfold the cotyledons and start to grow phototrophically by performing photosynthesis. Although the biochemistry and growth behaviour during this transition is well understood, the change in the mechanical properties during this transition has not been investigated. The plant CW can be expected to stiffen, because slower growing seedlings display higher moduli. Here we look at this transition in a transgenic line that carries a silent transgene and behaves like wild type (WT) in its growth and morphology (see section 5.8). The seedlings were grown for 2 d in the dark and 1 d under long day conditions, the control group was grown for 3 d in the dark. The transition to the light leads to reduced hypocotyl length of 70 % from (4.89 ± 0.30) mm to (1.51 ± 0.06) mm.

Figure 5.21 shows the storage E' and loss E'' moduli for the first eigenmode (a and b, respectively) and the second eigenmode (c and d, respectively). After the exposure to light, the growth gradient along the hypocotyl vanishes for both moduli.

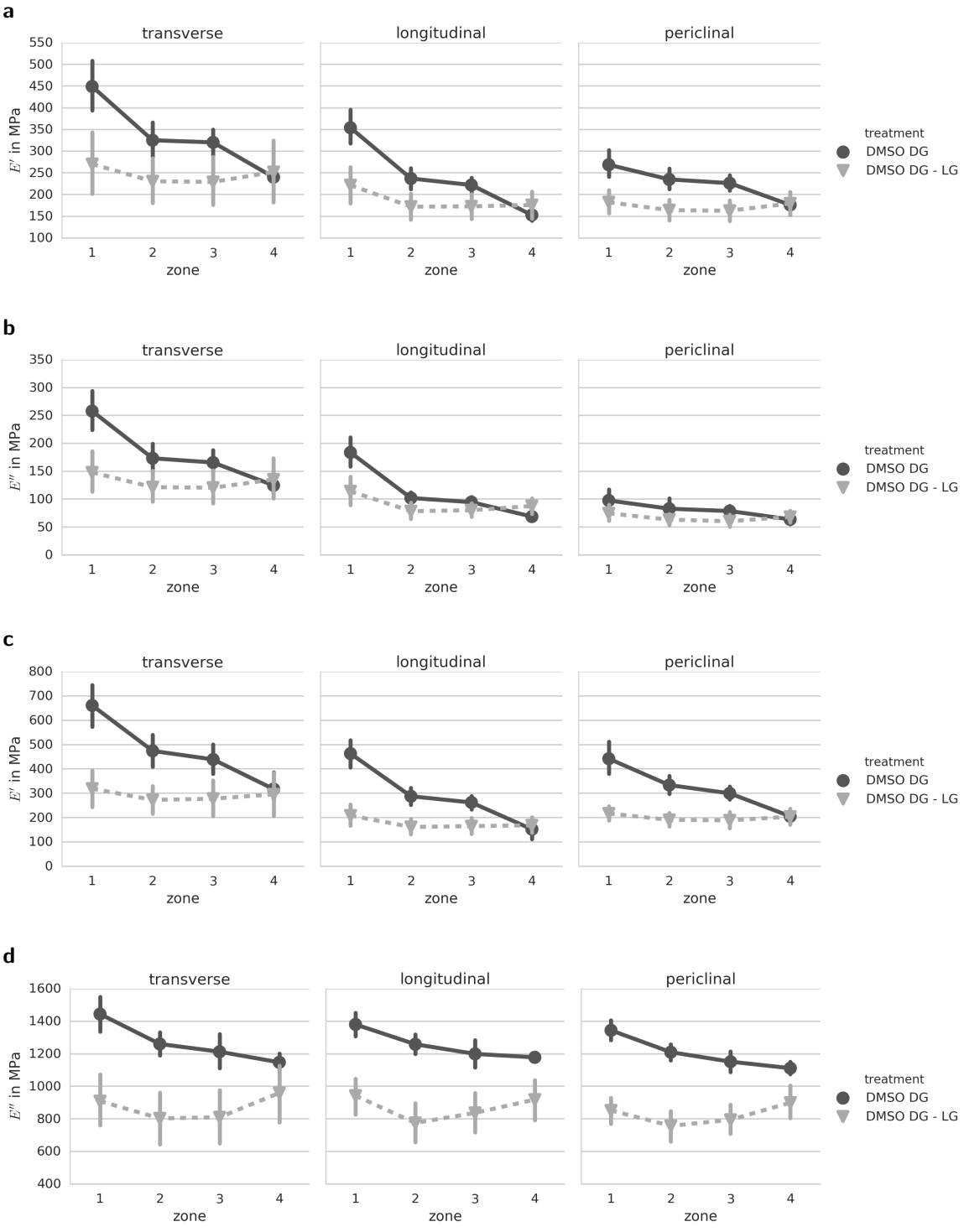


Figure 5.21: Storage and loss moduli for dark light transition of WT (RAB-E1d_DN background) seedlings. The seedlings were grown on media supplemented with DMSO only to ensure that the transgene remained silent throughout (see section 5.8) (a and b) show the first eigenmode and (c and d) show the second eigenmode for E' and E'' respectively.

This behaviour can be expected if the hypocotyl ceases growing. Surprisingly, the light exposure results in softer walls, i.e. lower moduli, at both eigenmodes, which is contrary to the expected behaviour. This suggests that the cells are growing at a higher rate than under completely dark grown conditions. Although this seems counter intuitive, it might well be that the cells display an increased radial growth. This is supported by the behaviour of the transverse, only radially growing, walls which moduli approach at the base the level of the apical cells and because the basal cells display at this age a reduced growth rate, the softening of both moduli after light exposure suggests an increase, especially in radial extensibility. In fact the diameter in light grown hypocotyls is about 30 µm increased compared to dark grown ones (Gendreau et al., 1997). Moreover, the literature suggests, that mainly the epidermal cells account for this difference and consequently, they must nearly double in radius. Under these conditions it is reasonable to imagine that after the transition to the light, the cells at the base, which have nearly ceased elongation growth begin to grow more rapidly than the dark grown ones. Homogeneous growth of the hypocotyl is supported by the fact that the growth gradient vanishes after transfer to the light. The mechanism that cessation of cell elongation is followed by rapid radial growth, might be important to achieve a high hypocotyl stability as quickly as possible, before the walls lignify. Additionally, the cells grow more isotropically. Indeed, if we compare the moduli of the light exposed seedlings, we observe similar values to the ones that seedlings display after IXB treatment. Obviously, the IXB intervention, affects not only the anisotropy but also the cellulose content in the walls and the cells show a severe phenotype. Therefore, it cannot be expected that the walls display similar structures.

Additionally, the CW extensibility does not depend only on the internal mechanical values but also on the wall geometry. In particular, the thicker the wall the lower its extensibility (eq. (5.10)). As a matter of fact, light grown hypocotyls dis-

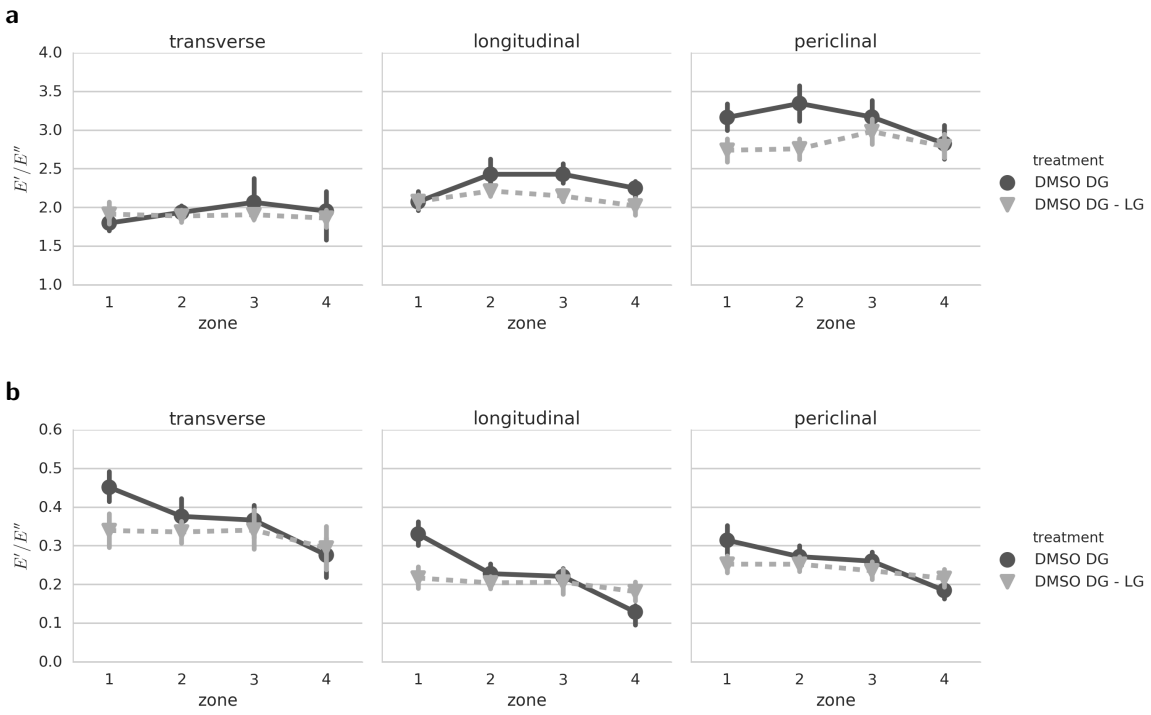


Figure 5.22: The inverse loss tangent E'/E'' for dark light transition of WT (RAB-E1d_DN background) seedlings. (a) shows the first and (b) the second eigenmode.

play thicker walls than dark grown ones (Derbyshire et al., 2007) and therefore an increased wall thickness by a factor of 1.5, would be sufficient to compensate for the softer walls.

Figure 5.22 shows the inverse loss tangent for the first (a) and second eigenmode (a). Both eigenmodes show that the dark grown seedlings are more elastic than the one with light exposure. This indicates that the transferred hypocotyls indeed grow more than the continuously dark grown ones. Moreover, at the second eigenmode the dark grown seedlings show the mechanical gradient, which vanishes for the transferred plant. This supports the idea that all cells grow at a similar rate to achieve the radius, which is required for the hypocotyl stability.

Finally, fig. 5.23 shows that the stiffness and the viscosity decrease for the light exposed seedlings as well, which is in agreement with the speculation that these seedlings grow at a higher rate. In particular the large difference for the k_{M} at the

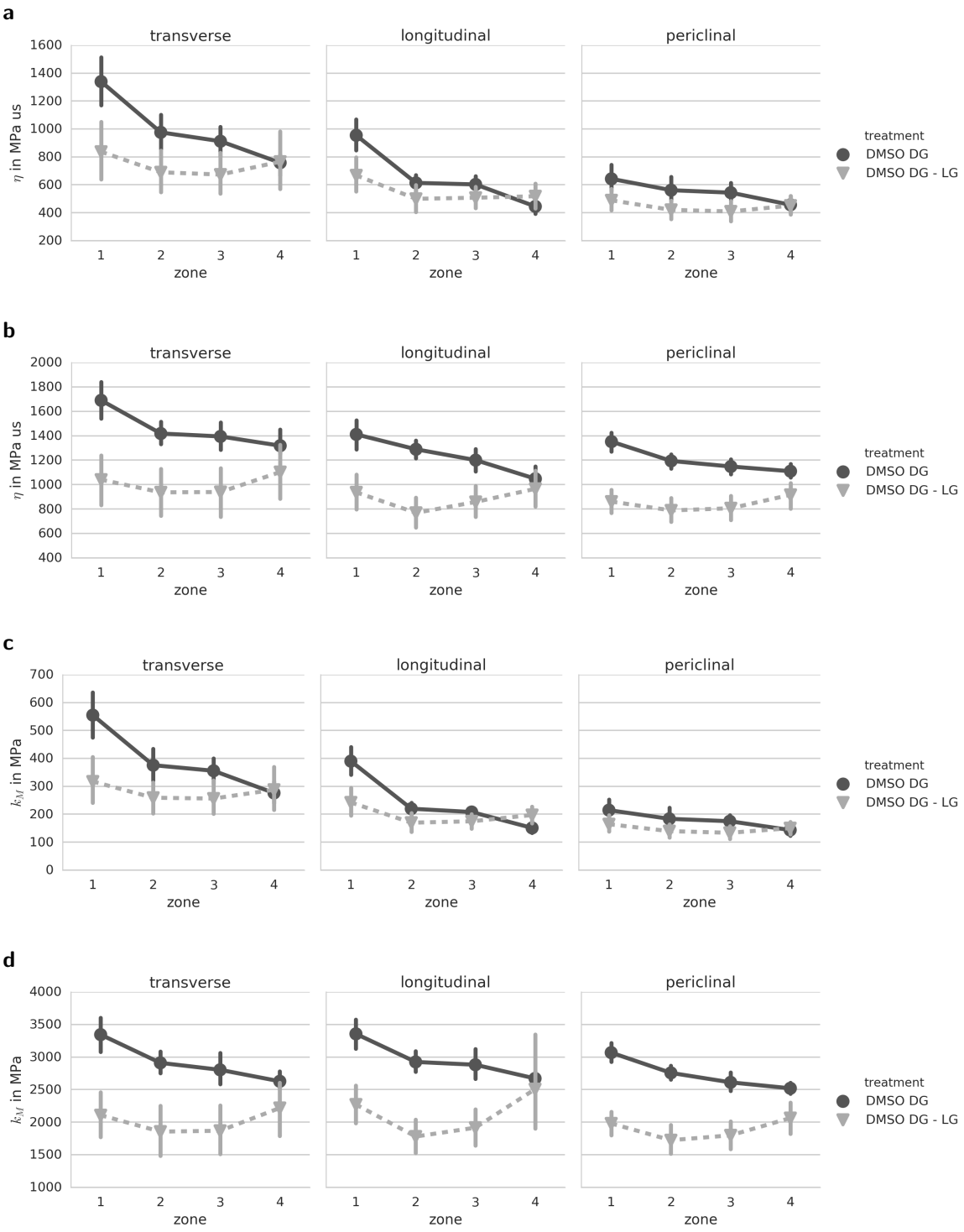


Figure 5.23: SLS quantities k_{M} and η for WT (RAB-E1d_DN background) seedlings for the dark light transitions. (a) and (b) show the first and second eigenmode for η respectively and row (c) and (d) show k_{M}.

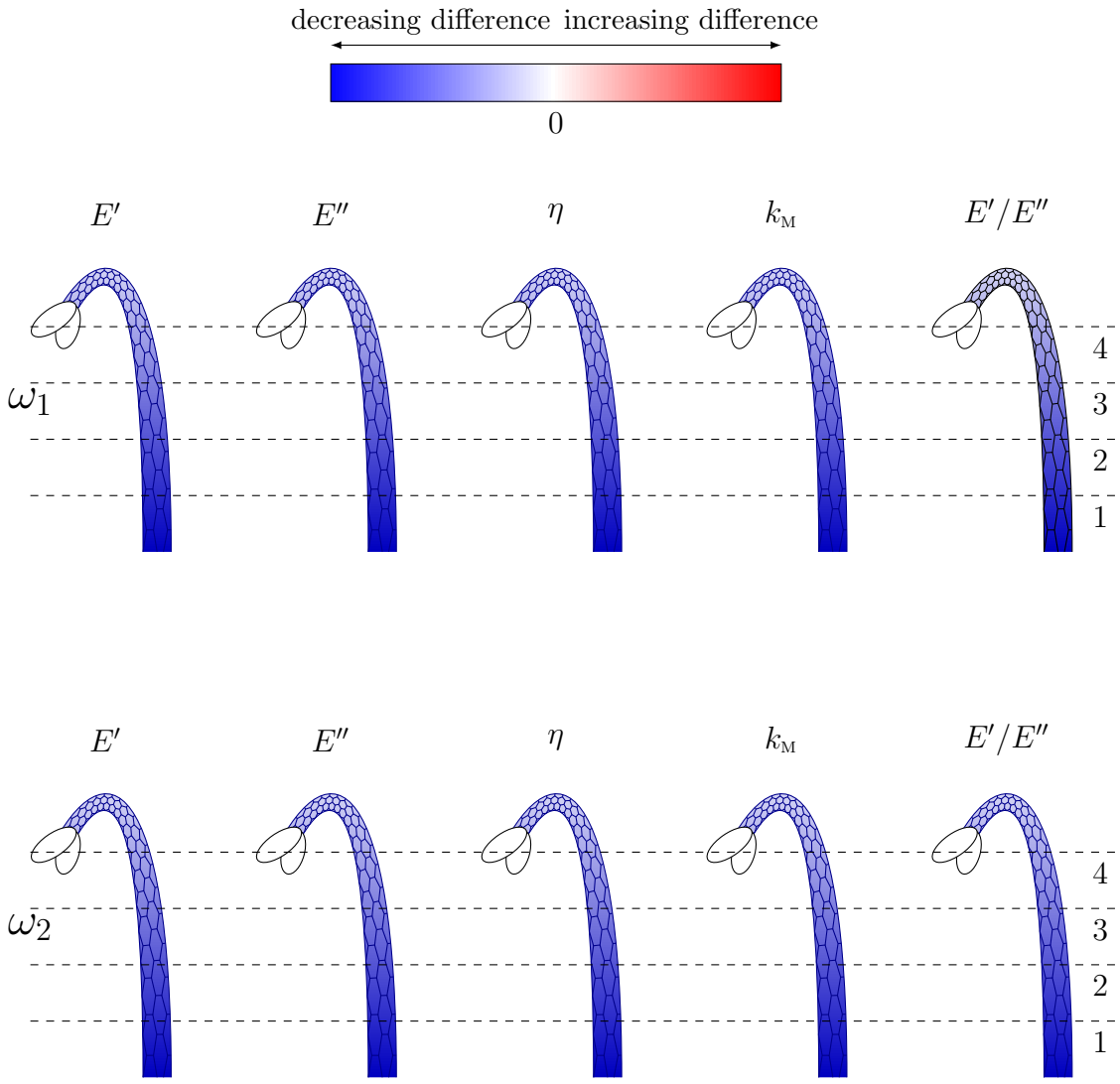


Figure 5.24: Mechanical differences of light grown seedlings with respect to dark grown. After transition to the light all viscoelastic properties are reduced for both eigenmodes. The colour gradient indicates that the reduction is less severe closer to the apex. The blue colour represents a reduction of the properties, while a red colour would show an increase of the properties. White indicates no significant changes. The black radial walls indicate no changes in the properties.

second eigenmode suggests, that after the transfer, changes at the short timescale happen, such as reduction in cellulose content or alteration of the matrix (glassy response). In fact Pelletier et al. (2010) showed on the *A. thaliana* hypocotyl that PMEs are involved and might even control the process of growth acceleration in the dark.

To sum up, light exposure of the hypocotyl leads to a decrease of all mechanical properties shown in figs. 5.21 to 5.23 as summarised in fig. 5.16. This is most likely caused by the fact that the cells have to grow radially to ensure the stability of the hypocotyl.

5.8 Exploring New Realms – An Investigation of The RAB-E1d Phenotype

After it was established that dynamic AFM viscoelastic mapping can measure alterations in CW architecture, caused by changes in the environmental conditions (light), growth rates, and chemical interventions, it is sensible to apply this method to obtain an indication of how the wall architecture differs in a phenotype with unknown changes in the CW structure. For this investigation we chose the RAB-E1d dominant negative mutant which shows a severe growth reduction in the hypocotyl. RAB-E1d controls trafficking from the Golgi to the PM (Zheng et al., 2004; Camacho et al., 2009). Therefore, it can be expected that the matrix is affected, although it would be possible that for example cellulose synthase (CESA), which is transformed via the Golgi (Kim and Brandizzi, 2016) cannot be delivered to the PM. Here we use an inducible dominant negative background to disturb RAB-E1d activity. Synthesis of the mutant protein can be induced by dexamethasone (DEX) at 1 µM in the growth medium (see chapter 2 for details). The control plants are grown on growth medium with a concentration of a thousand fold diluted DMSO, which was

used to dissolve the DEX. The resulting phenotype after growing in the dark for 3 d, displays reduced length growth by 55 % from (4.89 ± 0.44) mm (Mean ± SE) on DMSO to (2.22 ± 0.17) mm (Mean ± SE) with inhibition of RAB-E1d. This is a relatively weak phenotype, compared to 82 % reduction observed after growing in the dark for 6 d, where the control hypocotyls are almost at their maximum length of (19.10 ± 0.34) mm. We also tested that the DMSO treatment does not affect cell length (Mean ± SE = (19.03 ± 0.31) mm) and therefore also not the yielding behaviour of the CW (fig. 2.3)

Figure 5.25 shows E' and E'' of 279 cells (including 86 transverse, 178 longitudinal, and 279 transverse walls) on 10 DEX treated seedlings and 188 cells (including 63 transverse, 125 longitudinal, and 188 transverse walls) on 9 DMSO control seedlings for the first ($f_1 \approx 78$ kHz) and second ($f_2 \approx 524$ kHz) eigenmode. The growth zones represent cells 3–12 with about 2–3 cells in each zone. Zones 1–4 are from the base to the apex of the hypocoyl. At the first eigenmode the DEX treatment shows no main effect for either E' and E'' at the transverse walls but at the growing longitudinal and periclinal ones, they are slightly increased compared to the control seedlings. Furthermore, we can see that the moduli do not follow the same trend as the control seedlings, which implies that the growth gradient along the hypocotyl is disturbed with the inhibition of RAB-E1d activity. The second eigenmode shows no main effect for DEX compared to DMSO for the storage modulus E'. For E'' the main effect is even stronger than at the first eigenmode, because it displays also a difference for the transverse walls. This enhancement in the effect, affects also the behaviour along the growth gradient. In particular zones 1 and 2 show a more pronounced difference than at the first eigenmode, while zones 3 and 4 show no significant difference. The higher values in both moduli at the second eigenmode suggest that RAB-E1d is involved in the softening of the CW via alteration of the components of the wall matrix rather than a modification in the CMFs because the IXB treatment has shown that

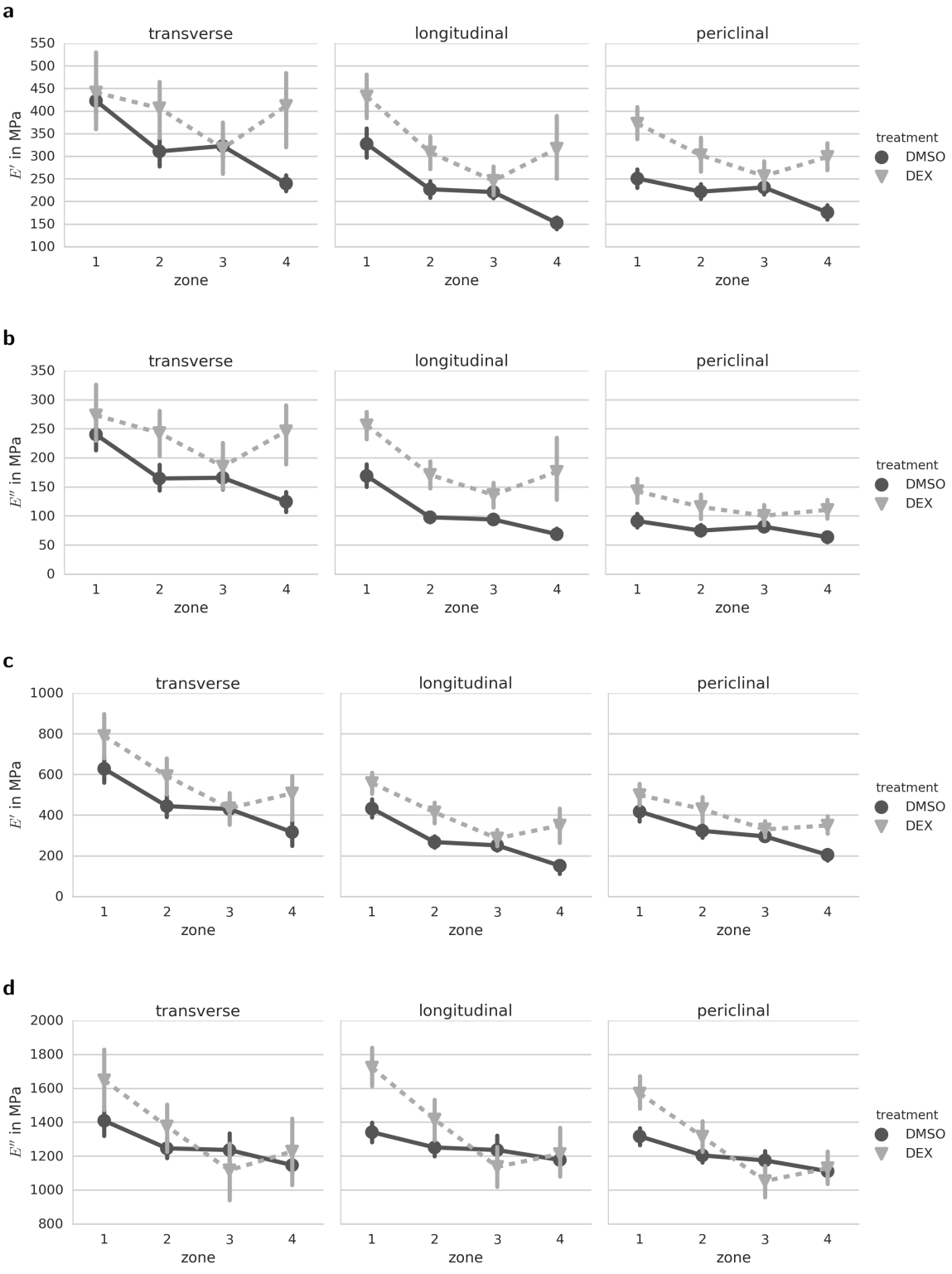


Figure 5.25: Loss and storage modulus for RAB-E1d_DN seedlings for induced phenotype (DEX) and control seedlings (DMSO). (a) and (b) show the first eigenmode and (c) and (d) show the second eigenmode for E' and E'' respectively.

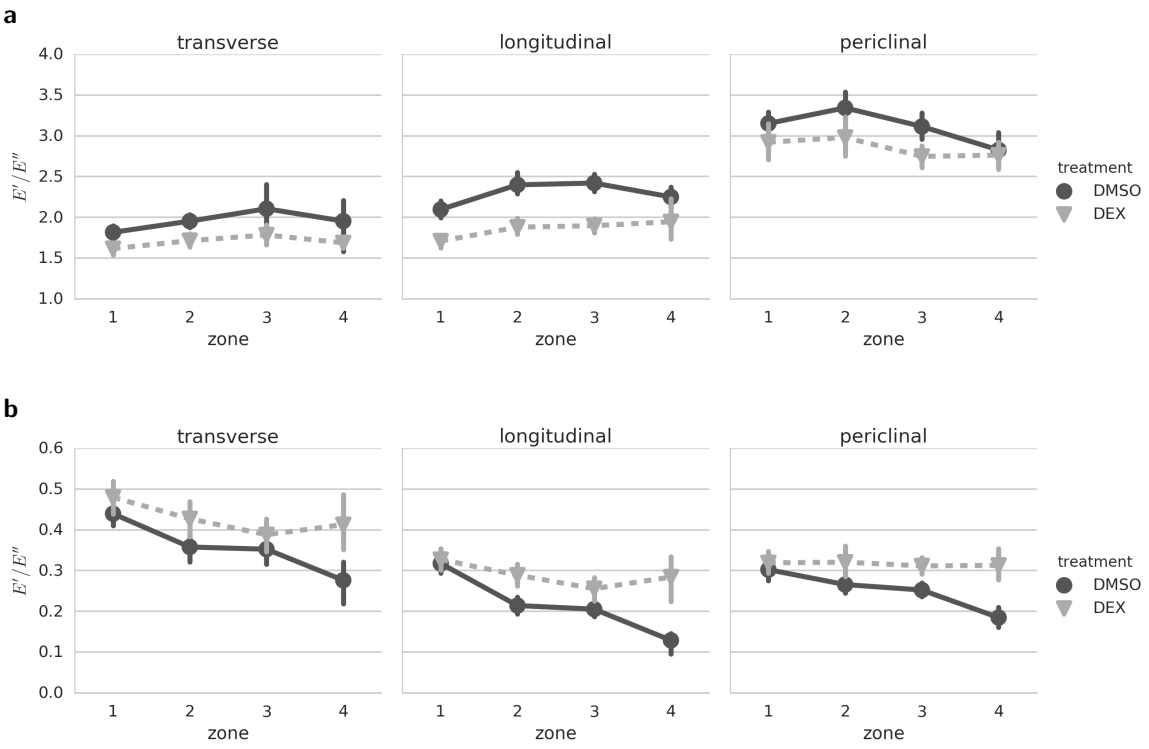


Figure 5.26: The inverse loss tangent E'/E'' for the RAB-E1d_DN seedlings, where DEX represents the induced phenotype and DMSO the control seedlings. (a) shows the first and (b) the second eigenmode.

a reduced cellulose content results in smaller moduli. This conclusion assumes that initiation of RAB-E1d would only cause a modification of the CW material whose biosynthetic pathway is controlled directly by RAB-E1d and does not result from strong secondary, compensatory, effects. Moreover, an increase in cellulose content would imply an increasing E' at the higher frequency but here we see only an increase in E'', which implies that at the second eigenmode more energy is dissipated in the treated seedlings. For example changes in polymer composition or internal growth factors, such as auxin or xyloglucan endotransglucosylases/hydrolases (XTHs) could be affected.

The issue of the relative energy dissipation can be investigated specifically by the inverse loss tangent E'/E'' which is shown for both eigenmodes in fig. 5.26. In fact, the RAB-E1d mutants exhibit a similar behaviour to that of the ECG intervention.

The RAB-E1d inhibited seedlings display a decreased ratio at the first eigenmode and a slight increase at the higher frequency. However, at the second eigenmode the difference between the two treatments almost vanishes and is only statistically significant for the growing periclinal walls, suggesting a similar behaviour at shorter relaxation times of both CW in radial direction. The major difference between the two measurements is that with the DEX intervention the hypocotyl loses the gradient along the zones and suggests a more uniform behaviour for cells at different developmental stages. This loss of variability indicates that a growth mechanism is affected, which is required to maintain the growth gradient along the hypoctyl.

The growth capability of the cells can be studied in further detail with the viscosity, which is shown in fig. 5.27. At the first eigenmode the RAB-E1d suppressed seedlings display an increased η compared to the control seedlings. This effect is particularly large at the growing longitudinal and periclinal walls but it is also present at the transverse walls. The increased viscosity is equivalent to a decreased cell extensibility and therefore this microscopic result is in agreement with the macroscopic observation of reduced cell length. The second eigenmode displays a similar behaviour with the difference that at this frequency the growth gradient in the phenotype is more present than at the longer relaxation time. One major difference between the inhibition of RAB-E1d and PME is revealed by k_{M} (fig. 5.27 third and fourth row). Here, we see increased values for both eigenmodes, while for the ECG treatment k_{M} was increased for the first eigenmode but decreased at the second one. Although, the difference in the stiffness at the second eigenmode is not statistically significant for the RAB-E1d mutation and control seedlings ($p = 0.09$), the behaviour between first and second eigenmode is different for RAB-E1d mutants and ECG intervention.

One problem with dysfunctional cells is that it is not clear if the morphological phenotype arises as a primary or secondary effect, i.e. if as a consequence of a direct CW alteration other, secondary, effects occur. One effect could be that the water

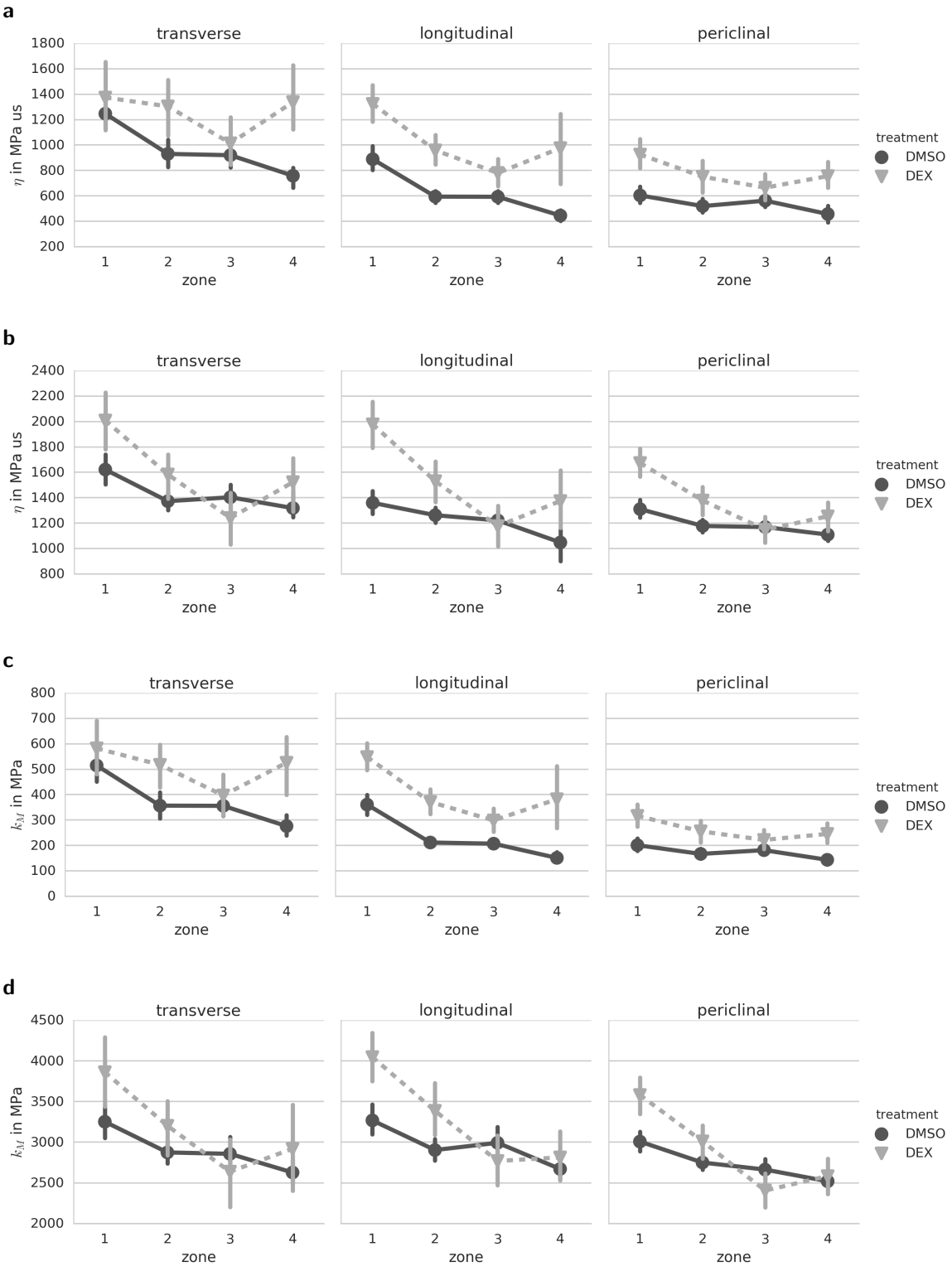


Figure 5.27: SLS quantities k_{M} and η for the RAB-E1d_DN seedlings for the induced phenotype and control (DMSO) plants. (a) and (b) show the first and second eigenmode for η respectively and (c) and (d) show k_{M}.

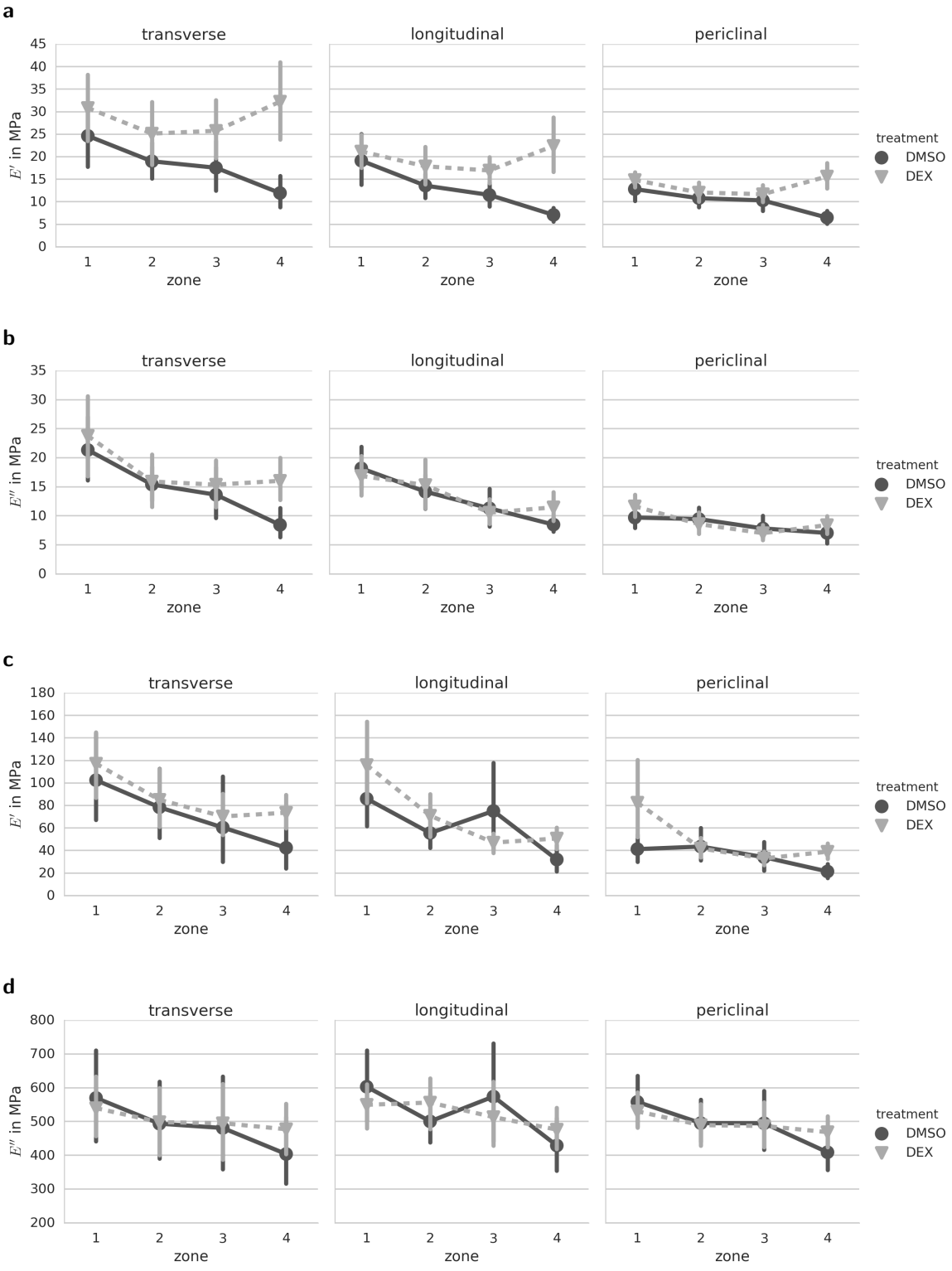


Figure 5.28: Loss and storage modulus for plasmolysed RAB-E1d_DN seedlings for induced phenotype (DEX) and control seedlings (DMSO). (a) and (b) show the first eigenmode and (a) and (b) show the second eigenmode for E' and E'' respectively.

potential, and consequently the turgor pressure, falls. This would cause the strain of the wall to change making CW properties difficult to compare. Furthermore, an investigation of relaxed CWs might provide insights into the yield threshold Y. To release the strain in the walls we plasmolysed the cells with an hyperosmotic solution of 0.55 M sorbitol dissolved in pure water. As expected, we observe about a tenfold decrease in E' and E''. At the first eigenmode, the gap in E' is now increased. Surprisingly, the deviation in E'' from the turgid state vanished completely. This suggests that changes in Y and k_∞ occur. The shift in Y could be caused by a change in the statistical distribution of the chain length in the network (Kothari et al., 2018) but also changes in the matrix or cellulose content can alter Y (Veytsman and Cosgrove, 1998; Dyson et al., 2012). At the second eigenmode all differences in both moduli vanished, whereas the turgid cells this shorter relaxation time revealed an even larger difference between the two treatments. That no larger deviation appeared at the higher frequency supports the hypothesis that mainly the yield threshold was affected. In fact it could be that the free volume, i.e. the volume with cannot be occupied by the polymer network, determines only the yield threshold. For example the free volume describes porosity and density of a polymer network and thus influences the elastic modulus of a polymeric material. However, if it contributes to k_∞ or k_M depends on the observed timescale. Slower timescales are dominated by poroelastic behaviour and quicker timescales by viscoelasticity, which can be modified by the density (Anirudh et al., 2014).

Even more interesting is the fact that at the first eigenmode $(E'/E'')_\mathrm{DEX} > (E'/E'')_\mathrm{DMSO}$, whereas this was the other way around for the pressurised cells. This indicates a more elastic behaviour due to RAB-E1d inhibition, which is in agreement with the speculation that the mutation leads to shorter chains in the matrix. The overall decrease in the ratio E'/E'' only supports the idea that the walls were in a relaxed state and hence they provide a reduced retracting force compared to the stressed material. At

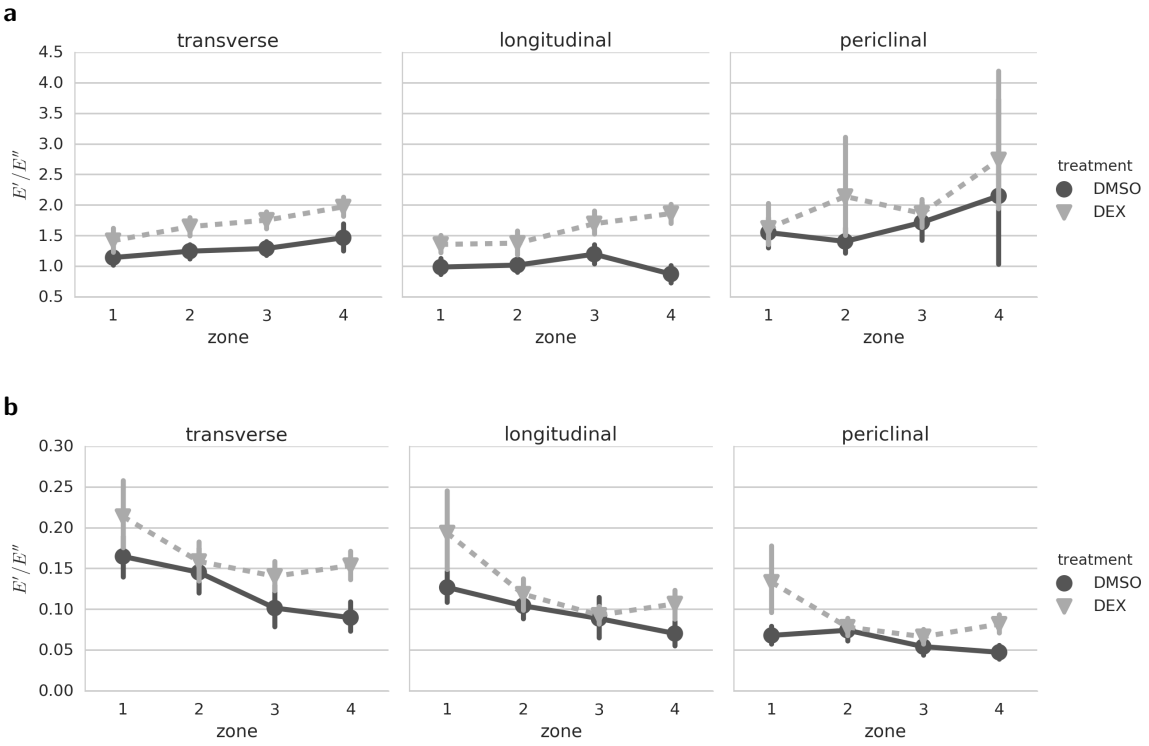


Figure 5.29: The inverse loss tangent E'/E'' for plasmolysed RAB-E1d_DN seedlings, where DEX represents the induced phenotype and DMSO the control seedlings. (a) shows the first and (b) the second eigenmode.

Table 5.2: Relative extension and yield threshold for $\delta \approx 300\,\text{nm}$. The outer cell radius was assumed to be $R_o = 10\,\mu\text{m}$ and the thickness of the CW was assumed to be $t \approx 1\,\mu\text{m}$. The standard error for both treatments and all walls is $\Delta Y \leq 0.01\,\text{MPa}$.

		DMSO		DEX	
Wall	Zone	ε_0[%]	Y[MPa]	ε_0[%]	Y[MPa]
transverse	1.0	30.51	1.47	16.98	1.27
	2.0	23.44	1.13	17.45	1.30
	3.0	24.71	1.19	16.48	1.23
	4.0	18.42	0.89	19.07	1.42
longitudinal	1.0	3.44	0.12	2.18	0.11
	2.0	2.18	0.07	1.91	0.10
	3.0	2.39	0.08	2.39	0.12
	4.0	1.45	0.05	4.08	0.21
periclinal	1.0	3.21	0.09	2.80	0.10
	2.0	2.70	0.07	2.70	0.10
	3.0	3.20	0.09	3.60	0.13
	4.0	2.30	0.06	5.56	0.20

the second eigenmode both ratios indicate a more dissipative behaviour and the values decrease and they approach each other. This similarity at the short timescale suggests that smaller structures in the phenotype are conserved.

If we look at the SLS quantities (fig. 5.30) we observe at the first eigenmode an increased viscosity, which is consistent with the macroscopic observation of the smaller seedlings. Potentially interesting is the fact that at the second eigenmode we observe $\eta_{\text{DEX}} < \eta_{\text{DMSO}}$ but there is no statistical significance and hence it is pointless to speculate about the meaning. Notably too, k_{M} is unchanged in the relaxed state of the wall. The fact that it is different for the first eigenmode in the pressurised cells, indicates that these differences come from the strain in the wall.

The plasmolysis data points towards a change in the Y, which can be caused by differences in chain length distribution, cross-linking density, coordination number, or enzymatic activity. In fact if we calculate the yield threshold as in section 5.3 we can observe a change for the induced RAB-E1d seedlings (table 5.2). It should be emphasised that the difference in Y and ε_0 between the DMSO data here and the

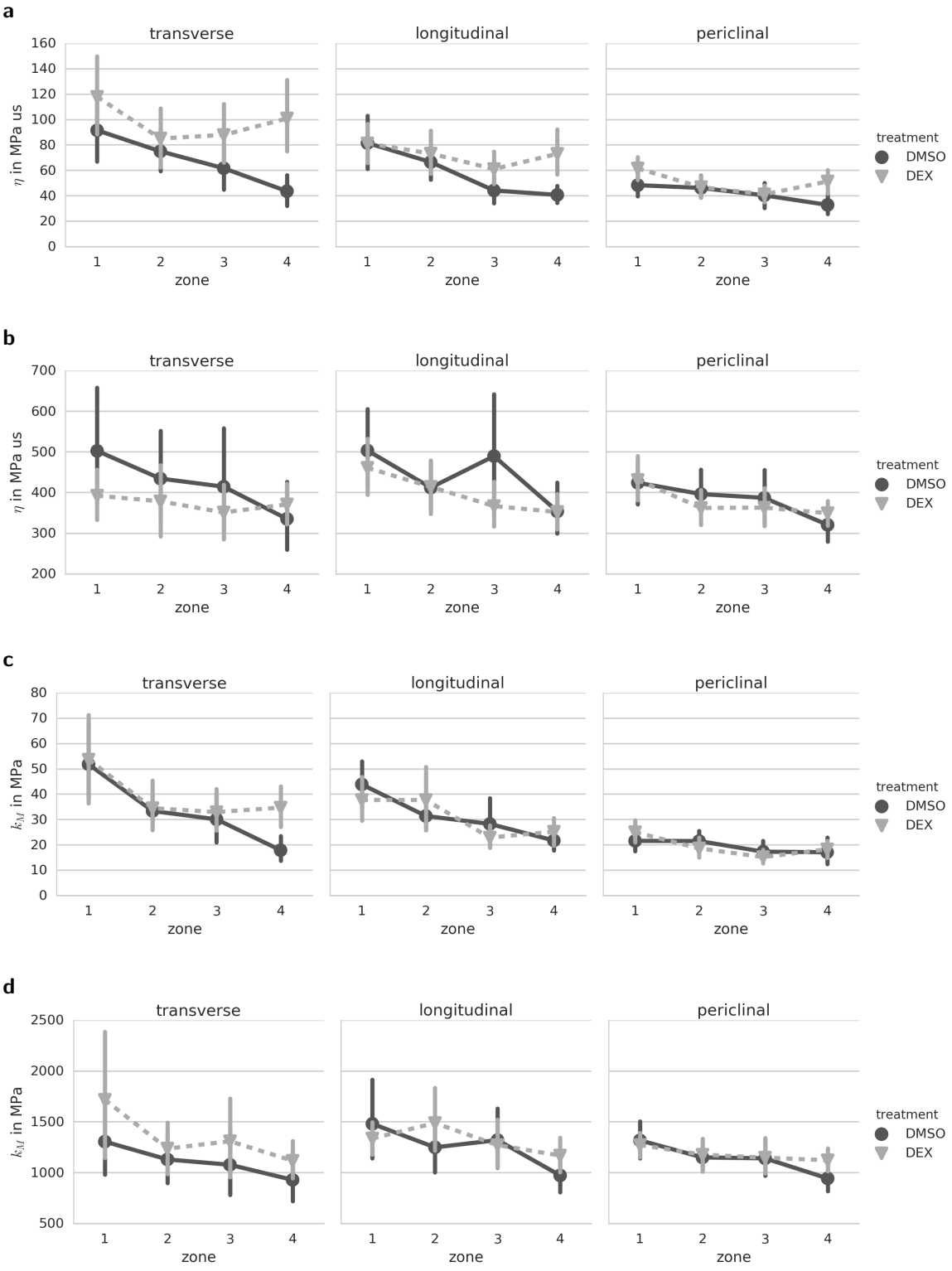


Figure 5.30: SLS quantities k_{M} and η for plasmolysed RAB-E1d_DN seedlings for the induced phenotype and control (DMSO) plants. (a) and (b) show the first and second eigenmode for η respectively and (c) and (d) show k_{M}.

data presented in section 5.3 is most likely caused by an age difference of 12 h.

In summary, the turgid data suggests changes in the CW matrix, as the comparison of the summary figures figs. 5.16 and 5.31 show similar changes in the mechanical properties. Additionally, the data of the plasmolysed cells indicate changes in the yield threshold, shown by the change of only E' and η. A summary of the plasmolysed results can be found in fig. 5.32.

5.9 Summary

In this chapter we showed that viscoelastic dynamic AFM mapping is sensitive to physiological changes. Those can be simply developmental differences, caused by different growth stages of cells, but they can also be induced artificially, for example by chemical and pharmacologial interventions or through light exposure. We demonstrate this at our example organ, the hypocotyl, but we also show, with the example of leaf cells, that it is possible to measure different cell types, which also seem to reflect developmental differences in their mechanics. The most important finding is that we establish a link between CW viscoelastic properties and growth models. In contrast, for the other physiological changes we find only non-quantitative mechanistic explanations due to the lack of an appropriate description of the phenomena. Nevertheless, this chapter demonstrates that it is possible that viscoelastic dynamic AFM model can provide information, relevant for plant development, about the physiological state of the plant and eventually it can be used to confirm or reject mathematical models of biological processes.

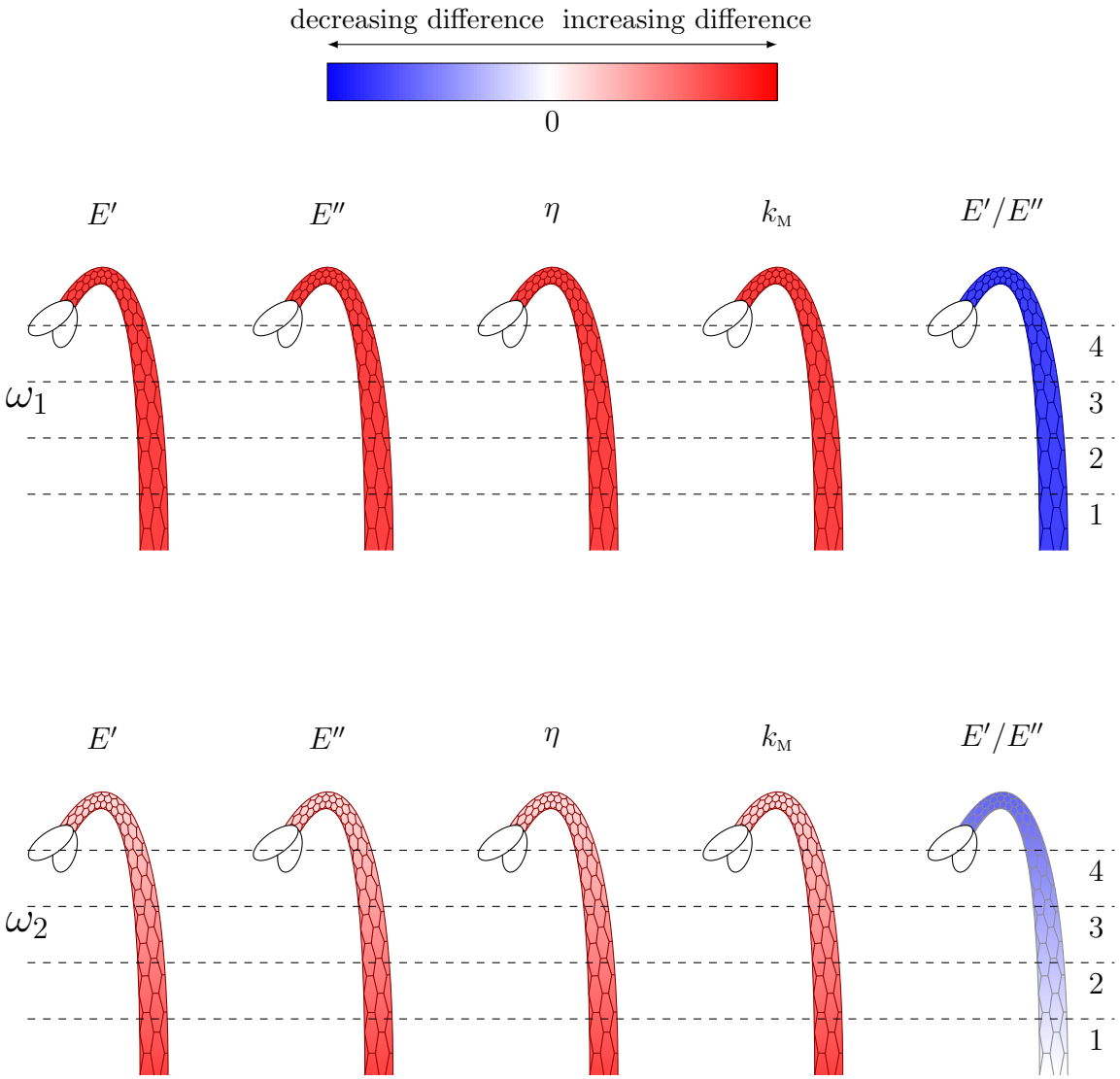


Figure 5.31: Mechanical difference of DEX treated RAB-E1d_DN under turgid conditions with respect to the DMSO (wild type like) treatment. The induction of the mutation increases most viscoelastic properties for both eigenmodes. The colour gradients indicate that the increase is less severe the whiter the colour. The blue colour represents a reduction of the properties, while a red shows an increase of the properties. White means no significant change.

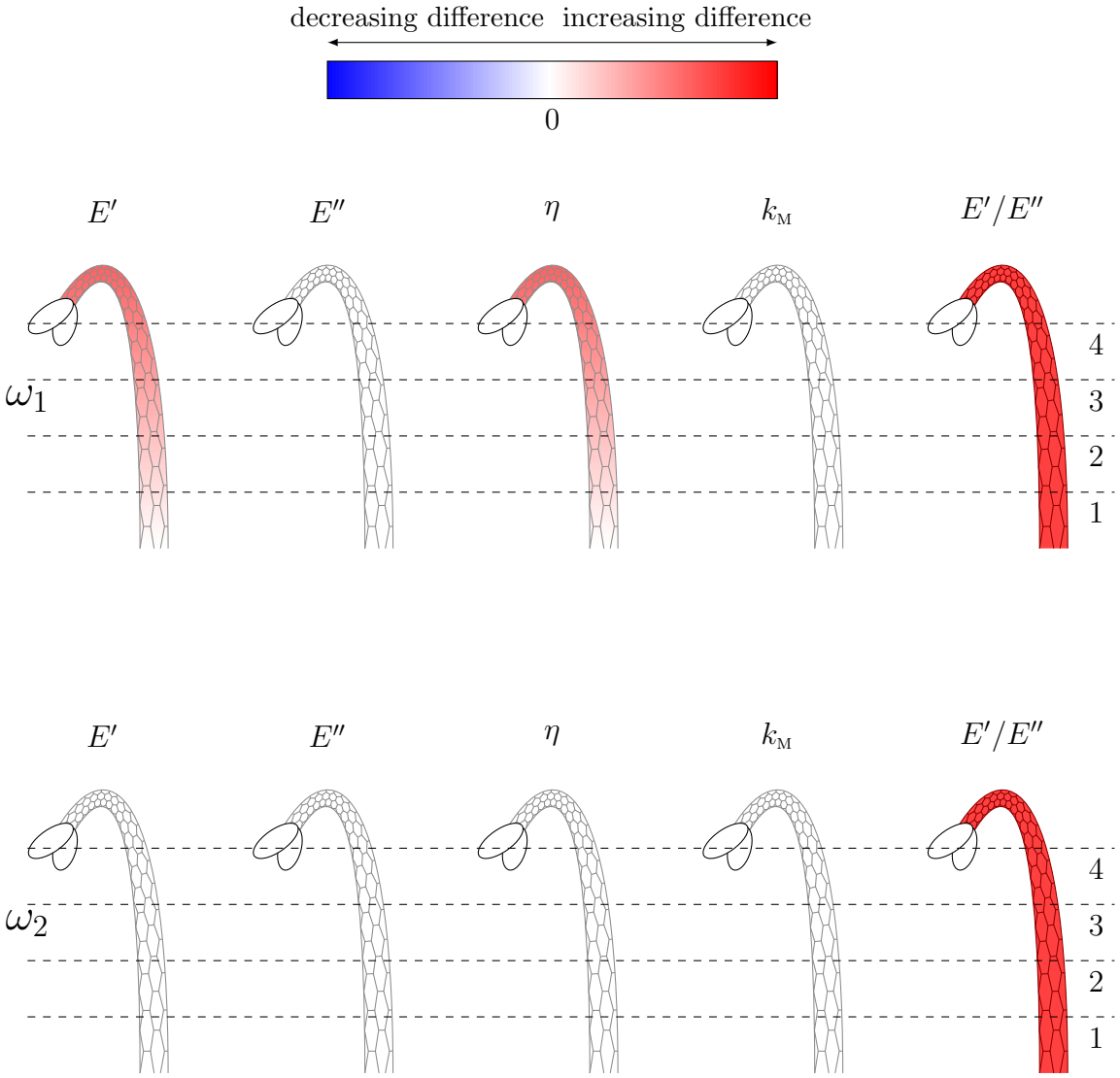


Figure 5.32: Mechanical difference of DEX treated RAB-E1d_DN under plasmolyzed conditions with respect to the DMSO (wild type like) treatment. The induction of the mutation does not change most viscoelastic properties for both eigenmodes. In fact the data suggests that only η changes and the other properties change under turgid conditions only as a result of stress. The colour gradients indicate that the increase is less severe the whiter the colour. The blue colour represents a reduction of the properties, while a red shows an increase of the properties. White means no significant change.

Chapter 6

Conclusions, General Discussion, and Outlook

In this chapter I summarise the methodological and biophysical results before I give an outlook on experiments that could be conducted in the future using the methods developed here. Additionally, I will provide some general implications of the biophysical findings for plant growth. Finally, I will give a brief outlook on the relevance of those implications to other fields.

6.1 Biophysical Findings

The primary aim of the thesis was to investigate for the first time the multiscale viscoelastic properties of the primary plant cell wall (CW) by establishing a method based on advanced dynamic AFM mapping on living plant tissues. Several experimental procedures had to be developed and tested to achieve this goal, which I summarise below.

6.1.1 Measurement Accuracy

In the beginning simple topography imaging caused problems because of the sample geometry. The large curvature of the epidermal hypocotyl cells under turgid conditions exceeds the short cantilever probes, which are standard for single cell imaging. This introduces imaging artefacts for large scale images, e.g. frames which include whole cells. Additional limitations are introduced by the setup of most AFMs, which have rather small piezo stages, for example $x \times y \times z = 90\,\mu m \times 90\,\mu m \times 15\,\mu m$ for the Asylum Research MFP-3D and $x \times y \times z = 30\,\mu m \times 30\,\mu m \times 5\,\mu m$ for the Cypher. This also restricts the frame size during imaging. While the confinement through the cantilever geometry can be circumvented by using cantilevers with different geometries, the size of the stages are a limitation inherent to the experimental setup and can be avoided only by choosing a different microscope. However, the choice of the microscope is not always available, because different commercial microscopes have different features, which can be important for the imaging, such as the photothermal excitation implemented in the Cypher. This technology enables direct actuation of the cantilever, which is crucial for quantitative dynamic mechanical AFM mapping in liquid. Although, photothermal actuation is not the only method for direct cantilever actuation, other techniques, such as Lorentz force actuation, introduce further problems. In contrast to the photothermal actuation, where nearly every cantilever can be used, Lorentz force actuation requires cantilevers, which are specifically designed for the method. This limits the cantilever choice significantly, and the options are restricted to soft levers with short probes. While the short probe can still work for simple cell imaging, the softness of the levers is a severe limitation for the dynamic mechanical mapping. The problem arises from the stiffness of the primary plant CW that exceeds the cantilever rigidity and, therefore, the walls cannot be sufficiently deformed with such a cantilever. Furthermore, for dynamic mechanical imaging in liquid, as it is required for *in vivo* measurements, a hydrodynamic coupling between

cantilever and surface, caused by the liquid, takes place. This is stronger for short than for long probes because the coupling parameter $k(d)$ depends on the distance d between cantilever and surface. Although this effect can be corrected with a calibration curve, it is better to keep the effect minimal by use of a longer probe. Additionally, imaging artefacts can be avoided if the cantilever is placed orthogonal to the major elongation axis of the sample, such as the growth direction of the hypocotyl. Such an orientation reduces the area of cantilever and chip above the sample and consequently the potential interaction sites.

The size and geometry of cantilever and probe are not only relevant for cell imaging and their viscoelastic mapping but they also influence force-volume measurements. In this thesis this type of measurement is used for calibration and is thus crucial for quantitative but not for qualitative results. Similarly, as for the other experiments the length of the probe is essential to avoid imaging artefacts. Additionally, the aspect ratio of the tip determines the contact mechanics model. The higher the aspect ratio (smaller opening angles for a cone), the smaller the effect of an inclination of the surface on the force. The increased contact area caused by the inclination reduces the measured force and would therefore lead to an incorrect dynamic modulus. However, if the aspect ratio is sufficiently large, this effect can be neglected. It should be emphasised that this is not only relevant for quasi-static indentation experiments but also for dynamic mechanical mapping. A positive side effect of a higher aspect ratio is that this also increases the resolution. One drawback of a smaller opening angle is that the sharper probe is more likely to damage the sample.

Damage can be caused by removal of CW material or cutting or piercing of a cell. The last two events lead to an immediate loss of turgor pressure and release the tension in the wall and consequently the measured mechanical properties are different. In the case of CW removal, an alteration of mechancial properties can appear but occasionally it does not result in a modification of the mechanical properties. In

general, cell injuries can be prevented by the usage of blunted probes, which, in combination with high aspect ratios, still reduce the mechanical artefacts.

In summary, imaging artefacts, both mechanical and topographical, can be reduced with long high aspect ratio probes. Additionally, the area of the cantilever above the sample should be reduced to reduce the likelihood for artefacts, which are outside the imaging area. To avoid cell injuries during imaging the use of blunt probes is advantageous. In fact high aspect ratio probes are not mutually exclusive with blunt ones.

6.1.2 Mechanical Properties of the Cell Wall

After the imaging and mechanical mapping was established, images of growing epidermal hypocotyl cell junctions were acquired. The junctions show three different types of walls (transverse, longitudinal, and periclinal) with various contributions to cellular growth. This difference is represented in a significant mechanical pattern with higher dynamic moduli at the anticlinal (radial) than at the periclinal walls. This is due to the different orientation at which the walls are measured, namely axial for the anticlinal and planar for the periclinal walls. However, not only the anticlinal walls display different mechanical properties than the perclinal walls but there is also a difference between the transverse and longitudinal ones. While the longitudinal walls contribute significantly to cellular elongation, the transverse walls do not. The correlation between material properties and differently growing walls suggests a mathematical relation between the two.

6.1.3 Connecting Plant Growth with Mechanical Properties

To connect plant growth with mechanical properties of the walls several steps were necessary. The problem arises from the fact that the dynamic AFM method from Cartagena-Rivera et al. (2015) describes the deformation of a Kelvin-Voigt (KV) ma-

terial, whereas plant growth is described in terms of a Maxwell (MW) fluid (Lockhart, 1965a; Ortega, 1985). One crucial difference between the KV and MW models is that the relaxation time in the first case is given by the loss tangent and in the second case by the inverse loss tangent. This implies that the relaxation times of these models are respectively inverse to each other. It is therefore fundamental to establish the applicability of the model. Before the viscoelastic properties can be linked to cellular growth it is necessary to determine which model is most appropriate to describe the CW. While this procedure is already established in stress-strain experiments, such a method does not exist for dynamic mechanical AFM methods. To obtain mechanical quantities which can be linked to cellular growth, I derived an expression that links the cantilever observables to the generalised MW model, which is the most universal linear viscoelastic model. The generalised MW model includes both the KV and MW model as particular cases. To circumvent this problem I have developed a simple mathematical model, which provides a relation between storage and loss modulus. Using this method I have demonstrated that the plant cell wall behaves like a standard-linear solid (SLS) material. With the certainty of the validity of the model and the spatial information of the mechanical properties maps, I found a mathematical derivation to obtain the relaxation time τ, the relaxation spring constant k_∞, the Maxwell spring constant k_M, and the viscosity η, which are the relevant parameters to describe a SLS material. Although these quantities were originally derived with the assumption of the SLS model, this method also works for more complex models, providing a measurement takes place at the significant timescale at which the material behaves almost nearly like an SLS material. This implies that with measurements at various frequencies, it is possible to extract the material parameters mentioned above and reconstruct the generalised MW model. In the case of continuous frequencies this should give the entire relaxation modulus of the material (Rubinstein and Colby, 2003, chapter 7.4). This opens a new branch of spectroscopy, which is mechanical.

A scheme for how this could possibly be derived is given below. Molecular bonds or side-chains are very small and, therefore, frequencies in the THz regime are required to identify them. This happens for example in Raman spectroscopy and Fourier-transform infrared spectroscopy. In contrast, polymer networks can have a radius of gyration R_g, i.e. spatial extension of the network, of the order of 1 µm–1000 µm (Mariani et al., 2017) and because (Kachman et al., 2017)

$$R_g^2 = \frac{1}{mk_BT} \sum_{i=1}^{N} \omega_i^{-2}, \tag{6.1}$$

the response of a polymer is dominated by the lowest frequency. Therefore, the significant frequency of a macroscopic polymer network is in the kHz to MHz range. This estimation assumes a network made only from glucose ($M = 180.156\,\mathrm{g\,mol^{-1}}$). For a cell of 10 µm radius and an amorphous completely cross-linked CW (this implies no cellulose microfibrils (CMFs)) this frequency is at $f_{\mathrm{cell}} \approx 60\,\mathrm{kHz}$. Therefore, the resonance frequency of the cantilever's first eigenmode ($f_1 \approx 80\,\mathrm{kHz}$), which was initially rather chosen by chance, is actually pertinent to image relevant material properties. This is an indication that the plant CW is a continuous polymer network.

The final theoretical step of my work is to link the mechanics to the growth equations. I chose an approach based on first principles, from non-equilibrium thermodynamics, the Onsager principle, to derive Lockhart's model from the mechanical properties. From this derivation I found that the extensibility Φ from Lockhart's model is inversely proportional to the viscosity of the CW. Although this connection was found previously in several studies (Dyson and Jensen, 2010; Ortega, 1985; Veytsman and Cosgrove, 1998), the derivation from the Onsager principle gives new insights into plant growth. First, the derivation from non-equilibrium thermodynamics implies that the plant is a thermodynamic system that is off equilibrium. This

in itself is not a novelty but the fact that it is possible to derive valid equations for plant growth from such a general principle suggests that further thermodynamic approaches can be chosen to describe plant development. Furthermore, the Onsager principle makes certain assumptions about the system and the variables involved over time that are useful to study the physics of plants. Those assumptions are:

(O1) $l(t)$ is reaches equilibrium much slower than the other variables. Hence $l(t)$ is called a slow variable and the other variables are called fast variables.

(O2) The fast variables are near equilibrium.

(O3) The relaxation time of the fast variables is much shorter than the one of the slow variables. This gives a link between length and timescales.

(O4) The slow variables change slower than the random forces.

These assumptions and the fact that the growth equation can be derived from the Onsager principle gives us additional information. Condition (O1) is rather intuitive, because the plant grows fairly slowly. At the same time the internal wall stress σ_w and the extensibility Φ are close to equilibrium (condition (O2)) and change much slower than the length. The last point implies that these variables relax much quicker towards their equilibrium position than the wall extension happens and is equivalent to condition (O3). Finally, condition (O4) states that plant growth must happen slower than thermal fluctuations. This means that growth is thermodynamically stable. Furthermore, it can be predicted from this theory that Lockhart's growth model is valid at any length- or timescale at which those conditions are fulfilled. For example if a cell changes Φ, Lockhart's growth model is valid as long as the relaxation time of Φ is shorter than the relaxation time of l. The same is true for the yield threshold. However, if the yield threshold is considered as the internal wall stress at growth equilibrium, it can be expected to reach equilibrium instantaneously

and, therefore, for this variable it can be expected that all four conditions are fulfilled at all times.

6.1.4 Experimental Results

With the developed mathematical and experimental tools we could start biological investigations of the viscoelastic behaviour of the primary plant CW. A basic, yet very important finding is the quantitative determination of $E' \approx 150\,\text{MPa}$–$450\,\text{MPa}$. Previous nano indentation studies found similar values only in combination with finite element modelling (FEM). This suggests that our experimental procedure gives for the first time immediately correct mechanical, elastic, values for the primary plant CW. This is achieved with nanometre resolution and at the same time this procedure is much quicker than traditional nano indentation experiments ($t < 2\,\text{min}$ for dynamic viscoelastic AFM mapping vs $t \sim 10\,\text{min}$–$30\,\text{min}$ for traditional nano indentation maps). However, it should be mentioned that modern peak-force nano indentation methods are much quicker than traditional force volume techniques. Yet, our method could be combined with high-speed AFM ($< 1\,\text{s/frame}$) and peak force indentation methods do not provide viscoelastic information.

The most immediately available viscoelastic information is given by the loss modulus $E'' \approx 40\,\text{MPa}$–$250\,\text{MPa}$. Both E' and E'' show a correlation with the growth potential. The smaller E' and E'', the higher the extensibility. However, the information given by the dynamic modulus cannot be related directly to plant growth, therefore, with the use of the spatial information of E' and E'' and the knowledge that the CW behaves like a SLS, we managed to obtain an expression for the viscosity $\eta \propto 1/\Phi$. The expression $1/\eta$ shows a linear relationship with the normalised growth velocity v/l for the growth gradient along the hypocotyl and also for linear cellular growth over time. The relevance here is that the values for η were obtained from pixels of $80\,\text{nm} \times 80\,\text{nm}$ and consequently the subcellular behaviour is connected for

the first time with Lockhart's growth equation. This finding confirms a prediction, which follows directly from the derivation of the growth equation from the Onsager principle, namely that Lockhart's equation is true at any length scale for which the conditions (O1) - (O4) are fulfilled. The immediate implications are that E' and E'' at this small length scale are not only related to growth but also that for any physiological changes they approach equilibrium much quicker than the cell length. This implies that abrupt length changes as indicated by the tethered network model are less likely to occur. On the other hand the mechanical 'hot-spot' model allows sliding between the CMF and is thus consistent with the Onsager principle. Furthermore, it seems that the mean field approach still works at this small length scale and that the CW at this level can be approached by continuum mechanics. Ultimately, from a linear fit of η^{-1} to the growth rate, it follows that we can calculate the effective driving pressure P^* and (with the knowledge of cell geometry and yield threshold Y) the turgor pressure can be calculated. Conversely, with the knowledge of the turgor pressure and the yield threshold, it is possible to determine the geometrical hoop factor. If we compare Φ with values from the literature we find that our $\Phi \approx 1.5 \times 10^7\,\mathrm{MPa^{-1}\,h^{-1}}$ is about nine orders of magnitude larger than previously reported at the cellular level (Cosgrove, 1985, $\Phi \approx 0.08\,\mathrm{MPa^{-1}\,h^{-1}}$). This huge discrepancy needs further work to connect the scales (see section 6.3).

Furthermore, the viscosity seems to depend on the geometric wall stress. This fact validates a prediction, made by Dyson et al. (2012), that stressed cross-links have a shorter life time. The fact that the viscosity decreases under plasmolysed conditions is not controversial, because the model assumes that the wall yields only after the threshold Y is exceeded.

In fact Y, or more precisely, the internal wall stress σ_w at growth equilibrium, can be determined from eq. (5.11) in combination with plasmolysis experiments. For this we assume a linear elastic material, which appears stiffer under strained conditions

than in the relaxed state. In reality it is more likely that the stress strain behaviour is non-linear (Veytsman and Cosgrove, 1998; Dyson et al., 2012), but our approach gives a good first-order approximation. With $Y \approx 0.06\,\mathrm{MPa}$–$0.34\,\mathrm{MPa}$, these values are close to those previously reported (Cosgrove, 1985).

As mentioned above, the excitation frequency of the first eigenmode is not the only relaxation timescale of the CW. Therefore, we perform measurements at the second eigenmode ($f_2 \approx 525\,\mathrm{kHz}$), which contributes about 15 % to the final relaxation time of the polymer network, according to eq. (6.1). With the excitation at the higher frequency we find that the plant CW does not follow the SLS model anymore. This indicates that continuous relaxation times of the polymer network exist, rather than discrete ones. Although this is consistent with the polymer physics of networks, this implies that further steps must be pursued to obtain a consistent theory. An outline of how to obtain such a theory is given below. With the measurements at the second eigenmode we find storage and loss moduli of $E' \approx 150\,\mathrm{MPa}$–$650\,\mathrm{MPa}$ and $E'' \approx 1000\,\mathrm{MPa}$–$1500\,\mathrm{MPa}$. This frequency dependency of the dynamic response of a polymer network is to be expected (Doi, 2013). Moreover, this shows that at the second eigenmode the energy dissipation dominates, whereas at the first eigenmode it was the elastic behaviour. This might be simply explained by the increased amount of energy that is put into the system (CW) at the second eigenmode. This could lead to an increased breakage rate of hydrogen bonds. Alternatively, the increased energy dissipation at the higher frequency might result from more non-adiabatic deformations of the polymer chains in the wall.

Another observation at the second eigenmode is that k_M increases from $150\,\mathrm{MPa}$–$500\,\mathrm{MPa}$, at the first eigenmode, to $2500\,\mathrm{MPa}$–$3500\,\mathrm{MPa}$, at the second eigenmode. A dramatic increase like this could be expected, because at shorter timescales, stiffer components are deformed. The question in this case is if the tenfold increase is caused by the CMFs or by probing the glassy behaviour of the polymer network. The Young's

modulus of CMFs is in the range 5 GPa–250 GPa Moon et al. (2011), while the glassy response shows a significant Young's modulus of the order of 3 GPa. On the one hand, it can be imagined that the actual modulus of cellulose at the second eigenmode is reduced due to the compliance of the pectin matrix and that this the increase in k_2 originates from the CMFs. On the other hand, Callens-Raadschelders et al. (1977) mentioned that there exists a relation between the behaviour of a material at a certain temperature and the response it displays at a certain timescale. With this in mind it might be that the higher frequency shows the glassy behaviour of the plant CW. This hypothesis is supported by the fact that, with plasmolysis, k_{M} at f_2 does not decrease about a factor ten as is the case at the first eigenmode. Glassy behaviour indeed shows only small changes until the transition towards the rubber behaviour occurs (Rubinstein and Colby, 2003), whereas this cannot be expected for the prestressed CMFs, because they behave most likely like a linear elastic material. However, if the difference between plasmolysed and turgid cells is caused by the stress in the matrix it could still be that the general increase of k_{M} at f_2 is caused by the CMFs.

Important for the question of the meaning of k_{M} at the second eigenmode are the findings of all the different experimental conditions. In fact k_{M} appears to be in the range 1.5 GPa–4.0 GPa, which implies that even for the isoxaben (IXB) treatment this change is not as severe as for the other quantities, which was already observed for the flaccid cells. This is obviously no evidence that the second eigenmode is capturing the glassy behaviour of the polymer network, however, it is the simplest explanation and, therefore, a strong indication that this is the case.

6.2 Biological Findings

The results so far are based on considerations from polymer physics and non-equilibrium thermodynamics and try to link the AFM results quantitatively to these theories. In

the final section of the thesis more biological questions were asked. Due to the lack of complete mathematical models it is possible to only make qualitative statements derived from the quantitative measurements of this work.

First, we demonstrate that the technique is applicable to other organs (leaves). Leaf epidermis is formed from different cell types, two of which are pavement and guard cells that serve different mechanistic purposes. Pavement cells give stability to the leaves and guard cells are responsible for opening and closing the pores for carbon fixation. Furthermore, both cell types grow more or less isotropically in two dimensions, in contrast to the unidirectional growth of hypocotyl cells.

From a mechanical point of view, guard cells have to perform very elastically during the rapid change of shape. Evidence for a slight increase in the elastic behaviour can be seen as inferred by the increase in the inverse loss tangent. Furthermore, guard cells display similar mechanical properties as the surrounding pavement cells (see below). This adaptation to the adjacent cells might be necessary to ensure mechanical stability. Another important feature of guard cells is the shape anisotropy in the inflated state. This form is achieved by a structural anisotropy of the CMFs. Although this morphological alteration was seen in previous elastic measurements (Sampathkumar et al., 2014), this cannot be observed in our measurements. An explanation for the lack of the visibility of the aligned CMF might be the indentation depth of $\delta \approx 300\,\mathrm{nm}$ in our experiments vs $\delta \approx 20\,\mathrm{nm}$ as reported by Sampathkumar et al. (2014). In this case they measure only a small layer of the CW, whereas in our experiments the mechanical properties of ten times as many layers contribute. Additionally, it can be expected that the cells in the swollen state exhibit a mechanical anisotropy between the pore facing side and the pore averted side. As a matter of fact, such an asymmetry can be observed at the very inside of the pore where the cells are evidently softer than at the outside. Moreover, the central, stress neutral, area of the cells appears to be softer as well as both inner and outer faces.

Pavement cells display a similar qualitative difference in the mechanical properties between anticlinal and periclinal walls. This result is expected because for all cells the anticlinal walls are measured in axial and the periclinal walls in planar direction. The axial direction is more influenced by the compression of the CMFs, whereas the planar direction has most likely a contribution from the bending modulus and the compliance of the pectin matrix.

In general, pavement cells are made of a softer CW than hypocotyl cells. Various explanations exist for this observation. First, it might be that the cells have a larger extensibility and, consequently, more growth potential than hypocotyl cells. This idea is supported by the fact that smaller, younger, pavement cells were substantially softer than maturer ones. However, if this is the case, the implication is that this higher extensibility is given by a tensorial quantity. Such a description is provided by Pietruszka (2009a) and could in principle also be derived from the Onsager principle, which is not restricted to one dimensional descriptions. Such an orientation dependant extensibility could also have further implications for the softer walls. On this matter it should be mentioned that it is not clear how much the influence of the x and y components of the material properties have on the AFM indentation measurements. It seems that the major contribution comes from the in-plane penetration. However, the conical shape of the indenter implies also a shear influence on the result and, therefore, the material properties from the x, y plane matter. In fact if the components in x, y are much softer than in z direction, the major contribution will arise from the x and y components. Furthermore, the oscillatory nature of dynamic AFM experiments might have an additional contribution from the x, y plane, depending on the penetration depth of the mechanical waves. With this in mind, it might well be that the more isotropic structure of the CW in the pavement cells results in the softer measured properties. One phenomenological explanation for this is that with an isotropic distribution of the CMFs the fibres must be less densely packed than

this is the case for very oriented fibres. For the second explanation of the softer wall, we should recall that the extensibility is highly dependent on cell and CW geometry. Therefore, the lower mechanical properties might just be a consequence of the cell shape or wall thickness of pavement cells. Finally, the literature suggests (Hayot et al., 2012) that leaves have a reduced turgor pressure compared to hypocotyls or stems. This implies that, with same architecture, the walls are less strained and, consequently, the internal wall stress is reduced. This would also lead to lower measured values.

Similar questions arise for the IXB treated hypocotyl cells. The IXB treatment results in a reduced cellulose content in the CWs, which in turn leads to more isotropic walls. For this treatment we confirm the intuitive hypothesis that the walls become softer. However, at the same time these cells display a significant reduction in the viscosity, which implies, for same cell geometry, a higher extensibility. Obviously, a chemical intervention in a living organism results not only in a primary but also in a secondary effect. For example IXB treated cells are shorter but show an increased cell radius. Furthermore, the reduction in CMFs prevents the cell from resisting turgor and, therefore, the cell might reduce its internal pressure. Alternatively, the cell could compensate for the loss in stability by producing thicker walls, which would also reduce the final extensibility.

A surprising result can be observed after a transition of *A. thaliana* from dark grown to long day conditions seedlings. After such a transition the hypocotyl ceases elongation. The fact that the mechanical properties show a negative correlation with cell extensibility, leads to the expectation that after the dark-light transitions the walls become stiffer. However, the experiments shows that after the transition the walls softened. It is known that in light grown hypocotyls epidermal cells display thicker walls and an increased diameter (Gendreau et al., 1997; Derbyshire et al., 2007). A sudden transition to light grown conditions might require a rapid change to

gain vital stability for the hypocotyl. During such an event the cells have to double their radius, thicken the walls, and perform major architectural changes in the wall, such as the change of the CMFs from anisotropic to more isotropic arrangements. Therefore, it can be imagined that for a short period the walls become significantly softer before they start to stiffen to obtain permanent stability. These rapid changes raise the question of whether this behaviour shows characteristics of phase transitions. Additionally, the walls display similar moduli to those of IXB treated ones. Although, this might explained by a transition towards a more isotropic wall, it is more likely that this is a coincidence.

In another experiment we change the architecture of the pectin matrix by targeting pectin methyl esterases (PMEs). While it was thought that pectin demethylation leads to a stiffening of the wall (Pelloux et al., 2007), it was recently shown that in the *A. thaliana* hypocotyl PMEs are involved in growth symmetry breaking and that demethylation results in CW softening (Peaucelle et al., 2015). Our results confirm these results qualitatively, including the mechanical asymmetry between transverse and longitudinal anticlinal walls. Furthermore, the outcome of the experiment shows an increased viscosity, which is in agreement with the macroscopic behaviour of reduced cell growth. One surprising result is that the inverse loss tangent E'/E'' changes from the first to the second eigenmode differently than for the other treatments. For all experimental conditions it was observed that $E'/E'' > 1$ for the first and $E'/E'' < 1$ for the second eigenmode, and that treatment that affected E'/E'' affected both eigenmodes. In contrast, for the epicatechin gallate (ECG) treatment E'/E'' was smaller than for the control at the first eigenmode but larger at the second one. This might be a characteristic change either for the pectin matrix in general or more special to the Ca^{2+} cross-links caused by demethylation. Of course, PME inhibition might not only lead to those obvious primary changes but it could also result in a more severe alteration of the pectin matrix or even of the whole CW.

With the knowledge gained from the various treatments, we used the technique to find clues about which aspects of the CW might be affected in the RAB-E1d mutant. As a reminder RAB-E1d is involved in membrane trafficking and acts in transport from the Golgi towards the plasma membrane (PM). With this knowledge the most likely scenario is an alteration of the wall matrix. We looked at dark grown two different conditions, namely turgid and plasmolysed. For both conditions we found stiffer cell walls with a higher viscosity for the phenotype. These findings are in agreement with the macroscopic observation of reduced hypocotyl length. Furthermore, the fact that under turgid conditions the inverse loss tangent displays the same transition between first and second eigenmode as observed during the ECG treatment, suggests that the matrix is indeed affected. This is further supported by the observation that for plasmolysed cells mainly E' is changed and not E''. It should be emphasised, that this means statistical significance and does not imply that there is no difference in the loss modulus. However, the reduced difference in the loss modulus in the flaccid state compared to the inflated one, suggests an alteration in the yield threshold. Such an alteration can indeed be caused by the matrix but also by the CMFs (Veytsman and Cosgrove, 1998; Dyson et al., 2012; Kothari et al., 2018). Therefore, it is not surprising that such a change in the yield threshold can be observed.

To summarise, it is possible, for various changes in physiological conditions to give rise to measurable viscoelastic differences. Although, initial cell geometry contributes crucially to its expansion and, therefore, it is hard to make a statement about cellular growth from pure mechanical measurements, viscoelastic dynamic AFM mapping has the potential to answer more general questions of the physics of plant growth. This can be achieved by linking mechanical properties to models from polymer physics or non-equilibrium thermodynamics. Such a general achievement is the demonstration of the connection between the viscosity on a subcellular level and cellular growth. This makes it possible to develop a thermodynamic model of plant growth and theoretical

approaches to the multiscale nature of this process.

6.3 Future Work

The application of dynamic mechanical mapping to plant CWs opens many new possibilities to answer theoretical predictions and to ask new questions. In particular, the application with polymer physics can lead to major advances in the understanding of plant growth and development. In this section I give an overview about the questions which are directly raised by this thesis and a short outline how they can be answered.

One problem of the AFM method was the occasional occurrence of injured cells. One reason for these incidents is that contact mode AFM experiments, i.e. the feedback is on the deflection, are very invasive, particularly for soft samples. The destructive nature of contact mode AFM imaging can be avoided by tapping mode experiments, i.e. the feedback is on the amplitude or frequency. Amplitude modulation/frequency modulation (AM-FM) AFM combines tapping mode imaging and dynamic mechanical mapping and was shown recently to be very successful in viscoelastic imaging of wide range dynamic moduli of any polymeric materials, DNA, and artificial membranes (Kocun et al., 2017; Al-Rekabi and Contera, 2018). In future work it would be useful to apply this technique to cells and thus gain a less invasive technique for viscoelastic mapping of cells. Additionally, the possibility to measure with one cantilever a wide range of mechanical properties might be useful in the comparison of very soft and very stiff cells as they might occur in roots. Furthermore, AM-FM AFM relies on different theoretical considerations and could give control measurements of for the results in this thesis.

Before we look at further AFM experiments, it is useful to look at the mathematical theories and the measurements of plant growth, because we have seen in this thesis that these models can be matched quantitatively to cell growth. One problem

hereby is that the whole correlation between extensibility and growth rate is obtained through a population average. For a more accurate study it is necessary to find such a link between growth rates and mechanical properties of individual cells, or more precisely, regions at the cells. One experimental technique to measure growth rates for unidirectional growth of individual plants was published recently by Bastien et al. (2016). Although this method lacks subcellular resolution it provides spatial resolution, which should be sufficient to obtain better results than currently in this thesis, because with this method it is possible to use growth rates for individual seedlings.

Furthermore, in this thesis we assumed a linear elastic material to calculate the yield threshold, which arises from Lockhart's growth model. However, previous theoretical work suggests that the stress strain behaviour is more complicated (Veytsman and Cosgrove, 1998; Dyson et al., 2012). This stress strain behaviour can be measured indirectly with the application of hyperosmotic solutions of different concentrations. This results in various states of plasmolysis. With more data points the same procedure as in this thesis can be applied to see how the effective stiffness changes under a variety of pressure conditions. At the same time the strain dependency of the viscosity can also be investigated. Such an experiment opens the possibility to confirm or reject the models of Veytsman and Cosgrove (1998) and Dyson et al. (2012), which both explain the stress-strain response of the growing plant CW with slightly different foci.

A major achievement of this thesis is the theoretical foundation, which enables the reconstruction of the detailed parameters of a generalised MW model, with spatial resolution, for an arbitrary material, because this enables a detailed investigation of polymeric materials. We mentioned above that the assumption for this model was a discrete timescale behaviour, while, in reality a polymer displays continuous relaxation times. This requires both a more complete mathematical description of the generalised MW model and a technique which is suitable to measure continuous

time responses.

For the storage and loss moduli such a continuous model could be derived from eq. (4.14) by the transition from $\sum \rightarrow \int$

$$E' = \int k(\tau) \frac{\omega^2 \tau^2}{1 + \omega^2 \tau^2} \, \mathrm{d}(\omega\tau) \tag{6.2}$$

$$E'' = \int k(\tau) \frac{\omega\tau}{1 + \omega^2 \tau^2} \, \mathrm{d}(\omega\tau) \, . \tag{6.3}$$

With the relaxation time dependent stiffness $k(\tau)$. A similar approach was previously chosen by Hansen et al. (2011) to calculate relaxation spectra of potatoes. The discrete equations can be obtained by choosing

$$k(\tau) = \sum_{i=1}^{N} k_i \delta(\omega\tau - \omega\tau_i).$$

In general $k(\tau)$ must be derived from polymer physics. Most likely, this could be achieved by the free energy landscape of the polymer network. The difficulty with this will be that the free energy landscape probably requires path integrals to cover all folding and cross-linking possibilities of the network. For a composite material, such as the plant CW, it might still be possible to describe the fibres and the matrix independently and introduce a coupling parameter or chose another perturbation approach.

Here we provide two solutions, where the first one will be for a constant distribution of $k(\tau) \equiv k \; \forall \; \tau$ and the second one for $k(\tau) = \eta/\tau$ assuming a constant viscosity. For constant k we obtain

$$E' = k_\infty + k\omega\tau - k\arctan(\omega\tau)$$
$$E'' = \frac{k}{2}\ln\left(1+\omega^2\tau^2\right).$$

And for constant η we obtain

$$E' = k_\infty + \frac{\eta\omega}{2}\ln\left(1+\omega^2\tau^2\right)$$
$$E'' = \eta\omega\arctan(\omega\tau).$$

Most likely none of the above models is the correct one but with an appropriate method the response for continuous relaxation times can be tested.

Furthermore, polymeric materials are characterised by their thermodynamic quantities. Of particular importance are the number of monomers N, the chemical potential μ, the entropy S, and the temperature T, because the free energy for a growing plant is given by

$$\mathcal{A} = p\mathrm{d}V - S\mathrm{d}T + \sum_i \mu_i \mathrm{d}N_i.$$

Using such an approach, Barbacci et al. (2013) derived a model which considers coupling between mechanical, thermal and chemical energy. It should be mentioned that the dissociation constant K_{AB} of an electrolyte $\mathrm{AB} \longrightarrow \mathrm{A}^+ + \mathrm{B}^-$ is related to the chemical potential by (Doi, 2013)

$$K_{AB} \propto e^{\frac{\mu^0_{AB}+\mu^0_A+\mu^0_{AB}}{k_B T}}.$$

The pK value is given by $\mathrm{pK}_{AB} = -\log_{10}(K_{AB})$ and, therefore, the binding affinity of the polymers is related to the pH of the environment. Similarly, the stiffness depends on T, because of the entropic part of the force (eq. (1.11)). These kind of relations are often used to investigate the characteristic thermodynamic behaviour of polymeric materials. In fact a dualism between pH and T was described in a theoretical framework by Pietruszka (2015). However, in living organisms, a variation of T or pH results not only in a response of the CW but also in metabolic and enzymatic reactions. This kind of thermodynamic measurement must therefore be done on isolated CWs, which can be extracted according to Zhang et al. (2014b). Once the response of the isolated wall is known, such an investigation can take place in the living organism and differences between the *in vitro* and *in vivo* behaviour can be investigated.

A method to obtain the time response of a material with continuous frequencies is the application of a chirp signal during the cantilever indentation. One problem with this would be that it is very time consuming to generate maps, with spatial resolution. However, one could imagine that it is possible to find the most interesting time response of the material with a chirp. Once the frequency range is known, that domain can be investigated with spatial maps. In the context of plant CWs such a frequency could show the difference between the matrix and the CMFs. A measurement below that significant frequency would mainly reveal the response of the matrix, while mapping at a frequency above the significant one, e.g. the second eigenmode of a cantilever, would emphasise the fibre network. Furthermore, if a relation between T and excitation frequency exists, this method would allow the thermodynamic phase transitions of the CW to be imaged *in vivo*.

Additionally, the possibility of frequency dependent measurements allow tests of poroelastic behaviour and the relationship between thermodynamic phases and time responses of the cell wall. The investigation of poroelastic behaviour is interesting for

plants to obtain information about diffusivity of within the plant CW. This knowledge can provide further information about the processes of CW synthesis and remodelling. Information about the relationship between response time and temperature would be particularly useful for living organisms, because the change of thermodynamic properties, such as temperature and pH, not only change the mechanical properties of the wall but also the entire metabolism and enzymatic activity (see above). Therefore, time response measurements over several orders of magnitude could reveal thermodynamic information about the CW without interfering with biological functions.

Finally, we faced the problem that, although we were able to relate the extensibility, obtained from the high frequency experiments, to the elongation rate of unidirectionally growing hypocotyl cells, our result was about nine orders of magnitude larger than from previously reported measurements at the cellular level and the slow timescale of growth. To find an explanation which links these two very different length- and timescales, a renormalization of the problem is necessary. Naturally, the scaling behaviour should arise from the scaling behaviour of polymers (Doi and Edwards, 1986). If this is not the case, a new, unknown, kind of physics might be involved in the process. Moreover, the existing mathematical models of plant growth, are based on concepts of fluid mechanics, which describe a kind of diffusive growth (Lockhart, 1965a; Ortega, 1985; Veytsman and Cosgrove, 1998). Simple particle diffusion scales with the square root of the time, which would lead in our case to a correction factor of the order of four orders of magnitude and a direct scaling with time would be necessary to cover nine orders of magnitude. This could be achieved by the simple consideration, that during the dynamic AFM experiments not only the timescale is nine order of magnitudes different but there is also a length scale difference of three orders of magnitude. Of course, if both scale with the square root, this does not result in the nine orders of magnitude which are required for such an explanation. However, the underlying behaviour is very different to simple diffusion.

In fact it is directed diffusion, driven by the potential given by the turgor pressure and inhibited by the intrinsic viscosity of the plant CW. This kind of description exists (Doi, 2013) for polymer solutions but must be extended for biochemically active composite polymers to describe plant growth correctly.

To conclude, in this thesis polymer physics and thermodynamic approaches have not only been very successful in the interpretation of the dynamic AFM data but they are also very promising to gain a better understanding of plant growth. Additionally, the application of viscoelastic mapping to plants opens the possibility to retain or reject many existing theories about the stress-strain response of plant CWs, which is crucial for a better understanding of plant cell expansion.

6.4 Relevance Beyond Plant Biophysics

In this section I will elaborate on the importance of cellulose in material sciences and how the research presented in this thesis might be influencing the field of advanced materials.

Cellulose is a natural green material which is used in many products we use in our daily life, such as cloths made from cotton, paper, furniture, but it has many potential application in advanced materials such as, antimicrobial films, transparent films, felxible displays, reinforcing fillers for polymers, templates for electronic components, drug delivery systems, batteries, electroactive polymers, etc. (Moon et al., 2011). Their mechanical strength makes these fibres particularly interesting for creating lightweight strong materials (Song et al., 2018). One problem during the manufacturing process of such materials is that topological entanglement of the fibres causes mechanically weaknesses(Dufresne, 2018). Although the degree of entanglement in plant CW is not known, structural data suggests that it is very little (Zhang et al., 2016). In this sense mechanical investigation of plant development can help

to understand how the plant avoids entanglement. The possibility to obtain spatial viscoelastic information at different frequencies is particularly useful because the relaxation spectra of a material can provide information about entanglements (Hansen et al., 2011). In combination with frequency sweep measurements (see above) and biochemical and pharmacological treatments, our method can provide detailed information of how, where, and why entanglements of the polymer network occur.

Furthermore, in the future our society might potentially want to grow advanced materials, for which a detailed understanding of the time evolution of the thermodynamics of plant CW expansion is crucial, because the CW is an evolutionary highly developed natural advanced material. The application in this thesis of the Onsager principle to plant growth indicates that during such a process the thermodynamic variables must be near equilibrium. Although it is not clear if this is a requirement for precise enzymatic activity or to ensure mechanical or thermodynamic stability, study of this process *in vivo* with nanometre resolution, will help to resolve those questions.

Acronyms

AFM	atomic force microscopy
AM-FM	amplitude modulation/frequency modulation
CESA	cellulose synthase
CFM	cellular force microscopy
CMF	cellulose microfibril
Col-0	columbia
CW	cell wall
DEX	dexamethasone
DMSO	dimethyl sulfoxide
ECG	epicatechin gallate
ECGC	epigallocatechin gallate
FEM	finite element modelling
FIV	force indentation variation
FWHM	full width at half maximum
GalA	galacturonic acid
GOF	goodness of fit
HC	hemicellulose
HG	homogalacturonan
IXB	isoxaben
KV	Kelvin-Voigt
l.h.s	left-hand side
MD	molecular dynamic
MT	microtubule
MW	Maxwell
OGA	oligogalacturonide
PCL	polycaprolactone
PDE	partial differential equation
PM	plasma membrane
PME	pectin methyl esterase
r.h.s	right-hand side
RG	rhamnogalacturonan
Rha	rhamnose
ROI	region of interest
ROV	ratio of variances
SAM	shoot apical meristem
SEM	scanning electron microscopy
SLS	standard-linear solid
SPM	scanning probe microscopy
SSNMR	solid state nuclear magnetic resonance

WLC	worm-like chain
WT	wild type
XEH	xyloglucan endohydrolase
XET	xyloglucan endotransglucosylase
XG	Xyloglucan
XTH	xyloglucan endotransglucosylase/hydrolase

Bibliography

Al-Rekabi, Z. and Contera, S. Multifrequency AFM reveals lipid membrane mechancial properties and the effect of cholesterol in modulating viscoelasticity. Proceedings of the National Academy of Sciences, In Press:201719065 (2018). doi:10.1073/pnas.1719065115.

Ali, O. and Traas, J. Force-Driven Polymerization and Turgor-Induced Wall Expansion. Trends in Plant Science, 21(5):398–409 (2016). doi:10.1016/j.tplants.2016.01.019.

Anirudh, Q.-m. W., Michelle, C. M., and Zhao, L. O. X.-h. Separating viscoelasticity and poroelasticity of gels with di ff erent length and time scales. Acta Mechanica Sinica, 30(1):20–27 (2014).

Atmodjo, M. a., Hao, Z., and Mohnen, D. Evolving Views of Pectin Biosynthesis. Annual Review of Plant Biology, 64(1):747–779 (2013). doi:10.1146/annurev-arplant-042811-105534.

Barbacci, A., Lahaye, M., and Magnenet, V. Another Brick in the Cell Wall: Biosynthesis Dependent Growth Model. PLoS ONE, 8(9):e74400 (2013). doi:10.1371/journal.pone.0074400.

Bastien, R., Legland, D., Martin, M., Fregosi, L., Peaucelle, A., Douady, S., Moulia, B., and Höfte, H. KymoRod: a method for automated kinematic analysis of rod-shaped plant organs. The Plant Journal, 88(3):468–475 (2016). doi:10.1111/tpj.13255.

Braam, J. In touch: Plant responses to mechanical stimuli (2005). doi:10.1111/j.1469-8137.2004.01263.x.

Braybrook, S. A., Hofte, H., and Peaucelle, A. Probing the mechanical contributions of the pectin matrix: Insights for cell growth. Plant Signaling & Behavior, 7(8):1037–1041 (2012). doi:10.4161/psb.20768.

Braybrook, S. a. and Peaucelle, A. Mechano-Chemical Aspects of Organ Formation in Arabidopsis thaliana: The Relationship between Auxin and Pectin. PLoS ONE, 8(3) (2013). doi:10.1371/journal.pone.0057813.

Bryngelson, J. D., Onuchic, J. N., Socci, N. D., and Wolynes, P. G. Funnels, pathways, and the energy landscape of protein folding: A synthesis. Proteins: Structure, Function, and Bioinformatics, 21(3):167–195 (1995). doi:10.1002/prot.340210302.

Burgert, I., Frühmann, K., Keckes, J., Fratzl, P., and Stanzl-Tschegg, S. E. Microtensile Testing of Wood Fibers Combined with Video Extensometry for Efficient Strain Detection. Holzforschung, 57(6):661–664 (2003). doi:10.1515/HF.2003.099.

Callens-Raadschelders, M., De Batist, R., and Gevers, R. Debye relaxation equations for a standard linear solid with high relaxation strength. Journal of Materials Science, 12(2):251–263 (1977). doi:10.1007/BF00566265.

Camacho, L., Smertenko, A. P., Perez-Gomez, J., Hussey, P. J., and Moore, I. Arabidopsis Rab-E GTPases exhibit a novel interaction with a plasma-membrane phosphatidylinositol-4-phosphate 5-kinase. Journal of Cell Science, 122(23):4383–4392 (2009). doi:10.1242/jcs.053488.

Cartagena, A. and Raman, A. Local viscoelastic properties of live cells investigated using dynamic and quasi-static atomic force microscopy methods. Biophysical Journal, 106(5):1033–1043 (2014). doi:10.1016/j.bpj.2013.12.037.

Cartagena-Rivera, A. X., Wang, W.-H., Geahlen, R. L., Raman, A., Cartagena, A., Wang, W.-H., Geahlen, R. L., and Raman, A. Fast, multi-frequency, and quantitative nanomechanical mapping of live cells using the atomic force microscope. Scientific Reports, 5(June):11692 (2015). doi:10.1038/srep11692.

Cavalier, D. M., Lerouxel, O., Neumetzler, L., Yamauchi, K., Reinecke, A., Freshour, G., Zabotina, O. a., Hahn, M. G., Burgert, I., Pauly, M., Raikhel, N. V., and Keegstra, K. Disrupting two Arabidopsis thaliana xylosyltransferase genes results in plants deficient in xyloglucan, a major primary cell wall component. The Plant cell, 20(6):1519–1537 (2008). doi:10.1105/tpc.108.059873.

Chanliaud, E., Burrows, K. M., Jeronimidis, G., and Gidley, M. J. Mechanical properties of primary plant cell wall analogues. Planta, 215(6):989–996 (2002). doi:10.1007/s00425-002-0783-8.

Cosgrove, D. J. Cell Wall Yield Properties of Growing Tissue. Plant Physiology, 78(1985):347–356 (1985).

Cosgrove, D. J. Assembly and enlargement of the primary cell wall in plants. Annual review of cell and developmental biology, 13:171–201 (1997). doi:10.1146/annurev.cellbio.13.1.171.

Cosgrove, D. J. Growth of the plant cell wall. Nature reviews. Molecular cell biology, 6(11):850–861 (2005). doi:10.1038/nrm1746.

Cosgrove, D. J. Re-constructing our models of cellulose and primary cell wall assembly. Current Opinion in Plant Biology, 22:122–131 (2014). doi:10.1016/j.pbi.2014.11.001.

Cosgrove, D. J. Plant cell wall extensibility: Connecting plant cell growth with cell wall structure, mechanics, and the action of wall-modifying enzymes (2016). doi:10.1093/jxb/erv511.

Cosgrove, D. J. and Jarvis, M. C. Comparative structure and biomechanics of plant primary and secondary cell walls. Frontiers in Plant Science, 3(August):1–6 (2012). doi:10.3389/fpls.2012.00204.

Crowell, E. F., Timpano, H., Desprez, T., Franssen-Verheijen, T., Emons, A.-M., Höfte, H., and Vernhettes, S. Differential regulation of cellulose orientation at the inner and outer face of epidermal cells in the Arabidopsis hypocotyl. The Plant cell, 23(July):2592–2605 (2011). doi:10.1105/tpc.111.087338.

Delbrück, M. A physicist looks at biology. Transactions of the Connecticut Academy of Arts & Sciences, 38:173–190 (1949). doi:10.1007/BF02837334.

Derbyshire, P., Findlay, K., McCann, M. C., and Roberts, K. Cell elongation in Arabidopsis hypocotyls involves dynamic changes in cell wall thickness. Journal of Experimental Botany, 58(8):2079–2089 (2007). doi:10.1093/jxb/erm074.

Dick-Perez, M., Wang, T., Salazar, A., Zabotina, O. a., and Hong, M. Multidimensional solid-state NMR studies of the structure and dynamics of pectic polysaccharides in uniformly 13C-labeled Arabidopsis primary cell walls. Magnetic Resonance in Chemistry, 50(8):539–550 (2012). doi:10.1002/mrc.3836.

Dick-Pérez, M., Zhang, Y., Hayes, J., Salazar, A., Zabotina, O. a., and Hong, M. Structure and interactions of plant cell-wall polysaccharides by two- and three-dimensional magic-angle-spinning solid-state NMR. Biochemistry, 50(6):989–1000 (2011). doi:10.1021/bi101795q.

Ding, S.-Y. and Himmel, M. E. The maize primary cell wall microfibril: a new model derived from direct visualization. Journal of agricultural and food chemistry, 54(3):597–606 (2006). doi:10.1021/jf051851z.

Ding, S.-Y., Zhao, S., and Zeng, Y. Size, shape, and arrangement of native cellulose fibrils in maize cell walls. Cellulose, 21(2):863–871 (2014). doi:10.1007/s10570-013-0147-5.

Discher, D. E., Janmey, P., and Wang, Y. L. Tissue cells feel and respond to the stiffness of their substrate (2005). doi:10.1126/science.1116995.

Doi, M. Onsager's variational principle in soft matter. Journal of Physics Condensed Matter, 23(28):284118 (2011). doi:10.1088/0953-8984/23/28/284118.

Doi, M. Soft Matter Physics. OUP Oxford (2013). ISBN 978-0-19-965295-2.

Doi, M. A principle in dynamic coarse graining–Onsager principle and its applications. European Physical Journal: Special Topics, 225(8-9):1411–1421 (2016). doi:10.1140/epjst/e2016-60128-5.

Doi, M. and Edwards, S. F. The Theory of Polymer Dynamics. Oxford University Press, Oxford (1986). ISBN 9780198520337.

Dufresne, A. Cellulose nanomaterials as green nanoreinforcements for polymer nanocomposites. Philosophical Transactions of the Royal Society A: Mathematical, Physical and Engineering Sciences, 376(2112):20170040 (2018). doi:10.1098/rsta.2017.0040.

Dumais, J. and Kwiatkowska, D. Analysis of surface growth in shoot apices. Plant Journal, 31(2):229–241 (2002). doi:10.1046/j.1365-313X.2001.01350.x.

Dyson, R. J., Band, L. R., and Jensen, O. E. A model of crosslink kinetics in the expanding plant cell wall: Yield stress and enzyme action. Journal of Theoretical Biology, 307:125–136 (2012). doi:10.1016/j.jtbi.2012.04.035.

Dyson, R. J. and Jensen, O. E. A fibre-reinforced fluid model of anisotropic plant cell growth. Journal of Fluid Mechanics, 655:472–503 (2010). doi:10.1017/S002211201000100X.

Dyson, R. J., Vizcay-Barrena, G., Band, L. R., Fernandes, A. N., French, A. P., Fozard, J. A., Hodgman, T. C., Kenobi, K., Pridmore, T. P., Stout, M., Wells, D. M., Wilson, M. H., Bennett, M. J., and Jensen, O. E. Mechanical modelling quantifies the functional importance of outer tissue layers during root elongation and bending. New Phytologist, 202(4):1212–1222 (2014). doi:10.1111/nph.12764.

England, J. L. Statistical physics of self-replication. J. Chem. Phys. Additional information on J. Chem. Phys. Journal Homepage: THE JOURNAL OF CHEMICAL PHYSICS, 139(139) (2013). doi:10.1063/1.4818538doi.org/10.1063/1.4818538.

Feynman, R. P. The Feynman Lectures on Physics; Vol. I, volume I. INGRAM PUBLISHER SERVICES US (1965). ISBN 9787532378784. doi:10.1119/1.1972241.

Forouzesh, E., Goel, A., MacKenzie, S. a., and Turner, J. a. In vivo extraction of Arabidopsis cell turgor pressure using nanoindentation in conjunction with finite element modeling. Plant Journal, 73(3):509–520 (2013). doi:10.1111/tpj.12042.

Fu, Y., Gu, Y., Zheng, Z., Wasteneys, G., and Yang, Z. Arabidopsis interdigitating cell growth requires two antagonistic pathways with opposing action on cell morphogenesis. Cell, 120(5):687–700 (2005). doi:10.1016/j.cell.2004.12.026.

Gardel, M. L., Shin, J. H., MacKintosh, F. C., Mahadevan, L., Matsudaira, P., and Weitz, D. A. Elastic behavior of cross-linked and bundled actin networks. Science, 304(5675):1301–1305 (2004). doi:10.1126/science.1095087.

Gavara, N. Combined strategies for optimal detection of the contact point in AFM force-indentation curves obtained on thin samples and adherent cells. Scientific Reports, 6(February):21267 (2016). doi:10.1038/srep21267.

Gavara, N. and Chadwick, R. S. Determination of the elastic moduli of thin samples and adherent cells using conical atomic force microscope tips. Nature Nanotechnology, 7(September):733–736 (2012). doi:10.1038/nnano.2012.163.

Gendreau, E., Traas, J., T. Desnos, O. G., Caboche, M., and Hofte, H. Cellular Basis of Hypocotyl Growth in Arabidopsis thaliana. Plant Physiology, 114(1):295–305 (1997).

Gjetting, K. S. K., Ytting, C. K., Schulz, A., and Fuglsang, A. T. Live imaging of intra- and extracellular pH in plants using pHusion, a novel genetically encoded biosensor. Journal of experimental botany, 63(8):3207–18 (2012). doi:10.1093/jxb/ers040.

Greenspan, P., Mayer, E. P., and Fowler, S. D. Nile red: A selective fluorescent stain for intracellular lipid droplets. Journal of Cell Biology, 100(3):965–973 (1985). doi:10.1083/jcb.100.3.965.

Guo, Y., Yuan, T., Xiao, Z., Tang, P., Xiao, Y., Fan, Y., and Zhang, X. Hydrogels of collagen/chondroitin sulfate/hyaluronan interpenetrating polymer network for cartilage tissue engineering. Journal of Materials Science: Materials in Medicine, 23(9):2267–2279 (2012). doi:10.1007/s10856-012-4684-5.

Hamant, O. Mechano-devo (2017). doi:10.1016/j.mod.2017.02.004.

Hamant, O., Traas, J., Brisson, N., and Mare, A. The mechanics behind plant development. New Phytologist, 185(2009):369–385 (2010). doi:10.1111/j.1469-8137.2009.03100.x.

Hansen, S. L., Ray, P. M., Karlsson, A. O., Jorgensen, B., Borkhardt, B., Petersen, B. L., and Ulvskov, P. Mechanical Properties of Plant Cell Walls Probed by Relaxation Spectra. PLANT PHYSIOLOGY, 155(1):246–258 (2011). doi:10.1104/pp.110.166629.

Harris, A. R. and Charras, G. T. Experimental validation of atomic force microscopy-based cell elasticity measurements. Nanotechnology, 22(34):345102 (2011). doi:10.1088/0957-4484/22/34/345102.

Haugstad, G. Atomic Force Microscopy: Understanding Basic Modes and Advanced Applications (2012). ISBN 9780470638828. doi:10.1002/9781118360668.

Hayot, C. M., Forouzesh, E., Goel, A., Avramova, Z., and Turner, J. a. Viscoelastic properties of cell walls of single living plant cells determined by dynamic nanoindentation. Journal of Experimental Botany, 63(7):2525–2540 (2012). doi:10.1093/jxb/err428.

Heim, D. R., Skomp, J. R., Tschabold, E. E., and Larrinua, I. M. Isoxaben Inhibits the Synthesis of Acid Insoluble Cell Wall Materials In Arabidopsis thaliana. Plant physiology, 93(2):695–700 (1990). doi:10.1104/pp.93.2.695.

Heimburg, T. Mechanical aspects of membrane thermodynamics. Estimation of the mechanical properties of lipid membranes close to the chain melting transition from calorimetry. Biochimica et Biophysica Acta (BBA) - Biomembranes, 1415(1):147–162 (1998). doi:10.1016/S0005-2736(98)00189-8.

Heimburg, T. Thermal biophysics of membranes. Wiley-VCH Verlag (2007). ISBN 3527611606.

Heimburg, T. and Jackson, A. D. On soliton propagation in biomembranes and nerves. Proceedings of the National Academy of Sciences of the United States of America, 102(28):9790–5 (2005). doi:10.1073/pnas.0503823102.

Herth, W. and Schnepf, E. The fluorochrome, calcofluor white, binds oriented to structural polysaccharide fibrils. Protoplasma, 105(1-2):129–133 (1980). doi:10.1007/BF01279855.

Hertz, H. R. Über die Beruhrüng fester elastischer Körper. Journal fur die reine und angewandte Mathematik, 92:156–171 (1882). doi:10.1038/055006f0.

Hocq, L., Pelloux, J., and Lefebvre, V. Connecting Homogalacturonan-Type Pectin Remodeling to Acid Growth (2017). doi:10.1016/j.tplants.2016.10.009.

Hong, L., Dumond, M., Tsugawa, S., Sapala, A., Routier-Kierzkowska, A.-L., Zhou, Y., Chen, C., Kiss, A., Zhu, M., Hamant, O., Smith, R., Komatsuzaki, T., Li, C.-B., Boudaoud, A., and Roeder, A. Variable Cell Growth Yields Reproducible OrganDevelopment through Spatiotemporal Averaging. Developmental Cell, 38(1):15–32 (2016). doi:10.1016/j.devcel.2016.06.016.

Hooke, R. De Potentia Reflitutiva, or of Spring. Explaining the Power of Springing Bodies. John Martyn (1678).

Horowitz, J. M. and England, J. L. Spontaneous fine-tuning to environment in many-species chemical reaction networks. Proceedings of the National Academy of Sciences of the United States of America, 114(29):7565–7570 (2017). doi:10.1073/pnas.1700617114.

Kachman, T., Owen, J. A., and England, J. L. Self-Organized Resonance during Search of a Diverse Chemical Space. Physical Review Letters, 119(3):038001 (2017). doi:10.1103/PhysRevLett.119.038001.

Keating, P. N. Relationship between the macroscopic and microscopic theory of crystal elasticity. I. Primitive crystals. Physical Review, 152(2):774–779 (1966). doi:10.1103/PhysRev.152.774.

Kim, S. J. and Brandizzi, F. The plant secretory pathway for the trafficking of cell wall polysaccharides and glycoproteins (2016). doi:10.1093/glycob/cww044.

Kirchhelle, C., Chow, C. M., Foucart, C., Neto, H., Stierhof, Y. D., Kalde, M., Walton, C., Fricker, M., Smith, R. S., Jérusalem, A., Irani, N., and Moore, I. The Specification of Geometric Edges by a Plant Rab GTPase Is an Essential Cell-Patterning Principle During Organogenesis in Arabidopsis. Developmental Cell, 36(4):386–400 (2016). doi:10.1016/j.devcel.2016.01.020.

Kocun, M., Labuda, A., Meinhold, W., Revenko, I., and Proksch, R. Fast, High Resolution, and Wide Modulus Range Nanomechanical Mapping with Bimodal Tapping Mode. ACS Nano, 11(10):10097–10105 (2017). doi:10.1021/acsnano.7b04530.

Kothari, K., Hu, Y., Gupta, S., and Elbanna, A. Mechanical response of 2D polymer networks: role of topology, rate dependence and damage accumulation. Journal of Applied Mechanics (2018). doi:10.1115/1.4038883.

Lee, D., Barber, J. R., and Thouless, M. D. Indentation of an elastic half space with material properties varying with depth. International Journal of Engineering Science, 47(11-12):1274–1283 (2009). doi:10.1016/j.ijengsci.2008.08.005.

Lewicka, S. and Pietruszka, M. Generalized phenomenological equation of plant growth. General Physiology and Biophysics, 29(1):95–105 (2010). doi:10.4149/gpb-2010-01-95.

Lewis, K. C., Selzer, T., Shahar, C., Udi, Y., Tworowski, D., and Sagi, I. Inhibition of pectin methyl esterase activity by green tea catechins. Phytochemistry, 69(14):2586–2592 (2008). doi:10.1016/j.phytochem.2008.08.012.

Lockhart, J. A. An analysis of irreversible plant cell elongation. Journal of theoretical biology, 8(2):264–275 (1965a). doi:10.1016/0022-5193(65)90077-9.

Lockhart, J. A. The Analysis of Interactions of Physical and Chemical Factors on Plant Growth. Annual Review of Plant Physiology, 16(1):37–52 (1965b). doi:10.1146/annurev.pp.16.060165.000345.

Lockhart, J. A. An interpretation of cell growth curves. Plant physiology, 48(3):245–248 (1971). doi:10.1104/PP.48.3.245.

Lopez-Sanchez, P., Rincon, M., Wang, D., Brulhart, S., Stokes, J. R., and Gidley, M. J. Micromechanics and poroelasticity of hydrated cellulose networks. Biomacromolecules, 15(6):2274–2284 (2014). doi:10.1021/bm500405h.

MacKintosh, F. C., Käs, J., and Janmey, P. A. Elasticity of semiflexible biopolymer networks. Physical Review Letters, 75(24):4425–4428 (1995). doi:10.1103/PhysRevLett.75.4425.

Manfield, I. W., Orfila, C., McCartney, L., Harholt, J., Bernal, A. J., Scheller, H. V., Gilmartin, P. M., Mikkelsen, J. D., Knox, J. P., and Willats, W. G. T. Novel cell wall architecture of isoxaben-habituated Arabidopsis suspension-cultured cells: Global transcript profiling and cellular analysis. Plant Journal, 40(2):260–275 (2004). doi:10.1111/j.1365-313X.2004.02208.x.

Mariani, G., Goujon, A., Moulin, E., Rawiso, M., Giuseppone, N., and Buhler, E. Integration of molecular machines into supramolecular materials: actuation between equilibrium polymers and crystal-like gels. Nanoscale, 9(46):18456–18466 (2017). doi:10.1039/C7NR04251E.

Milani, P., Gholamirad, M., Traas, J., Arnéodo, A., Boudaoud, A., Argoul, F., and Hamant, O. In vivo analysis of local wall stiffness at the shoot apical meristem in Arabidopsis using atomic force microscopy. Plant Journal, 67:1116–1123 (2011). doi:10.1111/j.1365-313X.2011.04649.x.

Mischke, C. and Shigley, J. E. Mechanical Engineering Design. McGraw-Hill (2001). ISBN 9780072373011.

Miyahara, Y., Roy-Gobeil, A., and Grutter, P. Quantum state readout of individual quantum dots by electrostatic force detection. Nanotechnology, 28(6):064001 (2017). doi:10.1088/1361-6528/aa5261.

Moon, R. J., Martini, A., Nairn, J., Simonsen, J., and Youngblood, J. Cellulose nanomaterials review: structure, properties and nanocomposites., volume 40. The Royal Society of Chemistry (2011). ISBN 1765496829. doi:10.1039/c0cs00108b.

Mravec, J., Kračun, S. K., Rydahl, M. G., Westereng, B., Miart, F., Clausen, M. H., Fangel, J. U., Daugaard, M., Van Cutsem, P., De Fine Licht, H. H., Höfte, H., Malinovsky, F. G., Domozych, D. S., and Willats, W. G. T. Tracking developmentally regulated post-synthetic processing of homogalacturonan and chitin using reciprocal oligosaccharide probes. Development, 141(24):4841–4850 (2014). doi:10.1242/dev.113365.

Murashige, T. and Skoog, F. A Revised Medium for Rapid Growth and Bio Assays with Tobacco Tissue Cultures. Physiologia Plantarum, 15(3):473–497 (1962). doi:10.1111/j.1399-3054.1962.tb08052.x.

Newman, R. H., Hill, S. J., and Harris, P. J. Wide-Angle X-Ray Scattering and Solid-State Nuclear Magnetic Resonance Data Combined to Test Models for Cellulose Microfibrils in Mung Bean Cell Walls. Plant Physiology, 163(4):1558–1567 (2013). doi:10.1104/pp.113.228262.

Ohmiya, Y., Samejima, M., Shiroishi, M., Amano, Y., Kanda, T., Sakai, F., and Hayashi, T. Evidence that endo-1,4-beta-glucanases act on cellulose in suspension-cultured poplar cells. The Plant Journal, 24(2):147–158 (2000). doi:10.1046/j.1365-313x.2000.00860.x.

Oosterveld, A., Beldman, G., Searle-Van Leeuwen, M. J., and Voragen, A. G. Effect of enzymatic deacetylation on gelation of sugar beet pectin in the presence of calcium. Carbohydrate Polymers, 43(3):249–256 (2000). doi:10.1016/S0144-8617(00)00174-0.

Ortega, J. K. Augmented growth equation for cell wall expansion. Plant physiology, 79(1):318–320 (1985). doi:10.1104/pp.79.1.318.

Park, Y. B. and Cosgrove, D. J. A Revised Architecture of Primary Cell Walls Based on Biomechanical Changes Induced by Substrate-Specific Endoglucanases. Plant Physiology, 158(4):1933–1943 (2012a). doi:10.1104/pp.111.192880.

Park, Y. B. and Cosgrove, D. J. Changes in Cell Wall Biomechanical Properties in the Xyloglucan-Deficient xxt1/xxt2 Mutant of Arabidopsis. Plant Physiology, 158(1):465–475 (2012b). doi:10.1104/pp.111.189779.

Pauly, M., Gille, S., Liu, L., Mansoori, N., de Souza, A., Schultink, A., and Xiong, G. Hemicellulose biosynthesis. Planta, 238(4):627–642 (2013). doi:10.1007/s00425-013-1921-1.

Peaucelle, A. AFM-based Mapping of the Elastic Properties of Cell Walls: at Tissue, Cellular, and Subcellular Resolutions. Journal of visualized experiments : JoVE, (89):1–6 (2014). doi:10.3791/51317.

Peaucelle, A., Braybrook, S., and Höfte, H. Cell wall mechanics and growth control in plants: the role of pectins revisited. Frontiers in Plant Science, 3(June):1–6 (2012). doi:10.3389/fpls.2012.00121.

Peaucelle, A., Braybrook, S. a., Le Guillou, L., Bron, E., Kuhlemeier, C., Höfte, H., Le Guillou, L., Bron, E., Kuhlemeier, C., and Höfte, H. Pectin-induced changes in cell wall mechanics underlie organ initiation in Arabidopsis. Current Biology, 21(20):1720–1726 (2011). doi:10.1016/j.cub.2011.08.057.

Peaucelle, A., Wightman, R., and Höfte, H. The Control of Growth Symmetry Breaking in the Arabidopsis Hypocotyl. Current Biology, pages 1746–1752 (2015). doi:10.1016/j.cub.2015.05.022.

Pelletier, S., Van Orden, J., Wolf, S., Vissenberg, K., Delacourt, J., Ndong, Y. A., Pelloux, J., Bischoff, V., Urbain, A., Mouille, G., Lemonnier, G., Renou, J. P., and Höfte, H. A role for pectin de-methylesterification in a developmentally regulated growth acceleration in dark-grown Arabidopsis hypocotyls. New Phytologist, 188(3):726–739 (2010). doi:10.1111/j.1469-8137.2010.03409.x.

Pelloux, J., Rustérucci, C., and Mellerowicz, E. J. New insights into pectin methylesterase structure and function (2007). doi:10.1016/j.tplants.2007.04.001.

Perrault, C., Brugues, A., Bazellieres, E., Ricco, P., Lacroix, D., and Trepat, X. Traction Forces of Endothelial Cells under Slow Shear Flow. Biophysical Journal, 109(8):1533–1536 (2015). doi:10.1016/j.bpj.2015.08.036.

Pietruszka, M. General proof of the validity of a new tensor equation of plant growth. Journal of Theoretical Biology, 256(4):584–585 (2009a). doi:10.1016/j.jtbi.2008.11.001.

Pietruszka, M. Self-consistent equation of plant cell growth. General Physiology and Biophysics, 28(4):340–346 (2009b). doi:10.4149/gpb_2009_04_340.

Pietruszka, M. pH / T duality – equation of state for plants. arXiv, (1505.00327):1–20 (2015).

Pietruszka, M. and Lewicka, S. Anisotropic plant growth due to phototropism. Journal of Mathematical Biology, 54(1):45–55 (2007). doi:10.1007/s00285-006-0045-7.

Plotkin, S. S. and Onuchic, J. N. Understanding protein folding with energy landscape theory. Part I: Basic concepts (2002). doi:10.1017/S0033583502003761.

Poletto, M., Pistor, V., and J., A. Structural Characteristics and Thermal Properties of Native Cellulose. In Cellulose - Fundamental Aspects. InTech (2013). ISBN 9789535111832. doi:10.5772/50452.

Popper, Z. A. and Fry, S. C. Xyloglucan-pectin linkages are formed intra-protoplasmically, contribute to wall-assembly, and remain stable in the cell wall. Planta, 227(4):781–794 (2008). doi:10.1007/s00425-007-0656-2.

Ralet, M.-C., Crépeau, M.-J., Buchholt, H.-C., and Thibault, J.-F. Polyelectrolyte behaviour and calcium binding properties of sugar beet pectins differing in their degrees of methylation and acetylation. Biochemical Engineering Journal, 16(2):191–201 (2003). doi:10.1016/S1369-703X(03)00037-8.

Raman, A., Trigueros, S., Cartagena, A., Stevenson, a. P. Z., Susilo, M., Nauman, E., and Contera, S. A. Mapping nanomechanical properties of live cells using multi-harmonic atomic force microscopy. Nature nanotechnology, 6(12):809–14 (2011). doi:10.1038/nnano.2011.186.

Ramos, D., Tamayo, J., Mertens, J., and Calleja, M. Photothermal excitation of microcantilevers in liquids. Journal of Applied Physics, 99(12) (2006). doi:10.1063/1.2205409.

Ray, P. M., Green, P. B., and Cleland, R. Role of Turgor in Plant Cell Growth. Nature, 239(5368):163–164 (1972). doi:10.1038/239163a0.

Routier-Kierzkowska, A.-L., Weber, a., Kochova, P., Felekis, D., Nelson, B. J., Kuhlemeier, C., Smith, R. S., Technologies, B., Routier-Kierzkowska, A.-L., Weber, a., Kochova, P., Felekis, D., Nelson, B. J., Kuhlemeier, C., Smith, R. S., and Technologies, B. Cellular Force Microscopy for in Vivo Measurements of Plant Tissue Mechanics. Plant Physiology, 158(April):1514–1522 (2012). doi:10.1104/pp.111.191460.

Roylance, D. Atomistic Basis of Elasticity. ACe, 5:3 (2000).

Rubinstein, M. and Colby, R. H. Polymer physics (2003). doi:10.1002/pi.1472.

Sader, J. E., Borgani, R., Gibson, C. T., Haviland, D. B., Higgins, M. J., Kilpatrick, J. I., Lu, J., Mulvaney, P., Shearer, C. J., Slattery, A. D., Thorén, P. A., Tran, J., Zhang, H., Zhang, H., and Zheng, T. A virtual instrument to standardise the calibration of atomic force microscope cantilevers. Review of Scientific Instruments, 87(9):093711 (2016). doi:10.1063/1.4962866.

Sampathkumar, A., Krupinski, P., Wightman, R., Milani, P., Berquand, A., Boudaoud, A., Hamant, O., Jönsson, H., and Meyerowitz, E. M. Subcellular and supracellular mechanical stress prescribes cytoskeleton behavior in Arabidopsis cotyledon pavement cells. eLife, 3:e01967 (2014). doi:10.7554/eLife.01967.

Saxe, F., Weichold, S., Reinecke, A., Lisec, J., Döring, A., Neumetzler, L., Burgert, I., and Eder, M. Age Effects on Hypocotyl Mechanics. Plos One, 11(12):e0167808 (2016). doi:10.1371/journal.pone.0167808.

Scheller, H. V. and Ulvskov, P. Hemicelluloses. Annual review of plant biology, 61:263–89 (2010). doi:10.1146/annurev-arplant-042809-112315.

Schrödinger, E. What is life?: The physical aspect of the living cell ; with Mind and matter ; & Autobiographical sketches. Cambridge University Press (1944). ISBN 0521427088. doi:10.1017/CBO9781107295629.

Sneddon, I. N. The relation between load and penetration in the axisymmetric boussinesq problem for a punch of arbitrary profile. International Journal of Engineering Science, 3(1):47–57 (1965). doi:10.1016/0020-7225(65)90019-4.

Song, J., Chen, C., Zhu, S., Zhu, M., Dai, J., Ray, U., Li, Y., Kuang, Y., Li, Y., Quispe, N., Yao, Y., Gong, A., Leiste, U. H., Bruck, H. A., Zhu, J. Y., Vellore, A., Li, H., Minus, M. L., Jia, Z., Martini, A., Li, T., and Hu, L. Processing bulk natural wood into a high-performance structural material. Nature, 554(7691):224–228 (2018). doi:10.1038/nature25476.

Thomas, L. H., Forsyth, V. T., Šturcová, A., Kennedy, C. J., May, R. P., Altaner, C. M., Apperley, D. C., Wess, T. J., and Jarvis, M. C. Structure of Cellulose Microfibrils in Primary Cell Walls from Collenchyma. Plant Physiology, 161(1):465–476 (2013). doi:10.1104/pp.112.206359.

Thompson, D. W. On Growth and Form. Cambridge University Press, Cambridge (1917). ISBN 9780486671352.

Vella, D., Ajdari, A., Vaziri, A., and Boudaoud, A. The indentation of pressurized elastic shells: From polymeric capsules to yeast cells. Journal of the Royal Society Interface (2011). doi:10.1098/rsif.2011.0352.

Veytsman, B. a. and Cosgrove, D. J. A model of cell wall expansion based on thermodynamics of polymer networks. Biophysical journal, 75(5):2240–50 (1998). doi:10.1016/S0006-3495(98)77668-4.

Villares, A., Moreau, C., Dammak, A., Capron, I., and Cathala, B. Kinetic aspects of the adsorption of xyloglucan onto cellulose nanocrystals. Soft Matter (2015). doi:10.1039/C5SM01413A.

Vlassak, J. J., Ciavarella, M., Barber, J. R., and Wang, X. The indentation modulus of elastically anisotropic materials for indenters of arbitrary shape. Journal of the Mechanics and Physics of Solids, 51(9):1701–1721 (2003). doi:10.1016/S0022-5096(03)00066-8.

Voïtchovsky, K., Kuna, J. J., Contera, S. A., Tosatti, E., and Stellacci, F. Direct mapping of the solid-liquid adhesion energy with subnanometre resolution. Nature nanotechnology, 5(6):401–5 (2010). doi:10.1038/nnano.2010.67.

Wang, C. X., Wang, L., and Thomas, C. R. Modelling the Mechanical Properties of Single Suspension-Cultured Tomato Cells. Annals of Botany, 93(4):443–453 (2004). doi:10.1093/aob/mch062.

Wang, T. and Hong, M. Solid-state NMR investigations of cellulose structure and interactions with matrix polysaccharides in plant primary cell walls (2016). doi:10.1093/jxb/erv416.

Wang, T., Park, Y. B., Cosgrove, J., Daniel, and Hong, M. Cellulose-Pectin Spatial Contacts Are Inherent to Never-Dried Arabidopsis thaliana Primary Cell Walls: Evidence from Solid-State NMR. Plant Physiology, 168(July):pp.00665.2015 (2015). doi:10.1104/pp.15.00665.

Wang, T., Yang, H., Kubicki, J. D., and Hong, M. Cellulose Structural Polymorphism in Plant Primary Cell Walls Investigated by High-Field 2D Solid-State NMR Spectroscopy and Density Functional Theory Calculations. Biomacromolecules, page acs.biomac.6b00441 (2016). doi:10.1021/acs.biomac.6b00441.

Wang, T., Zabotina, O., and Hong, M. Pectin-cellulose interactions in the arabidopsis primary cell wall from two-dimensional magic-angle-spinning solid-state nuclear magnetic resonance. Biochemistry, 51(49):9846–9856 (2012). doi:10.1021/bi3015532.

Weber, A., Braybrook, S., Huflejt, M., Mosca, G., Routier-Kierzkowska, A.-L., and Smith, R. S. Measuring the mechanical properties of plant cells by combining micro-indentation with osmotic treatments. Journal of Experimental Botany (2015). doi:10.1093/jxb/erv135.

Woodside, M. T., Anthony, P. C., Behnke-Parks, W. M., Larizadeh, K., Herschlag, D., and Block, S. M. Direct measurement of the full, sequence-dependent folding landscape of a nucleic acid. Science, 314(5801):1001–1004 (2006). doi:10.1126/science.1133601.

Yang, Z. Cell Polarity Signaling in Arabidopsis. Annual Review of Cell and Developmental Biology, 24(1):551–575 (2008). doi:10.1146/annurev.cellbio.23.090506.123233.

Zhang, T., Mahgsoudy-Louyeh, S., Tittmann, B., and Cosgrove, D. J. Visualization of the nanoscale pattern of recently-deposited cellulose microfibrils and matrix materials in never-dried primary walls of the onion epidermis. Cellulose, 21:853–862 (2014a). doi:10.1007/s10570-013-9996-1.

Zhang, T., Mahgsoudy-Louyeh, S., Tittmann, B., and Cosgrove, D. J. Visualization of the nanoscale pattern of recently-deposited cellulose microfibrils and matrix materials in never-dried primary walls of the onion epidermis. Cellulose, 21(2):853–862 (2014b). doi:10.1007/s10570-013-9996-1.

Zhang, T., Vavylonis, D., Durachko, D. M., and Cosgrove, D. J. Nanoscale movements of cellulose microfibrils in primary cell walls. Nature Plants, 3(5):17056 (2017). doi:10.1038/nplants.2017.56.

Zhang, T., Zheng, Y., and Cosgrove, D. J. Spatial organization of cellulose microfibrils and matrix polysaccharides in primary plant cell walls as imaged by multichannel atomic force microscopy. The Plant Journal, 85:179–192 (2016). doi:10.1111/tpj.13102.

Zhao, Z., Crespi, V. H., Kubicki, J. D., Cosgrove, D. J., and Zhong, L. Molecular dynamics simulation study of xyloglucan adsorption on cellulose surfaces: Effects of surface hydrophobicity and side-chain variation. Cellulose, 21(2):1025–1039 (2014). doi:10.1007/s10570-013-0041-1.

Zheng, H., Kunst, L., Hawes, C., and Moore, I. A GFP-based assay reveals a role for RHD3 in transport between the endoplasmic reticulum and Golgi apparatus. Plant Journal, 37(3):398–414 (2004). doi:10.1046/j.1365-313X.2003.01969.x.

Zieschang, H. E., Brain, P., and Barlow, P. W. Modelling of root growth and bending in two dimensions. Journal of Theoretical Biology, 184(3):237–246 (1997). doi:10.1006/jtbi.1996.0259.